Interaction of fast (keV) hydrogen ions/atoms with surfaces : diffraction and negative ion formation

Yang Xiang

ORSAY
N° D'ORDRE:

UNIVERSITE DE PARIS SUD
U.F.R. SCIENTIFIQUE D'ORSAY
THESE

présentée pour obtenir le grade de

DOCTEUR EN SCIENCES
DE L'UNIVERSITE PARIS XI, ORSAY

par

Yang XIANG

Sujet:

Interaction d'atomes /ions hydrogène rapides (keV) avec des surfaces: diffraction et formation d'ions négatifs

Soutenue le 14 septembre 2012 devant la commission d'examen:

M. Didier LEMOINE	Rapporteur
M. Francisco PERALES	Rapporteur
M. Jacques ROBERT	Président
M. Serge MARTIN	Examinateur
M Philippe RONCIN	Directeur de thèse
M. Hocine Khemliche	Invité

Acknowledgements

First, I would like to thank my supervisors Philippe RONCIN and Hocine KHEMLICHE for the continuous support of my Ph.D study and research, for their patience, motivations, enthusiasms, and immense knowledge; their guidance helped me in all the time of research and writing of this thesis.

It is great pleasure to work with my colleagues Anouchah MOMENI, Nenad BUNDALESKI, Pierre SOULISSE, Boubekeur LALMI, Maxime DEBIOSSAC. My special thanks to them for their helps, encouragements, numerous discussions and sharing the valuable ideas throughout my PhD. The international ambience reigning in the group enriched my personal experience through the contact of many international researchers such as Esteban A. Sanchez, Oscar Grizzi, Leonardo De Jesus Salazar from Atomic Energy Centre Bariloche in Argentina. I am truly indebted to Esteban A. Sanchez for his patience in answering me all kind of questions and his helps during my short stay in Argentina.

I wish to thank all the people who are working in ISMO (former LCAM), for their kindness, and generous hospitality. Many thanks to Dr. Andrei BORISOV, Dr. Laurent GUILLEMOT Dr. Vladimir ESAULOV, Catherine LACAN, and Nicolas BRIANT for their pedagogically answer of all my questions concerning the physical aspects, computer science, and experimental technique. I deeply thank the many people worked in the PhD office, Marie Taillandier, Erika Porcel, Lin Chen, Li Sha, Pierre Soulisse, Maxime Debiossac, Chengjun Li, Jie Shen and Juanjuan Jia, for their repeatedly helped me in all kind of problems which happens to an international students.

I owe a great deal of appreciation and gratitude to Catherine and Jacques Lieutaud, thanks for their kindness, generous hospitality during the 4 years. I would also like to thank Pascale Elbaz who taught me French and many other things.

I could not have undertaken the research and writing my thesis without the support of my parents and parents-in-law. Many thanks also to my wife, Hong ZHU, for her supports, encouragement and understanding in all these years.

I wish to thank my many friends and family that have each contributed in their own ways and have helped to make my research journey all that more rewarding, In no particular order, and with apologies to those I have missed, I wish to thank Ping Xiang, Rong Xiang, Yanhui Jia, Liang Chen, Weiguo Bao, Chongjian Chen, and Wenhua Zhang. I especially want to convey my gratitude to Nenad BUNDALESKI, who was of enormous help in the revision of this manuscript.

I take this opportunity to sincerely acknowledge the CHINA SCHOLARSHIP COUNCIL for providing living cost to me for four years in France.

Besides, I would like to thank the rest of my thesis committee: Prof. Didier LEMOINE, Dr. Francisco PERALES, Prof. Jacques ROBERT, Prof. Serge MARTIN, for their encouragement, insightful comments, and hard questions.

Contents

Synthèse

Le transfert de charge est un processus majeur de l'interaction de particules lourdes (atomes, ions, molécules) avec des surfaces. Il intervient dans la chimie des surfaces, le dépôt d'énergie (potentielle) et sa compréhension est primordiale pour la bonne interprétation des techniques d'analyse de surface telles que LEIS (Low Energy on Scatering) ou ISS (Ion Scattering Spectroscopy).

Bien qu'étudié depuis plus de trente ans, la très grande sensibilité du transfert de charge aux caractéristiques chimiques et structurales de la surface empêche la généralisation de modèles simples. Par ailleurs, le transfert d'électrons dépend fortement de la structure électronique de la surface; celle-ci étant parfois différente de celle du volume (relaxation, états de surface, etc.), le transfert de charge peut servir de sonde de cette structure électronique superficielle.

Lorsque les particules incidentes ont une énergie dans le régime du keV, d'autres processus liés au transfert d'énergie cinétique peuvent intervenir, éjection d'électrons de la surface (émission secondaire) ou d'atomes de la surface (pulvérisation). L'énergie cinétique des atomes éjectés, ainsi que celle du projectile diffusé, est déterminée par des considérations purement cinématiques. Nous pouvons distinguer deux situations extrêmes:

- incidence normale à la surface ; dans ce cas le transfert d'énergie ne fait intervenir qu'un nombre très réduit (1 ou 2) d'atomes de la surface. Cette géométrie est celle souvent choisie pour la technique LEIS.

- incidence rasante ; le transfert d'énergie implique un grand nombre (10 à 30) d'atomes de la surface. Cette géométrie permet de limiter la quantité d'énergie transférée à la surface, le projectile suit une trajectoire parfaitement définie. Cette géométrie est idéale pour étudier tous les mécanismes non cinématiques, c'est-à-dire la diffusion élastique ainsi que les processus d'échange de charge.

Les expériences menées dans ce travail de thèse ont toutes été effectuées en incidence rasante afin de pouvoir mieux identifier les processus électroniques lorsqu'ils sont présents (émission d'électrons Auger, formation d'excitons de surface, ionization, etc. ou bien de caractériser au mieux la diffusion élastique [1]).

L'objectif de ce travail de thèse était d'étudier les processus électroniques ayant lieu lors de la diffusion, en incidence rasante sur des surfaces cristallines, d'ions d'énergie proche du keV. Dans cette configuration, les ions incidents sont diffusés au-dessus de la première couche de la surface, évitant ainsi toute pénétration dans le matériau. Nous avons ainsi pu nous

concentrer sur la capture d'électrons de la surface vers des ions ou des atomes, menant dans ce dernier cas à la formation d'ions négatifs.

La thèse est divisée en deux parties : la formation d'ions négatifs H^- sur le graphite HOPG (Highly Oriented Pyrolytic Graphite) et la diffraction inélastique impliquant des ions H^+ sur LiF(001). Dans les deux cas, l'approche expérimentale a consisté à détecter en coïncidence les particules diffusées, éventuellement analysées en état de charge et en énergie (par mesure de leur temps de vol avec un faisceau pulsé), et les électrons (dont on mesure la statistique et l'énergie à partir de leur temps de vol) éjectés lors de l'interaction. Ce type d'approche nous permet par exemple de corréler, pour une particule diffusée dans un état de charge donné, la perte d'énergie au nombre d'électrons émis. Cette caractérisation quasi complète de l'interaction permet non seulement de mieux comprendre les processus fondamentaux mais donne également accès à des éléments de la structure électroniques de la surface (énergie des excitons de surface, position de la band de valence, affinité électronique, etc.).

1.1 Formation d'ions négatifs H^- sur le graphite

L'intérêt de la formation d'ions négatifs d'hydrogène est lié à deux besoins distincts :

- Celui lié au développement de sources intenses d'ions H^- (ou ses isotopes) pour la fusion thermonucléaire [2, 3], ici les ions négatifs sont accélérés à une énergie du MeV avant de subir une détachement par interaction avec un gaz. Les neutres ainsi obtenus sont ensuite injectés dans un tokamak soit pour chauffer le plasma (D°) ou bien à des fins de diagnostic pendant le fonctionnement du tokamak (H°).

- Celui lié à la détection de particules neutres dans l'espace. Là il s'agit d'augmenter significativement l'efficacité de détection de particules neutres de très basse énergie (thermique ou hyperthermique) en les convertissant en ions négatifs par interaction sur des surfaces appropriées.

Cette partie du travail de thèse se place dans la perspective du projet du réacteur ITER et a été mené dans le cadre d'une ANR (ITER-NIS) ayant pour but d'explorer les alternatives à la production d'ions négatifs avec des sources fonctionnant au césium. En effet, la méthode la plus efficace utilisée à ce jour pour produire des faisceaux intenses d'ions négatifs repose sur l'utilisation de Cs afin de recouvrir les parois de la grille d'extraction de sources à plasma. Les surfaces ainsi recouvertes par du Cs voient leur travail de sortie diminuer, augmentant ainsi le taux de production d'ions négatifs. Au vu des performances recherchées pour ITER, les quantités de Cs qui seront utilisées sont assez conséquentes ; alliée au caractère polluant du Cs pour le plasma de fusion, cette solution comporte des problèmes encore non résolus. La solution alternative passe par la production d'ions négatifs, avec une efficacité comparable, sans injection de Cs.

Par ailleurs la nécessité de passer par des ions primaires négatifs pour produire les faisceaux de neutres s'explique par la faible efficacité de capture électronique par des ions positifs à des énergies proches du MeV.

Du point de vue expérimental, le moyen le plus efficace de produire des ions négatifs est par interaction d'un atome ou d'un ion avec une surface. Sur un métal, la formation d'ions négatifs transitoires, c'est-à-dire proche de la surface, est très efficace; cependant une majorité des ces ions perdent leur électron en quittant la surface, résultant au final en un petit nombre d'ions négatifs observés en sortie. Ce rendement est sensiblement augmenté en réduisant le travail de sortie de la surface, ce qui est possible par adsorption d'alcalins (Cs, K, etc.). Un rendement intermédiaire entre un métal nu et recouvert d'alcalins est observé sur des isolants ioniques (LiF, NaCl, etc.). En dépit de la forte énergie de liaison des électrons de valence des isolants ioniques (par exemple 14 eV pour LiF), le transfert d'électrons de la bande de valence vers le niveau d'affinité du projectile est efficace grâce au potentiel de Madelung. Une fois l'ion transitoire formé, sa survie dans la phase de sortie est favorisée par la présence de la bande interdite qui empêche la perte de l'électron vers la surface.

De manière surprenante, des rendements d'ions négatifs H^- comparables voire supérieurs à ceux obtenus sur LiF(001) ont été mesurés en incidence rasante sur les matériaux carbonés, en particulier le graphite HOPG. Au vue de la structure électronique de ce matériau (c'est un semi-métal, les bande de valence et de conduction sont légèrement superposées, conférant ainsi au matériau des propriétés plutôt métalliques), ces résultats restaient inexplicables par les modèles connus sur les métaux et les isolants ioniques.

C'est afin de répondre à ce paradoxe que nous avons étudié par notre technique de mesures en coïncidence l'interaction de H°/H+ avec une surface de HOPG, dans une gamme d'énergie allant de 500 eV à 5 keV. Les résultats montrent que la fraction d'ions H- quittant la surface est sensible tout aussi bien à la vitesse parallèle qu'à la vitesse normale à la surface. En ce qui concerne la vitesse parallèle à la surface, nous observons une forme de résonance comparable à celle observée sur les isolants ioniques. Cet effet tend à montrer l'existence d'un défaut d'énergie locale durant le transfert d'électron de la surface vers le niveau d'affinité du projectile (transfert du type Demkov). Cette résonance résulte de la compétition entre la probabilité de formation et la probabilité de détachement de l'ion négatif, les deux augmentant de façon monotone avec la vitesse parallèle. On mesure ainsi dans le flux de particules diffusées par la surface en incidence rasante une fraction d'ions négatifs de 10% à une vitesse de 0.35 u.a. soit environ 3.5 keV. Cette fraction de 10% est obtenue à une énergie normale de 5 eV, la valeur la plus haute accessible dans notre dispositif. Il semblerait qu'une fraction supérieure à 10% puisse être obtenue à des énergies normales plus élevées. Ces fractions sont par ailleurs comparables à celles rapportées dans la littérature.

La mesure du rendement d'électrons secondaires montre des valeurs élevées (de l'ordre de 0.2 électron/projectile à 500 eV), proches de celles mesurées avec LiF(001). Finalement, autant

du point de vue de la fraction d'ions négatifs que du rendement d'électrons secondaires, le graphite HOPG montre un comportement comparable à celui des isolants ioniques. En revanche, la mesure des pertes d'énergie des particules diffusées montre une gaussienne asymétrique centrée vers des valeurs élevées (65 eV à une énergie incidente de 500 eV), une caractéristique propre aux surfaces métalliques. Cette ambivalence du graphite, isolant vis-à-vis de la formation d'ions négatifs et métallique du point de vue des pertes d'énergie peut s'expliquer en exploitant pleinement les mesures en coïncidence.

Outre la gaussienne asymétrique centrée vers les hautes valeurs (65 eV à 500 eV), le spectre de perte d'énergie des particules diffusées comporte une faible contribution aux basses valeurs. Ce signal, composé de pics équidistants et séparés d'environ 10.5 eV, rappelle fortement les structures de perte d'énergie observées sur les isolants ioniques. Une analyse fine de ces structures, sur la base du traitement effectué sur LiF(001) par exemple, montrent que ces structures peuvent être interprétées comme des cycles de capture d'électrons de la surface vers le niveau d'affinité de l'ion H^-. L'intensité relative des pics successifs est d'ailleurs très bien reproduite par une loi binomiale, en cohérence avec les études menées sur les isolants ioniques. Ce type de traitement des données permet d'extraire les points suivants :

- la formation d'ions H^- sur la surface du graphite procède par capture d'électrons localisés avec une énergie de liaison initiale de l'ordre de 10.5 eV

- la perte éventuelle de l'électron vers la surface a lieu vers des états placés légèrement sous le niveau du vide

- il existe deux processus distincts à l'origine de la perte d'énergie et de l'émission électronique. L'un produit une perte d'énergie de type métal, avec des électrons émis de relativement basse énergie ; l'autre produit les structures de type isolant à faible perte d'énergie et des électrons secondaires de plus haute énergie.

L'information majeure tirée de ce traitement est l'énergie de liaison des électrons participant à la formation des ions négatifs. La valeur obtenue de 10.5 eV est bien supérieure au travail de sortie de la surface (4.7 eV). A ce stade de l'analyse, nous devons rappeler deux éléments essentiels. D'une part il a été montré expérimentalement et théoriquement que le transfert d'électrons se fait préférentiellement dans la direction normale à la surface ; la probabilité de ce transfert dépend donc fortement de la direction du moment initial de l'électron, celle-ci est plus favorable dans la direction Γ de la zone de Brillouin. D'autre part, le graphite est composé de deux populations d'électrons : les électrons π délocalisés, assurant la conduction dans le plan et produisant la faible interaction entre plans du graphite, les électrons σ localisés et formant les liaisons dans le plan. La bande π est proche du niveau de Fermi, la bande σ se trouve en dessous, sauf au point Γ. En effet, des mesures de photoémission résolue en angle (ARPES) montrent qu'au point Γ, la bande π plonge sous la bande σ, celle-ci se trouvant autour de 10 eV d'énergie de liaison. Simultanément, une bande interdite s'ouvre dans cette

direction ; de sorte que le graphite adopte la propriété électronique d'un isolant le long de la direction Γ.

Sur la base de ces éléments, l'interprétation la plus plausible consiste donc à identifier les électrons σ comme ceux intervenant dans la formation de l'ion négatif. Ces électrons étant localisés, le comportement devient similaire à celui d'un isolant. La bande π quant à elle reste pleinement active dans les processus de collisions binaires projectile-électron. Ces collisions produisent les valeurs élevées dans le spectre de perte d'énergie ainsi que la deuxième contribution à l'émission d'électrons.

Une question fondamentale reste toutefois en suspend, elle porte sur la localisation des trous formés dans la bande σ suite à la formation d'un ion négatif. L'interprétation donnée ci-dessus, dérivée des observations sur des isolants ioniques, suppose implicitement que ces trous restent localisés pendant l'interaction. A supposer que la mobilité d'un trou isolé soit élevée, la présence d'un ion négatif à proximité pourrait laisser supposer que l'interaction coulombienne bloque la diffusion du trou pendant la durée de l'interaction.

Une suite possible à cette étude pourrait consister en une étude systématique en faisant varier le ratio des liaisons sp2 et sp3 car ce rapport influence fortement la structure électronique du matériau.

1.2 Diffraction

Généralement, les techniques d'analyse des surfaces utilisant les interactions particules surface (LEIS, SIMS, ISS, etc.) reposent sur les mécanismes fortement inélastiques pour extraire les propriétés chimiques ou électroniques de la surface. En ce qui concerne l'information structurale (cristallographique), la diffusion d'atomes d'hélium à des énergies thermiques (HAS) a longtemps été la seule technique utilisant des atomes ou molécules. La raison simple est qu'à ces basses énergies, la diffusion purement élastique est très probable. La diffraction d'atomes thermiques, découverte en 1930 par Esterman and Stern, a constitué pour les particules lourdes la première preuve de la dualité onde-corpuscule postulée par de Broglie. Un demi-siècle plus tard, l'avènement des jets supersoniques a permis le développement d'un outil puissant pour l'analyse de la structure cristalline des surfaces.

Avec des énergies incidentes comprise typiquement entre 10 et 100 meV, la longueur d'onde de De Broglie des atomes d'hélium est de l'ordre de l'Angstrom, c'est-à-dire comparable aux paramètres de maille des cristaux, rendant favorable l'observation de la diffraction. Par ailleurs, ces faibles énergies résultent en la réflexion de l'atome incident au-dessus du premier plan atomique ; cette technique est donc exclusivement sensible à la première couche de la surface et est non destructive.

Malgré le grand nombre de groupe à travers le monde travaillant sur la diffusion d'ions ou d'atomes rapides (énergie proche du keV) sur des surfaces cristallines, personne n'avait imaginé que la diffraction puisse être observée dans ce régime d'énergie. C'est donc contre toute attente que le groupe de L'ISMO a observé pour la première fois la diffraction d'atomes d'hydrogène rapides sur une surface de NaCl(001) en incidence rasante. Peu de temps après, le groupe de H. Winter à Berlin a rapporté les mêmes observations.

La méthode, relativement simple, repose sur la capacité à produire des petits (de l'ordre de 100 microns) faisceaux neutres rapides (~keV) de très faible divergence, c'est-à-dire inférieure au mrad. Le faisceau de neutres est obtenu par neutralisation d'un faisceau d'ions par passage dans une cellule de gaz. Le faisceau de neutres est ensuite dirigé vers la surface à des angles de l'ordre de 1 deg. , de sorte que l'énergie normale à la surface reste inférieure à 1 eV. Cette technique, baptisée GIFAD pour Grazing Incidence Fast Atom Diffraction, combine la haute sensibilité de la diffraction d'atomes thermiques (HAS) à la surface et la rapidité du RHEED (Reflection High Energy Electron Diffraction), cette dernière utilisant des électrons d'énergie de 5 à 50 keV diffusés en incidence rasante. Finalement GIFAD adopte la géométrie du RHEED en apportant des informations supplémentaires ; en plus du paramètre de maille, GIFAD fournit des données fines sur la corrugation de la densité des électrons de valence, une information similaire à celle donnée par un microscope à force atomique (AFM).

GIFAD représente un régime de diffraction originale qui ouvre plusieurs voies de développement :

- aux énergies du keV, de nombreux processus inélastiques deviennent probables, représentant autant de source de décohérence, en comparaison avec la diffraction d'atomes thermiques. Ces questions fondamentales et récurrentes en mécanique quantique ouvrent un nouveau champ de recherche: quel est le rôle des excitations électroniques? Quelle est l'influence de la localisation de ces excitations? etc.

- développer GIFAD comme technique de routine pour l'analyse des surfaces, avec une application prioritaire pour le suivi en temps réel de la croissance de couches minces dans un bâti d'épitaxie.

Cette deuxième partie de la thèse s'inscrit clairement dans le premier champs de recherche. Elle a pour but d'explorer les limites de la diffraction dans le cas d'échange de charge entre un ion incident et la surface.

La diffraction de particules rapides est généralement observée par diffusion d'atomes ou molécules (neutres). La raison est que, pour une surface donnée et caractérisée par sa température de Debye, la décohérence due aux vibrations thermiques augmente rapidement avec l'énergie normale. De manière plus concrète, pour des températures de Debye de l'ordre de 300°K et à température ambiante, le signal de diffraction devient négligeable au-delà d'une énergie normale supérieure à 0.5 eV. Expérimentalement, le réglage de cette énergie normale

se fait simplement en jouant sur l'énergie totale (E_0) et l'angle d'incidence (θ), $E_n=E_0 \sin^2(\theta)$. Lorsque la particule incidente est un ion, l'énergie normale ainsi définie est augmentée lors de l'approche vers la surface par l'effet de la charge image. Sur des métaux, ce gain d'énergie peut dépasser 1 eV, augmentant donc sensiblement l'énergie normale effective. Sur ces considérations purement cinématiques, on voit donc immédiatement la difficulté d'observer la diffraction avec des ions.

Pour contourner cette limitation, nous avons choisi un système relativement favorable, H^+ sur LiF(001). D'une part LiF possède une température de Debye parmi les plus élevées, 750°K en volume et 530°K en surface [4], permettant d'emblée d'atteindre des énergie normales élevées (proche de 1 eV) en régime de diffraction. D'autre part, le proton se neutralise sur LiF par capture résonante à des distances relativement loin du pont tournant. Ainsi le gain d'énergie due à la charge image reste faible car cet effet cesse au moment de la neutralisation.

Ces expériences ont été menées en utilisant un faisceau d'ions pulsé et combinant les mesures en coïncidence décrites au début de ce résumé. Les particules diffusées, analysée en temps de vol mais pas en charge, sont collectées par un détecteur sensible en position et fournissant l'image de diffraction.

Le spectre de perte d'énergie des particules diffusées (H° à plus de 95%) comportent une succession de pics espacés d'environ 12 eV (énergie de formation d'un exciton de surface). Le premier de ces pics, situé à une perte d'énergie de 1 à 2 eV, correspond à la diffusion de l'ion neutralisé sans aucun autre processus électronique. A noter qu'en voie d'entrée, le couplage de l'ion avec les phonons optiques de la surface produit une faible perte d'énergie. Lorsque l'image enregistrée sur le détecteur est filtrée par la perte d'énergie (ou temps de vol) en ne sélectionnant que le premier pic du spectre de perte d'énergie, un profil de diffraction apparait clairement.

Comparé au profil de diffraction obtenu avec des projectiles neutres et à une énergie normale effective comparable, l'image ainsi obtenue est moins contrastée, signe que la capture électronique introduit tout de même un facteur de décohérence. Ce facteur de décohérence a pu être déterminé expérimentalement en comparant les profils de diffraction d'ions et d'atomes d'hydrogène aux mêmes énergies normales effectives, c'est-à-dire éventuellement corrigée du gain image. La perte de cohérence liée à la capture électronique, mais contenant également les effets liés à l'excitation des phonons optiques, représente 20% du signal total. Au préalable et sans entrer dans les détails, la valeur du gain image a été déterminée par la mesure de la corrugation du potentiel extraite des images de diffraction de H^+. Cette valeur est égale à 0.45±0.05eV.

Nous avons ainsi pu mettre en évidence la diffraction lors d'une diffusion inélastique, en l'occurrence une capture électronique. Cette observation est d'autant plus importante que le

groupe de Winter a récemment rapporté l'absence de diffraction dans le cas de la formation d'exciton de surface par H° sur LiF(001).

L'interprétation et les implications de cette observation soulèvent un grand nombre de questions. A supposer que l'étape de capture puisse être découplée du reste de la trajectoire menant à la diffraction, la capture ne fait que disperser les conditions initiales (par exemple l'angle d'incidence effectif). Ici on sépare donc l'étape classique menant à la capture loin de la surface et la phase quantique caractérisant la diffraction. Or ces deux processus, capture et diffraction, ont lieu tous deux dans une région où le projectile « voit » la densité électronique de la surface, il n'est donc pas évident de séparer spatialement ces deux phases de la trajectoire.

En résumé, cette étude représente un exemple du type de questions fondamentales auxquelles GIFAD pourraient apporter des éléments de réponse. L'expérience complémentaire à celle décrite ici serait de vérifier l'existence de la diffraction dans le cas d'une capture électronique d'un atome neutre H° vers un ion négatif H^-. Contrairement à la neutralisation d'un projectile ionisé, la formation d'un ion négatif a lieu dans la partite de la trajectoire proche de la surface. Ce détail aura cependant comme conséquence défavorable d'augmenter la valeur du gain d'énergie image proche.

1. Introduction

Charge transfer, neutralization and ionization are the basic physical processes of ions (atoms) interacting with solid surface. They play a major role in surface chemistry, energy deposition by electronic process, nanofabrication, surface treatment and have been widely studied over last 30 years. Still, many applications are limited by the lack of a better understanding of ion surface processes. The high sensitivity to the detailed composition of the surface prevents the generalization of simple models. At the same time quite some efforts has been devoted to take advantage of this high elemental/structural sensitivity and to apply ion beam techniques to surface analysis. Though significant technical and scientific progress have been achieved, it is still difficult to predict what electronic processes will govern the fate of an ion surface collision.

In addition to a significant internal energy (much larger than room temperature), ions can easily be accelerated. A simple voltage difference between the target surface and the ion-production region can result in ion kinetic energies ranging from eV to keV. Collision of such atoms (ions) with the surface atoms can result in scattering of the primary particle and recoiling of the surface atoms. The kinetic energies of these scattered and recoiled ions and atoms are determined by the nature of the events taking place along the trajectory. For collision physics which focuses on the electronic processes (change of internal energy), two ideal situations can be analyzed in more details:

-simple head-on collision, where a single topmost atom is hit whereas all others will only participate as a perturbation via a mean electronic environment. From the electronic point of view, these are the most violent events in that all the primary energy can participate to electronic processes.

-grazing incidence on top of a perfect surface where the projectile will never penetrate below the topmost layer. Such event necessarily involves several collision partners but can be most gentle from the electronic point of view as is demonstrated with the observation of elastic diffraction.

For these situations the exchange of kinetic energy due to elastic collision (in the electronic point of view i.e. billiard ball collisions) momentum conservation can easily be calculated so that any inelastic process will have a clear contribution to the final translational energy.

In general however, the trajectory is rather complex with penetration below the topmost layer. Some of the primary particles are reflected from the surface, and also some of the target atoms

can be recoiled in such a direction that they also leave the surface. These particles may be in neutral, positive or negative charge state depending strongly on the electronic structure of individual surface atoms and also of the surface band structure. The electronic excitations will produce various phenomena such as Auger electrons, secondary electrons, exciton, photon emission and ionization of the projectile and surface atom [5].

In this thesis, two general topics are involved, which are:

1.1 Negative ion formation:

The interest in negative ion formation is related to the development of intense neutral particles beam for their application in fusion research [2, 3] and as well as the electron level structure. In fusion experiments, neutral beams are used for heating the plasma, diagnose its characteristic properties—particle density and momentum distributions, fuel the device with fresh deuterium and to sustain the higher temperature where fusion can occur[1]. Within the tokamak, the magnetic fields are used to control the plasma which produces a heating effect. The magnetic fields create a high-intensity electrical current through induction, and as this current travels through the plasma, electrons and ions become energized and collide. Collisions create 'resistance' which result in heat, but paradoxically as the temperature of the plasma rises, this resistance—and therefore the heating effect—decreases. Heat transferred through high-intensity current, known as ohmic heating, is limited to a defined level. Therefore, in order to obtain still higher temperatures and reach the threshold where fusion can occur, additional heating methods must be applied from outside of the tokomak[2].

Previous generation of reactors has confirmed the efficiency of this external heating. For instance, beam of deuterium atoms with energy 120 keV are used to heat the plasma in TFTR (Tokomak Fusion Test Reactor), a beam of 160 keV has been employed for JET (Joint European Torus). However, for the third generation of fusion reactor—ITER (International Thermonuclear Experimental Reactor), its large plasma volume and the higher expectations will impose new requirements. MeV deuterium particles are required to penetrate far enough into the plasma. This is three to four times faster than in previous systems. The problem is that the method used before consisting of neutralizing a positive (deuteron+) beam by electron capture in a gas cell can not be used any more. Indeed, electron capture cross section drops by three orders of magnitude between 100 keV and one MeV as illustrated in Figure 1.1; it *becomes almost impossible for an unfortunate electron sitting in the cell to jump on a fast train (the MeV D^+) passing by six times faster than it moves around a target atom*! The only alternative is to use a negative primary ion beam because the detachment cross section does not decrease very rapidly, *now the poor electron is sitting on the fast train and it does not take*

[1] http://www.iter.org/mach/heating

[2] http://www.iter.org/sci/plasmaheating

too many efforts to force it down. Therefore, a negative deuterium production system is the first priority for the heating of ITER with 1MeV neutrals.

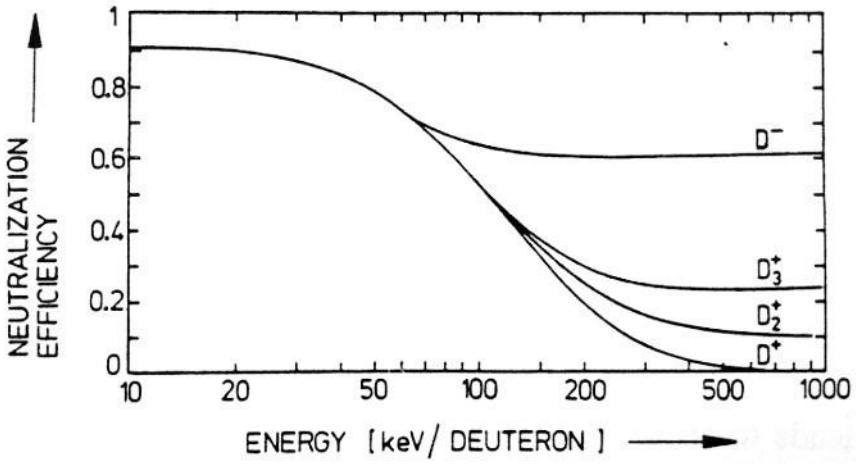

Figure 1.1 The neutralization efficiency for deuterium ions passing through a gas cell, as a function of the particle energy [6].

There are several mechanisms to produce intense beams of negative ions. One of the earliest way is to pass a positive ion beam through an alkali vapor [7], a first electron is captured to form a neutral and then, in a second collision a negative ion is formed. Whatever the velocity, this second step is less efficient because the H^- (D^-) affinity level is only 0.75 eV compared with few eV on the alkali, where the affinity level is the energy gain, when an electron is taken from infinity to the valence level of an atom. Another technique is to take advantage of the tremendous density of quasi-free electron at the vicinity of metal surface. This so called, 'surface effect' production of negative ion has been intensively studied, the physical process of electron attachment to D^- is resonant charge exchange from the conduction band of the converter surface to the affinity level of scattered particle. So far, the best conversion efficiency close to 67% (for oxygen ions [8]) was reached on the Cesiated tungsten surface which has the lowest work function. Unfortunately, so far, this technique leads to excessive Cesium contamination and alternate routes are needed.

Surprisingly, several percent of H^- has been detected when H^+/H^0 grazing scattered from LiF surface [9-11], although the binding energy (e.g. 14 eV for LiF(100)) of the valence electrons is much larger than the typical work function of metals, population of the affinity level becomes possible due to the Madelung potential (owing to the surrounding point charge lattice lower the defect energy). Following the electron transfer to the atom affinity level, its survival probability is much favoured because the band gap prevents electron loss back to the surface. However, a significant negative ion fraction has been measured when H° and H^+ scattering at grazing incidence from carbonaceous surface, lower work function or big band gap can't be employed to explain this phenomenon anymore.

1.2 Surface diffraction

The interest of atoms and ions-surface interaction is maintained not only by the fundamental importance of the process, but it is also a base for several surface analysis methods, such as SIMS (Secondary Ion Mass Spectrometry), and HAS (Helium Atom Scattering), LEIS (Low Energy Ion Scattering) etc. Because the diffraction pattern or scattering particle reveals directly the surface information, such as surface defect, composition, the periodicity and lattice parameters of the surface structure.

Particles being successfully employed as surface analysis probe have a long history. The first coherent scattering of atoms from surfaces has played a historical role in the funding of quantum theory. The diffraction of thermal He atoms on LiF(100) by Esterman and Stern (1930[12]) was the first evidence that atoms as a entire system can exhibit a wave nature. It was only 50 years later, with the advent of supersonic expansion that helium diffraction (HAS) was turned into a surface analysis technique [13]. With kinetic energies in the 10-100meV range, the de Broglie wavelength λ of the incident atoms is close to one Å, the same order of magnitude as the interatomic spacing so that diffraction is easily achieved. In addition these low energy particles are physically unable to penetrate into the solid and interact only with the outermost atoms. Thus, this technique has a very high surface sensitivity and does not cause any damage to the sample.

Fast atom diffraction is much more recent, it has been observed for the first time in 2003 by the group of Multicharged Ions (MCI) at the Institut des Sciences Moléculaires d'Orsay (ISMO). They observed diffraction of 500 eV hydrogen atoms on a NaCl(001) [14] surface at grazing incidence, the schematic experiment structure is present in Figure 1.2. Later, the research group led by Helmut Winter, in Humboldt University of Berlin, has proven independently this phenomenon on a mono-crystal LiF (100) surface [15].

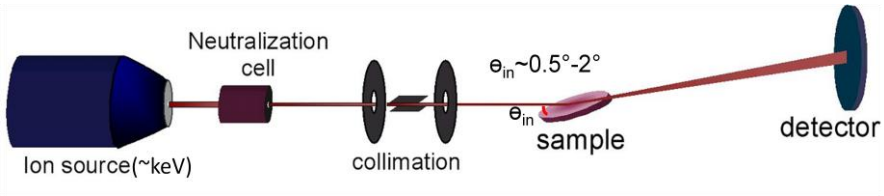

Figure 1.2 Basic scheme of grazing incidence fast atom diffraction (GIFAD). The ion beam extracted from ion source with energy at several hundreds eV to few keV, is neutralized before impacting on the sample surface with incident angle(0.5°~2°) [16].

As depicted in Figure 1.2, the experimental geometry of grazing incident fast atom diffraction (GIFAD) is exactly the same as that of Reflection High Energy Electrons (RHEED) where 10-30 keV electrons are diffracted on the crystal. Both techniques easily give access to the surface lattice parameter but atoms and electrons do not interact in the same manner. Fast electrons mainly interact with matter close to nuclei. As the fast electrons penetrate the electron cloud, the screening of the nuclear charge decreases so that coulombic interaction

becomes very strong. The electrons have to reach the first atomic plane (z=0 by definition) and nothing can prevent sub surface penetration (z<0).

Generally, atoms interact with the surface before reaching the first atomic plane. Schematically, Pauli principle prevents the helium electronic density to penetrate freely the surface electronic density. It takes energy to push the surface electrons to leave room for the helium atom. Several eV are needed to bring a helium atom below the first atomic plane. Because of the grazing geometry, the energy normal to the surface $E_{\perp} \sim E_0 \sin^2(\theta) \sim E_0 \theta^2$ is three to four orders of magnitude smaller than $E_{//} \sim E_0$, so that the projectile helium atom are reflected few Å above the surface plane making the technique sensitive only to the first atomic layer. In recent years efforts have concentrated along two lines,

-exploring the range of possible applications like exploring GIFAD with ionic crystals, insulators, metals and semi conductors.

-Exploring the physics of fast atom diffraction, what causes decoherences on insulators? What is the influence of electronic excitations? Does it make any difference if it is localized or not? Can diffraction be observed with reactive species? Etc…

The chapter 6 of thesis addresses such questions trying to contribute to this new field of GIFAD [16-19].

Outline of this thesis:

The guideline of this thesis is the study of electronic processes taking place when an ion approaches a surface in the keV range. This velocity is much smaller than that of all electrons whereas the energy is very large compared with the typical binding energies of atoms and electrons of the surface. To concentrate on electronic processes, the experiments are performed under grazing incidence to avoid penetration and thus all “mechanical” effects associated with “close collisions”. The electronic processes observed are electron capture from positive ions and neutral (to form neutrals and negative ions) and electron excitation to localized or delocalized states of the target surface. The second chapter describes the experimental technique, the beam line system, and the detectors and data acquisition. Then the third chapter describes higher level control of the setup and recent programming development. The chapter 4 and 5 mainly focuses on the basic principle of the interaction between atoms/ions and surfaces, it emphases the specific aspects of grazing incidence.

The fourth and fifth chapters focuses on the production of negative H^- ion of H° and H^+ projectile grazing incidence on various surfaces. Firstly, we review the negative ions formation on metal and insulator surfaces by electron population by image charge and Madelung potential, respectively. Then we will focus on our result of H^- production on Highly

Oriented Pyrolitic Graphite (HOPG) surface via hydrogeneous particle grazing scattering with various kinetic energy (0.5~5keV) and incident angle (0.5~2.5deg.). At the same time, energy loss of the scattered particle and secondary electron are also analyzed. The results indicate that the carbonaceous surfaces have unique electron structure which differs from that of metal and insulator. Comparing with results from the literature shows that there are still many open questions.

The sixth chapter explores the possibility to study electronic processes in the diffraction regime. In this chapter, the general concept of GIFAD has been addressed firstly, empirical analysis model—Hard Wall model—is involved to describe the projectile and surface atoms interaction, a modified Debye model to fit the experiment data. And the three decoherence factors also will be discussed—thermal vibration, electron excitation and electron capture. For the inelastic collision (proton neutralization) regime, clear diffraction evidence has been observed for proton coherently scattering on LiF(001) surface and it will be presented in this chapter.

After carefully analyzing the negative ion formation on HOPG surface, and inelastic diffraction with proton scattering on LiF(001) surface, the conclusion will be presented in chapter 7, as well as the perspective.

2. Experimental setup

This chapter describes the experimental setup and the associated techniques used in this work as well. The setup of the Multicharged Ions (MCI) group in LCAM (Laboratoire des Collisions Atomiques et Moléculaires) (now part of SIREN— 'Surfaces, Interfaces : Réactivité et Nanostructuration'—group at ISMO) was designed to study particle surface interactions, with emphasis on ion scattering experiments. The detail experimental setup description has been explained in the thesis of JéromeVillette [20], Anouchah Momeni [21] and Patrick Rousseau [22]. Here, I will only give a general description in section 2.1, with emphasis on the deceleration system and the new control system that I developed will be presented in section 2.2.

2.1 Beam line system in ISMO

The original scientific tradition at the LCAM was to analyze the collision process in gas phase collision. One central technique developed for these studies was the so called "collision spectroscopy" also called energy loss spectroscopy or translational spectroscopy. Ideally, the energy balance defines the final states of the collision partners while the differential cross sections (the associated angular profiles) is a complete signature of the collision process (where and when do the electronic transitions take place). This usually requires energies on the order of few hundred eV to allow good detection efficiency and detection of the two collision partners in coincidence. Obviously, this second aspect is not possible with surfaces. Nevertheless, in grazing collisions with the surface, the projectile survives the interaction with the surface and can be analyzed in details. The major unknown factor was whether or not it could be possible to understand something in such a multiple collision regime where each projectile interacts with many target atoms. Originally the experiment was developed to study the interaction of highly charged ions with surfaces where many secondary electrons [23-25] as well as atoms and molecules and ions [26, 27] are emitted. The main applicative interest as being the creation of nano-size modifications of the surface under individual ion impacts [28].

Accordingly, the experimental system in MCI group of ISMO was built at the end of the 1990s to investigate the interaction of low energy particle with solid surface, as presented in Figure 2.1. It includes ion production, selection and collimation systems, interaction chamber and data acquisition systems, for the incident particles one can choose continuous or pulsed

mode with the energy from few hundred eV to several keV, and a gas cell for the neutral beam production.

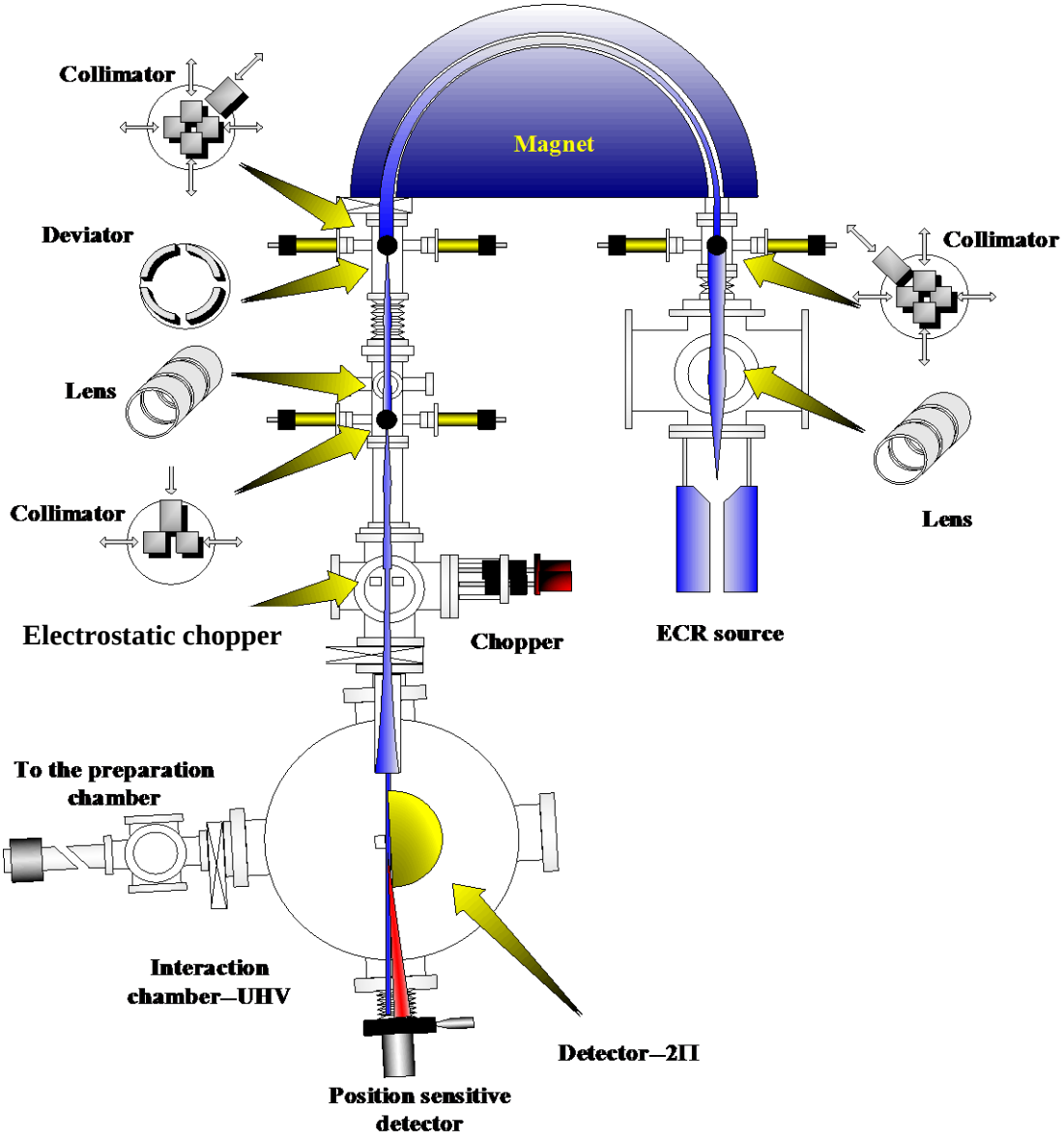

Figure 2.1 The schematic of the beam line, which consists of different elements for the production, guiding, analysis, pulsing and neutralization of the beam, and driving the beam to the sample in the interaction chamber. In particular three sets of collimators driven by stepper motors (one locates before and 2 after the magnet) each including a Faraday cup to monitor the beam current during operation.

The line was entirely controlled by a program developed by the team. The detailed will be presented in section 2.2. The complete control system had to be changed. I have installed a set of small slave micro controllers each taking care of a specific task such as 1) driving/stabilizing the magnet, 2) operating the stepper motors, 3) driving the high voltages, etc….. All these slaves are connected via USB ports to the main PC where they are controlled by a graphic interface in the program of LabVIEW.

2.1.1 Selection of the ion species.

A. ion source

The lab acquired a multicharged ion source—ECR (Electron Cyclotron Resonance) in 1996, which is the model Nanogan produced by Pantechnik Company. This type of ion source is a compact ECR source with a frequency of 10 GHz hyper frequency (HF) wave and magnetic field provided by permanent magnets which can produce multicharged ions (eg.Ar^{11+},Xe^{16+}) at medium current (μA).

The ECR source is plasma confined by a magnetic field in which the electrons are "heated" by HF waves to ionize the ions by successive collisions. The plasma electrons are accelerated in the region where the frequency matches the cyclotron resonance frequency, and the magnetic confinement of the discharge is provided by a longitudinal field created by a combination of axial and radial field created by a permanent magnet assembled in a multipole structure.

We use a signal generator (HP 8683D) to create the HF waves which is amplified by a travelling wave tube (Varian EN61010) to have a power of up to 20 watts for a wave of frequency 10 GHz. With such a configuration, we can get mono-charged ion beams of several hundred nA and few nA multicharged ion beams Ar^{8+} to the sample with kinetic energy 2keV per charge.

During the operation, the pressure inside the source is around 10^{-6} mbar so that the consumption of the gas in the ion source is very low. This is possible because the ionization efficiency is very high, above 50% meaning that most neutral introduced (or present) in the source will be ionized. As a result a low pressure bottle 200 ml is enough for a month of operation. Alternately, the gas can be obtained from the evaporation of powders in a miniature furnace. We have two gas reservoirs allowing operation with a gas mixture; it is well established that to optimize highly charged ion production, a carrier gas lighter than the desired species can be helpful. The admitted explanation being that during ion-ion collisions between the carrier gas and the target gas, momentum will equilibrate so that the lighter ions will take away part of the kinetic energy of the heavier ion allowing a longer lifetime in the magnetic bottle i.e. more chances to undergo multiple electronic impacts and higher charge state. Plasma conditions are set by the source gas pressure, the power injected and by a

voltage (~150V) which can polarize a metal plate opposite to the extractor electrode to emit secondary electrons to feed the plasma.

B. specific ion selection by analyzing magnet

The ions created in the source are extracted by applying an electrostatic potential on the source. As the target is grounded, the energy of the ions: E=q*V, where E is the energy of the ions, q is the charge state and V is the voltage applied to the source. They are then focused by a set of electrostatic lenses located between the source and the magnet.

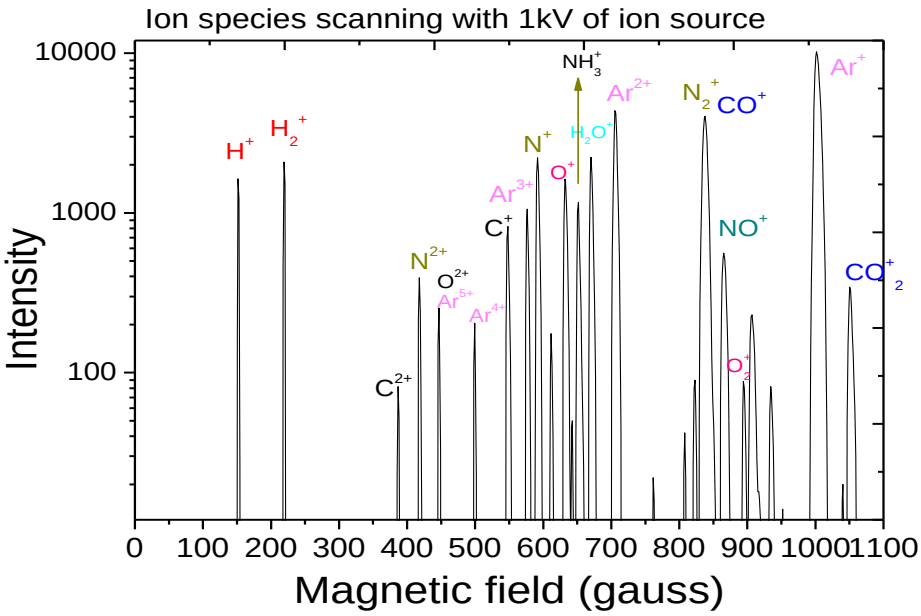

Figure 2.2 Ion Spectrum recorded for 1kV extraction (software described Figure 2.23).

The source produces different charge states and contains several pollutants (protons, H_2^+, etc.) coming from the residual gas of the chamber and desorption of inner walls induced by the plasma. To select a single ionic species, analysis magnet is necessary, and in the lab, 180-degree semi-circular electromagnet has been employed in order to improve the mass resolution. Selection is made according to the Lorentz law, for an ion with charge state q and extraction voltage V, the magnetic field must be:

$$B = \frac{\sqrt{2}}{R} \cdot \sqrt{\frac{M}{q}} \cdot \sqrt{V} \qquad (2.1)$$

where R is the curvature radius of the magnet.

A typical mass spectrum (obtained during optimization of the software and not in optimized operation) is displayed in Figure 2.2 for 1 kV potential in the ion source. In order to facilitate

the transport of beams of low energy ($E_0 \leq 500$ eV), a negative voltage can be applied to the selection magnet which can be floating over the beam line (the detail is presented in the section 2.1.2). Similarly we can carry heavy ions (Xe^+) or an energetic ion beam by reducing their energy with positive potential biased in the magnet.

The beam is optimized by groups of vertical and horizontal slits located before and after the magnet. By tuning the width of these slits, we can adjust the divergence of the ion beam. Behind each slits system, we also have a movable Faraday cups that allow the measurement of beam current. Each of the slits is actually composed of two independent plates controlled by stepper motors (see the section 2.2.3).

Due to the various thermal instabilities, we observe a drift of the beam in time. Base on the current measurement by the pair of horizontal slits located after the magnet, we have made a self-read adjusting system to compensate the magnetic drift field, (stabilization of the beam position on the slits) see 2.2.3. After selecting ionic species, the beam is guided to the interaction chamber by a set of electrostatic lenses and deflectors but it also could be chopped by a specific electrostatic pulser.

2.1.2 Acceleration-deceleration beam line system

Ion beam formation at low energy (~1 keV or less) is much more difficult to achieve than at high energy because of beam spread by space-charge forces in the uncompensated region within the extractor. To generate an ion beam with higher current at low energy, electrode acceleration-deceleration system by biasing the negative potential at the analyzing magnet is a possible solution. A high extraction field can be achieved applying a large negative potential to the acceleration electrode, even if the ions are decelerated between the negative electrode and ground electrode again to the desired beam energy. As stated above, part of the beam line, including the magnet can be floated which allows transport at higher energy than that delivered to the target at ground.

For working with low energy but high current, there is another option which is biasing the target at positive potential and to progressively decelerate the ion beam to the desired energy ($E=q*\Delta V$, where ΔV is potential difference between the ion source and the sample). Ion beam deceleration systems and focus lenses are often working together because ion beam after decelerating has a higher divergence and stronger space charge effects at lower energy. However, the lens consists of some combination of electrical fields that shapes the flow of ion passing through it. Just as a glass lens shapes for the spotlight to focus light ray. Otherwise, the intensity of the beam arriving at the target decrease exponentially with decelerated voltage without focus lens systems [29].

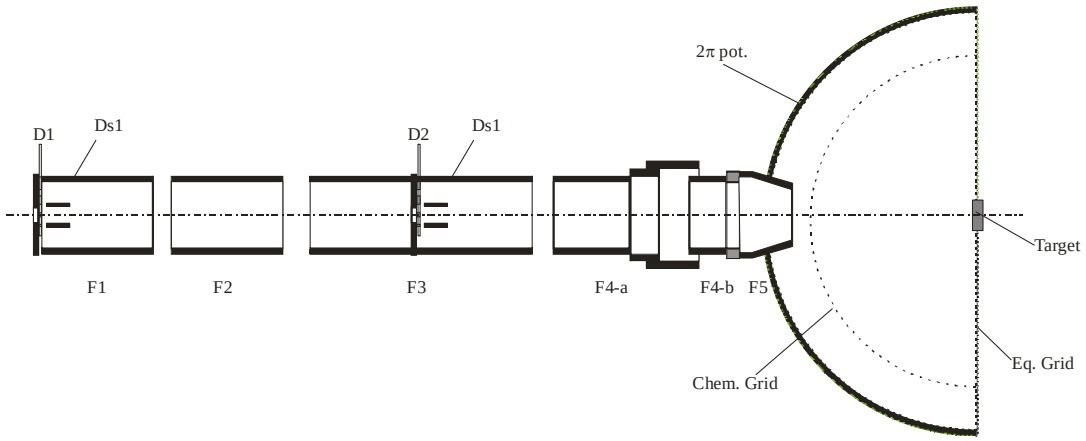

Figure 2.3 The scheme of deceleration system (see the text for the detail structure).

Figure 2.3 is our deceleration systems, focus lens and deflection systems. It consists of 5 electrodes F1-F5, and two diaphragms (D1 and D2) followed by 2 deflection systems (Ds1 and Ds2). F1 is always grounded although but the diaphragm is isolated from it (in order to measure the beam current when preparing the beam), while the potentials of other electrodes increase as the beam approaches the target. The grids, the target and F5 are all at the same potential which defines the ion energy.

With our current deceleration system, we have simulated the ion beam transport and the potential distribution in the deceleration tube with SIMION, as presented in Figure 2.4. Those studies indicates that ion beam convergence in the deceleration system required for focus lens confining the upheaval of the ion beam due to the space charge effect depends on the electric potential distribution applied to these electrodes. Potential distribution during those electrostatic stages provides small beam emittance and momentum spread which is beneficial for efficient deceleration and high resolution experiments with the decelerated ion beam.

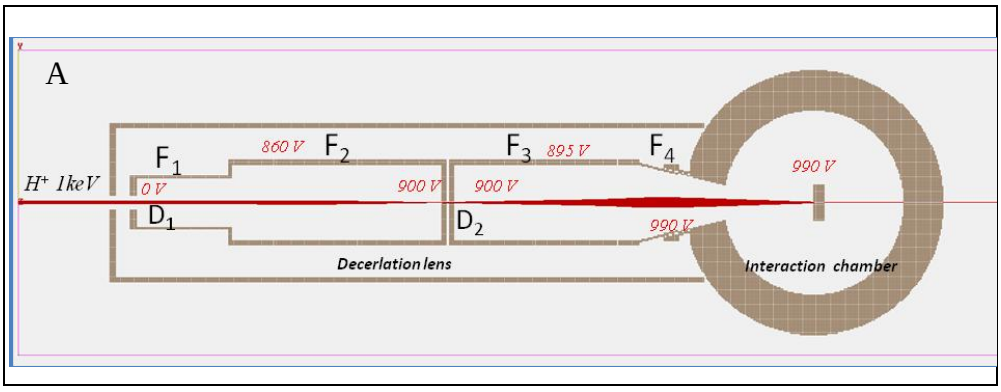

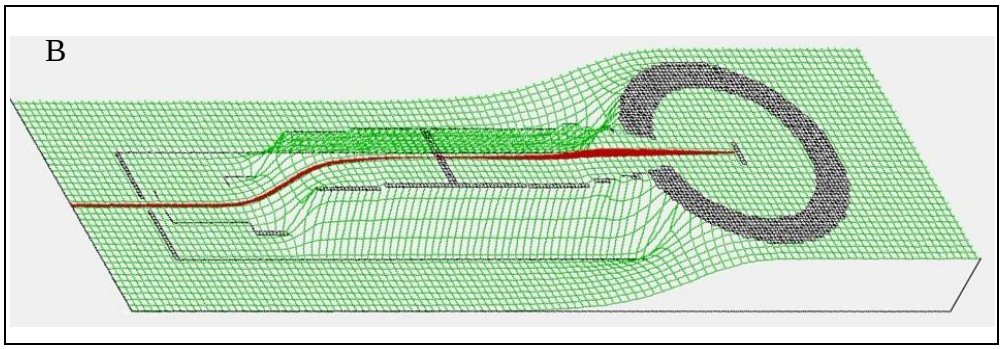

Figure 2.4 A: The diagram of ion beam (H^+ 1keV) shape changing inside the deceleration system and reaction chamber (simulated by SIMON)(D: deflector; F: Focus lens. They are insulated from each other.), B: Potential energy distribution inside the deceleration tube according to the potential marked in A (simulated by SIMION).

We have extracted Ar^{3+} with 3keV to the sample HOPG for testing the beam diameter before and after the deceleration. By moving the target and measuring the secondary electrons on the 2-π detector (the detail is presented in 2.1.4), we can get the information about the profile of the beam because the sample (HOPG) and the target holder have different secondary electron yields. Therefore the target shift changes the beam intensity from one constant value (the beam is hitting only the sample) to another constant value (the beam is hitting only the sample holder). By measuring the electron yield vs. the coordinate, and then differentiating this function, we get the profile of the primary beam as presented in Figure 2.5, it shows that the effect is still limited (50% increase) in spite of deceleration by a factor 60.

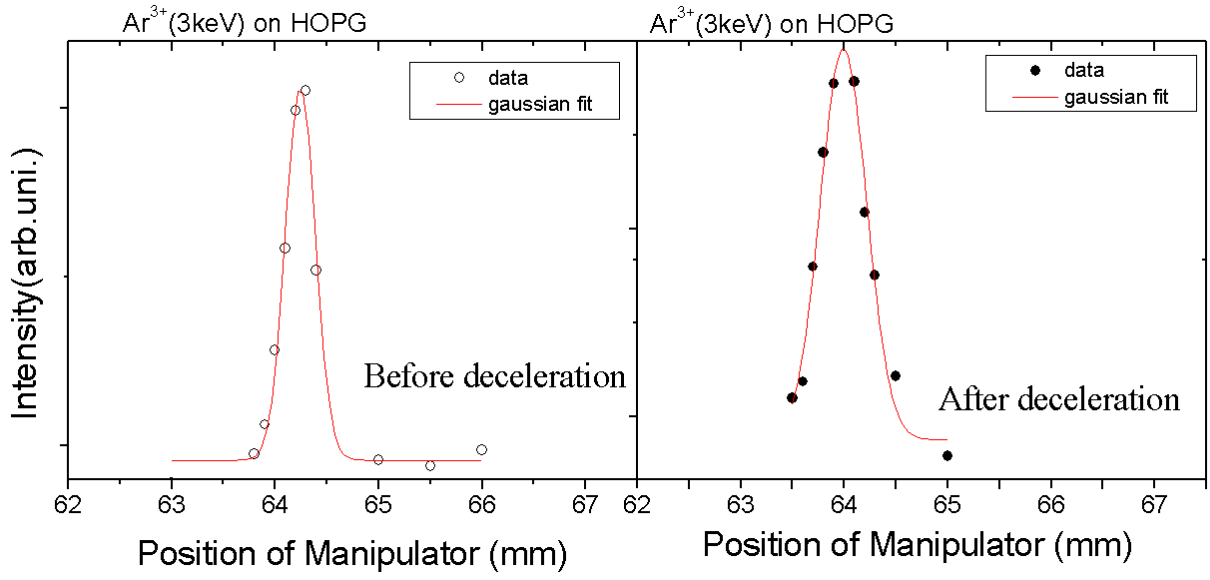

Figure 2.5 Beam profile measured on target in vertical direction before and after deceleration. The FWHM increases from 0.340mm to 0.531mm when the ion beam energy is decelerated from 3000 eV to 50eV/q.

2.1.3 Ion beam collimation and pulsing system

The beam line guides the ion beam to the interaction chamber. This is achieved with step by step adjustment with 3 collimators, located before and after the analyzing magnet and before the neutralization chamber, respectively. They are made of stainless steel 0.5 mm thick foils or jaws holding a razor blade and controlled by a stepper motor to set the size of the slit limiting the beam form, and some of them are isolated from each other in order to measure the current on each jaw to stabilize the beam position see Figure 2.1 and 2.2.3 for detail.

For specific purpose, such as energy loss spectroscopy, coincidence measurement, etc, a pulsed beam is required. In order to generate a pulsed ion beam, the ion beam is rapidly swung periodically back and forth from left to right. As it passes in front of a hole, some ions have a chance to reach the interaction chamber. This temporal gate opens and immediately closes twice every cycle. In fact less than an ion is present in each gate but since few million gates are generated (MHz frequency) an ion beam of few thousand ions per second can be produced. The beam preparation consists in improving the time resolution until a "perfect beam" of 2000 to 4000 ions per second is produced. Good energy resolution requires a well-defined beam (spatial resolution and energy) and large sweeping field inside the chopper. The resolution of the chopper is defined by: $\Delta t = \frac{\phi_f + \phi_d}{v_b}$ where v_b is the scanning speed and ϕ_f is the beam diameter and ϕ_d is the diameter of the diaphragm. The choice was to achieve large field with moderate voltage by bringing two plates very close to each other.

The chopper system consists with an entrance slit that determines the size of the beam and two plates on which is applied the sweeping voltage. The orifice is the entrance aperture for the main interaction chamber with a diameter about 80μm. The rapid and periodic changing electric field between the two plates sets the scan rate and therefore the resolution of the pulse, and the field is defined by the distance between the plates and the applied voltage. These slits are controlled by stepper motors allowing fine adjustment of the slit size and the distance between the plates of the chopper which allow us to place the plates closely and use a low voltage (few volts) to create a strong electric scanning field, there is an example presented in Figure 2.6.

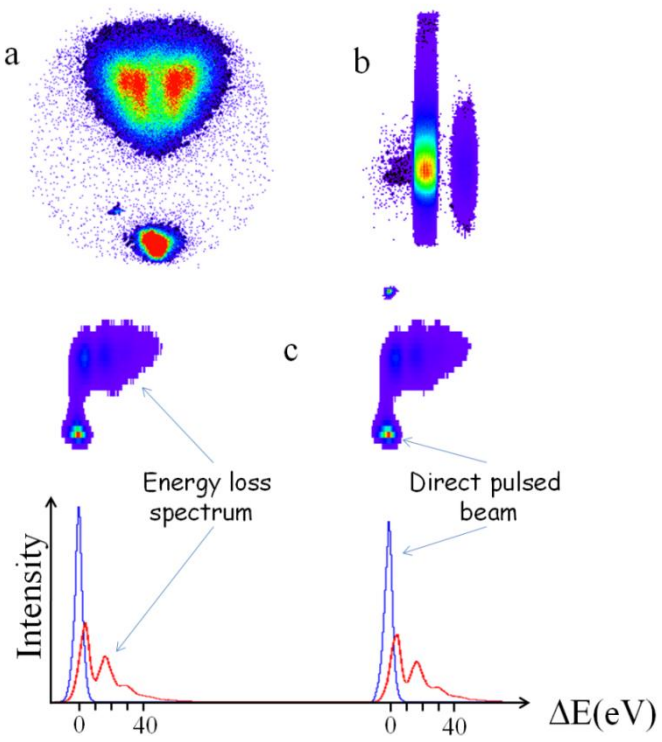

Figure 2.6 2D images of scattered beam for 1keV protons grazing scattering on LiF(001) surface with (b) and without (a) electrostatic deflect slit, and the energy losses of scattered particles (c). Two almost similar patterns are present in these 2D images because in a sweeping cycle, the ions are allowed to pass twice, once during the left to right sweep and once during the return sweep. In the bottom of the figure, the two red spots (blue line below) are for the part of the direct beam that did not hit the surface whereas the ions that did hit the surface are quasi-specularly reflected and appear on top as a blue pattern (red line below).

Once the pulsed ion beam is obtained, we can neutralize it by charge exchange with a gas cell. The neutralization cell is located after the beam chopping system and prior to injection into the interaction chamber. The non-neutralized ions are deflected away by an electric field. With this neutralization method, we could get pulsed neutral beams with high energy (several hundred eV).

However, neutralization increases the beam divergence and therefore pulsed ion beam lose a little energy resolution. This divergence induced by the electron capture collision is governed by the differential cross section. The only adjustable parameter is to change the nature of the gas used to neutralize the ion beam.

2.1.4 Preparation of the samples

The particle-surface interaction and measurement take place in the interaction chamber with a pressure around 10^{-10} mbar to limit the pollution of the sample surface during operation. In this ultra-high vacuum chamber, we have a target holder with 3 free-degrees of freedom to adjust the sample position as well the incident and azimuthal angle.

Inside the target holder there is a tungsten filament to heat the surface for desorbing the contamination on surface and annealing of surface atom after sputtering. Also for some specific operation such as controlling the sample temperature to avoid “charging up” of the surface. The surface temperature is monitored by a thermocouple located inside the target holder.

2.1.5 The detectors

Two detectors are located in this chamber which allows us to study particle-surface interaction: one is devoted to the analysis of the scattered particle and the other one to the secondary particles.

- A single particle time-resolved position sensitive detector (PSD) permits the measurement of the X, Y and t coordinated of the scattered particles. X corresponds to lateral deflexion (parallel to the surface whereas Y is normal to the surface and t measures the time from the chopper reference. For calibration purpose, the target is not fully inserted inside the beam so that some ions fly over the surface until the edge without touching it. These ions produce a little spot on the image allowing precise definition of the angle of incidence and their arrival time is the time reference for energy loss measurements.

- A hemispherical detector array consisting of 16 units designed to collect with high efficiency the secondary particle emissions from the surface.

The details for the detectors can be found in the thesis of Jérôme Villette, Anouchah Momeni and Patrick Rousseau and are briefly recalled below.

2.1.5.2 Position sensitive detector (PSD)

For the position information of scattering particles, a resistive anode is set after the last MCP (micro-channel plate) to localize the ~10^6-10^7 electrons produced by the two MCP.

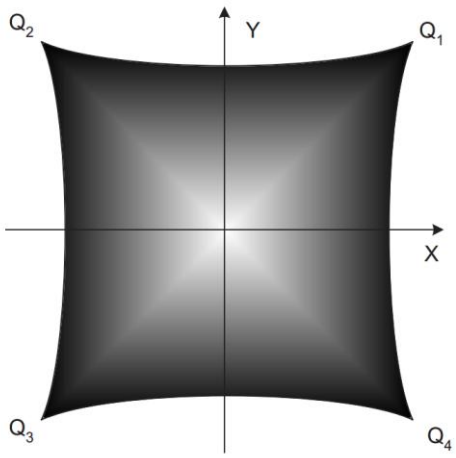

Figure 2.7 Resistive anode used to recover the position of the impact on the MCP. If impact took place in the center, all four charges (Q1...Q4) will be equal. Measurement of the actual four charges allows reconstruction of the X,Y coordinates on the detector. The special cuss ion shape of the collector reduces the aberration's. (thesis of Anouchah Momeni [21]).

The choice of this special anode from QUANTAR Technologies (in Figure 2.7), (http://www.quantar.com/) minimizes the distortions caused by the diffusion of the charges (so called Gear conditions). The four charges are encoded in an AD811 CAMAC module and transferred to VME card containing a PC operated in Windows XP. The acquisition program is written in C++ Builder.

At this level, the data are already 3D when time of flight is included and difficult to display in 2D. Two examples are selected below, a 2D (X, Y) showing the direct and scattered beam and another 2D (Y, t) plot showing the time of flight as a function of the vertical position.

2.1.4.1 2π detector

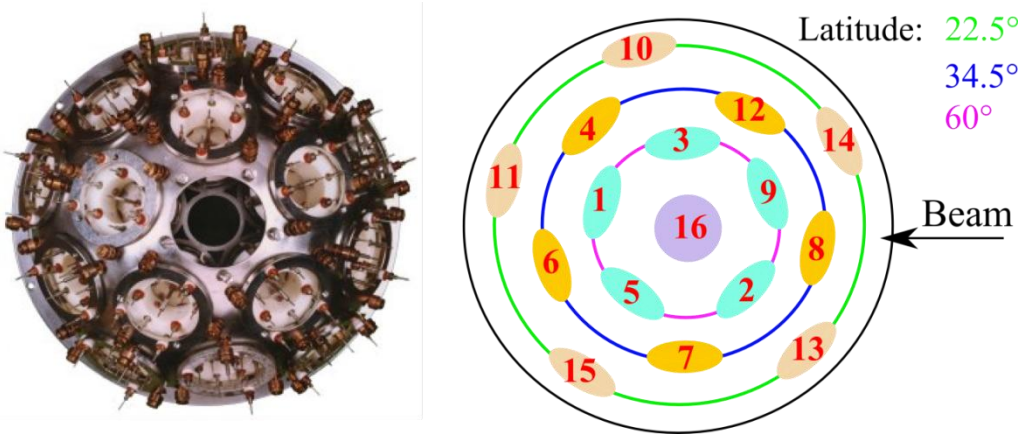

Figure 2.8 2π detector is composed of sixteen micro-channel plate detectors, and the three groups' (4 detectors located on the circle) latitude distribution are 22.5°, 34.5° and 60°, respectively, the sixteenth is removable for in the case of beam impact perpendicular on the sample surface and is locates in the pole of the hemisphere.

Each detector output is analyzed by a discriminator to decide whether or not a particle has been detected. When such detection is granted a logical pulse is emitted and sent to a specific channel of the TDC.

Acquisition program records various signals which are stored and analyzed online during the acquisition. It allows setting filters to analyze the data and study, for example, the results according to the charge states, the number of electrons emitted in coincidence measurement and so on.

A reference time signal for coincidence measurement is necessary to trigger the data recording as start signal, and certain time delay for the terminal signal. Accordingly, this relevant signal from detector is inverted and amplified by a pre-amplifier and validated by a discriminator comparing to the threshold. This discriminator provides a logic signal that opens a time gate during acquisition and time-to-digital convertor will acquire the time information of signals from the 2π detector and PSD and then transfer them to the bus CAMAC.

The arrival times of secondary particles on each of 16 units of 2π detector are determined by discriminators. A bus ECL sends these signals to time-digital convertor. The four charges used for imaging are amplified and delayed relative to the reference time signal and encoded on the bus by a converter charge camac-digital.

2.1.4.1 Coincidence measurement

For the ion/atom—surface interaction research, coincident measurement is an effective method to get detailed information on the individual processes, our coincidence measurement system is presented in Figure 2.9.

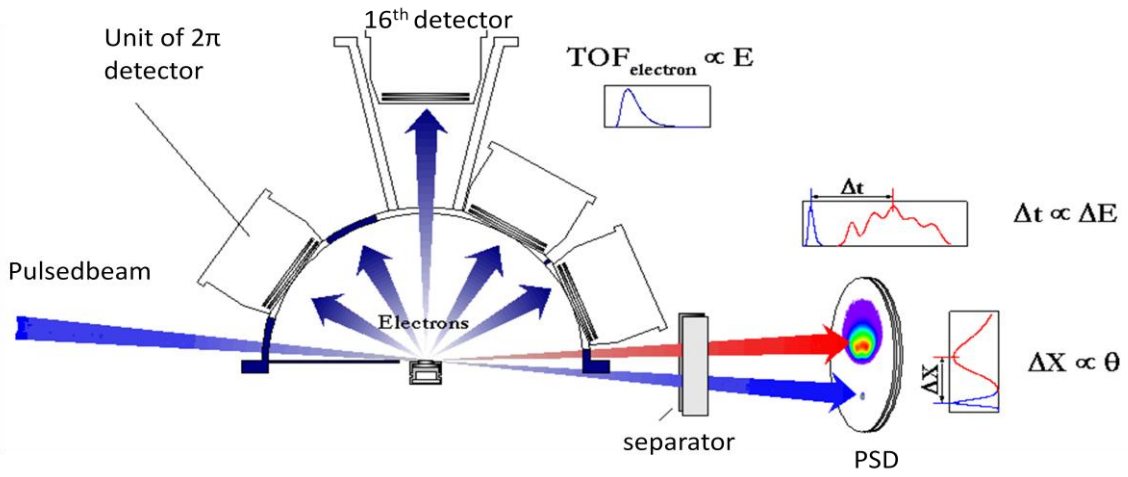

Figure 2.9 schematic of coincidence measurement system [30], 2π detectors surround the sample just 6cm above, the PSD locates downstream around 615mm after the sample, the movable separator is set between sample and PSD for final charge state analysis.

For the data acquisition system, especially for the coincidence measurement, coincidental and unambiguous signal recording is crucial important for possibly recovery the experiment scenario. In order to decrease the statistic error, a relative large number of effective “event” are needed.

Our data acquisition relies on a multi-channel multi-stop time to digital converter (TDC). Each particle detector as well as the beam chopper is connected (after discrimination has taken place) to one specific channel (i.e. 18 channels PSD + 16 secondary + Chopper). In general, a common stop signal is taken from the PSD, since its time of flight from the interaction region is on the order of microseconds, all secondary light particle are supposed to be already detected and present (in the past). In case of doubt an additional delay can be introduced. Once the arrival time distribution of the primary beam has been analyzed, its mean value serves as a reference for the energy loss of all ions. In addition, since the distances from sample to PSD is known, the mean impact time is also known and is used as a reference for secondary particles.

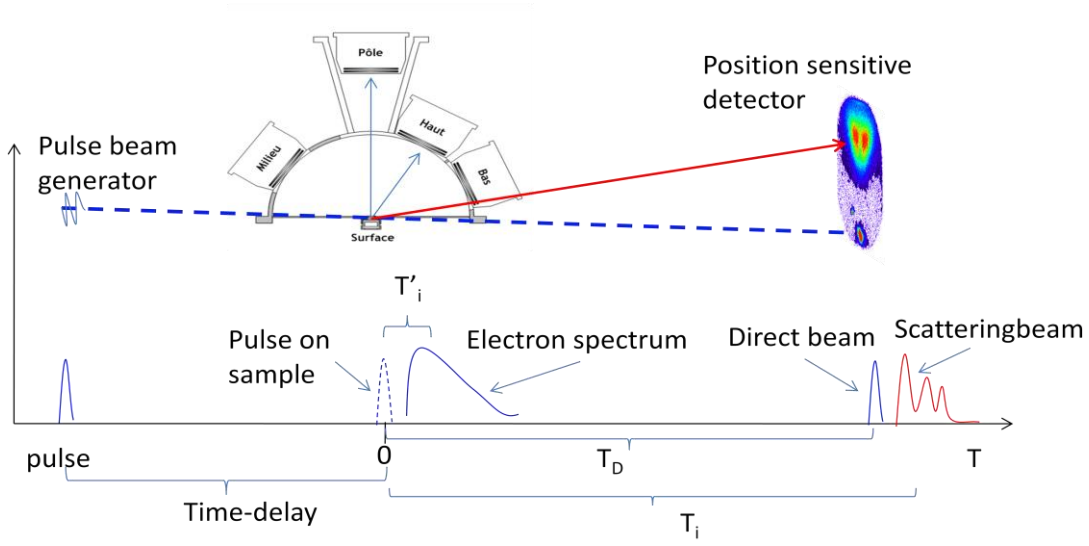

Figure 2.10 schema of coincidence measurement principle.

The accuracy variation of delay lines is calibrated by the difference of time arrival of secondary electron detected from 16th detector to the rest 15 detector, because the secondary particles are emitted with low energy of the order of eV, and the distance difference between 16th detector and the rest 15 is few centimeters, so the time interval in few nano-second, which is three order of magnitude smaller than that of the heavy particle from sample to PSD (position sensitive detector).

The detectors used in the measurement are made of micro-channel plate; this kind of detector could detect all types of secondary particles from the interaction, even atom with few hundred eV, the detail information can be found in the thesis of Jérome Villette [20].

2.2 Computer control of the setup

As I arrived at the lab, the setup was controlled by a computer operated under window98 allowing programs to directly access the EISA (Extended Industry Standard Architecture) bus where the three interface card were sitting; a 16*12bit DAC card, a 16*24bit counter card , a general digital I/O card. When the computer collapsed, it was not possible anymore to buy any computer with several EISA bus. It was also not possible anymore to operate new PC under operating systems without hardware protection via so called “Hardware Abstraction Layer” preventing hardware conflicts. All the control of the experiment control had to be redesign.

The instruments to be controlled are:

-a LeCroy HV1451 High Voltage crate with two sets (one positive and one negative) of 12 channels 0-3kV High voltage cards

-a set of 8 floating power supply designed to operate steerers on the floating beam line.

-a set of stepper motors linear actuators controlling the mechanical actions; moving the jaws of the slits, the faraday cup etc…

-a set of counters used to read sensitive buttons to control the action when operation at distance from the computer is needed.

-ADC and counters were used to measure voltages and currents at high voltage (less than 5kV).

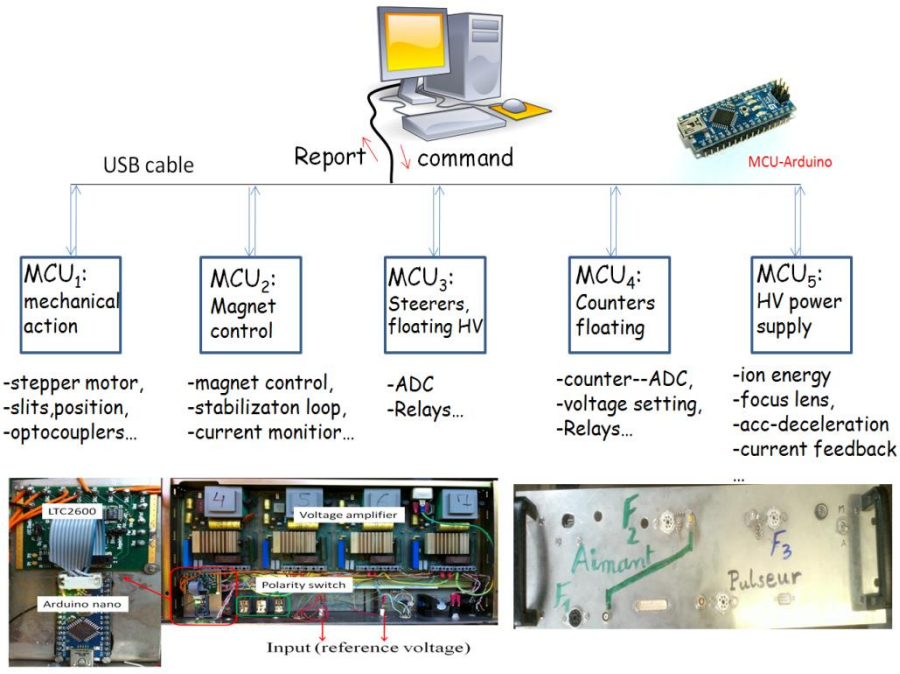

Figure 2.11 General idea of programming control the hard ware in the beam line system.

The decision was taken to use separate microcontrollers to transform each system into an independent robot and to drive and coordinate them with LabVIEW (short for Laboratory Virtual Instrumentation Engineering Workbench). Microcontrollers (MCU) are some sort of simple microprocessors (CPU) but designed to be self-standing, they have their own internal memory, and internal registers directly connected to the outside world, ADC, counters, timers etc… The operating system (OS) is usually most simple and not multitasks (though mobile phones have more and more complex OS showing that nowadays the distinction between MCU and CPU, as found in personal computers, is unclear). These MCU exist since many years, what have made these more attractive is the fact that, now, one can find for 10-20€ platforms such that there is no need of any specific hardware to load the program into their memory or to interface them with computers. With this approach, any program can have direct access to specific hardware without having to inform the Operating System. This is important because the task of writing a driver recognized by Windows is not an easy one. We have chosen the Arduino platform because the C++ compiler and integrated development environment (IDE) is free and open source (http://www.arduino.cc/). The support is provided by the user's community and thousands of examples are available. The Arduino platform simply hosts a USB connection recognized as a virtual COM interface by the operating system. The USB interface is used both to load the program into the Arduino and, when the program is running, to communicate with the host PC via a Virtual COM protocol recognized by most software e.g. Excel®, Wordpad®, Arduino IDE, Borland C++®, Origin®, LabView®…. In few words, it is now possible to change the values from 0 to 5V of any physical pin whereas this simple action is prohibited by Windows inside the PC. From there on, any electronic device can be controlled on a basic level. The general sketch is presented in Figure 2.11.

The program inside the MCU (directly written in C++) performs the needed I/O actions and analog input/outputs. This usually requires an oscilloscope to check all steps of the actions, fortunately, a simple print command inside the MCU program is directly displayed onto the PC screen making development easier. Then, once the program is performing all the basic actions, a simple interpreter allows each action to be triggered or controlled by the host PC. For instance one can choose the following syntax "MOTOR A3 +1500.", to be interpreted as select Motor number A3 and go forward by 1500 steps whereas another string will control the step resolution, the power to be used, the acceleration rate, the cruising speed, the end/stop software or hardware conditions etc, etc. At completion of the action (or periodically) the MCU sends confirmation string such as "MOTOR A3 +1500. Done 1230. End of Motion Encountered" specifying what have been actually done. Within this approach, the test can be performed with a simple terminal window sending and receiving such command lines. The next step is to program a graphic interface to the various MCU as well as the general logic so that any operator can simply click on a so called "virtual button" without any knowledge of the system. This can be done within a general purposed program but I have chosen to do it inside the LabVIEW interface. Three such examples are briefly described below.

2.2.1 High voltage power supply

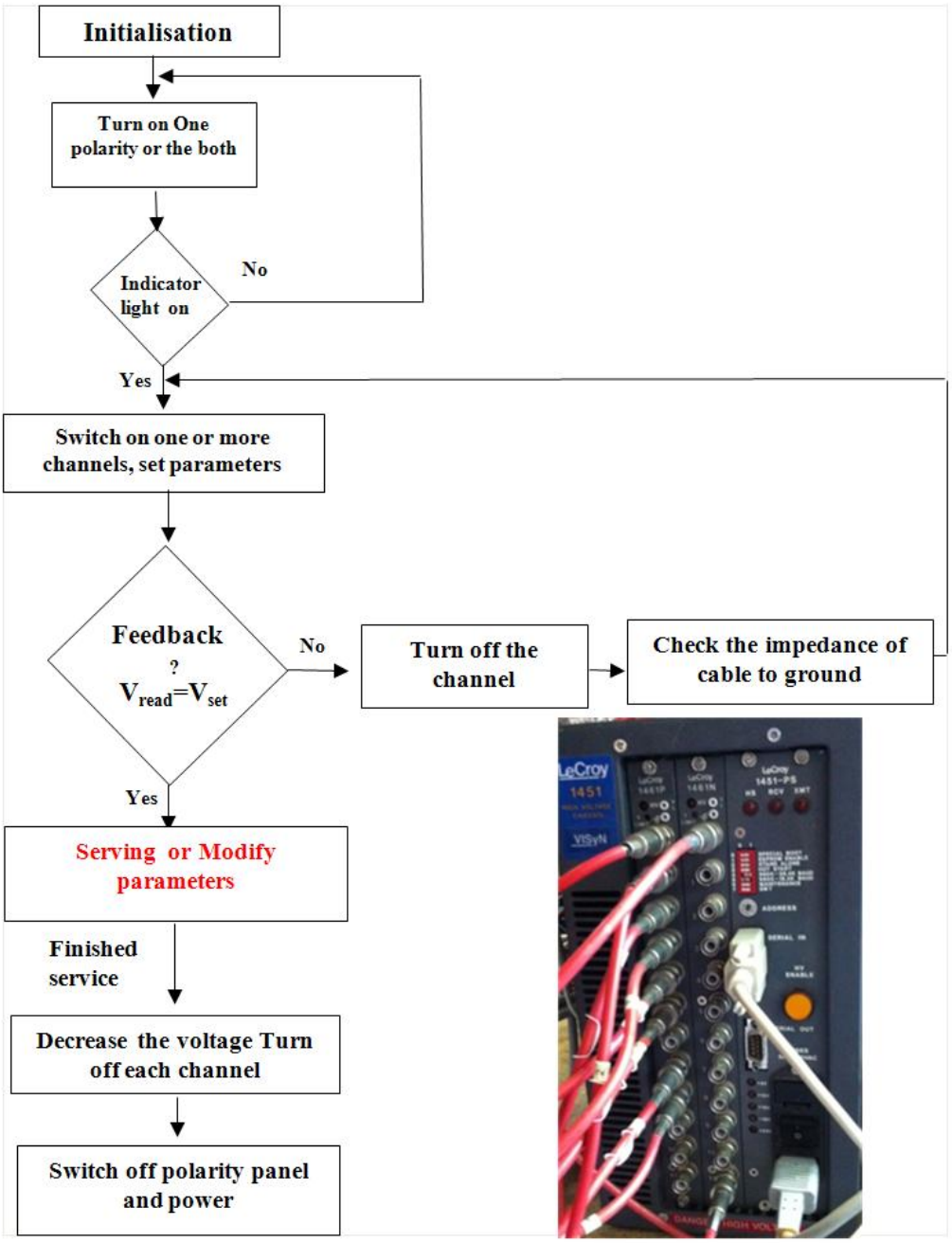

Figure 2.12 The logical diagram for LabVIEW driving HV LeCroy1451 and the front plane of HV LeCroy 1451.

In our experiment several high voltage power supplies are needed; the ECR (Electron cyclotron resonance) source and all the electrostatic lenses needed to guide and decelerate the ions need high voltages. In this particular case, there has been no hardware change and no need to develop our own MCU card since there is already one MCU inside the LeCroy

HV1451 frame. It answers to text strings such as "Set HV on" etc… and reply back execution reports. Inside the HV1451 we have two HV 1461 card each with 12 outputs between 0 and 3kV (-3kV for the negative card) with a programmable maximum current between 10 microampere to 1 milliampere. The LabVIEW program will be in charge of calculating all the combined voltage to guide and decelerate the ions. The logic diagram for programming this high voltage power supply is presented in Figure 2.12.

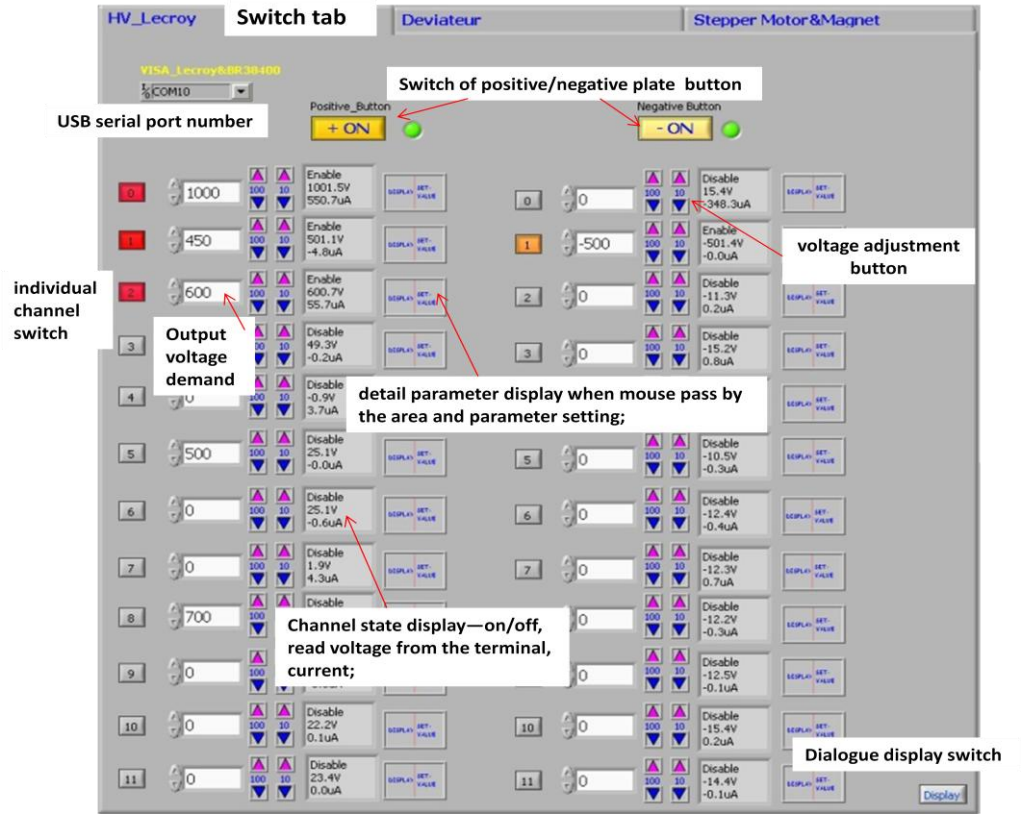

Figure 2.13 Screenshots of the interface for driving HV LeCroy1451 from LabVIEW.

For the programming, the syntax sent to the HV system has to comply with the protocol defined by LeCroy. Comparison the demanded voltages with the measured values is a good way to diagnose the HV supply operation. The user interface to control LeCroy HV1451 is presented in Figure 2.13, in its "independent mode" i.e. in a mode where each channel can be tuned independently.

2.2.2 The Floating Steerers

The guiding of the ions also required the ability of finely directing them up and down as well as left and right. This is achieved through simple deflecting plates which have to be biased symmetrically. Previously, this was achieved by a set of 8 floating power supplies with two input connectors, one receiving eight low voltage commands and another one receiving eight logic signal indicating the polarity. These two connectors were associated with EISA card

inside the former PC. We have replaced all these cards and cables by a MCU unit together with an eight channels Digital to Analog converter (DAC) to generate the analog values. To avoid electronic design, we have purchased for 50$ a fully assembled demo board (DC579A) hosting a LTC2600 –"Octal 16-Bit Rail-to-Rail DACs SSOP-16" and its reference voltage and a 20 bit 8 channels readout Analog to Digital Converter (ADC) LTC2428; The only hardware implemented in this application is a ADUM6401 directly wired on a generic DIP support. This component allows transmission of the digital signals needed to drive the demo board through a 3kV isolation barrier while also providing 30mA of 5V power supply. All these little components have been inserted into the rack hosting the floating steerers so that no external components are visible.

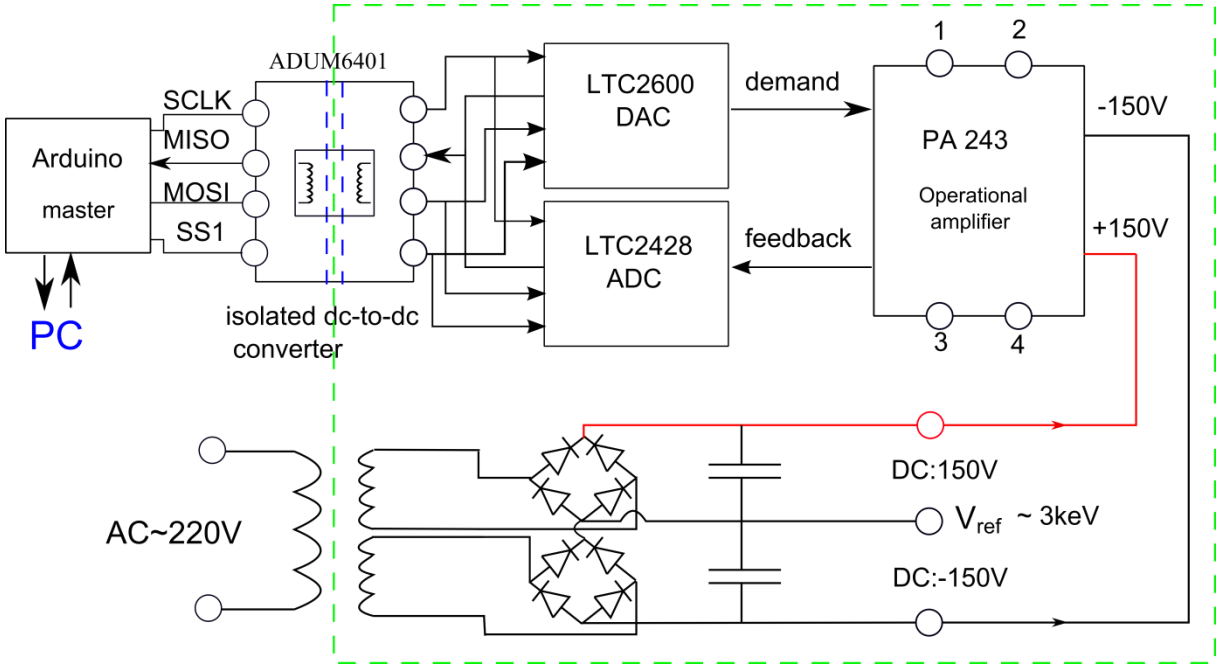

Figure 2.14 Schematic diagram of the floating steerer and its power supply, the green zone can be floating according to V_{ref} (can be up to 3keV), the number 1-4 are the four output for deflector.

For the deceleration optics, additional steerers are needed which also need to be floated but at different voltages. Since we did not have any spare power supplies and from Vladimir Essaulov, we have decided to use high voltage operational amplifiers. The PA243 host two channels of 300V (+/- 150V) OPA so that we have designed a printed circuit holding two ADuM6401 for insulation of digital commands, one LTC2600 for low voltage control of the 4 OPA and a LTC 2824 to readout the signals (Figure 2.14). Two such boards are displayed in the photo below.

From the operator point of view there is no difference between the operations of these two setups.

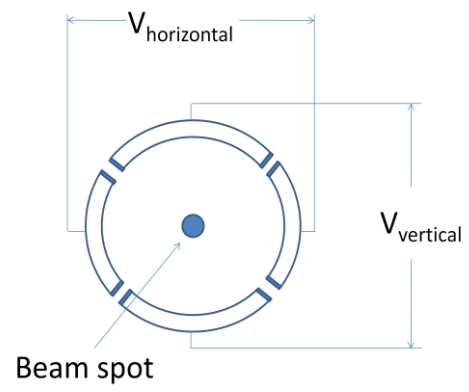

Figure 2.15 Schematic view (perpendicular to the beam) of the deflection systems.

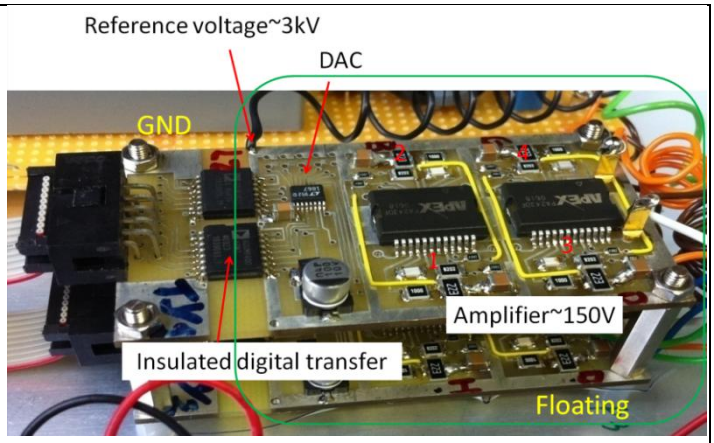

Figure 2.16 Insulated digital-analogue convertor (floating voltage can up to 3keV); "1-4" are four output for four poles of deflector: up, down, left, right.

As discussed above, the LabVIEW program allows independent programming of each steerer, but combined actions are also programmed. Automatic scan are also easy to program etc... The interface for adjusting the potential of deflection systems is present in Figure 2.17. Each action can be executed via three separate scrollbar allowing different sensitivity.

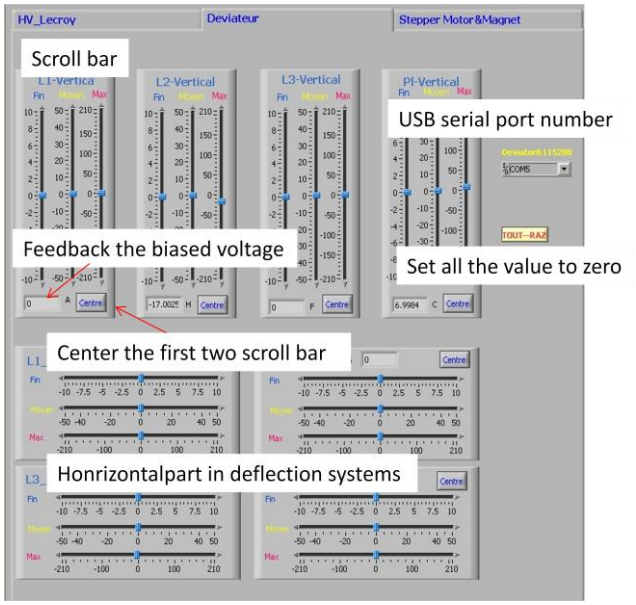

Figure 2.17 Interface for controlling biased voltage in deflection systems created by LabVIEW.

2.2.3 The collimator-step motor

Three stages of collimators systems are employed in our beam line. These are located before and after the analyzing magnet and before the neutralization chamber, respectively. The three collimators systems are made by 4 jaws slit equipped with a 5th retractable plate used as a faraday cup, as indicated in the Figure 2.1 and Figure 2.18.

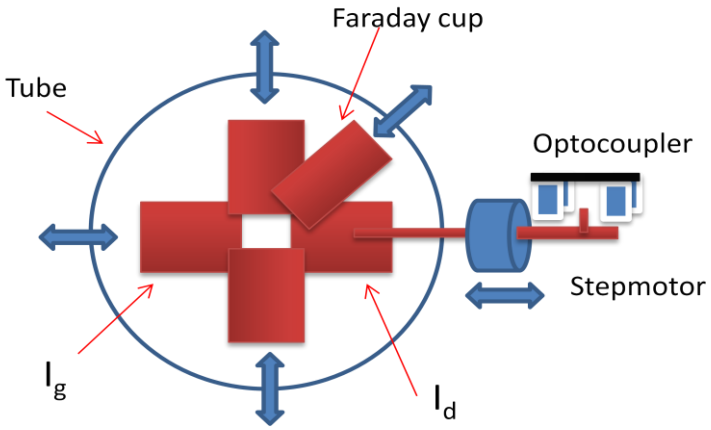

Figure 2.18 Structure of collimators systems.

In addition, the beam chopper is also equipped with four movable parts, two jaw defining a horizontal slit and two plates generating a high electrical field when brought close to each other. These are moved by 20 linear stepper motors (Steggman 3550 and Haydon-kerk 3644(3)-5) with a step resolution of 12 micrometer) driven by only two general purpose stepper motor drivers (MI-452A : the maximum output current is up to 2A and micro step down to 1/64[3]). Indeed, the linear decoupling prevents the stepper motor movement when these are not biased so that only one driver can move all motors. However to performed combined action of two jaws i.e. open the slit (change the size) without changing center position or, at variance, moving the slit without changing the size two drivers are needed to operate simultaneously. Thus each motor is labeled A1… A10 and B1…B10. When two motors have the same number i.e. A3 and B3, they control opposite jaws i.e. Top and Bottom jaws or Left and Right. Each movement is mechanically restricted to avoid damaging the vacuum bellows while simple optocoupler fork (Figure 2.18) at both end of the motion allow software security and recalibration of the actual motor positions in case of failure of the software. In addition, some translation systems are also equipped with a actual measure of the position. This is the case for the beam chopper plates equipped with an analog position feedback. This system was previously controlled by a 25 channel DIO connector plugged to the PC via a bulky cable plus height channels of ADC to read out analog position sensors. Here again, all these cards and cables have been replaced by a single MCU and usb cable. No modification has been done to the existing hardware. A small PCB hosting the MCU and the position feedback plugs into the Sub-D db15 connector instead of the bulky cable (see Figure 2.18). In reception of a text commands “Group_mode: A_only” and “Motor:3:+1500:” the MCU takes control of relay switch selecting the 3rd stepper motor, selects only the A driver (keeping the B out), it adjust the proper current and stepping values, and generate the selected acceleration and deceleration (trajectory) while checking, at each step, the optocoupler to ensure that the end of motion security is not encountered.

[3] *http://www.midi-ingenierie.com/index.php/produits/amplificateurs/mi452a*

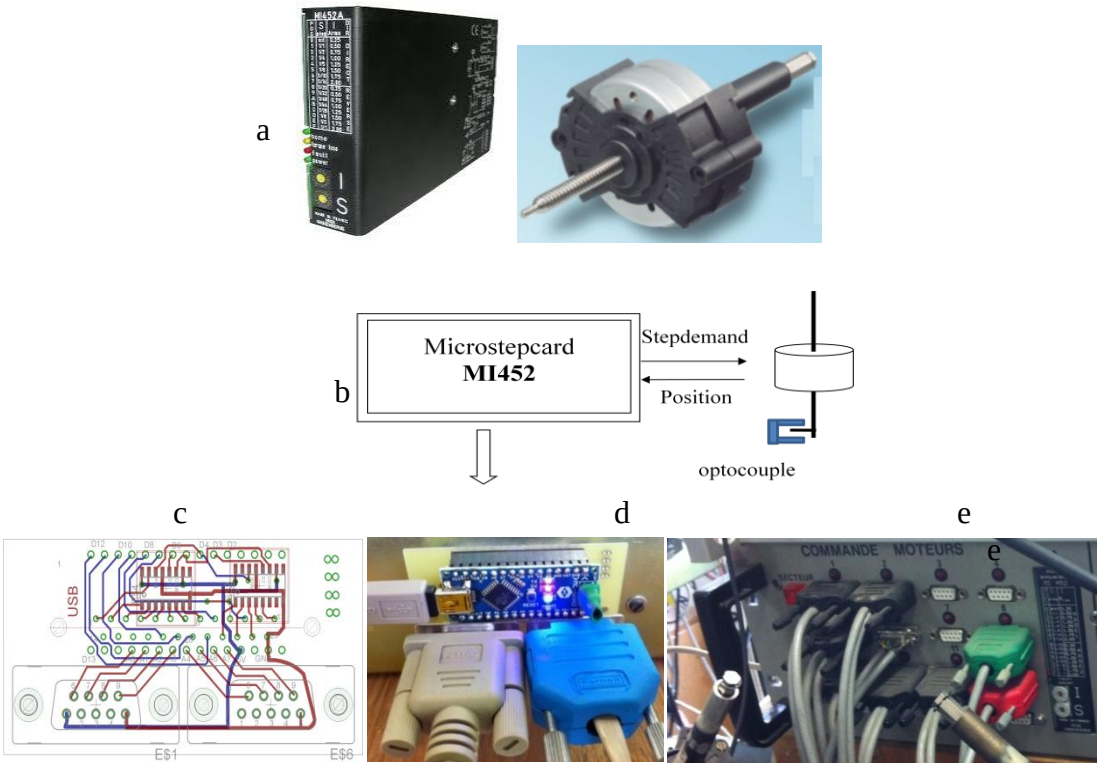

Figure 2.19 The schematic of stepper motor controller (a. the instrument corresponding to b; b. the connection of the step motor; c. printed circuit board between connection of Arduino Nano and the existing rack hosting the 24 relay switches and the two MI452Microstep card; d. photo of the printed circuit plugged into the rack and hosting the two Sub-D db9 connectors used for analog return of the position sensors; e. the front panel of step-motor driving system.)

For each number 1...20 the “group mode” can be A_only, B_only, AB_parallel, AB_antiparallel so that combined actions are easy to program. The system has extra connector and can accept almost any model of bipolar or unipolar stepper motor.

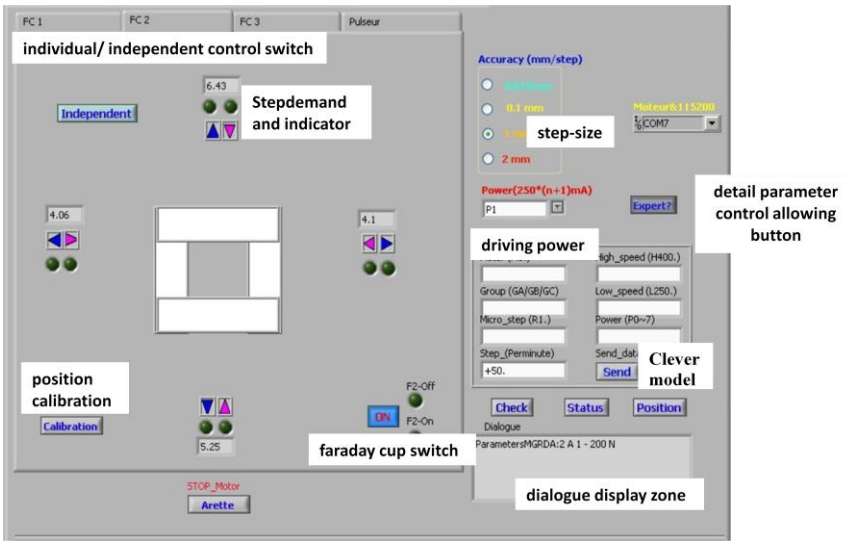

Figure 2.20 Interface of collimator created with LabVIEW.

In order to be compatible with rest of interface control system, we also have created a LabVIEW interface for the collimator control platform, in Figure 2.20. The general idea is to adjust the slit and switch each Faraday cup—a 5th retractable plate on and off by sending the step demand to the step motor. The limit or security is setting by the signal from optocoupler, and the faraday cup only can be switched on and off when adjusting the beam line. As mentioned above, step motor driver has very high step resolution, so we can choose different step size when finely adjusting ion beam. Furthermore, during the interface designing, we left a gate for a specific motor control for in case, but this operation should strictly respect the protocol of 'human-computer interaction', else it couldn't understand anything and the system could be paralyzed during the operation.

2.2.4 Magnet system

The ions extracted from ECR source correspond to different species and different charge states. Accordingly, it is extremely important to select a well-defined ion. In our beam line system, we use a 180 degree electromagnet, as described in Figure 2.1. To control this magnet we have purchased a new power supply [4](the previous one was not stable enough). It can be programmed manually but also programmed (and readout) via analog values into a specific Sub-D db15 connector. Here again, an Arduino is in charge of driving the power supply, reading its actual working parameter as well as reading out the Hall probe and the current at the slits or faraday cups.

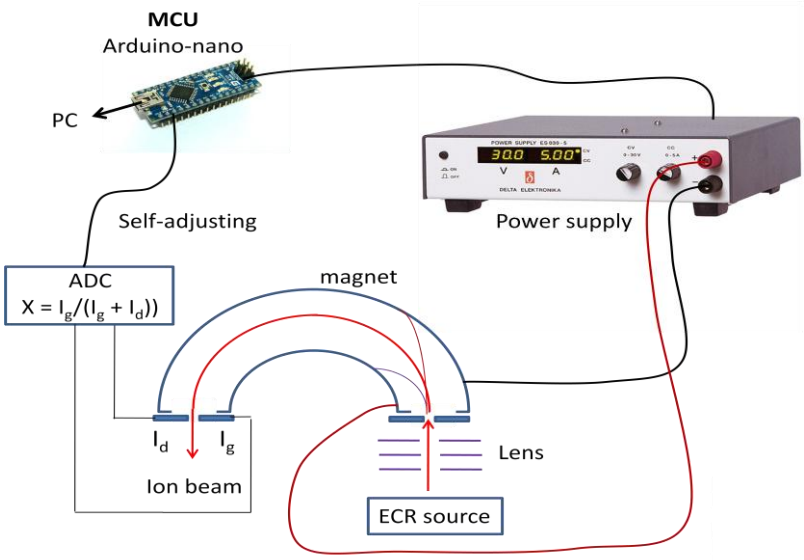

Figure 2.21 Schematic of mass analyzing magnet and self-adjusting for the drift of magnetic field.

As mentioned before, because of the electromagnet heating (thermal drift) and power supply instability, the magnetic field could drift a little during the operation. A stabilization system of the beam has been developed to offset this kind of drift base on the current measurement by the pair of horizontal slits located after the magnet, as indicated in Figure 2.21. If the beam is well centered on the exit slit, and then the current measured on both slits are equal. If the beam drifts to one side or the other, this $X = \frac{I_1}{I_1 + I_2}$ will change providing a key for readjustment.

In the present case, all ions are extracted from the source at a voltage Vs and analyzed by the magnet floating at a voltage V_m. All ions have an energy $E=q(V_s-V_m)$ and a velocity $v=\sqrt{\frac{2E}{M}}$,

[4]Delta Elektronika ES030-5

so the magnetic field should follow Eq (2.1). Accordingly, the magnetic field should show a linear relationship with square root of mass-charge ratio, as calibrated from see Figure 2.22.

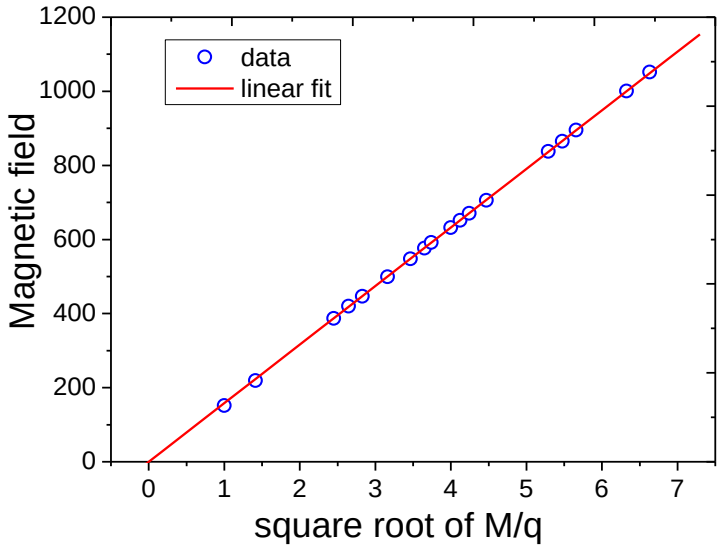

Figure 2.22 Relative intensity of magnetic field of detected peak position vs. root square of mass-charge ration associated to Figure 2.2.

As already stated, the dipole magnet (our mass analyzer) can be floated either to negative voltage to favor easy extraction of low energy ions (less than 1keV) or, at variance to positive values to comply with the power limitation of our magnet. Here, again in order to be compatible with the rest of the interface control system, we also have created a LabVIEW interface, as the figure below.

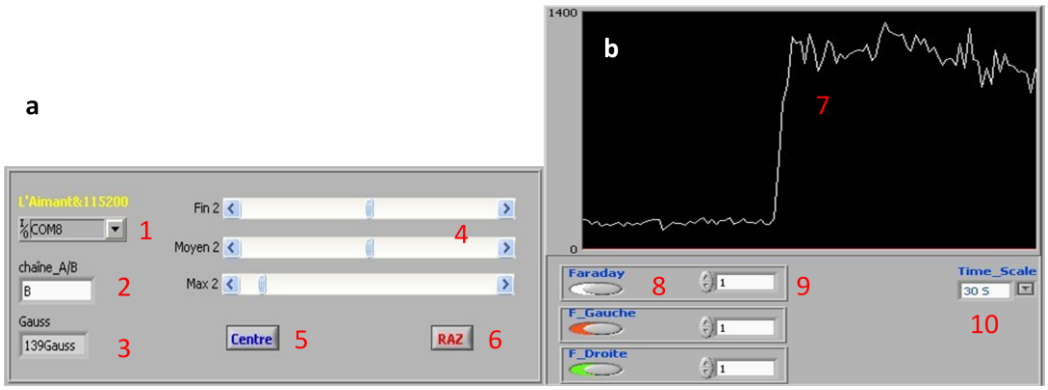

Figure 2.23 Magnet control interface (a) and display current reading from Faraday cup in collimator two after magnet (b). 1. USB serial port number; 2. Channel-B is using now and channel-A is available; 3. Magnetic field read out; 4. Scroll bar for adjusting the magnetic field; 5. Centered the first two scroll bar; 6. Set magnetic field zero; 7. The current read display from the Faraday Cup in collimator 2; 8. Switches for displaying current read; 9. Dividing factor for the three currents display because these orders of magnitude are different; 10.Time scale for current display, here 30s is full scale.

And an example of block diagram of LabVIEW for adjusting magnet field illustrated in Figure 2.24.

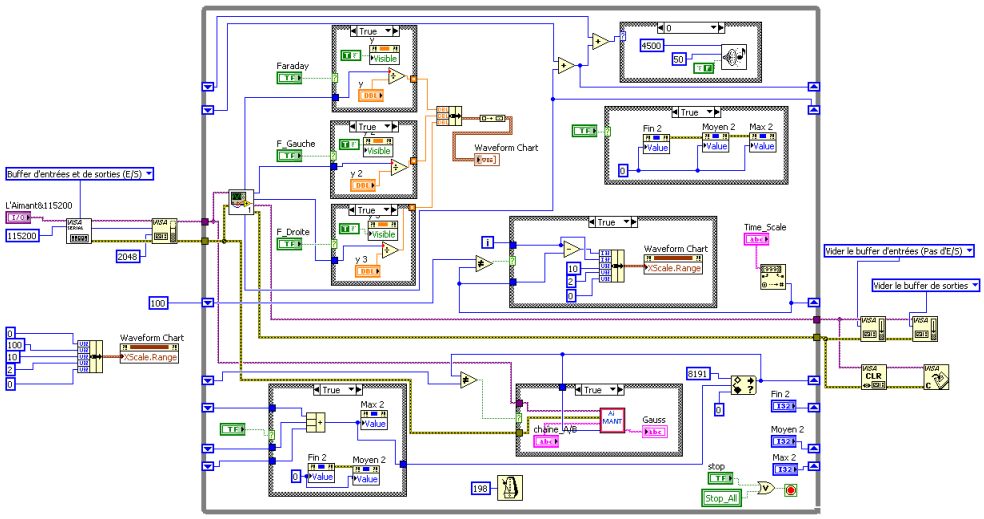

Figure 2.24 Block diagram of the LabVIEW section controlling the magnetic field.

3. Concepts of atom and ion collision

The collision of an ion or atom with a surface is a complex problem. Depending on the property under study, the multiple scattering of atom with materials is dominated by violent events or by a succession of weak interactions. This depends on the geometry and on the dominant processes taking place at a given collision energy. At high energy (100keV/amu-MeV/amu) most materials can be modeled as simple electron reservoir, at variance, in the quasi molecular regime the detailed evolution of the electronic levels of the system is needed. In both cases, a simple approximation is to decouple the "classical" trajectory from the electronic part. Most often one has to concentrate on specific part of the trajectory where the projectile is closer to one particular atom of the surface or of the bulk. We review here some ingredients from classical mechanics needed to understand the different regimes of interaction especially the two simple limiting cases were the trajectory of the projectile can be well defined; head on collision and very grazing incidence.

3.1 The gas phase binary collision.

Since such binary collisions can be solved analytically it is the basic unit of scattering process. Classical mechanics of point like particles (having no internal structure) is fully determined as soon as the forces acting on the system are known. The first ingredient is the determination of the interaction potential between the projectile and the surface. To a first approximation (good enough for insulators) this potential can be decomposed as the sum of binary interaction potentials between the projectile and the individual surface atoms. Since keV projectiles are used in the present work, we need a description of the forces acting on the projectile as it tries to penetrate the solid i.e. when the interaction energy is between few eV and hundreds of eV where the pair potential is essentially repulsive[5].

The simplest situation is that of the elastic collision where no change of internal energy of the partners occurs.

[5] http://www.virginia.edu/ep/Interactions/3__potentials_&_collision_dynamics.htm

3.1.1 Elastic collision

3.1.1.1 : energy vs angle : E(θ)

For an incident energetic particle of mass M_1, and velocity v_0, its kinetic energy E_0 is given by $E_0 = \frac{1}{2} M_1 v_0^2$, while the target atoms of mass $M_2$is at rest. After the collision, the values of the velocities v_1 and v_2 and energies E_1 and E_2 of the projectile and target atoms, respectively, are determined by the scattering angle θ and recoil angle φ. The notation and geometry for the laboratory system of coordinates are presented in Figure 3.1.

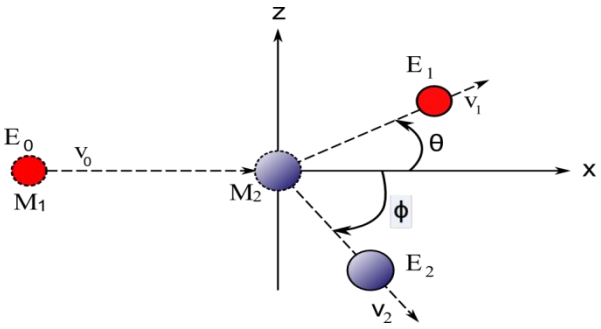

Figure 3.1 schematic of classical binary collision

Conservation of energy and momentum parallel and perpendicular to the direction of incidence are expressed in following:

$$\frac{1}{2} M_1 v_0^2 = \frac{1}{2} M_1 v_1^2 + \frac{1}{2} M_1 v_2^2 = E_0 \tag{3.1}$$

$$M_1 v_0 = M_1 v_1 \cos\theta + M_2 v_2 \cos\phi \tag{3.2}$$

$$0 = M_1 v_1 \sin\theta - M_2 v_2 \sin\phi \tag{3.3}$$

These three Eq.(3.1)(3.2)(3.3) can be solved in various forms, but we focus on the scattered the projectile, eliminate the φ and v_2, the ratio of velocity is:

$$\frac{v_1}{v_0} = \frac{M_1}{M_1 + M_2} \cos\theta \pm \left[\left(\frac{M_1}{M_1 + M_2} \cos\theta \right)^2 + \frac{M_2 - M_1}{M_1 + M_2} \right]^{1/2} \tag{3.4}$$

For determining the scattering angle or diffusion angle, which is also the range of scattering particle that could be measured. More conveniently, the equation

$$v_0^2 \left(1 - \frac{M_2}{M_1}\right) + v_1^2 \left(1 + \frac{M_2}{M_1}\right) = 2 v_0 v_1 \cos\theta \tag{3.5}$$

is often be used. If $M_1>M_2$, according to the Eq.(3.5) the backscattering is physically impossible, therefore the scattering angle is $0<\theta<\frac{\pi}{2}$, and the maximum scattering angle is given by (at $\frac{v_1}{v_0}=\sqrt{\frac{M_1-M_2}{M_1+M_2}}$):

$$\cos^2\theta_m = 1-(\frac{M_2}{M_1})^2 \tag{3.6}$$

For the condition $M_1<M_2$, all values of θ from 0 to π are possible. Therefore the plus sign in equation (3.4) is chosen while the minus sign always leads to negative values of v_1/v_0, and it's not realistic. Thus the ratio of the projectile energies for $M_1<M_2$ is:

$$\frac{E_1}{E_0}=\left[\frac{(M_2^2-M_1^2\sin^2\theta)^{1/2}+M_1\cos\theta}{M_1+M_2}\right]^2=k(\theta) \tag{3.7}$$

According to energy conservation, the energy of recoiling particle (also called recoil energy) is equal to the energy loss of projectile: $E_2=E_0-E_1$, i.e.:

$$\Delta E=E_2=E_0(1-\frac{1}{(1+\mu)^2}(\sqrt{1-\mu^2\sin^2\theta}+\mu\cos\theta)^2) \tag{3.8}$$

Where μ is the mass ratio M_1/M_2, and it also can be calculated by recoil angle $E_2=E_0\frac{4M_1M_2}{(M_1+M_2)^2}\cos^2\phi$. Note here that recoil energy can amount to hundred eV whereas we will see that in grazing incidence it may reach meV.

Small angle scattering:

When the scattering angle θ «1 rad i.e. sine$\theta\sim\theta$, the elastic energy loss formula can be simplified as (for the detail of calculation, please check the Appendix A):

$$\Delta E=\mu E_0\theta^2 \tag{3.9}$$

This formula will be particularly well adapted to understand grazing collisions where the small angle scattering is itself made of many very small angle deflections.

3.1.1.2 The differential cross section dσ/dθ.

At this point, momentum and energy conservation was enough to establish a relation between final energy and scattering angle as a function of the mass ratio. Note that no information of the interaction potential has been needed so far. This information is needed only if one is

interested in the probability that the events described above actually occurs i.e. what is the probability that the particle is deflected at an angle θ: P(θ). It is this quantity called the differential cross section and labeled σ(θ) or dσ/dθ that carries the information on the interaction potential *i.e*. the details of the two collision partners. For instance, a careful measurement of the differential cross section of *MeV* alpha particles on gold foil has allowed Ernest Rutherford to understand that atoms are made of a tiny central nucleus positively charged whereas the negative charge is diffuse. Assuming a pure coulombic interaction, we find an angular dependence known as the Rutherford scattering cross section:

$$\frac{d\sigma}{d\theta} = (mz_1Z_2e^2)^2 \frac{1}{4P^4 \sin^4(\theta/2)} \tag{3.10}$$

where P is the momentum of projectile.

In general, the differential cross section is complex nature and also depends on quantum effects (Stückelberg oscillations). For binary collision there is a rotational symmetry and the geometry is perfectly defined and characterized by a quantity called the impact parameter b.

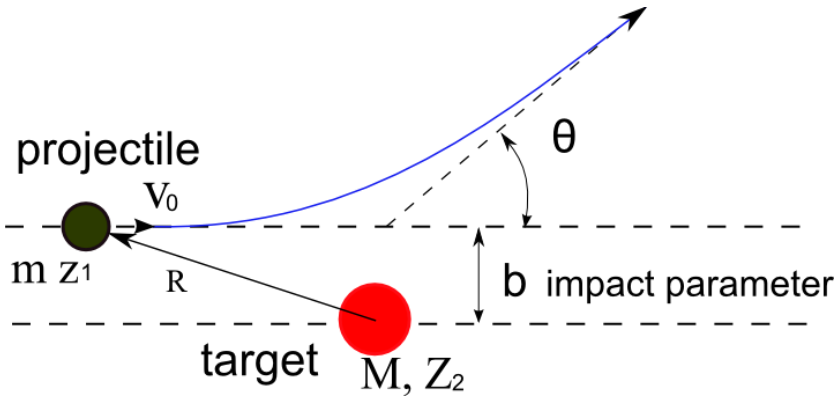

Figure 3.2 The scattering of a particle with mass m, initial velocity v_0, from a center of force at the origin.

Returning to the small angle case, scattering angle can be evaluated $\tan\theta \approx \frac{p_z}{p_0}$, where p_z and p_0 are momentum of scattering particle in Z-axial and its initial state, respectively. This is particularly simple because the action of the force can be evaluated in a straight line trajectory approximation. The projectile deviating very little from its original path, we assume the uniform rectilinear motion along the line of equation (z = b). The distance between two partners and incident velocity defined by: $R = \sqrt{b^2 + x^2}$ and $v_0 = dx/dt$. Therefore, based on Molière single binary potential [31]: $U(R) = \frac{A}{R}\exp(-\Gamma.R)$, by integrating the fundamental relation of dynamics: $\frac{\vec{dp}}{dt} = -\vec{\nabla}.U(R)$, so the momentum transfer according to (Oz), along the trajectory:

$$p_z(b) = \frac{A.b}{v_0}\int_{-\infty}^{+\infty}\frac{1+\Gamma R}{R^3}\exp(-\Gamma R)dx \tag{3.11}$$

We finally obtain an expression for a *numerical* calculation of the scattering angle:

$$\theta(b) = \frac{180}{\pi}\arctan[\frac{Ab}{2E_0}e.Sum(b)] \tag{3.12}$$

Where $\frac{A.b}{v_0}.Sum(b)$ is an approximation of Eq.(3.11), and e=0.1 [32].

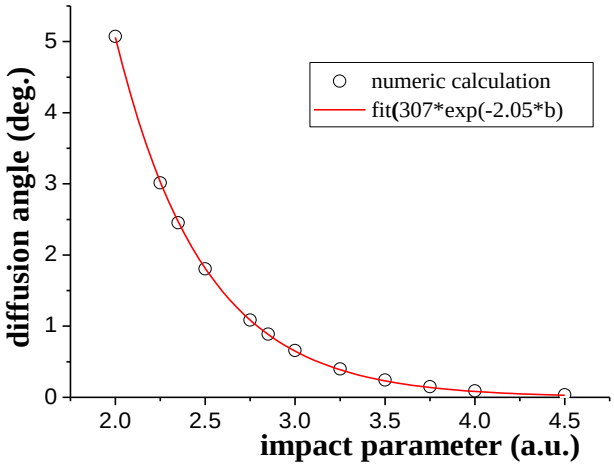

Figure 3. 3 Diffusion angle vs. impact parameter of binary collision with an approximation by Molière potential [32].

The evolution of $\theta_{diffusion}$ according to the impact parameter, although not determined analytically, can be written in the form

$$\theta_{diffusion}(b) = \alpha.\exp(-\gamma.b)$$

The interesting result is that the whole area of impact parameter (2.5 a.u. <b <5 a.u.), the scattering angle decreases exponentially with the impact parameter and the coefficient of the exponential is close to that of the binary potential.

3.1.2 Inelastic collision

In general, the change of internal energy is a complex problem that can be treated only with quantum mechanics. It involves several electronic states of the target and of the projectile coupled in a time dependant way as the partners approach and separate. When the projectile kinetic energy is much larger than that of the possible electronic transitions, the projectile

trajectory is usually a meaningful quantity that can be evaluated independently in a first step allowing a simpler evaluation of the time dependence. Then, along the elastic trajectory, one can study the quantum problem of the atomic collision as a time dependant problem. At high collision velocity, the atomic orbitals do not have time to deform and the problem is usually treated with atomic orbital basis on each center and a sudden approximation. In the quasi molecular regime, the choice of molecular orbitals is usually better adapted but the final choice also depends on the strength of the coupling favoring a diabatic or adiabatic representation. At variance with the elastic regime, inelastic collisions can be rather difficult to address theoretically.

From the experimental point of view inelastic collisions are identified either through a variation of charge state, or emission of electrons or photons or through energy loss measurements. Typically, if at a given scattering angle, the measured energy departs from that predicted by the elastic formula derive above, the energy excess or defect is attributed to changes of internal energy.

$$Q = E_0 - (E_1 + E_2) \tag{3.13}$$

As early as 1970s, Bierman and his coworkers has measure the inelastic energy loss of binary collision [33], noble gas atoms (Ar^+—Ar, and Ne^+—Ne) with 30keV, they found that inelastic energy loss Q (13.1eV and 35.9eV) are associated to the electron promotion of Ar, 28eV and 64eV for the atom of Ne. Recent measurements [34-36] of inelastic energy losses with higher resolution have shown that, the total inelastic energy loss mostly can be attributed to discrete excitation processes in target and projectile. Transitions of electrons to an unfilled level at a crossing can leave a promoted electron in a higher level after the collision.

3.1.3 Inter-atomic pair potential

The interaction potential between two atoms is complex problem because, it depends on the exact quantum state (energy level, alignment, orientation, spin state etc...) of the two partners. This is obviously much beyond the present level of details of this introduction. For ground states atoms and assuming that these can be modeled as rare gas i.e. full shell with symmetrical electron density, the only strong contribution left in the 1-100 eV range is the coulombic repulsion between the positively charged nuclei due to imperfect screening of the nuclear charge as the inter-nuclear distance becomes small enough.

The natural scale for such effect is the Bohr radius of the hydrogen atom, a_0=0.053nm, which gives an indication of the extent of the atomic electron shells. For distances much smaller than a_0 the electrons do not shield the nuclear charge and the unscreened repulsive potential V(r) is (the one used by Rutherford):

$$V(r) = \frac{Z_1 Z_2 e^2}{r} \tag{3.14}$$

For the distance between the atoms much larger than the expansion of the electron shell ($r >> r_0$), the electrons completely shield the nuclear charge and the potential is almost zero ($V(r) \sim 0$ for $r >> r_0$). However, in the solid the situation is intermediate ($a_0 < r < r_0$), the potential and screened Coulomb potential is required, it can be expressed[37]:

$$V(r) = \frac{Z_1 Z_2 e^2}{r} f(r) \tag{3.15}$$

where $f(r)$ is the electron screening function defining the amount of screening ($f(0)=1$ and $f(\infty)=0$) . The appendix_B I details various approaches to describe the screening function. Many pioneers of quantum theory have associated their names to such screening functions; Bohr, Lindhard Thomas-Fermi, Lenz-Jensen and Molière, Firzov etc… Some atomic screening functions are illustrated in Figure 3.4. Probably the most practical is the one adjusted by Zeigler, Biersack and Mark Litt (ZBL) (marked "Universal" in Figure 3.4) [38] starting from Molière analytical form they have empirically adjusted the coefficient to fit a large set of experimental data (based on 261 randomly selected atom pair combinations).

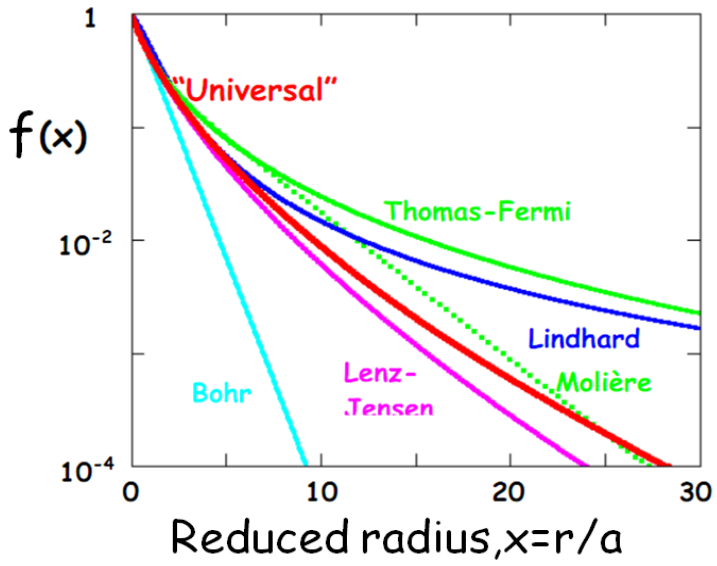

Figure 3.4 Different atomic screening functions[6].

Comparing the expression of Molière and universal or ZBL potential, both of them have a compact form:

$$V(r) = \frac{Z_1 Z_2 e^2}{r} \sum_i a_i e^{-\frac{b_i}{a_F} r} \tag{3.16}$$

[6] http://www.hzdr.de/FWI/GENERAL/Fundam_ISI.pdf

where a_i and b_i are the constant parameters, the detail indicated in Appendix_B I, a_F is the interatomic screening length, which depends on the different species of collision parteners.

3.2 Collisions on surface

3.2.1 Projectile-surface potential

In this thesis, two different collision regimes will be addressed, grazing incidence without any penetration below the surface and larger angle incidence associated with subsurface penetration. In this later case the interaction potential is dominated by that of the closest surface atom (and possibly the second closest) so that inter-atomic pair potentials as optimized by ZBL[38] are probably the best choice to calculate the projectile trajectory inside most materials. This is not the case for grazing incidence where the projectile probes inter-atomic distances on the order of the lattice parameter that are not encountered in the bulk. In terms of energy, typical inter-atomic potential exceed ten eV for distances smaller that a/2 (a is the lattice parameter) which is the maximum distance to an atom in the bulk. As a consequence, the optimization procedure by ZBL had no influence on the inter-atomic values below 10 eV. This means that the values below ten eV derive from extrapolation of well-adjusted values above ten eV. As in any extrapolation, the error is probably limited between ten and few eV but the error can be very large in the eV and sub-eV range. The other important contributions in this range are the long range interactions such as Van der Waals and polarization forces as well as the part of the potential which is not attached to the target atoms. This is, for instance, the component which could derive from electrons in the conduction band. For these situations only more extensive calculations such as DTF (density distribution function) on model slab can produce a more reliable expression.

We try here to outline the specificity of grazing incidence in a, *a priori*, favorable case such as a large band gap insulator. We take Helium (~1 keV) grazing scattering from LiF surface as an example, as illustrated in Figure 3.5.

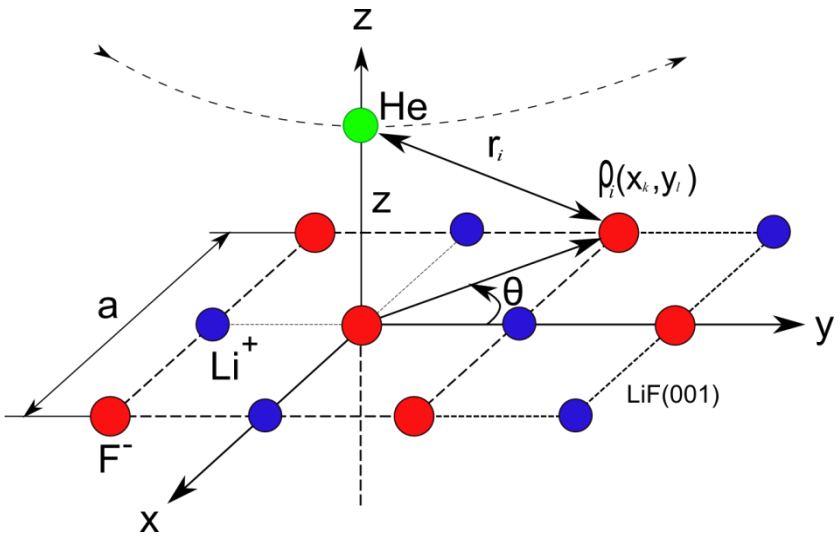

Figure 3.5 schematic of He scattering from LiF surface with grazing incidence angle (a is lattice constant, i, k and l are polarity integral numbers—0, 1, 2, 3…).

Thus, the inter-atomic potential between projectile and surface atom is the summation of each surface atom's contribution:

$$V(r) = \sum_{k=-\infty}^{\infty} \sum_{l=-\infty}^{\infty} V(\sqrt{Z^2 + \rho_i^2(x_k, y_l)}) \tag{3.17}$$

For analytic purpose it can be interesting to evaluate the average value at a given "altitude" z. Writing $r_i = \sqrt{z^2 + \rho_i^2}$ and $dr = \frac{\rho_i d\rho_i}{\sqrt{z^2 + \rho_i^2}}$. The integral of potential from the superposition of pair potentials is given by [20]:

$$V(z) = n \int_0^{2\pi} d\theta \int_0^{\infty} V(r) \rho d\rho \tag{3.18}$$

where n is surface atom density. Combine the coulomb potential(3.15) and Molière screening function of TF model (see in Appendix_B), the expression is:

$$V(r) = \frac{Z_1 Z_2 e^2}{r} \sum_{i=1}^{3} a_i \exp(-b_i \frac{r}{a_s}) \tag{3.19}$$

where a_s is the screening length, and the parameters $\{a_i\}$, $\{b_i\}$ characterize the specific potential, here a_i={0.35, 0.55, 0.1}, and b_i={0.3, 0.2, 6}.

Potential of the form (1/R)*exp (-ΓR) integrates exactly so that combining the Eq. (3.18) and(3.19), the projectile-surface mean potential can be expressed as:

$$V(z) = 2n\pi . Z_1 Z_2 e^2 \sum_{i=1}^{3} \frac{a_i}{b_i} \exp(-b_i \frac{z}{a_s}) \tag{3.20}$$

If one component dominate at a given distance z the potential can be simplified on the form of [20]:

$$V(z) = V_0 \exp(-\Gamma z) \tag{3.21}$$

where Γ is the potential range parameter between projectile and surface atom, V_0 is the potential energy at zero point. Though oversimplified, this expression is extremely useful for simple estimations. For instance, the trajectory on such a potential is analytic so that the length of the trajectory, the momentum and energy transfer to the surface can be evaluated.

Such exponential potential model (3.21) is often employed to describe the potential between projectile and surface atoms, this is because most properties depend on the electron density which, at large distance, always end up to depend exponentially with the distance to the supporting nuclei.

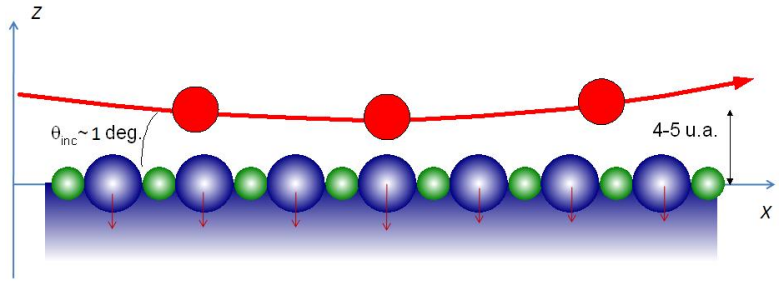

Figure 3.6 Multi-scattering centers with projectile at grazing incident angle, a part of kinetic energy is transfer to surface atoms.

Along the trajectory of projectile, as presented in Figure 3.6, the kinetic energy normal to the surface depends on its position in coordinate Z, because total energy is conserved. Its initial energy normal to the surface is given by $E_{\perp} = E_0 \sin^2(\theta_{in})$, thus, according to the energy conservation:

$$E_{\perp} = \frac{1}{2} m v_z^2 + V_0 e^{-\Gamma z} \tag{3.22}$$

where v_z is perpendicular velocity and depends on the distance in Z coordinate. So the normal velocity is:

$$v_z = \frac{dz}{dt} = v_{\perp} * \sqrt{1 - \alpha * \exp(-\Gamma z)} \tag{3.23}$$

where $\alpha = \frac{V_0}{E_{\perp}}$ and $v_{\perp} = \sqrt{\frac{2E_{\perp}}{m}}$. Integrating of the v_z, we can get the position z(t) of projectile in coordinate Z, which is:

$$z(t) = z_0 + v_{\perp} t + \frac{2}{\Gamma} \ln[\frac{1 + \exp(-\Gamma v_{\perp} t)}{2}] \tag{3.24}$$

Therefore, the angle can be calculated at any point of the trajectory, $\theta = \frac{dz(t)}{v_{//} dt}$, take the value of Eq.(3.24) into this formula, we have

$$\theta(t) = \theta_0 \left[1\text{-}2.\ e^{(\Gamma v_{\perp} t/2)} / \cosh\left(\Gamma v_{\perp} t / 2\right)\right] \tag{3.25}$$

θ_0 is initial incident angle. Therefore, within this averaged potential approximation, the trajectory of atoms at grazing incidence on surface is well defined. One important outcome of this simple model is that it provides a clear definition of a seemingly ill-defined quantity—the trajectory length. A simple way is to visualize the restricted length over which the projectile is changing direction. Multiplying by the mass, it corresponds to density of momentum transfer to the surface (in Figure 3.7).

Concerning the conservation of momentum during the collisions, each recoiled atom's momentum transfer should be the same as momentum change of projectile in normal to the surface direction, i.e. $dP=mv_{//}d\theta$. Therefore, according the Eq.(3.25), the momentum transfer: $dP \propto d\theta \propto \cosh(\Gamma v_{\perp} t/2)^{-2} = \cosh(\Gamma v_{//}\theta t/2)^{-2}=\cosh(\Gamma.\theta.x/2)^{-2}$. For the simple reason, we take $\Gamma.\theta.x/2=X$, then we have $d\theta \propto \cosh(X)^{-2}$ and plot it in a figure and simulated by a Gaussian distribution, in Figure 3.7.

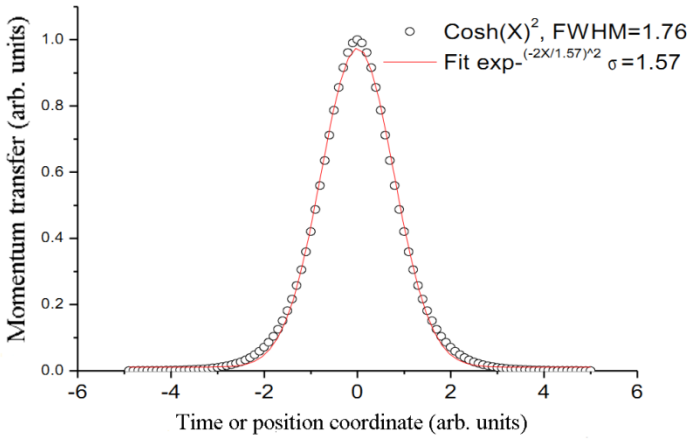

Figure 3.7 pulse transfer function of time and fitted by a Gaussian modeling [20].

The curve looks like a Gaussian and its FWHM is analytic: $\Gamma.\tan(\theta).W_x=3.52$. It shows that, within the exponential assumption, the length of the trajectory scales as $L_{eff}=W_x=3.52/(\Gamma.\tan(\theta))$. This "continuous" model can be arguable by assuming that surface atoms are placed regularly every lattice parameter a so that the number of collision sites can be defined: $N_{eff}= L_{eff}/a$. Based on the expression of the momentum transfer, the effective trajectory length has been calculated by Kristel [32], i.e.

$$N = \frac{4}{\Gamma a \theta_{in}} \tag{3.26}$$

where a is the lattice constant.

Of course, the planar approximation is very coarse but it allows very simple estimate of fundamental quantities associated with a "mean trajectory". A much less restrictive approximation considers that the projectile does not significantly zigzag on top of the surface. Applying the above description to the motion in the y direction, it means that the effective length in the y direction is much larger than a lattice constant a. Then, the straight line approximation suggests to integrate along the projectile direction to produce so called "string potential" V(y,z)=integral along x of V(x,y,z) [4, 20].

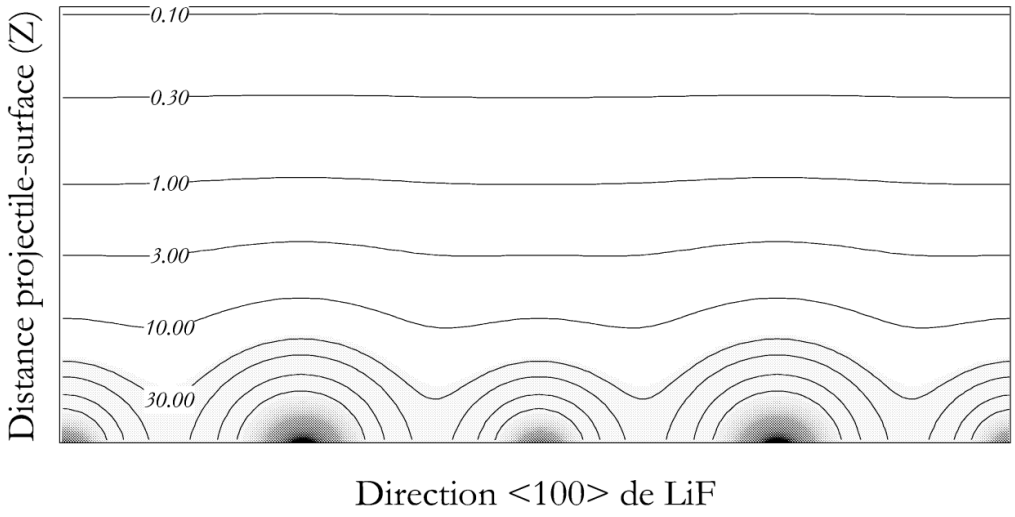

Figure 3.8 Surface equipotential on LiF(001) along <100> direction. All equipotential lines represent V (x, z). The unit of the corrugation line $\xi(E_z, y)$ is in eV.

In practice, the crystal surface may be composed of several species, Sometime, as in alkali halide, one is dominant (in term of electronic density) but this is not always true in particular when the selected equipotential surface corresponds to energies larger than one eV as shown in Figure 3.9 [37]. The equipotential corresponds here to 3 eV. An equivalent drawing at 0.3 eV would not allow a clear vision of the Li atoms.

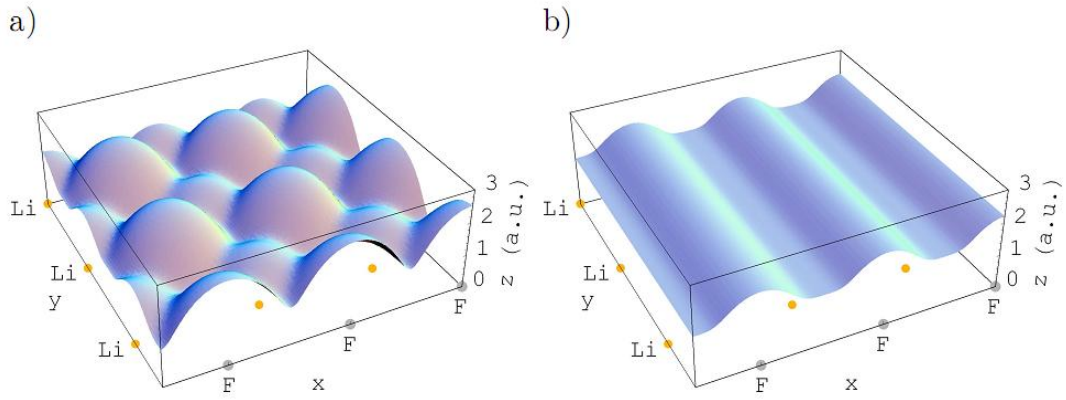

Figure 3.9 a) Equipotential surface V(x, y, z) = 3 eV of the interaction potential between a He atom and LiF (001) from the superposition of HF-pair potentials. The positions of the F-and Li-lattice sites are marked in gray or yellow. b) equipotential surface of the effective potential with axial surface channeling as a) but after axial averaging along <110> [37].

3.2.2 Nuclear and electronic energy loss

The nuclear energy loss is defined as the energy transferred to the nuclei of the target. Classically, it corresponds to the recoil energy defined above in the gas phase. In a crystal it should be identified as the energy transferred to phonon system. When the collision time is

very fast compared with vibration time, both approaches should merge. In other words the energy is transferred locally in a time t~a/v and will decay to delocalized phonons at larger time scales.

The electronic energy loss is defined as the energy transferred into the electronic system, either projectile or target excitation or ionization. Eventually these will decay into phonon modes on a longer time scale.

At high energies, the ratio between these energies is statistically well defined because matter is represented as a given density of electrons and nuclei considered to be almost at rest (with respect to the projectile).

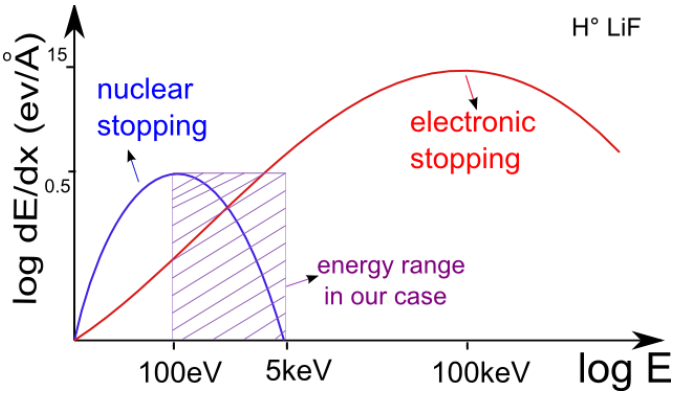

Figure 3.10 Ratio between nuclear and electronic stopping power. The maximum of the nuclear stopping curve typically occurs at energies between 10-100 keV, of the electronic stopping power at MeV energies, here we take hydrogen impacting on LiF as an example. For very light ions slowing down in heavy materials, the nuclear stopping is weaker than the electronic at all energies[7].

From Figure 3.10, we can see that the direct energy losses are function of impact velocity. At very high energy level ($v>>v_{bohr}$), the former part is usually been ignored because it is smaller than the electronic energy loss by three order of magnitude. Contrarily, when the impact particle at the lower energy level ($v<v_{bohr}$), the nuclear energy loss is larger than the electron energy loss. Firstly, we will discuss the elastic collision process based on classical dynamic mechanics, and then continue our second topic inelastic collision.

3.2.2.1 Nuclear energy loss

When a particle collides with target surface, a part of its energy will transfer into the target systems. Since we consider here condition where the projectile is detected outside the target, it means that at least its initial momentum has to be exchanged (reversed in specular condition) with the surface. This can be a large amount of momentum exchanged in few collisions for large angle collision or, at grazing incidence a small amount of momentum spread among

[7] http://beam.acclab.helsinki.fi/~knordlun/mdh/rangetext.html

several scattering centers. Some recoiling energy should be associated with this momentum transfer. In a classical picture, the energy transferred is the sum of the binary recoil energies.

According to the classical binary collision model, energy loss of single collision depends on the mass ratio and scattering angle. With this grazing incidence geometry, each scattering angle is smaller than 1°, so the Eq.(3.9) is often used to calculate the energy loss. Within the effective trajectory model, there are~N sites participating to the scattering process. Thus, each target atom contributes by an amount $\delta\theta = 2*\theta_{in}/N$ where the incidence angle and the factor 2 is coming from specular condition with $\theta_{out}=\theta_{in}$.

$$\theta_{tot} = \sum_{i=1}^{N} \theta_i \approx N\theta_i \tag{3.27}$$

To obtain the energy transfer to the N atoms along its trajectory, we made an approximation that each diffusion angle after one collision site is equal, i.e. $\theta_i=\theta_{tot}/N$. Thus, during the passage of the projectile above the surface, the energy loss per atom is also equal. According to the small angle scattering energy loss, the total energy lost by the projectile in successive collision is given by

$$\Delta E_{tot} = N\Delta E_i = NE_0 \frac{m}{M}\theta_i = E_0 \mu \frac{\theta_{tot}^2}{N} \tag{3.28}$$

When projectile begins interacting with surface atom, the diffusion angle is a function of velocity normal to the surface which can be expressed as: $d\theta = \frac{d^2 z(t)}{dt^2}\frac{1}{v_{//}}dt$, consequently, for the energy loss:

$$dE = E_0 \frac{m_1}{M_2}\frac{\Gamma^2}{4}\frac{v_z^4}{v_{//}^2}\frac{1}{ch^4(\frac{\Gamma}{2}v_z t)}dt^2 \tag{3.29}$$

Where E_0 is initial impacting energy, a is the lattice constant, Γ is the potential parameter between projectile and surface atom, v_z and $v_{//}$ are the velocity normal and parallel to the surface, and m_1 and M_2 are the mass of projectile and surface atom, respectively. For single collision/interaction, $dt=a/v_{//}$, and $dx=v_{//}*dt$, a is the distance of the two adjacent atoms), so

$$dE_i = E_0 a \frac{m_1}{M_2}\frac{\Gamma^2}{4}(\frac{v_z}{v_{//}})^4 \frac{1}{ch^4(\frac{\Gamma}{2}\frac{v_z}{v_{//}}x)}dx \tag{3.30}$$

The density of energy transfer is presented in Figure 3.11, the effective number of collision, as defined before, where $f(x+\frac{\Delta x}{2}) = \frac{1}{2}f_{max}(x)$.

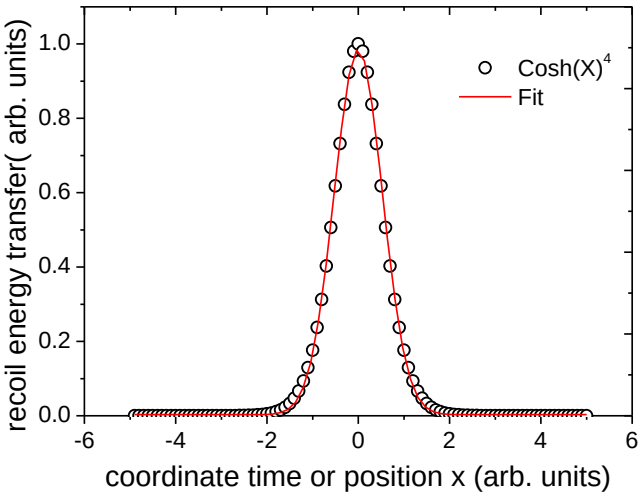

Figure 3.11 elastic energy loss by consecutive binary collision and fit (FWHM=1.21, Gaussian fit exp-$(2x/\sigma)^2$, σ=1.06).

So $\Delta x = \frac{4}{\Gamma\theta}\mathrm{Argch}(2^{0.25})$, accordingly, the effective collision number is

$$N_{eff} = \frac{\Delta x}{a} = \frac{2.423}{\Gamma a \theta_{in}} \tag{3.31}$$

However, the model above we considered energy loss from the assumption of an effective number of equivalent sites defined at FWHM. In this particular case, the total energy can also be obtained by integrating analytically the Eq.(3.30):

$$\begin{aligned}\Delta E_{total} &= \int dE_i = \int E_0 a \frac{m_1}{M_2}\frac{\Gamma^2}{4}\left(\frac{v_z}{v_{//}}\right)^4 \frac{1}{ch^4\left(\frac{\Gamma}{2}\frac{v_z}{v_{//}}x\right)}dx \\ &= \frac{2}{3}\frac{m_1}{M_2}E_0 a\Gamma\tan^3(\theta)\end{aligned} \tag{3.32}$$

As mentioned above, the total energy loss is the sum of all the single binary collision energy loss, so combine the Eq.(3.28) , the total collision number is:

$$N = \frac{6}{\Gamma a \theta_{in}} \tag{3.33}$$

The two methods mentioned above are calculated with the same classical energy loss model, the result of the "exact" integration is almost three times larger than that of energy loss intensity. The main reason is probably due to the fact that the mean deflection is much smaller than the peak deflection (the approximation for the integral of a Gaussian profile I =~ h*σ for a Gaussian requires that h is close to the peak value).

It is interesting to note that, the expression of collision sites have same form, inversely proportional with incident angle, as illustrated in Figure 3.12.

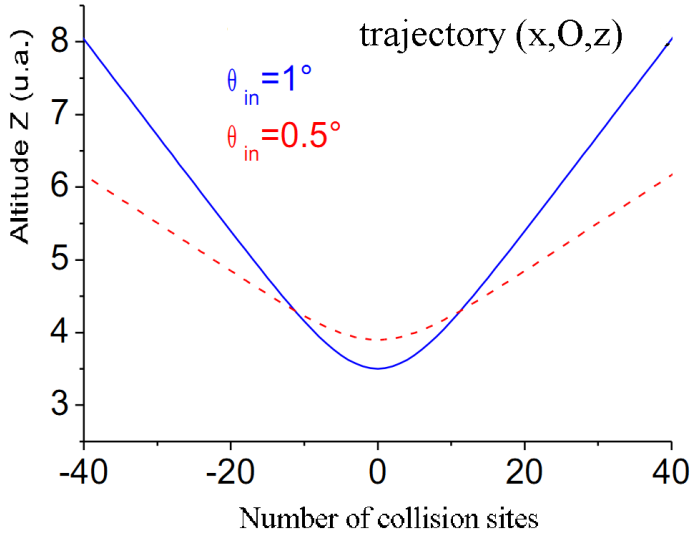

Figure 3.12 comparing trajectory lengths with incident angle, cited from thesis of Pierre Soulisse [39] Larger angle get closer to the surface but interact on a shorter distance.

Since the successive target atoms recoil in the same direction, it is most likely that this transferred energy will concentrate in acoustic phonon modes with a wavelength on the order of the trajectory length.

Another way to excite phonons was discovered by Borisov *et al* [40]. As a positive ion flies over an ionic crystal, it attracts the alkali ions and repels the halogen. As the projectile ion flies away, the target ions oscillate in opposite direction, a mode known as optical phonons. In our group, Villette et al [41] have identified skipping motion of Ne^+ ions on top of LiF(100) where tens of eV are transferred to optical phonons whose energy quantum is around 30 meV.

3.2.2.2 Inelastic energy loss (Electronic)

At high energy or on metal, valence electrons appear quasi free and "simple momentum transfer" to the electronic system is the dominant source of inelastic energy loss. On insulator electrons are in bound states and, in the quasi molecular velocity regime binary knock off model would not predict any ionization and is inadequate to explain excitation. In this regime a quantum treatment is needed to explain the electronic excitation and ionization.

As discussed in section 3.1.2, Bierman and his coworkers has measure the inelastic energy loss of binary collision [33], noble gas atoms (Ar^+—Ar, and Ne^+—Ne) with 30keV, they found that inelastic energy loss Q (13.1 eV and 35.9 eV) are associated to the electron

promotion of Ar, 28eV and 64eV for the atom of Ne. Recently, with coincidence technique measurement, our group has found that, proton impact on LiF surface with grazing incident angle, the main energy loss associated the electron capture, transfer the electron in deep valance band into vacuum (around 14eV), creation a pair of a hole and an electron—exciton on LiF surface (around 12eV) [23], as presented in Figure 3.13. In a short, the total inelastic energy loss mostly can be attributed to discrete excitation processes in target and projectile.

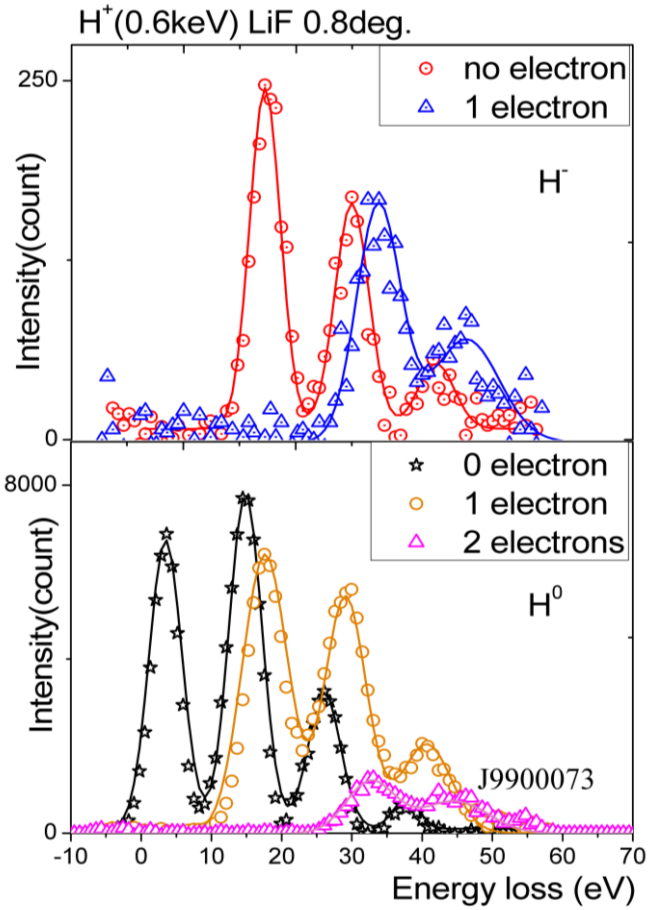

Figure 3.13 Energy loss of scattered H° and H^- when proton grazing incidence on LiF surface, the energy loss are associated to emit electrons or create excitons on the surface [23, 34].

The mean number (1.5) of extracted electrons has been measured by the 2π detector, and the probability distribution for the removal of n electrons is well reproduced by the binomial law, the detail will be discussed in Chapter 5.

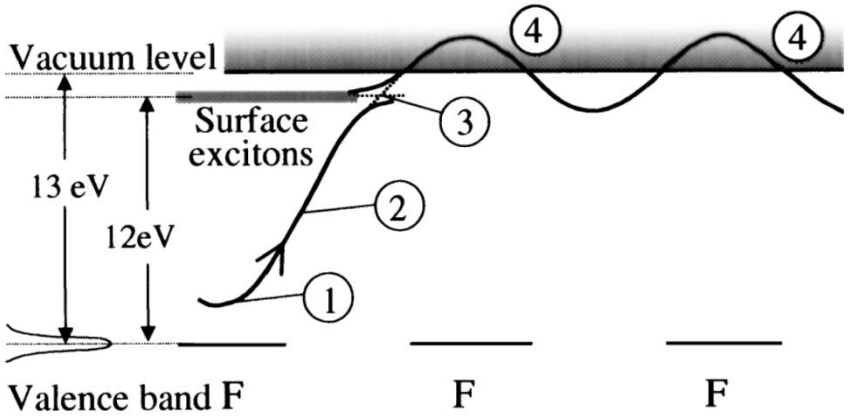

Figure 3.14 Schematic representation of potential energies experienced by the H^- ion along its trajectory close to the surface. First, at close distance to an F^-center, electron capture takes place onto H^- (1). The Coulomb attraction raises the H^-+ F° level (2). When leaving the lattice site electron transfer to the exciton level can occur (3). The H^- that passes the crossing is efficiently detached at the next F^- site (4). The energies measured in this experiment are indicated on the left side [34].

Here we will make short conclusion for the energy loss of binary collision. Because the mass of incident particle (atom or ion of hydrogen, or helium and so on) is much bigger than that of electron, the direction of particle movement is hardly changed by collision with electron. Which guarantees that, at the grazing incidence condition, even the inelastic energy loss is one order of magnitude bigger than that of elastic collision, quasi-specular reflection is still qualified. It also proves the presumption that the inelastic energy loss doesn't affect the dynamical collision, but just enters as a source of energy loss.

However, elastic collision with nucleus, the energy loss strongly depends on the scattering angle, incident energy, the mass ratio of impact particle divided by target atom and incident angle. Thus, the elastic energy loss can be up to half of the impacting energy, down to almost zero. Therefore, Time-of-Flight elastic recoil detection has been immensely used for the surface species analysis despite up to several tens of inelastic energy loss, based on special collision-detection geometry [42, 43]. When the inelastic energy loss was focused, according to elastic energy loss formula (3.8), the extremely small scattering angle has been chosen, such in the case of grazing incidence scattering [34, 40].

3.2.3 Electron capture, Auger emission and detachment

As mentioned above, at short impact parameter many binary collisions are accompanied with inelastic processes. This inelastic energy loss via electronic process during binary collision, charge exchange, electron promotion, ionization, leads to electron emission. In brief, two basic excitation mechanisms contribute to electron emission: (1) Kinetic electron emission induced by the projectile motion, it has been discussed in section 3.1.2. And (2) potential electron emission caused by internal energies stored in a projectile ion [44]. The two

processes are characterized by kinematic and atomic potential energy thresholds, respectively. So the total electron yields depend on the projectile, its energy, and the collision geometry.

The electron transitions between the states of close energy are effective in slow collisions i.e. $v<v_{bohr}$. For the thermal energy binary collision, resonant charge exchange could happen between the same species of collsional partners, i.e.:

$$A^+ + A \rightarrow A + A^+ \tag{3.34}$$

With this process, there is no electron emission or excitation, it turns out that the projectile is resonant neutralized and the inelastic energy loss is zero. This has been widely used as an effective neutralization method when thermal energy neutral beam is demanded. However, if the collisional partners are different species or the initial and final state of transferred electron are not at the same levels, like:

$$A^+ + B \rightarrow A + B^+ \tag{3.35}$$

The electron is more likely transferred from the higher energy level to lower one, resulting in a release of energy. Although sometimes this energy is released in the form of an emitted photon, the energy can also be transferred to another electron, which is ejected from the atom. This is called Auger electron emission.

However, the electron emission detached from negative ions has been measured [34, 45], despite of a big difference between affinity level and big deep valance band. Due to the image charge effect, negative ions levels are shifted downwards, electrons can be resonantly captured and to form a negative ion when affinity level crosses the Fermi level [1]. As soon as the affinity level is shifted out of resonance, the negative ions may decay by resonant loss into unoccupied states above the Fermi level, or emits the surplus electron to vacuum by detachment [45]. Our group has found that double electron captured from two adjacent halogen sites when F^+ grazing scattering on LiF(001) surface [46]. While when the F^- ion recedes from the (double electron) capture region, its affinity level rises and crosses the level of the trion state, the additional electron could be detached via several possibilities. The highest detachment possibility is that the electron been recapture by the surface, but in the excitated state (~3eV to vacuum level), i.e. formed a trion on surface. The second way is that the additional electron is emitted into vacuum, left two holes in the deep valence band.

In short, the incoming ions can be neutralized by electron capture from its collisional partner. In the reverse process, electron from incoming ions or atoms can be captured by target; either process can result in excited electronic states. These processes strongly depend on the relative energies of filled and unfilled energy levels. As a result of electron exchange and energy level crossings in the close collision encounters, electrons can be promoted to highly excited states that can relax by either photon or electron emission. Due to electron level shifting by image

charge effect, a large fraction of temporal negative ions can be formed. Therefore, electron emission by negative ion detachment can be detected; the detail will be discussed in chapter 4.

3.3 Local tilt model, scattering profile

3.3.1 Surface vibration, Debye model[8]

Theoretically, at absolute zero temperature, the atoms of a crystal lie at their lowest energy position without moving at all. As thermal energy is added to the crystal, it produces atomic displacements around their equilibrium location, named thermal vibration. The thermal energy of the lattice, in the rule of quantum mechanics, pulsates as a complete assembly in discrete energy steps of ħω (phonons, ħ is Planck constant divided by 2π, ω is vibration frequency). The phonon is related to both the frequency of vibration and the temperature. If the temperature is raised, the amplitude of atomic vibration increases, and the number of phonons in the system also increase in quantum terms [13].

However, both in the bulk and on surface, the phonon always has a maximum frequency limit. Its highest frequency is bound by the medium of its propagation—the atomic lattice of the solid, known as cut-off frequency or Debye frequency—ω_D. In Debye theory, the Debye temperature is the temperature of a crystal's highest normal mode of vibration, i.e., the highest temperature that can be achieved due to a single normal vibration [47]. The Debye temperature is given by

$$\Theta_D = \frac{h\omega_D}{2\pi k_B} \tag{3.36}$$

where h is Planck's constant, k_B is Boltzmann's constant.

The decoherence surface scattering is mainly caused by surface atom thermal vibrations, and is usually interpreted by Debye model. The Debye method is a simple approximation to the thermal vibrations made that each atom fluctuates independently about its own lattice position. Known more generally as the Einstein model of a solid, it denies the existence of phonon lattice excitations. It is a good approximation for elevated temperatures but shows stronger discrepancies at very low temperatures.

In solid physics, the fixed lattices positions are only ever average positions with atoms oscillate with a motion in three dimensions, which is a function of temperature. Such dynamic fluctuations can be represented by the displacement Δu(t) being a function of time and the instantaneous position at a time t can then be written:

$$R(t) = R_0 + \Delta u(t) \tag{3.37}$$

[8] http://laex.org/stuart/thesis/node13.html

where R_0 is the balance position or the position of atom in bulk at absolute zero temperature. The experimentally observed intensity is a time average of the scattering; so strictly speaking, it is a thermal average of the atomic motions which will be observed.

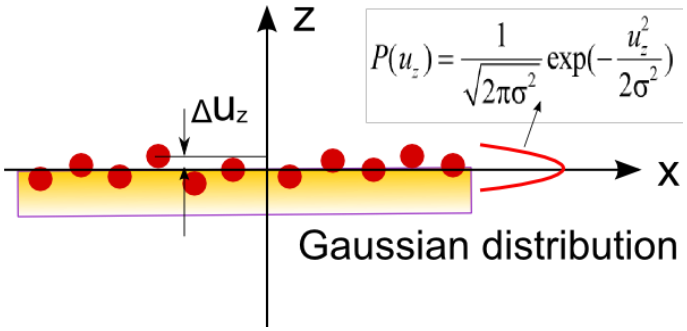

Figure 3.15 Surface atoms vibration distribution.

To model the thermal vibrations, one can find that the first approach is the theory of Debye, which considers that the atoms oscillate in a quasi-harmonic around their equilibrium position. Thermal displacement of the atoms of the target in a direction i (i = x, y or z) with respect to their equilibrium position in a static lattice, can be estimated first order by the probability density distribution of an oscillator harmonic.

The result of Debye's formulation is achieved by displacement disorder (the detail will be discussed in next section). A simplification is to assume that the function Δu(t) has no correlation with the scattering direction. However, more realistically, a spherical displacement function can be used which allows for different vibration modes along the various crystallographic directions. It is then only the component of displacement along $\Delta k_\perp$, the component normal to the diffraction plane, which will be of consequence to the scattering. Thermal displacement of surface atoms have Gaussian distribution with respect to their equilibrium position [39]:

$$P(u_z)=\frac{1}{\sqrt{2\pi\sigma^2}}\exp(-\frac{u_z^2}{2\sigma^2}) \tag{3.38}$$

Therefore, projectile with vector K scatter on surface, the coherence scattering factor decrease by a factor D, which is Debye-Waller factor, i.e.

$$\exp(-D)=\exp(-\frac{1}{2}k^2<\Delta u_z^2>) \tag{3.39}$$

which is known as the Debye-Waller factor, and where $D=\frac{1}{2}k^2<\Delta u_z^2>$. The intensity lost is redistributed throughout reciprocal space by the second term; similar to the disorder term, it is known as thermal diffuse scattering.

The term$<\Delta u_z^2>$ is the mean-square displacement of an atom and will obviously be a function of temperature. The value may be estimated most simply by relating the vibrations to that of a classical harmonic oscillator, the thermal average potential energy of which is

$$\frac{3}{2}k_B T = \frac{1}{2}M\omega^2 < \Delta u^2 > \tag{3.40}$$

Here *M* is the mass of the atom, and the temperature *T*. Δu is the mean square displacement of the atom left its equilibrium position. For harmonic oscillators, the thermal energy is equipartitioned between kinetic and potential energy, which is (k_B T)/2 into each degree of freedom. From this the Debye-Waller factor now becomes $D = \frac{1}{2}k^2\frac{3k_B T}{M\omega^2}$, according to the Debye frequency definition, bring Eq.(3.36) into this formula, finally we get the Debye-Waller factor

$$D = \frac{1}{2}k^2\frac{3\hbar^2 T}{Mk_B\Theta_D^2} \tag{3.41}$$

It becomes clear that the scattered intensity will decrease exponentially with increasing temperature, and large values of scattering vector also affects reflections.

3.3.2 The lognormal angular distribution

If the surface potential is exponentially repulsive as in Eq.(3.21) and additionally if each element of the surface is subject to a random displacement in the vertical direction, the distribution of final scattering angles is lognormal [4, 39], as presented in following figure.

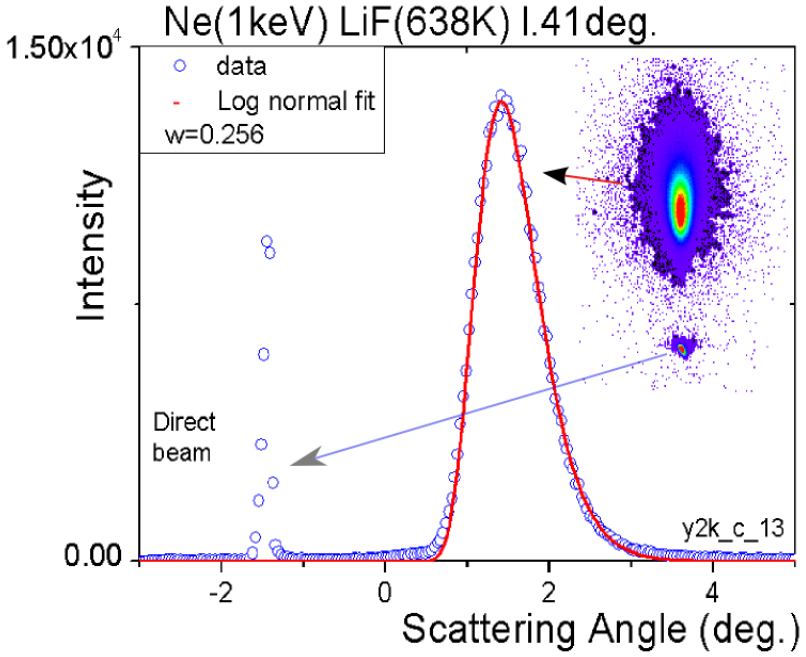

Figure 3.16 Scattering beam profile of Ne° (1keV) with 1.41 degree incident angle on LiF surface with temperature 638K in random azimuth angle, and fitted by lognormal model, the detail explanation is in text.

With small incident angle atom-surface scattering, the final diffusion angle can be approximated as $\theta_f \approx \theta_{in} \approx \frac{v_{z\infty}}{v_x} = \frac{\sqrt{2E_z/m}}{v_x}$, and this can be related to the classical turning point (z_0) through

$$\theta_f \approx \theta_{spec} \approx \frac{\sqrt{2V_0/m}}{v_x} e^{-\Gamma z_0/2} \tag{3.42}$$

where $\theta_{spec} = \theta_{in}$ is specular scattering condition. During consecutive collision with surface atom, the incident angle or diffusion angle is the function of normal velocity, $\theta_z = v_z/v_{//}$. Now suppose that the surface is subject to random displacements u_z in the vertical direction whose probability distribution is Gaussian distribution (3.38).

Furthermore, comparing the time scale of their motion, fast projectile scattering and thermal vibration, the collision time is much shorter than a typical phonon period. Thus, from the view of projectile, it just encounters disordered atoms with displacement u_z around its trajectory due to the surface atoms are “frozen” during this short time (~ps). So for any scattering particle, its diffusion angle will change to be:

$$\theta_f(u_z) \approx \frac{\sqrt{2V_0/m}}{v_x} e^{-\Gamma(z_0-u_z)/2} \tag{3.43}$$

Therefore, at any moment the deflection angle associated also follows an exponential law [4]:

$$P(\theta_f) = \sqrt{\frac{2}{\pi\sigma^2}} \frac{1}{\Gamma\theta_f} \exp\left\{ -\frac{2[\ln(\frac{\theta_f}{\theta_{spec}})]^2}{\Gamma^2\sigma^2} \right\} \tag{3.44}$$

where $\sigma^2=<u_z^2>$. Which was first found by Jérôme Villette in his thesis [20], and named it lognormal distribution. According to the lognormal distribution, the scattering beam width only depends on potential range parameter and thermal vibration displacement, i.e. Γu_z. Due to the potential range parameter only depends on projectile-surface atoms system, i.e. the property of species, the scattering beam width only increases with temperature of sample, as presented in Figure 3.17.

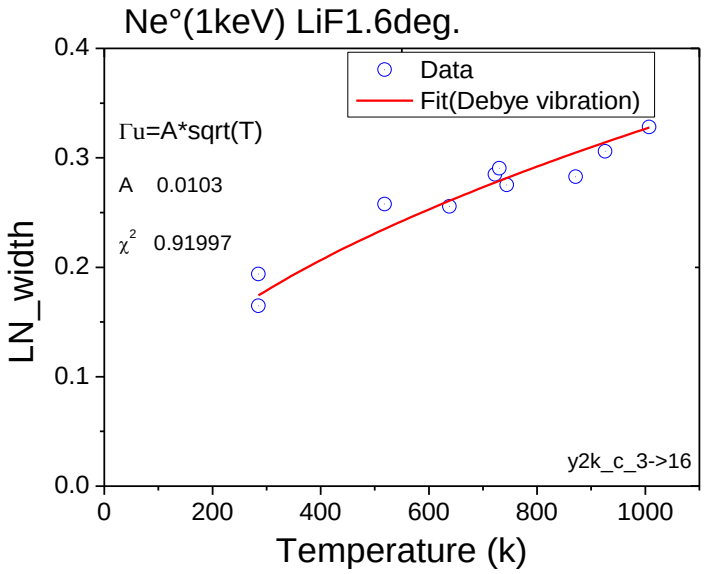

Figure 3.17 Diffusion beam lognormal width vs. sample temperature and fitted by Debye vibration model. With this fit, it gives 0.07 Å displacement of surface atom at 600Kelvin of sample, which agrees well with theoretic calculation, the value of Γ is taken from the report of Kistel [32].

From Figure 3.16, the scattered beam profile was observed in random azimuth angle with 1.6 degree incident angle. In these directions, the arrangement of rows of atoms seen by the beam is arbitrary, and the surface has a periodic arrangement of rows of atoms aligned along the transverse direction. Therefore, the averaged transverse corrugation along the propagation direction is very low and only depends on the thermal vibration amplitude Δu_z. The scattering beam profile was well fitted by the lognormal distribution model expect at very low diffusion angle.

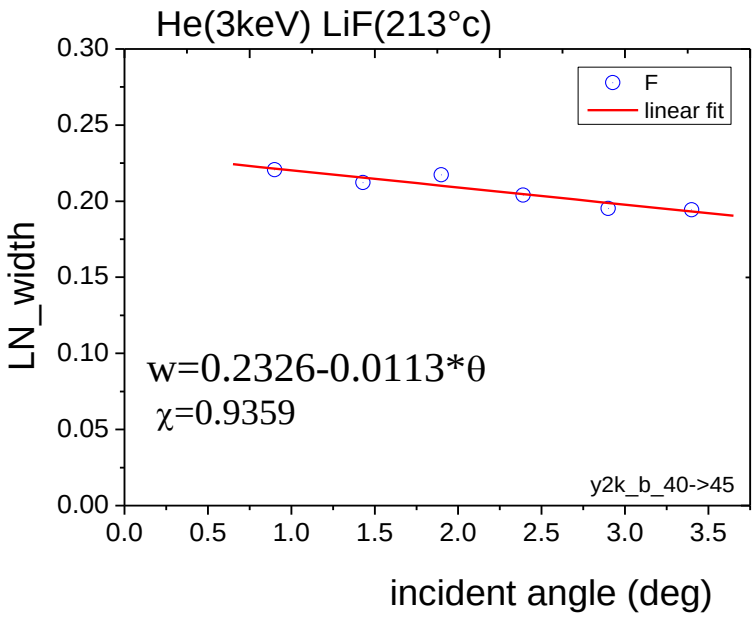

Figure 3.18 The width of diffusion beam profile slightly decreases while increasing the incident angle.

In lognormal model, as we mentioned before, the width of scattered beam dominates by potential range parameter and displacement of surface atoms thermal vibration. However, from Figure 3.18 and Figure 3.19, we can clearly see that the lognormal widths slightly decrease while increasing incident angle showing that the Log_Normal profile is not yet a quantitative model.

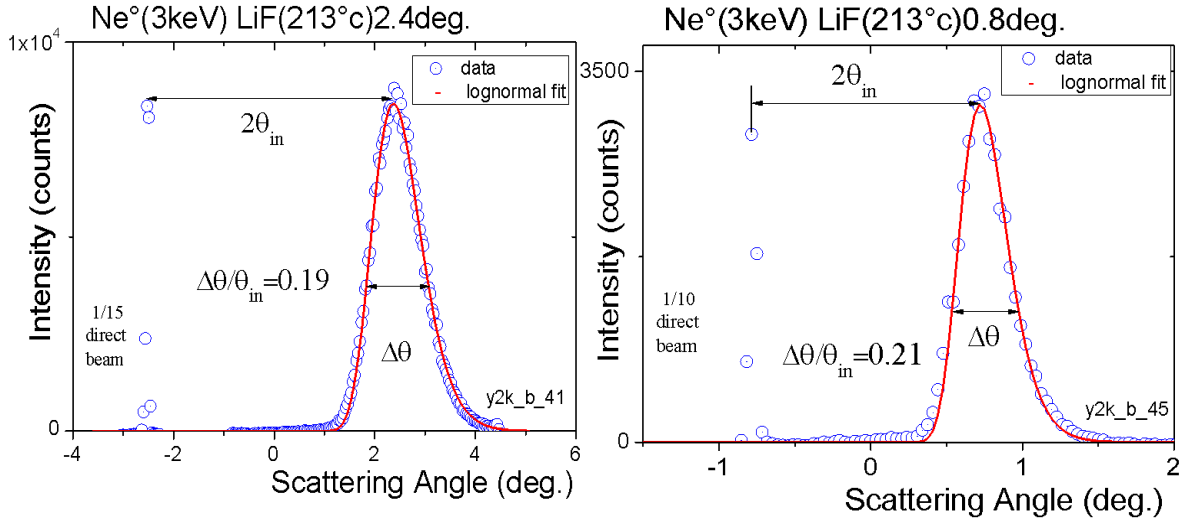

Figure 3.19 Scattering beam profiles with Ne atom 3keV grazing incidence on LiF surface, the incident angles are 2.4 and 0.8 degree, respectively (please note that the scale is not the same).

3.3.3 Slope of the mean surface atom vibration

The origin of the surface atoms displacement is thermal motion, and its mean-square amplitude can be derived very precisely from LEED or HAS measurements, because the projectile is just rebounded by a single surface atom. However, for the grazing incidence scattering, the interaction is more like the local collective effect rather than single binary collision. Furthermore, the surface atoms displacement appears static to the fast-moving projectiles because the collision times are much shorter than typical phonon periods [4].Thus the projectile encounters surface atoms which are "frozen" but distorted from the ideal situation, due to the atoms are randomly displaced from their equilibrium position. Therefore, the instantaneous distribution of surface atoms during the short collision time, dominates the profile of scattering beam.

The scattering beam profile was well fitted by the lognormal model except at the very small or even at large diffusion angle, when carefully analyze Figure 3.16 and Figure 3.19. In the model of lognormal, the average displacement of surface atoms has been considered. However, in some case, the average value could be zero but there is a slope among the N_{act} (the number of interaction sites) atoms, as presented in Figure 3.20 b) and c). accordingly, their contributions for the scattering profile are different. This local tilted model was first mentioned in the thesis of Jérôme Villette [20] and quantitatively explained in the thesis of Pierre Soulisse [39].

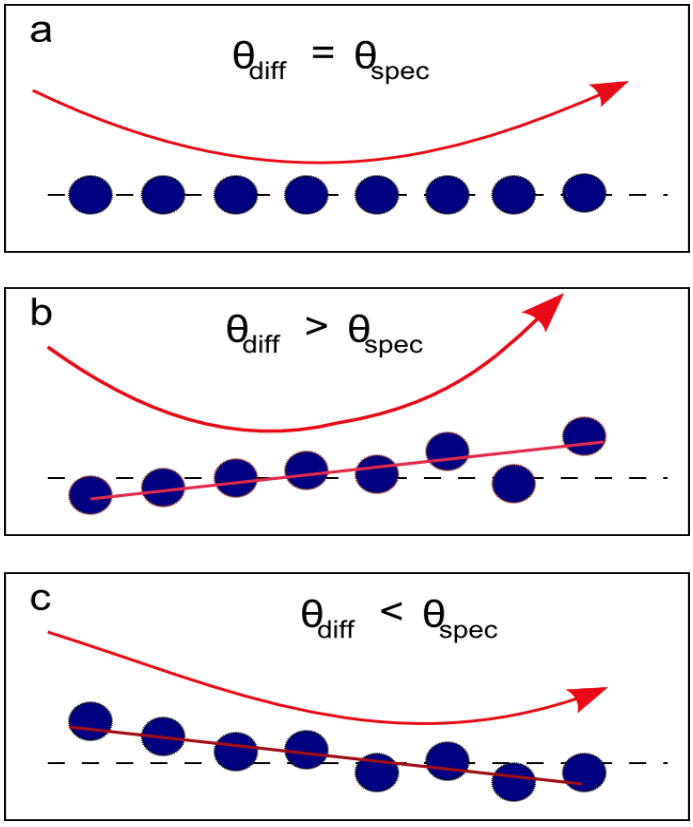

Figure 3.20 Surface atoms (N_{act}) may have different instantaneous local orientations induced by thermal agitation. a. average surface is atomically flat encountered which leads to a specular diffusion. b) and c).

different local orientations can guide the projectile diffusion with greater or smaller outgoing angle than that of specular scattering [20].

Qualitatively, this amounts to consider that N_{act} particular atoms of the surface, they are given a local slope. Starting from the Debye model, this amounts to the question of the distribution $z(x)=\alpha+\beta x$ with slope β and offset α that exists within a set of harmonic oscillators N_{act} variance in z $\sigma^2=<u_z^2>$of regularly lattice constant a is such that with x = 0 was taken at the center, so for each individual atom, we have $x_i = a(i - \frac{N}{2})$.

A linear regression through this particular set gives us the slope and offset. The variance of these distributions is a function of the variance in z positions. Following the analysis presented in Numerical Recipes [48] and the displacement of the average row σ_α of N atoms is $\sqrt{N}$ times smaller than that of a single atom and that the distribution of slope σ_β is of the order of:

$$\sigma_\alpha = \frac{\sigma}{\sqrt{N}}$$
$$\sigma_\beta = \frac{\sigma}{6a}\sqrt{(\Gamma^3 a^3 \theta^3} \qquad (3.45)$$

In the Figure 3.16, which is Ne (1keV) with incident angle 1.6 degree on LiF surface, the bump at the lower diffusion angle and which couldn't be fitted by lognormal model, if this associate to the local tilted of surface atoms, the max tilted angle across with X-axial is 0.4° in this scattering experiment, as illustrated in Figure 3.21.

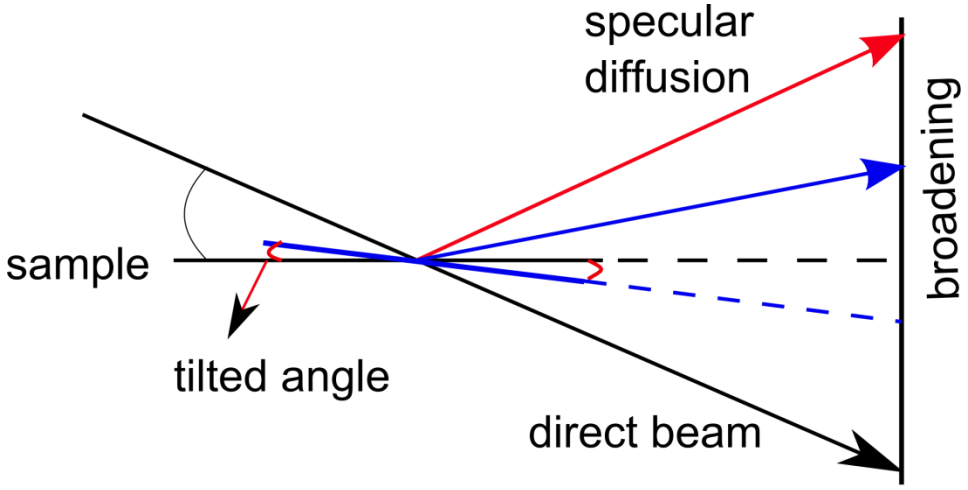

Figure 3.21 Schematic of instantaneous local tilted angle.

3.4 Image charge acceleration for ions

Contrary to the atom grazing scattering on the surface, ion scattering mechanic is much more complicated, and there are many processes needed to take into account, such as electron capture (neutralization), image charge effect, local excitation and so on. Due to the dynamic image force produced by the charged projectile in front of the surface, its trajectory of multi-charged ions is modified. Especially for grazing incidence for ion scattering, the image energy is comparable or even higher than its initial energy normal to the surface. At these years, many efforts have been dedicated to the research of image charge effect with multi-charge ion or even highly charged ions grazing incidence on insulator, metal surfaces [49-53].

In general, the ion near the surface leading to electron at the surface move towards the region close to the ion, creating a screening charge cloud which compensates the ion induced field. In the adiabatic limit ($v_{ion\perp} < v_{bohr}$), the screening effect can be described in terms of a classical image potential, in which a charge +q (number of charge state) at a distance d in front of a conductor at z=0 interacts with a self induced charge –q at –d inside the conductor, as presented in Figure 3.22. For real surfaces, the image plane z=0 is located slightly above the first atomic layer, and the image plane is located about 1 Å on front of the first atomic layer [1], due to the target electron density decrease exponentially outside of surface.

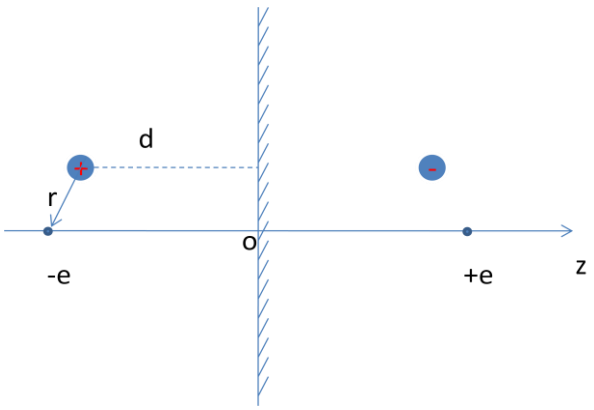

Figure 3.22 Ion and its image charge located symmetrically beside surface plane.

One of the prominent effects of the image interaction, especially for multiply charged ions, is the acceleration of the ion towards the surface. This yields a lower bound on the time the ion spends in front of the surface. The classical image force experienced by an ion charged q at a distance z is $F_{im} = -\frac{q^2}{4z^2}$, taking the integral from infinity to the distance z_0 at which the ion is effectively neutralized gives the total energy gain:

$$E_{im} = \int_{\infty}^{z_0} -\frac{q^2}{4z^2} dz \tag{3.46}$$

However, before being able to evaluate this integral, the boundary condition has to be determined. The interaction between ion and metal in front of the surface is described by a classical "over-barrier" model. If the total potential barrier between the projectile and the target is lowered to potential energies such that resonant electron transfer is classically allowed [53]. The neutralization of the ions proceeds at rather large distances from the surface by the resonant transfer of conduction band electrons into (multiply excited) Rydberg levels of the projectiles, forming so called "hollow atoms" [54].Accordingly, the image acceleration will be switched off when the ion totally neutralized.

The potential felt by an electron at a position r in the vicinity of the ion at distance d to the surface, is simply given by the sum of the ionic potential V_{ion}, the image potential of the ion and the self-image potential of the electron. This yields a total potential:

$$V_t(z) = -\frac{q}{r} + \frac{q}{d} - \frac{1}{4d} \tag{3.47}$$

The lowering of the potential barrier between ion and surface for decreasing z purely stems from the electron image charge, the other two contributions cancel at z=0.

Firstly, we discuss the image charge effect of ion in front of metal surface, because of the different property between conductor and insulator, thus the image energy is different. The polarization charges induced in a semi-infinite metal by the application of a uniform electric field or by the presence of an external point charge far from the surface. The polarization charges due to an external point charge Q located at the distance d from the surface of a metal are familiar from elementary electrostatics, they are idealized as being located on s mathematical surface of zero thickness and, if the metal is grounded so that its potential is zero, the electric field outside can be calculated by replacing then by an image charge –Q located inside the metal at a distance d from the surface. This interaction energy between the charge Q and the metal is the variation of energy when this charge is brought from infinity to the distance d, the energy E_{im} gained by the projectile is given by [55, 56]:

$$E_{im}(q) = \frac{W_\phi}{2\sqrt{2}}\left[\frac{2}{3}q^{3/2} - \frac{3}{4}q^{1/2} + 0.521\right] \tag{3.48}$$

where W_Φ is the work function and q is the charge state of ion.

However, the electronic structure and the dielectric response of insulators are clearly different from metals. We adopt the over-barrier stair-case model to the interaction of multicharged ions in front of insulator surface. Normally, in contrast to a metal, there is a broad energy gap, and the binding energies for the band of occupied electronic states are clearly higher, 12eV for LiF, for instance. Furthermore, the dielectric response of insulator clearly differs from that of a perfect conductor. The dynamic image potentials of the electron and ion core along the surface normal are calculated for a projectile with velocity $v_{//}$in local response from [49]:

$$E_{im} = \frac{q}{2\pi}\int \frac{d\vec{Q}}{Q} e^{-Q(R+z)} \frac{1-\varepsilon(\omega)}{1+\varepsilon(\omega)} \tag{3.49}$$

where R is the position of the charge and ε(ω) is deduced from optical constants [49]; $\omega = \vec{Q}.\overrightarrow{v_{//}}$ and $\vec{Q}$ denotes the momentum $\vec{k}$ parallel to the surface $\vec{k} = (\vec{Q}.\vec{k}_z)$. In the limit $v_{//}$~0,Eq.(3.49) gives

$$E_{im}(z) = \frac{1-\varepsilon(0)}{1+\varepsilon(0)} \frac{q}{R+z} \tag{3.50}$$

Electronic polarization induced by low energy ions near solid surfaces at grazing incidence considerably modifies the collision geometry. The comparison of experimental data with theoretic calculation by over barrier model has been presented in Figure 3.23.

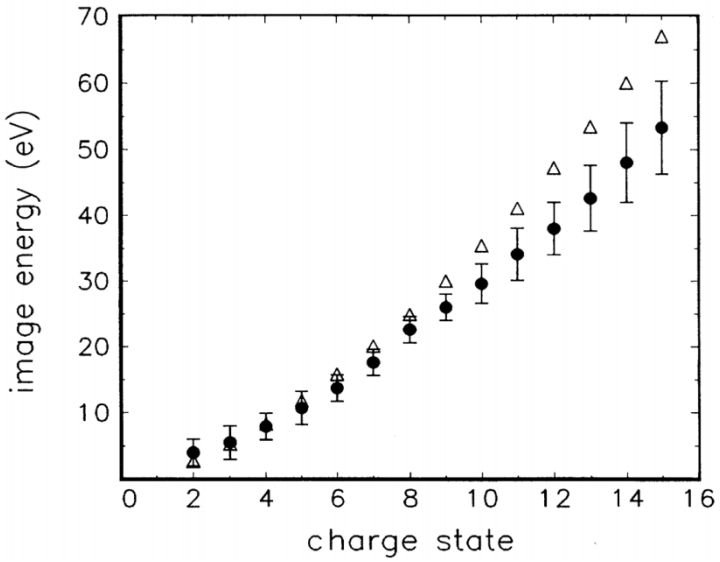

Figure 3.23 Image interaction energies for the scattering of Xe^{q+} ions (50keV) with a LiF(100) surface (full circles). The open triangles represent results obtained with a classic over barrier model of stepwise neutralization in front of surface, cited from Ref. [49].

Because of the different charge exchange processes occurring outside and inside the solid, the incident ions can hit and leave the surface as charged or neutral particle. Thus, during the trajectory, image potential greatly modifies the collisional geometry and provides some perturbation in the local surface atoms. Indeed, in grazing geometry the solid exerts an attractive force on charged species owing to electronic polarization near the surface [52]. The detail discussion will be hold in chapter5 of proton grazing scattering on LiF surface.

The image charge effect, besides it accelerates the ion towards the surface, it also the shifts and broadens the electron levels of the incoming or outgoing particle. The image charge perturbation thus leads to a shift of the projectile states, an important result of this level shift is that at a certain distance from the surface, the energy level of the particle is the same as the

energy of the filled or unoccupied levels and resonant processes of electron capture or loss became possible [1]. Further discussion will be hold in the chapter 4 formation of negative ion.

3.5 Excitation of optical phonons

During ion grazing incidence scattering on surface, solid exerts an attractive force on charged species due to electronic polarization near the surface. Accordingly, local vicinity atoms are also attracted by the same force but in the opposite direction, it turns out that the local vibration has been amplified. However, the vibration process is different from ion-conductor to ion-insulator system. In front of conductor or metal surface, surface electron is usually be treated as free electron gas, therefore, a screening charge cloud is easy to be formed when ion approach to metal surface. But this is not the case of in front insulator surface, electrons are confined to a number of bands of energy, and forbidden from other regions, thus different the species of ionic crystal are bared into the Coulomb field of the ion. All along the trajectory the long range Coulomb field of the projectile ion interacts with the crystal lattice, attracting the negative ions and repelling the positive ions, the target ions oscillate in opposite direction after ion flying away. Thus, it leading to the excitation of optical phonons [57] on the surface, as illustrated in Figure 3.24.

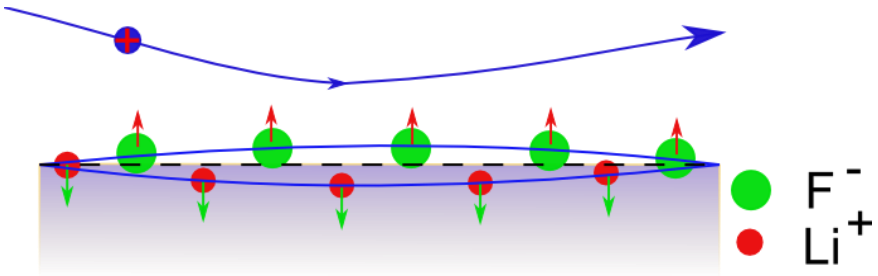

Figure 3.24 Optical phonon creation by ion grazing incidence on LiF surface (as a positive ion flies over an ionic crystal surface, it attracts the halogen ions and repels the alkali, left a bunch of halogen and alkali ions vibration in opposite direction).

In these collisions, the excitation of collective optical phonons is due to the interaction of the coulomb field of the ion with the point charge of ionic insulator. Throughout the ion trajectory of the projectile, in the case of LiF surface, the $F^-$and Li^+ ions are moved in opposite directions (Figure 3.24). After the collision, the ions begin to vibrate in phase which so-called optical phonon mode as associated with a dipole moment. Since the coulomb interaction begins at a great distance from the surface, the excitation of these modes takes place throughout the trajectory; therefore, it takes responsible for part of energy loss.

In the case of collisions of ions with insulator, the presence of a large band gap limits access to electronic excitation of the target [21]. Under these conditions Echenique and Howie [58] concluded that only the excitation of collective modes of low frequencies, that is to say, the optical phonons, could potentially contribute to stopping power.

The first optical phonon created in laboratory was hold by Brusdeylins et al [59] with He^+ scattering on NaF(001) surface in 1985. The beam energy was less than 100meV but with

large incident angle~30-40degree. The inelastic energy loss peaks are associated to the multi-phonon creation. One year later, the same technique was performed on LiF(001) surface by Bracco [60], in the both case, the He atom interacts mainly with fluorine ion which has the larger size, but the optical vibrational amplitude of F- is larger in NaF than in LIF because of the low Li-to-F mass ration. Borisov et al [40] demonstrated experimentally in 1999 that the excitation of these modes whose quantum energy ħω is only few meV had dominated the energy loss of tens of eV Ne^+ projectile for slow collisions ($v \leq 0.1$ au) on LiF.

In our group, Villette et al [41, 57] have identified skipping motion of Ne^+ ions on top of LiF(100) where tens of eV are transferred to optical phonons whose energy quantum is around 30 meV.

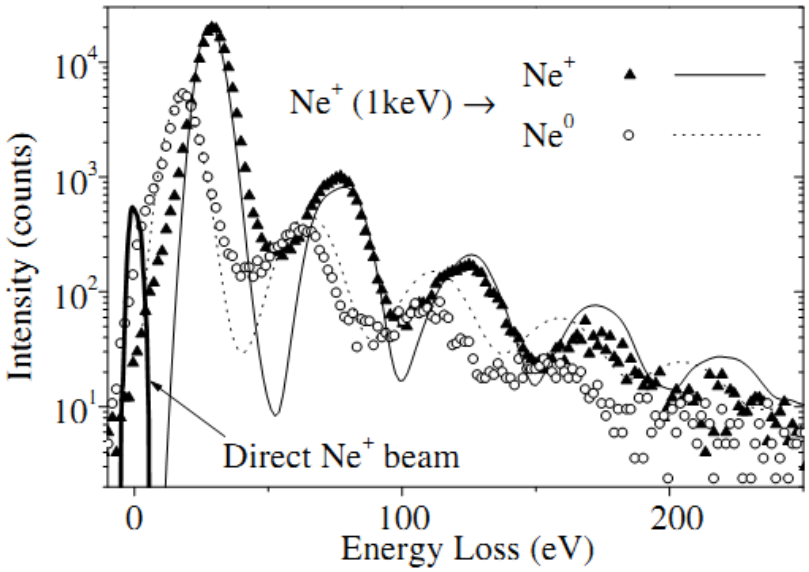

Figure 3.25 Energy loss spectra for Ne^+ and Ne° particles scattered from LiF(001) after 1 keV collisions at 0.95° incidence. The results of the simulation are superimposed as lines after a 1.5 scaling factor in the energy axis [57].

The energy transfer is described by the imaginary part of dielectric constant ε(ω). The interaction with phonons also explains qualitatively that Ne^+ ions scattered at more grazing angles lose more energy as they fly for a longer time close to the surface.

The energy loss spectrum then shows peaks separated by a distance ΔE, 3ΔE, 5ΔE etc. ... This odd progression has been described by Villette et al [20] as due to rebound off the surface. The angular broadening (Log-normal) of the collision with the ions of the surface is such that some ions are distributed below the critical angle $\theta_c = \arcsin(\sqrt{E_{im} / E_0})$. Below this critical angle the ions are bound and evolve like Rydberg electrons relatively far away from the surface before eventually hitting again the surface and start a new scattering process with Log_normal redistribution etc…. The quasi-Rydberg part of the trajectory is coupled with the optical phonons because the coulomb interaction has a very long range. In the case studied the

energy lost in each bounce is (accidentally) almost twice that associated with that lost during the combined way in and way out producing the odd progression.

4. Negative ion formation on surface

Formation of negative ion on surface is one of most prominent property of projectile-surface interaction mechanism at keV energy range. Although lot of efforts has been dedicated to this field, incomplete negative ion formation knowledge till now prevents us completely understanding projectile-surface interaction process. This is the biggest motivation for this thesis study, as well as the various application demands, like negative ions source will be used for production of large intensity neutral beam for Tokamak in ITER; Particle detection in interplanetary and interstellar space [8, 61] for neutral at low energy detection efficiency problem. While, here a surface is used to convert neutrals into negative ion, which greatly increases the detection efficiency [62]; Nevertheless, negative ion is also largely used in semiconductor production, because it can avoid surface charging on insulator, due to the incoming negative charge of negative ions is easily compensated by the outgoing negative charge of secondary electrons [63].

For the negative ion formation, there are several mechanisms to produce intense beam of negative ions. Passing a positive ion beam through an alkali vapor [7] is one of the earliest way, a first electron is captured to form a neutral, and then in a second collision, a negative ion is formed by one more electron transfer. However, this second step is less efficient because the H^- (D^-) affinity level is only 0.75 eV compared with few eV on the alkali.

But on solid surface, so far there are two basic mechanisms for negative ions production. The first mechanism was described by the lowering of the atom affinity level induced by the image potential, and subsequent resonant electron transfer from the surface Fermi level (E_f). However, the negative ion production is largely limited by electron loss back to the empty levels of surface conduction band when negative ion is escaping from surface.

The other method for an efficient production of negative ions has been identified on ionic insulators. Although the binding energy (e.g. 14 eV for LiF(100)) of the valence electrons is much larger than the typical work function of metals (~few eV), population of the affinity level becomes possible due to the Madelung potential. Following the electron transfer to the atom affinity level, its survival probability is much favoured because the band gap sufficiently prevents electron loss back to the surface.

4.1 Negative ion formation on metal surface

The perturbation of a particle by the presence of a metal surface can be described in a simple manner by the concept of image charges [44]. For the acceleration and energy gain from

conductor and insulator surface due to image charge we have discussed in the section 3.4, but here we continue discuss the electron levels being shifted and broadened by the image charge. At a certain distance from the surface, when the shifted energy level of the particle is the same as the energy of the Fermi level, resonant processes of electron capture or loss became possible [1]. This so called, 'surface effect' production of negative ion has been intensively studied [8, 64-67], the physical process of electron attachment to D^- is resonant charge exchange from the conduction band of surface to the affinity level of scattered particle.

4.1.1 Electron level perturbation by image charge

The presence of a surface will modify both the ionization energy and the electron affinity of a projectile. For simplify, let us consider a hydrogen atom in front of a perfect conductor, as illustrated in Figure 4.1. The image potential (3.48) is then given by [68]

$$\begin{aligned} V_{im} &= -\frac{e^2}{2}\left[\frac{1}{|2R|}+\frac{1}{|2R+r+r'|}-\frac{1}{|2R+r|}-\frac{1}{|2R+r'|}\right] \\ &= -\frac{e^2}{4}\left[\frac{1}{Z}+\frac{1}{z}-\frac{2}{Z+z}\right] \end{aligned} \tag{4.1}$$

If we remove the electron from the hydrogen to infinity, we have to put some effort against the image charge force $\partial V_{im}/\partial z$ from both the image charge of electron itself and the positive ion.

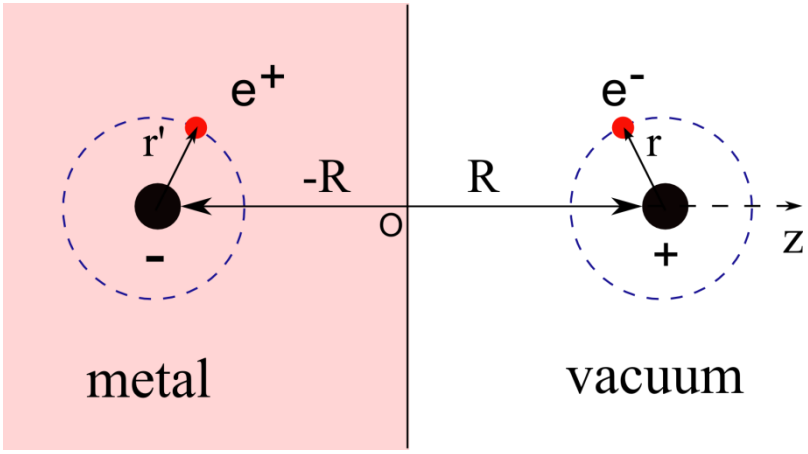

Figure 4.1 Schematic illustration of a hydrogen atom in front of a perfect conductor interaction with its image charges [68].

Comparing the attraction by the electron of its own image with the repulsion by the negatively charged image of the ion, the repulsion is overcompensated to the attraction. Thus, the ionization energy of the atom in front of the surface is decreased by

$$\int_{Z=z}^{\infty} \frac{\partial V_{im}}{\partial z'} dz' = -\frac{e^2}{4z} \tag{4.2}$$

Before comparing the energy level shift, we need to define the ionization energy *I* and the electron affinity *A*. The energy to remove an electron from a neutral atom and bring it to infinity—vacuum level is defined as ionization energy. The affinity level is the energy gain, when an electron is taken from infinity to the valence level of an atom. It corresponds to the energy difference between the neutral atom and the negatively ionized atom—plus an electron at the vacuum level. It can be both positive and negative depending on whether the negative ions are stable or not.

Hence the effective ionization energy in front of a perfect conductor is given by

$$I_{eff}(z) = I - \frac{e^2}{4z} \tag{4.3}$$

On the other hand, if we want to add an electron to a neutral atom in front of a surface, we gain additional energy due to the interaction of the electron with its own image charge. Therefore, the electron affinity is increased to

$$A_{eff}(z) = A + \frac{e^2}{4z} \tag{4.4}$$

The influence of the image potential on the ionization and affinity levels is presented in Figure 4.2. When projectile approach to surface, its affinity and ionization level have been shifted down and up, quantitatively described by Eq.(4.3) and (4.4), respectively. The shifting amount depends the distance between projectile to surface, i.e. 1/(4z), added to the final result, the affinity level decreases rapidly, while ionization level increases slowly, mainly due to the fact that ionization energy is much large than affinity level.

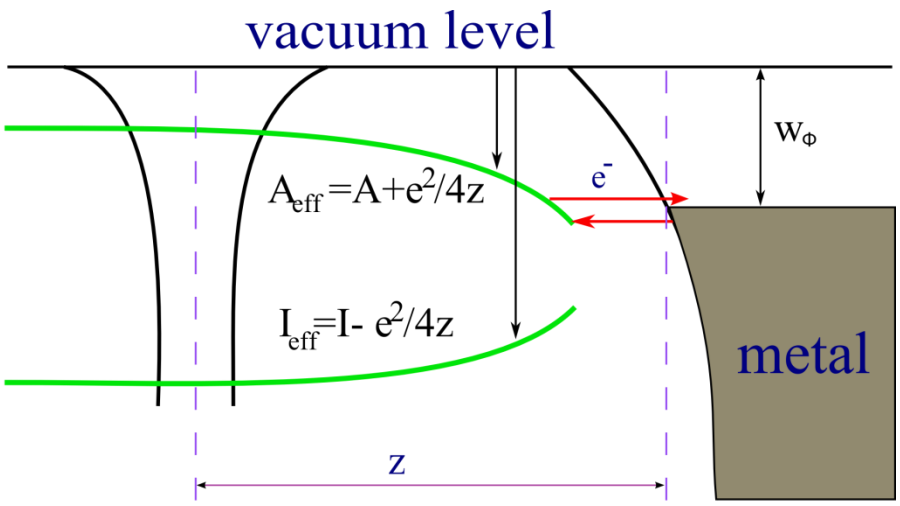

Figure 4.2 Influence of the image potential on the ionization and affinity energies of an atom in front of metal surface. The work function of metal is denoted by W_Φ, the shaded areas represents reservoir of electron on metal surface, cited from [13].

In short, as we have discussed in section 3.4, the ionization and affinity levels of projectile in front of metal surface are shifted by its image charge. The modification of electron level decreases the defect energy which makes resonant electron transfer possible, as we will talk it in next section.

4.1.2 Negative ion formation via electron transfer

As we discussed above, the ionization and affinity energies of particle have been shifted by its image charge in conductor when atom approaches to surface. These modifications have been evaluated with the help of classical electric image theory, when the distances sufficiently large to have a negligible overlap between the atom and surface atoms.

Physically, at relative large distance to the surface, we have $A_{eff} < I_{eff}$. In a very qualitative way, three cases can be distinguished depending on the value of the metal work function [1, 13]:

a. $I-e^2/4d>W>A+e^2/4d$, (d is the distance at turning point) i.e. the Fermi level lies between the effective affinity ($-A_{eff}$) and ionization levels ($-I_{eff}$), under these conditions the projectile tends to remain neutral, since the transfer of an electron to or from the metal would cost some energy.

b. $W>I-e^2/4d> (I+A)/2$, i.e. the effective ionization level is above the Fermi level of the metal, the projectile tends to become a positively charged ion since one gains the energy $W-I_{eff}$, when transferring one electron from the projectile to the metal surface.

c. $W<A+e^2/4d<(I+A)/2$,i.e. the effective affinity level is below the Fermi energy of the

metal. The projectile tends to become a negatively charged ion since one gains the energy A_{eff}-W when transferring one electron from the metal to the projectile.

Briefly, depending on whether the affinity level or the ionization level crosses the Fermi energy of the metal when the atom approaches the surface, the projectile will become negatively or positively charged state. Alternatively, the hydrogen may be neutral, if the Fermi energy remains between the ionization and the affinity levels.

For the negative ions formation, it lies in the case c. of these scenarios we described above. In the following, we will focus in this situation. While the electron level is shifting by image charge, it also begins to broaden, as presented in Figure 4.3. The increased level width $\Delta(z)$ leads to decrease ion-surface separation and the state lifetime $\tau(z)$, but increase the transition probability. The direction of electron transition is determined by the position of the energy level of the particle and the valence band of the solid, but its width determines the transition probability [1].

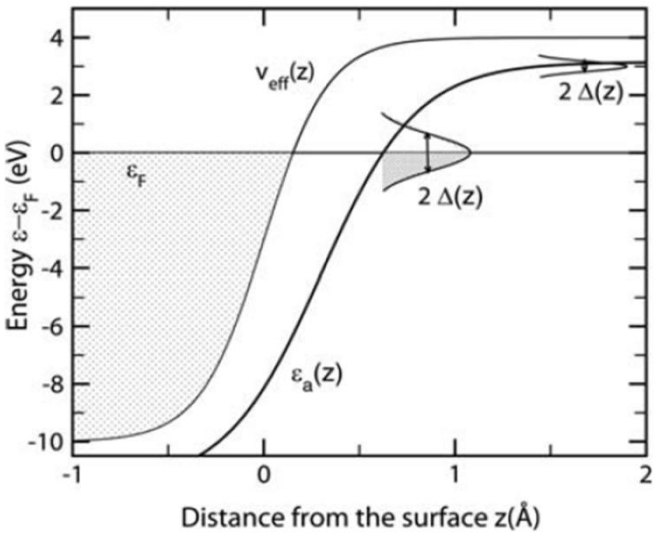

Figure 4.3 Schematic sketch of the shift and the broadening of an atom valence level $\varepsilon_a(z)$ upon approaching a surface. $v_{eff}(z)$ corresponds to the effective one-electron potential of the bare surface. The shaded areas represent the filled levels on conductor surface [68].

However, the exact determination of the charge transfer is very difficult since it involves the treatment of electronic interactions. Rabalais [1] has given a quantitatively approximation, in this approximation, the width of the broadened atomic state is proportional to coupling between the metallic and atomic wave functions, and is directly related to the electron exchange transition rate $\chi(z)$, or the transition probability per unit time along the incoming and outgoing trajectories

$$\chi(z) = \frac{1}{\tau(z)} = \frac{\Delta(z)}{\hbar} \tag{4.5}$$

The atomic and metallic orbital both have a decaying exponential spatial dependency. As a result, the transition rate has an exponential dependence on the ion surface distance z

$$\chi(z) = \chi(0)\exp(-\mu z) \tag{4.6}$$

where μ (distance^{-1}) determines the ion-surface interaction range, the decay rate length of the coupling matrix element, and $\chi(0)$ denotes the maximum transition rate.

The negative ion could be formed via a resonant transition of electron from the occupied valence band of a solid to the affinity level of the scattered particle, due to the downshifted affinity level crosses the Fermi level. At a small distance z_c, where the affinity levels cross the Fermi level, it can be populated by resonant capture of electrons from conduction band. While at $z>z_c$, the affinity level is higher than E_f and the resonant charge transfer occurs in the opposite direction—a negative ion may decay by electron loss into unoccupied states of solid. As discussed above, the affinity level population depends on its width and the time of the particle spends near the surface where resonant processes occur. The time spent near the surface is inversely proportional to the normal velocity of the particle $v_\perp$. Between incoming and outgoing trajectory, assuming that the electron capture and loss rates are equal, the probability of formation of negative ion can be written [1]:

$$P^- = \{1-\exp(\frac{\phi\chi(0)}{\mu v_\perp})\}\{\exp[-\frac{\phi+1}{\mu v_\perp}\chi(0)]\} \tag{4.7}$$

where $\Phi=exp(-\mu z_c)-1$. In this equation, the first term describes the affinity level population via electron resonant transfer during the time spend at the region $z<z_c$. While the second term describes electron detachment of the primary negative ion outside this region $z>z_c$.

For negative ions formed on the outgoing part of the ion surface trajectory, the situation is the time-reverse of the description above. At the surface, the electron density reaches bulk values, and a negative ion cannot exist. While particle moving away from the solid, its affinity level can be populated by resonant capture of a conduction band electron. Once the affinity level is shifted out of resonance, the additional electron may resonant loss into unoccupied states above the solid's Fermi level. The survival probability for negative ion state crucially depends on the capture and decay rates involved and on the distance z_c.

It's interesting to note that the negative ion fraction of scattered particles are independent of the charge state of incident particle [69, 70] at relative higher impact velocity. Neutralization of primary ion occurs on the incoming part of the trajectory at large distance from the surface. The scattered particle loses its memory of its initial charge state, and the final charge state is defined by the interplay of electron loss and capture between the particle and surface on the outgoing part of trajectory.

Base on the negative ion production in reference [2, 71-73], it was shown that the process of negative ion formation is determined by both electronic structure of surface and projectile, the velocity of the particle (Figure 4.4), and by the multiple-level character of interaction. The result showing in Figure 4.4 was taken from ref. [73], with Iodine atom grazing scattering on Al(111) surface. We can find out that the negative ions formation increases very fast with increasing the perpendicular energy. It also shows a pronounced dependence of the negative-ion fractions on the velocity component parallel to the surface, a signature of a kinematically assisted charge-transfer process.

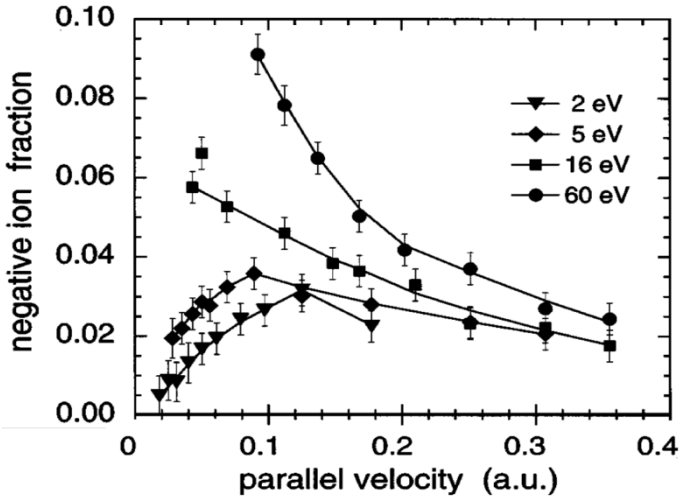

Figure 4.4 I^- negative-ion fraction as a function of the velocity component parallel to the surface for the I atoms grazing scattering from an Al(111) surface [73].

From the references, negative ion production via electronegative projectiles scattering, a relative high negative ion fraction (95%) of fluorine has been report [74], which is much higher than oxygen and hydrogen. These high ion fractions are explained by the relatively high energy of the affinity level, while that for O is 1.3eV [75], H is 0.75eV, but for fluorine and Iodine, they are 3.45eV and 3.28eV, respectively, which almost match the work function of metal [76]. On the outgoing part of the trajectory, the affinity level of the ion crosses the Fermi level at fairly large distance 8-9 a.u. At these distance, the width of the affinity level $\Delta(z)$ and rate of charge exchange $\chi(z)$ are small, it turns out that the electron loss probability for negative ion fraction with increase the particle energy shows that only the capture process is responsible for the observed ionization probability. Contrary to F^- case, the decay process is much more efficient for H^- formation, as the affinity levels cross the Fermi level at significantly smaller distances in this case.

More efficient negative ion sources use cesium deposited on its surfaces in order to reduce work function and increase surface production. For instance, Cs- or Ba-covered surface with work functions between 1.9 and 2.5eV, which dramatically increase the negative ion fraction [77, 78]. This phenomenon is mainly explained by the lower work function permits the shifted affinity level is down to the Fermi level at large distance. Because at higher distance, as

mentioned before, the width of the affinity level $\Delta(z)$ and rate of charge exchange $\chi(z)$ are small, which largely increase the negative ion survival possibility.

4.2 Negative ion formation on insulator surface

A much higher negative-ion fraction has been measured on insulator surface rather than metal surface [44] (Figure 4.5), here, the mechanism of image charge shift the affinity level down to resonant electron capture is not working anymore. Because for insulator targets, the typical binding energy is general much bigger than work function of metal surface, for instance, ~14eV for LiF while 4.7eV for copper (Figure 4.6). And on insulator surface, the image charge shift of the affinity level is relatively small. Therefore, the high negative-ion fraction on insulator surfaces indicates that there must be a new mechanism, which differs from the concept of resonant electron transfer processes for metal surfaces.

The most used model for interpretation of negative ion on insulator surface is Demkov model, with Madelung potential shifting the projectile affinity level [44, 79, 80]. According to this model, the probability for electron capture can be estimated of near-resonant electron transfer, the electron transfer possibility decrease rapidly with distance [80].

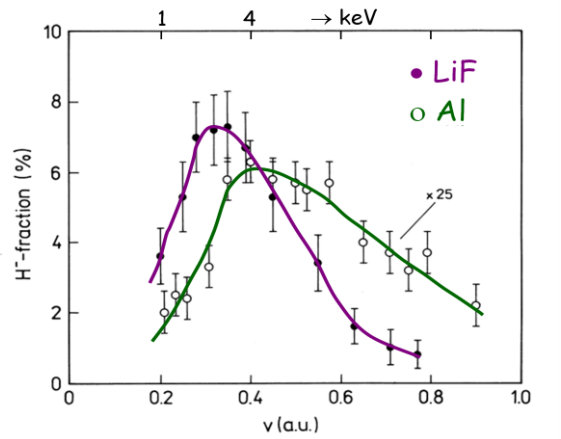

Figure 4.5 H^- fraction as a function of projectile velocity for protons scattered under ϴ=1° from LiF(001) surface and Al(111) surface, note that data for Al are multiplied by a factor 25 in order to match data for LiF [44].

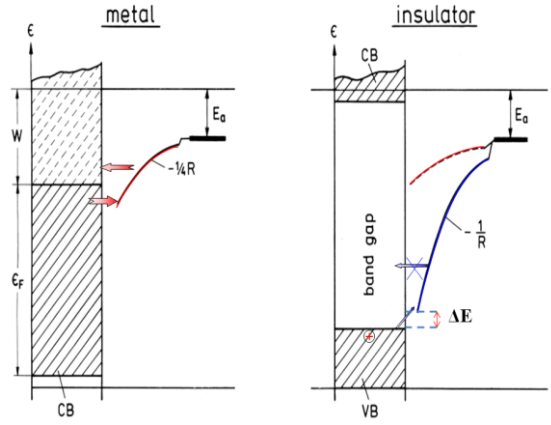

Figure 4.6 Sketch of electron structure from metal and insulated atoms. The hole created by the electron transfer remains localized on the halogen site, which decrease the energy defect due to coulomb interaction.

Consecutive binary collision was employed to explain the efficient formation of negative ions during grazing scattering of fast ions/atoms from the surface of ionic crystals. For each binary collision, the electron transfer probability is given by

$$P_{bin} = \frac{1}{2}\mathrm{sech}^2\left[\frac{\pi}{2}\frac{(\Delta E + v^2/2)}{\gamma v}\right] \tag{4.8}$$

where $\gamma = \frac{\sqrt{2E_t} + \sqrt{2E_p}}{2}$, v is the projectile motion with respect the active sites, and E_t, E_p are the ionization energy of target and projectile respectively, ΔE is the energy difference of initial and final energies in the binary collision with large impact parameters (Figure 4.6), i.e.

$$\Delta E(\vec{R}) = E(Hal^{-} + A^{q}) - E(Hal^{0} + A^{q+1}) \tag{4.9}$$

It is approximated by [72]

$$\Delta E(\vec{R}) \approx \Delta E_{binding} + E_{Mad} + \frac{q}{R} \tag{4.10}$$

Where R>>a (a is lattice constant), $\Delta E_{binding}$ is the difference of binding energies for valence electrons and final projectile level, E_{Mad} is the Madelung potential created by the ionic lattice at active sites (E_{Mad} ~12eV for LiF) and q is the final charge state of projectile (q=0: neutral atom, q=-1: negative ion), i.e. $-1/R$ for negative ions, due to coulomb interaction between scattering particle and positive charge state of hole in active sites, which efficientlly lowers the energy ΔE in the collisions with atoms of active sites (Figure 4.6).

In grazing scattering, the projectiles are scattered from the surface after a series of collisions, so that the final capture probability experiences an effective number of collisions N:

$$P_{final} = 1 - (1 - P_{bin})^{N} \tag{4.11}$$

Where the collisional sites N in grazing scattering has been discussed in chapter3, it strongly depends on the projectile-surface atoms system and incident angle.

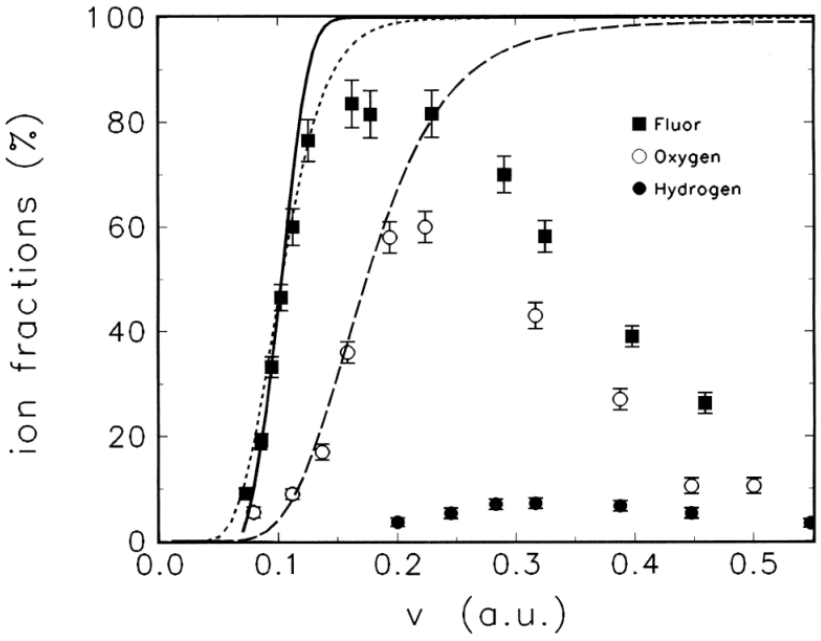

Figure 4.7 negative ion fraction for scattering of H, O and F from LiF(001) surface, dash line represent description of data for O^- and F^- by Demkov approach, solid curve calculations for F^- [81].

Base on this mechanism, Winter et al [72, 80] successfully interpreted the electron capture probability for negative-ion formation on insulators at small parallel velocities (about 0.1 a.u.), by applying the Demkov model (Figure 4.7). However, at higher velocities this model

fails to reproduce the experimental data, since electron loss dominates electron transfer cycles and determines the final negative-ion fraction, which was not included in this model.

Very recently, Chen Lin et al [82], has proposed electron detachment model, which combine with Demkov model to simulate the negative ion formation on insulator surface. With their suggestion, as the negative ion is formed on the active anion site, the interaction between these two negative partners is Coulomb repulsive. The electron tunneling action related to the barrier penetration process occurs on the outgoing trajectory after a close collision with the anion site. Thus the probability of electron detachment is given by

$$P_{\det}(E_{\perp}) = \exp\left[-2\xi(E_{\perp})\right] \tag{4.12}$$

where $\xi(E_{\perp})$ is the decay rate, and $E_{\perp}$ is the scattering energy normal to surface. Where the units used here is an atomic unit. And the decay factor $\xi(E_{\perp})$ given by

$$\xi(E_{\perp}) = \int_{r_1}^{r_2} \sqrt{2(V(r) - E_{\perp})}dr \tag{4.13}$$

where *V(r)* is potential between projectile and surface atom, which is proportional to 1/r. For the boundary condition, the upper limit $r_2 = 1/E_{\perp}$, corresponds to the turning point, while $r_1 = 1/(E_{\perp} + I)$, where *I* is the affinity level of projectile. Thus, combine Eq. (4.12) and (4.13), the probability of electron detachment is given by

$$P_{\det}(E_{\perp}) = \exp\left[-\frac{2\sqrt{2}}{\sqrt{E_{\perp}}}(\arctan\sqrt{\frac{I}{E_{\perp}}} - \frac{\sqrt{IE_{\perp}}}{I + E_{\perp}})\right] \tag{4.14}$$

For a single collision between the incident atom and the active anion site, the final probability of negative ion formation can be described by

$$P^{-} = P_{bin}(1 - P_{\det}) \tag{4.15}$$

The incoming atom experiences a series of collisions with the active anion sites with grazing incidence; thus the total probability of negative-ion formation is simply given by $P(N+1) = P(N) + (1-P(N))P(1)$, where $P(1) = P$, $P(N+1)$ is the final negative-ion fraction after $(N+1)$ sequential collisions. From Figure 4.8, we can see that the modified Demkov model fit very well with experimental data in the overall impact velocity range.

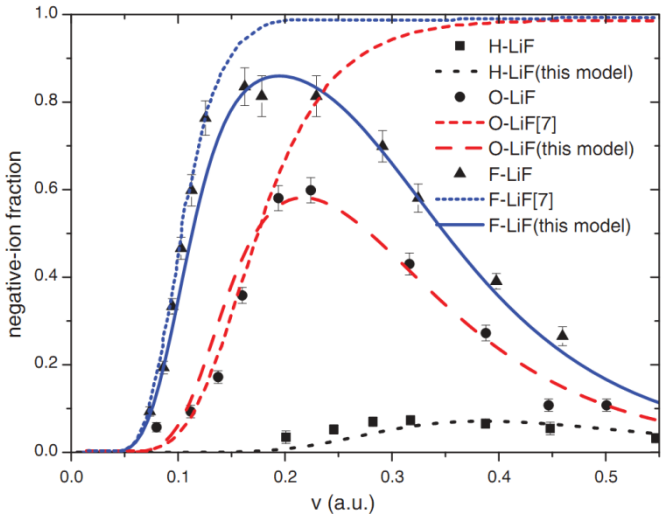

Figure 4.8 Negative-ion fractions as a function of velocity for F, O, and H atoms in grazing scattering from a LiF(100) surface. Short dash lines are theoretic calculation with Demkov model, the solid line and long dash line are calculated with the modified Demkov model [82].

In a short, in grazing ion surface collisions, the normal component of the velocity v_z <<1a.u. so that time scales of atom–surface interactions are sufficiently long to apply quasi-adiabatic concepts to describe charge transfer phenomena [44]. Even with a big gap in insulator surface, population of the affinity level becomes possible due to the Madelung potential. Once the negative ion has formed on insulator surface, its survival probability is much favoured because the band gap sufficiently prevents electron loss back to the surface.

With the same of electronegative particle in front of metal surface, the affinity level also has a big effect for negative ion production in front of insulator surface. From Figure 4.8, while the increase of the electron affinity *I*, the position corresponding to the maximum of the fraction shifts to lower velocities. Meanwhile, the maximum increases rapidly. These phenomena are interpreted by the distance z_c where electron can be resonant transfer to affinity level when the effective affinity level across Fermi level. Thus, for low electron affinity (0.75eV) of hydrogen, the distance where effective affinity level crosses Fermi level should be closer to the surface than the others. Thus, it needs a large velocity to overcome the repulsive coulomb potential and complete electron capture. On the contrary, it also makes the detachment efficient at short distance. Consequently, the final H^- fraction is the smallest.

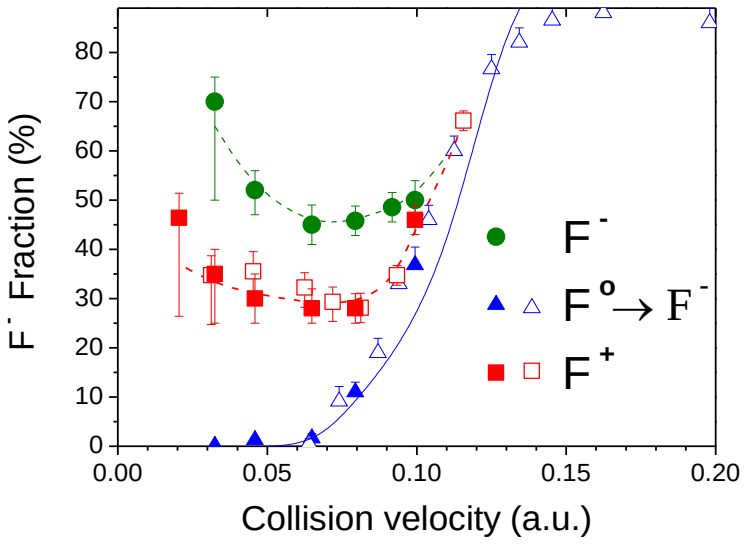

Figure 4.9 Negative ion fractions of scattered particle for impact of F^+, F°, and F^- projectile on LiF(001) surface under 1° incidence. The solid line is a theoretic calculation and dash lines are only to guide the eyes, cited from reference [46].

For negative fluorine ion formation on LiF(001) surface, our group has found that a large probability of F^- ions are formed from F^+ projectiles at low velocities grazing incidence on LiF(001) surface, while the negative ion formation when F° scattering is quite small at lower velocity, it seems there is a threshold to form F^- by F° scattering [46], as presented in Figure 4.9. Because at these low velocity, on the time scale of the binary collision, the hole created by electron transfer remains localized on the halogen site, which decrease the energy defect and lowers the velocity threshold for negative ion formation, this phenomena also have been observed when O^+ and proton scattering on MgO(100) surface [83]. Therefore, two electron capture to form negative F^- ion by F^+ scattering can't be explain by independent sequential one electron capture events, since the final F°—F^- step is not efficient for low velocities.

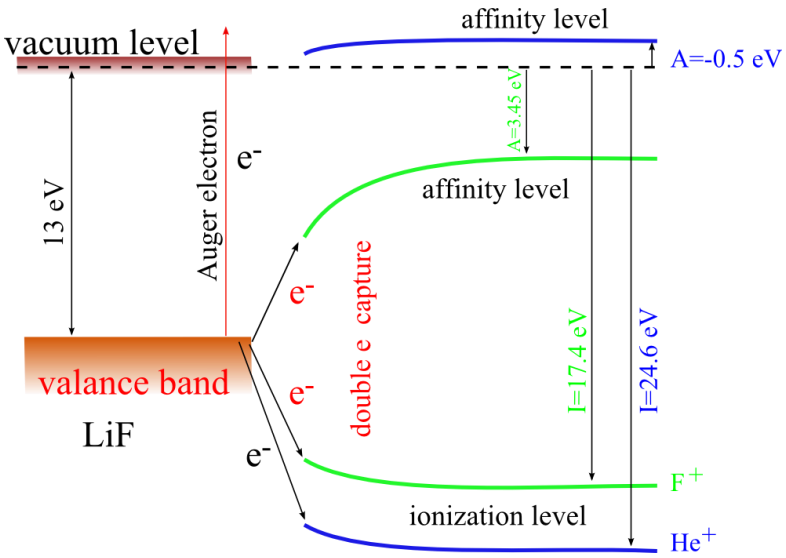

Figure 4.10 Schematic illustration of double electron capture via F^+ scattering on LiF(001) surface, and comparing with Auger electron emission when He^+ scattering.

As we discussed above, the electron transfer process strongly depends on the electron structure systems of projectile and target. When F^+ ion approach to the LiF surface, due to outmost electron missing, it tends to be neutralized by capturing one from LiF surface, especially at low impacting energy, the time scale of collision interaction is large enough for electron transition. Since the ionization energy of fluorine lies below the valance band of LiF (Figure 4.10), the electron falling into its vacancy level result that the energy difference between these two levels has to be released via electron excitation or photo emission. However, due to big gap between valance band and vacuum level, electron excitation has largely been prevented, therefore, the resonant electron population to affinity level become favored. While for He^+ scattering, due to electron level structure [84] (Figure 4.10), Auger electron emission are likely to be measured [85].

5. Negative ion H^- formation on highly oriented pyrolytic graphite

The mechanism of negative ion formation on metal and insulator surfaces is now well understood, and numerous experiments and reports can be found in the literature. But on carbonaceous surfaces, the experimental results reported in the literature are not readily explained by the mechanisms described in chapter 4. Therefore, we applied our coincidence scheme to study the negative hydrogen ion formation on HOPG (Highly Oriented Pyrolitic Graphite) using neutral hydrogen and proton grazing incidence scattering. A better understanding of the hydrogen-graphite system is of a particular interest as it has strong implications in plasma fusion devices and more generally in all applications using negative hydrogen ions.

The two mechanisms discussed in chapter 4, describe well negative ion formation on metals and insulators. However, a significant negative ion fraction, comparable or even larger than that measured from ionic insulators, has been reported on graphite [86-89]. These high negative ion H^- yields are comparable to those measured on Cs and Ba covered surfaces [89]. Graphite being a semi-metal with a work function close to 5 eV, negative ion formation should follow the model used for metals; however the observed yields are well beyond expectations.

During the grazing scattering, electron transfer and excitation may occur all along the trajectory. These processes may give signatures in the electron emission, the energy loss as well as the charge state fractions of the scattered particles. Measuring these quantities have proven successful in analyzing particle-surface interactions [90-92]. Therefore, we have studied the negative ion yields resulting from hydrogenous (H^+ and H^0) particle scattering from HOPG, by measuring in coincidence the charge state and energy loss of the scattered particles together with electron emission; this is the first experiment of this type on this system.

5.1 Experimental method

Primary beams of H^+ are extracted from an ECR ion source at keV energies, and then mass analyzed for pure beam selection. Before impinging on an HOPG sample, the beam could be neutralized, pulsed or just continuously scattered from the sample at grazing incident angles (around 0.5~2.5 deg.). The HOPG sample is cleaved in air using the adhesive tape technique and then loaded into the vacuum chamber with a pressure in the 10^{-10} mbar range. The sample was further heated in UHV to 500 °C in order to remove adsorbed contamination species.

The scattered particles from HOPG are collected on a position sensitive detector located downstream. Charge state analysis of the scattered beam was performed by inserting a slit followed by electrostatic deflection plates between sample and detector (in Figure 5.1). The scattered particles can also be analyzed in energy loss by pulsing the incident beam and performing time of flight measurements. Neutral beams, obtained by neutralization of the primary ion beam by resonant electron capture in a charge exchange cell, are also used for comparison.

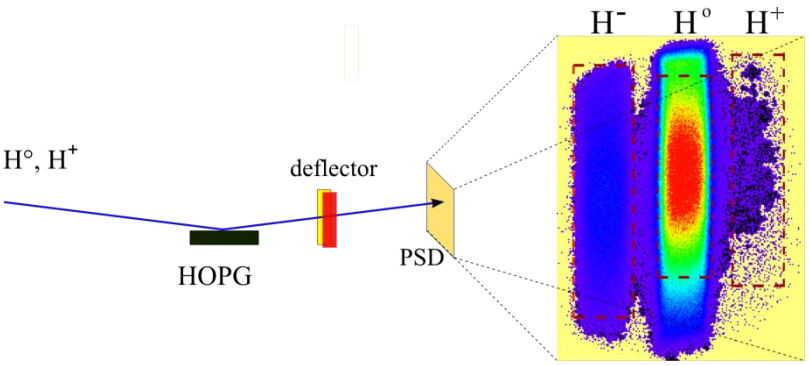

Figure 5.1 Charge state analysis of the scattered beam from HOPG measured by position sensitive detector (PSD) after electrostatic deflection.

Emitted electrons were detected in coincidence with 2π detector (a set of 16 detectors) located on a hemisphere surrounding the sample. Electron detection is performed in coincidence with quantities measured for the scattered particle. This technique has been successfully used to measure the energy loss associated to zero, one, two electron emission, and exciton creation by proton scattering on LiF(001) [34].

5.2 Kinematically assisted negative ion formation

5.2.1 Negative charge fractions vs. normal energy

Normal energy dependence of the negative ion fractions measured with incident atoms and ions are presented in Figure 5.2; the total energy is between 0.5 and 5 keV. With our current conditions, the maximum negative ion fraction approaches 10% at the maximum normal

energy 5.7eV. These high fractions of H^- are comparable to those found on low work function surfaces, such as Cs- and Ba-covered metals [93, 94]. They are slightly larger than those reported on alkali-halide surfaces [95]. It is also considerably higher than observed on a carbon surface at high incident energies [96].

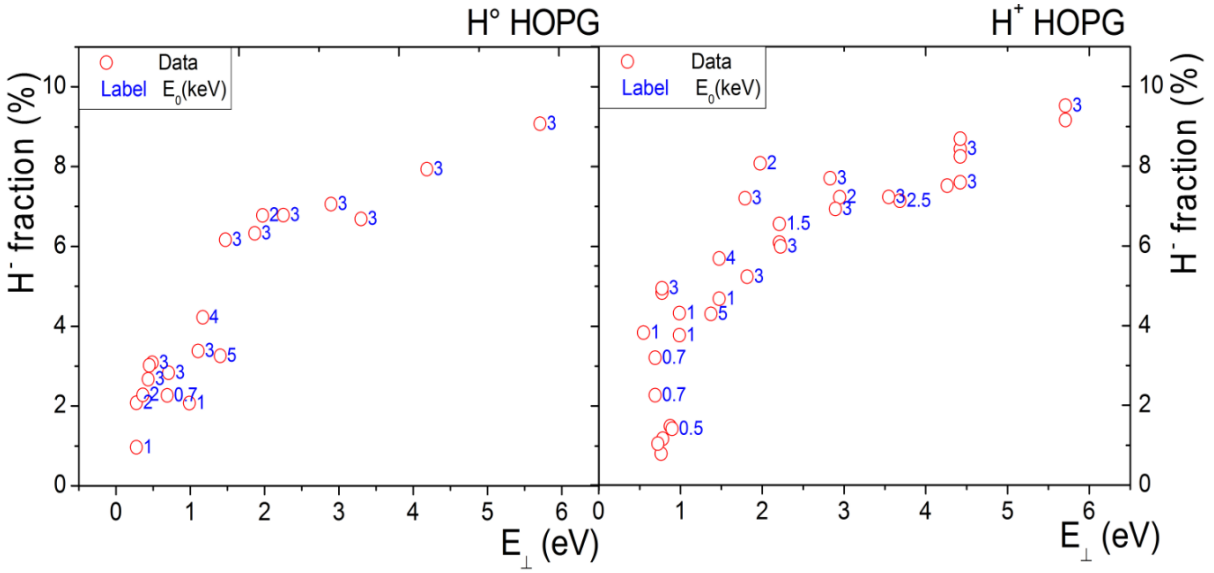

Figure 5.2 Negative H^- ion production via hydrogen (left) and proton (right) scattering on HOPG, the number around the data is impacting energy in keV.

A more rigorous dependence of the normal energy can be obtained considering a constant total energy of 3 keV. Both proton and neutral hydrogen show the same behavior—negative ion fractions increase nearly linearly with normal energy, see Figure 5.3. This is consistent with observations made on both metals and insulators.

At normal energies below 1 eV, the negative ion fraction produced by H° is smaller than that of proton. The most plausible explanation is that image charge acceleration increases the effective normal energy of protons, setting a lower limit just above 0.5 eV. At higher energies (above 2eV) no effect of the projectile charge on the final charge fractions is observed, i.e., any "*memory*" of the incident charge is lost, certainly because neutralization of the incident ion occurs in a resonant process before the turning point. This phenomenon was also observed of O^- ion fraction when O^+ and O° (few keV energy) grazing scattering on MgO surface [83].

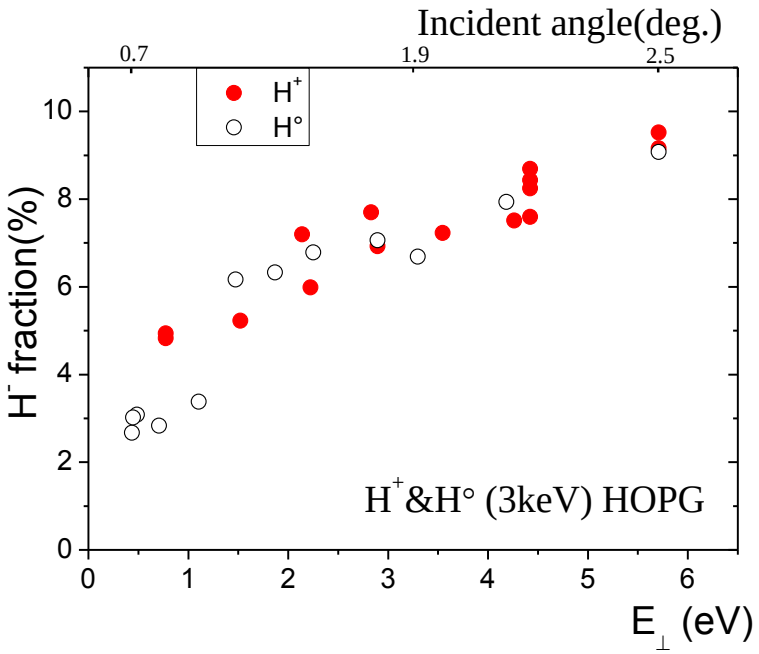

Figure 5.3 Negative ion fraction of proton (full circles) and hydrogen (empty circles) with kinetic energy 3keV on HOPG, the incident angles vary from 0.7 to 2.5degrees.

The effect of the image charge acceleration on the effective trajectory can be seen on the polar exit angle distribution of the different charge states when using neutral projectiles, see Figure 5.4. We can clearly see that scattered H^- has a smaller outgoing angle than scattered H°; this difference arises from the image charge acceleration leading to a lower outgoing angle. Once we know the direct beam position, the absolute image energy gain can be derived, providing insight on properties of the particle-surface interaction [49]. In our case as presented in Figure 5.4, the normal energy difference between scattered H° and H^- is around 1.4 eV, this energy difference mainly caused by image charge acceleration. This outgoing image charge energy is slightly higher than incoming proton scattering since, at the incoming trajectory, image charge acceleration will be quenched once proton neutralized at certain distance above surface; while for outgoing part, the image charge acceleration keeps on from turning point to infinite distance.

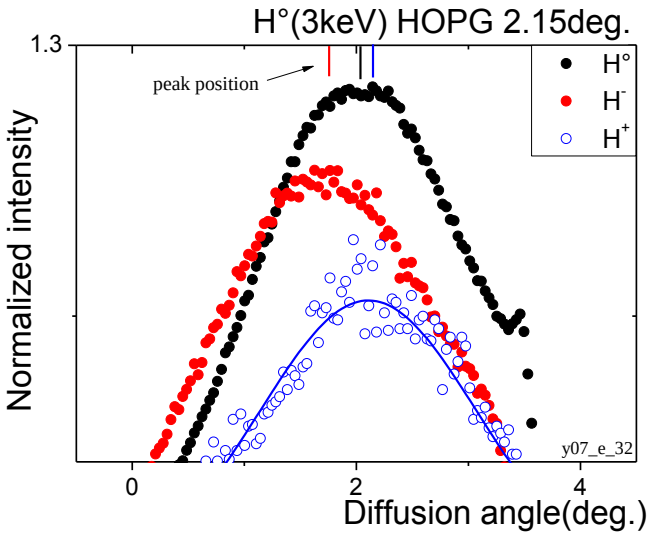

Figure 5.4 Polar angle distribution of outgoing particles in scattering of H° (3keV) on HOPG, note that for better comparison, these intensities are first normalized and then multiplied 1.2 for neutral hydrogen, divided by 1.2 for diffusion proton, solid line is drown for guiding eyes only. $\Delta\theta$ ($H°$-H^-) =0.3°, $\Delta\theta$ (H^+-H°) =0.05°.

5.2.2 Parallel velocity effect

The dependence of the negative H^- ion fractions on total energy is depicted in Figure 5.5. It shows the typical behavior of kinematically assisted electron capture with a velocity threshold around 0.1 a.u. and a clear maximum of 9% around a parallel velocity of 0.32 a.u. In the gross features (peaked distribution with a threshold), this curve is similar to those measured on metals [97] and insulators [44].

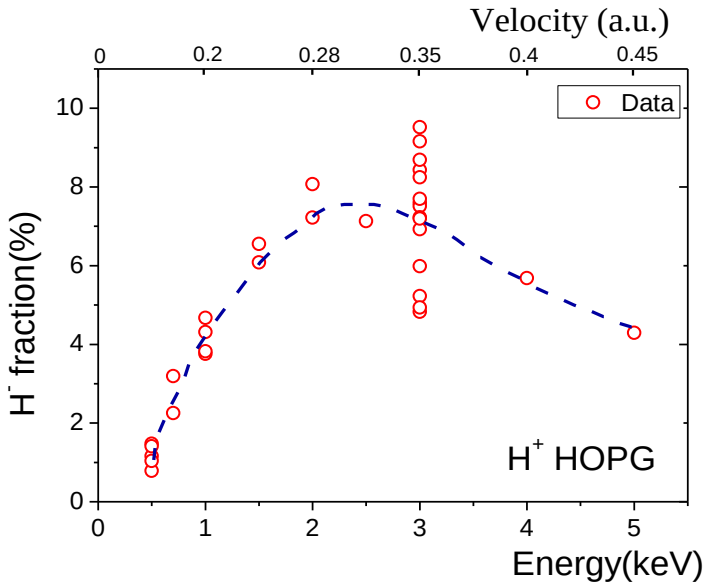

Figure 5.5 Negative H^- ion fraction vs. impacting proton energy with grazing incidence (0.5-2.5deg.), dashed line is drawn as a guide; multiple points at fixed total energy correspond to different incidence angles.

Looking now in more details (threshold value and peak position), similar properties have been observed by J. Lienemann [96] with H°, proton and O°, O^+ grazing scattering on a DLC (diamond-like carbon) surface, see Figure 5.6. Comparing our result with the work of Lienemann shown in Figure 5.6, the maximum negative ion H^- fraction from HOPG is slightly higher than that from DLC, more or less 20 times higher than on Al (111); it is even slightly higher than with LiF(001), the ionic insulator with the largest band gap. But carefully analysis these data, only incident angle for around 1deg.(data limited) have been chosen to compare with that on DLC surface (in Figure 5.7), from this figure, the negative ion productions are comparable, and the image charge modification affects the H- fraction at lower energy. After noting that DLC is an insulator with a band gap close to 5 eV (but depends on the ratio of sp2 over sp3 bonding), we conclude that HOPG produces more negative ions than good insulators.

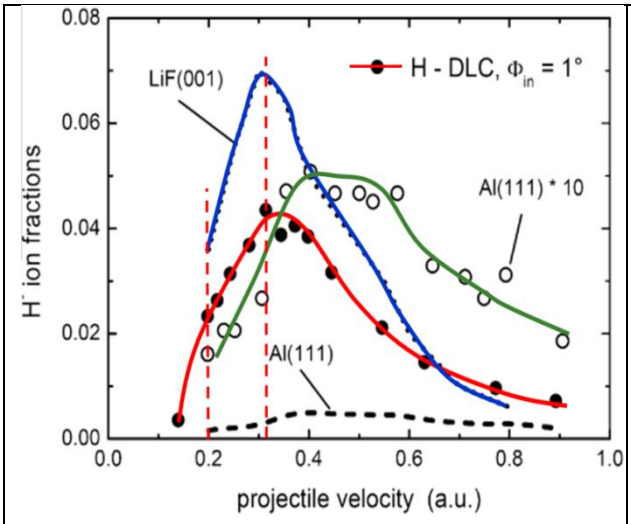

Figure 5.6 Negative ion fractions as function of projectile velocity for scattering of H atoms from Diamond-Like Carbon surface under θ_{in} =1.0 deg (full circles). Dotted curve represents data for scattering from LiF(001), open circles data for Al(111), thin dashed curve data for Al(111) enhanced by factor of 10, cited from Ref. [96] and references therein.

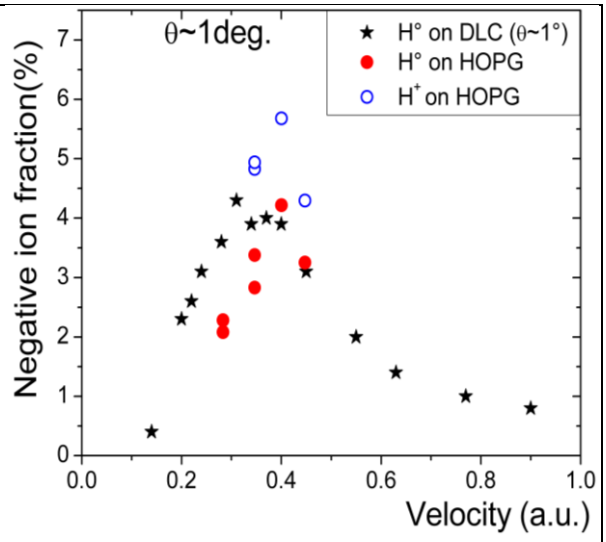

Figure 5.7 Comparison of negative ion H- fraction on HOPG surface to DLC surface at around 1 degree incident angle. The data on DLC is taken from Figure 5.6.

It is clear from Figure 5.6 that the parallel velocity effect translates in different manner depending on the material. On LiF, DLC and HOPG, the maximum negative ion fraction is observed at velocities around 0.32 a.u., while on Al(111) this peak shows up at higher velocity, above 0.4 a.u. Finally, although HOPG and DLC are two different forms of carbon, but with very different content of sp2 and sp3 bonding, dynamic properties of H formation and outgoing fractions look very similar surface [98].

Table 5.1 Maximum negative ion H^- fraction on various surfaces.

material	Maximum H^- fraction	Velocity(max H^-)	$E_{\perp}$(eV)	Reference
HOPG	**9.52±0.5 %**	**0.35a.u**	**3.1±0.3**	**This work**
DLC	5%	0.35a.u	0.93±0.2	Ref.[96]
LiF	7%	0.31a.u	0.73±0.2	Ref.[97]
Al	0.5%	0.45a.u.	1.54±0.3	Ref.[99]

5.3 Metal-like electronic structure of HOPG

According to our measurements, a high negative H^- ion fraction has been observed; to our knowledge this is the highest fraction ever reported on surfaces of insulators, metals and semiconductors, see Table 5.1. On metal surfaces, the highest H^- fraction is observed for the low work function Cesiated tungsten surface [100], in the region of constant work function (i.e. 2.15eV at high alkali coverage) with grazing incidence, the H^- fraction is ~6%, comparable with the HOPG measurements. From the work of Gleeson et al [101], the H^- fraction doesn't change after Cs deposited on HOPG surface. Although their results demonstrate that Cs adsorption does not result in significant structural changes to the graphite surface, but does alter the electronic properties as evidenced by a change in the work function. This is in contrast with observation made on metals where adsorption of Cs has a drastic effect on measured negative ion yields [102]. Thus the strong dependence of the metal work function on the dynamics of negative ion formation [103] is obviously not suitable to describe for large fraction of H^- on HOPG surface.

The observed H^- fraction on HOPG is comparable to that from a LiF surface, see Table 5.1. For ionic crystals, negative ions are formed in local electron capture events from tightly bound electrons located at halide sites, where the considerable energy defect in the collision is reduced by the Madelung potential owing to the surrounding point charge lattice [104]. But HOPG, from its electronic structure, is very similar to gold: both are good conductors and have comparable work functions (5.1eV for gold and 4.6eV for graphite [105]); on the other hand, their Fermi energies (approximately 7.6eV for gold [106], 21.3eV for graphite [107]) are quite different.

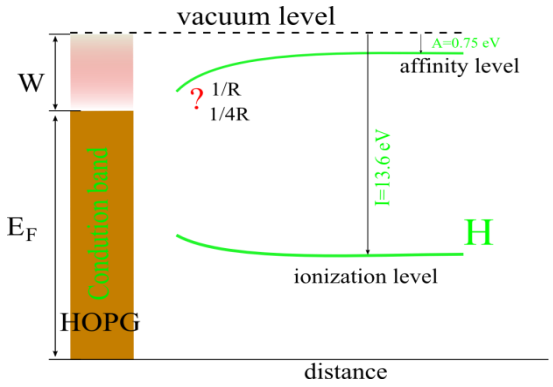

Figure 5.8 Metal-like electron structure of HOPG and electron level shifting in front of HOPG.

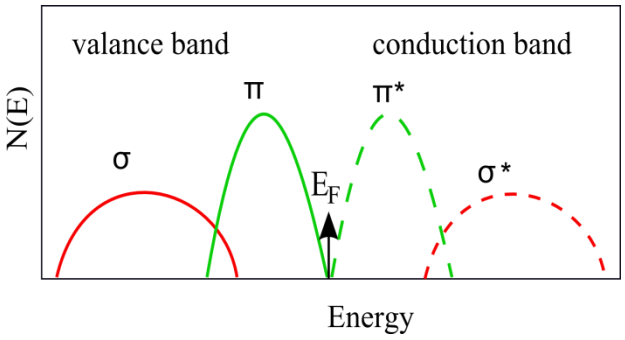

Figure 5.9 Schematic diagram of σ and π states in a-carbons [108].

In graphite, three of the electrons from each carbon atom form σ bonds which hybridize as sp^2 in the plane, the fourth electron of the carbon atoms forms a delocalized π band, with orbitals extending out of the plane and providing inter-plane interaction [109] (Figure 5.9). When considering the density of states at the Fermi level [110, 111], it is actually close to zero, which may be seen as a very small band gap. Therefore, applying the same scenario than that

used for metals, electron capture from the conduction band might be less efficient due to the increased effective binding energy. At the same time, the small pseudo-gap should prevent electron loss back to the surface, at least for short distances.

5.4 Energy loss and electron yield

In grazing incidence scattering, the projectile travels nearly parallel to the surface for long distances, multiple processes of electron transfer and excitation occur all along the trajectory. We have measured the electron number statistics and the time-of-flight of the emitted electrons in coincidence with charge state and energy loss of the scattered projectile when 500 eV incident protons are used.

First, the dependence of the energy loss on the outgoing charge state is shown in Figure 5.10 for incident H° at 3 keV. The spectra are well described by a skewed Gaussian peaked around 550 eV with a straggling of 150 eV. At first glance, the large values of the mean energy loss are comparable to those observed on metals [112]. On metals, the energy loss derives from excitation in binary collisions of conduction electrons near the Fermi level. So from the point of view of energy loss, the metallic character of HOPG appears clearly. The observed small fraction of scattered H^+, arising from ionization of incident projectiles [88, 113], is characterized by an additional energy loss around 15eV with respect to scattered H° and H^- (Figure 5.10).

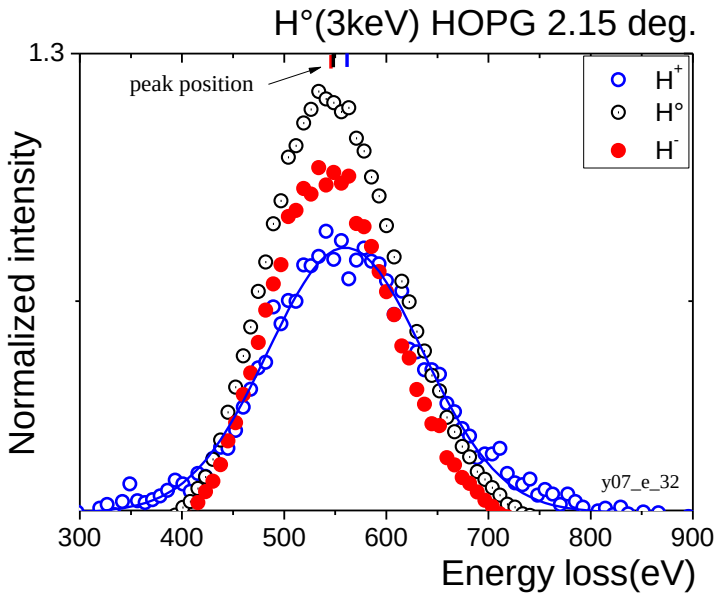

Figure 5.10 Energy loss of scattered particles in grazing scattering of H° (3keV) HOPG. For better comparison, these intensities are first normalized and then multiplied by 1.2 for neutral hydrogen and divided by 1.2 for scattered protons, solid line is drown to guide the eye.

Coming now to the coincident data, the results are shown in Figure 5.10 and Figure 5.11. The upper panel in Figure 5.11 shows the energy loss spectra of the scattered H° in correlation with 0, 1 and 2 emitted electrons; the lower panel shows the energy loss spectra of scattered H^- in correlation with 0 and 1 emitted electron.

In the experimental conditions of Figure 5.11, a yield of 0.2±0.03 electrons per projectile has been detected for scattered H°, while for scattered H-, the electron emission is slightly lower and amounts to 0.16±0.02.

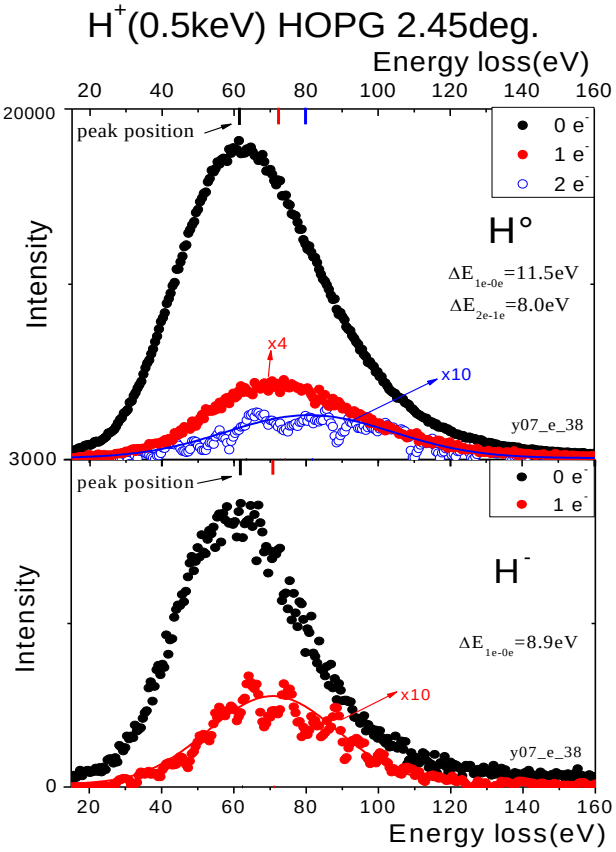

Figure 5.11 Energy loss spectra of scattered H° (upper panel) and H- (lower panel) correlated to 0,1 and 2 emitted electrons. In these experimental conditions, the outgoing fractions are: H- :1.41%, H+:0.19%, H°:98.4%. Solid lines are to guide the eye only.

The electron emission η increases very fast with increasing impacting energy; for 1keV incident particles, the electron yield is up to 1.2 per projectile for H+, 1.1 for Hydrogen, these yields do not depend on the incident charge state, see Table 5.2. When increasing the kinetic energy, the binary collisions become violent and the energy transferred to the electrons increase equally, resulting in a larger electron emission. We should point out that the measured electron yield is much larger than observed on Aluminum [112, 114], where at 1 keV the electron yield amounts to only 0.1 electron per projectile (see Figure 5.12). In similar conditions, comparable electron yields are observed on LiF(001) [34]. We are thus facing a dilemma: with respect to energy loss, HOPG behaves just as a metal, while electron emission is more consistent with that observed on ionic insulators. These exotic phenomena greatly tempt us to continue the following analysis.

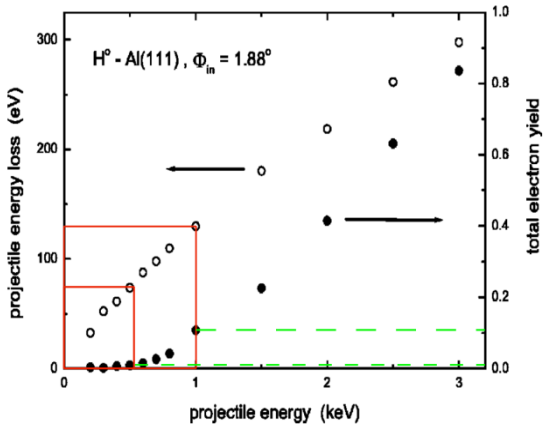

Figure 5.12 Total electrons yield (full circles) and mean energy loss (open circles) as a function of projectile energy for scattering of H° atoms from Al(111) under θ_{in}=1.88° [112]. Energy loss and electron emission are marked by red and green lines for 0.5keV and 1keV.

It's interesting to compare the electron emission and the projectile energy loss with different materials, since different materials have different electron structures, then the electron emission and energy loss process are different, this is done in Table 5.2.

Table 5.2 Electron emission yield η and energy loss ΔE(eV) of Hydrogen and Helium on various materials

	H_HOPG		H°_LiF(001)		H°_Al(111)		He_HOPG		He_LiF(001)	
	η	**ΔE**	η	ΔE	η	ΔE	η	ΔE	η	ΔE
0.5keV	**0.2**	**~65**	0.2 (0.6keV)	~3 (average)	0.01	~60				
1keV	**1.1(H°)** **1.2(H^+)**	**145 (1.5keV)**	1	~7.5 (average)	0.11	~130	0.06(He°) 0.26(He^+)	~3	0.01(He°1.5keV) 0.27(He^+)	~2 ~6
Ref.	**Thesis' work**		[115]	[34, 115-117]	[112]	[112]	Our experiment data			

Again, we note a strong similarity in electron emission yields between HOPG and LiF(001) [115], while HOPG compares much better to Al(111) with respect to energy loss. On LiF(001), we recall that energy loss spectra are composed of successive peaks separated by an energy close the band gap value (see Figure 5.13) , these peaks are due to successive electron captures from the valence band to the affinity level [34, 115-117]. Note that at low incident energies, the first peak (elastic scattering) dominates the energy loss spectrum.

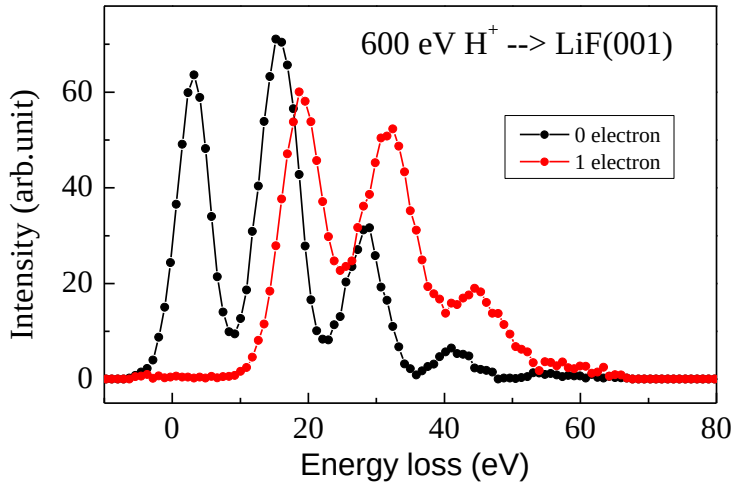

Figure 5.13 Energy loss spectrum from grazing scattering of H^+ on LiF(001), the curves correspond to scattered H°.

For comparison, the electron emission and energy loss of He scattered at grazing incidence (1.8 deg.) from HOPG and LiF(001) are also listed in Table 5.2. The energy loss is extremely small compared to that of hydrogen. The large electron yields observed with He^+ are due to the contribution from Auger neutralization (see Chapter 4).

Finally, these coincidence data provide a valuable insight into the properties of HOGP. Although its electronic structure may be similar to that of a metal, hints from measured electron yields point to a specific property of graphite. When considered together, electron emission and negative ion fractions are consistent with measurements made on LiF(001).

5.5 New features in the energy loss

For the energy loss of scattered particles, a peculiar behavior can be seen in the dependence with outgoing angle. Figure 5.14 shows the mean energy loss of scattered H° and H^- as a function of outgoing angle; both of them exhibit a decreasing energy loss with increasing exit angle. This is the reverse of what is observed with proton scattering on LiF(001) [118, 119]. We should precise here that the effective incidence angle is the average of the incident angle (fixed in the data of Figure 5.13) and the exit angle.

For particle grazing incidence on surfaces, the projectile encounters a large number of surface atoms; the trajectory length is inversely proportional to the incidence angle (see Chapter 3). At the same time, larger angles correspond to the projectile traveling through a higher average electron density. These two counteracting effects may combine to provide either a positive or negative slope in the energy loss vs. exit angle variation. It seems that with the system H^+-HOPG, increasing the trajectory length is more efficient in increasing the energy loss than reducing the closest distance of approach. These observations are confirmed by former studies performed by grazing scattering of H^+ on C(0001), see Figure 5.15.

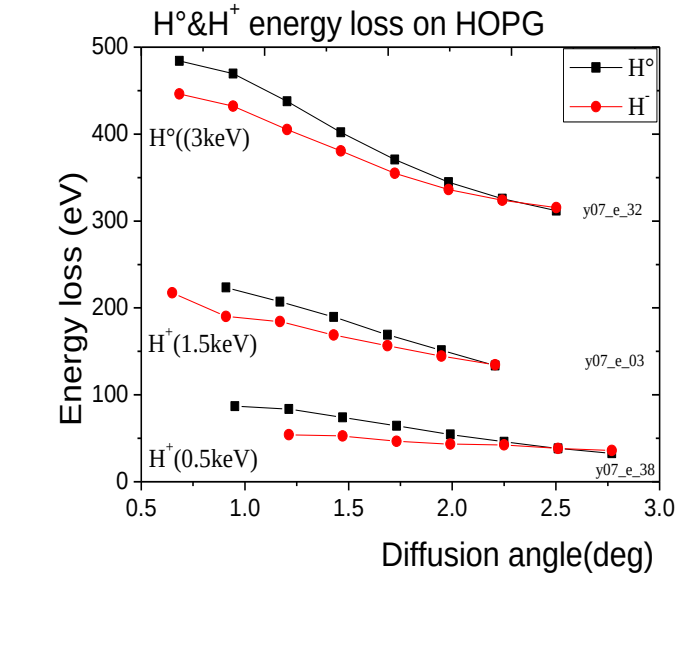

Figure 5.14 Energy loss of diffusion H° and H^- via H° and H^+ grazing scattering on HOPG vs. diffusion angle, incident angles are around 2deg.

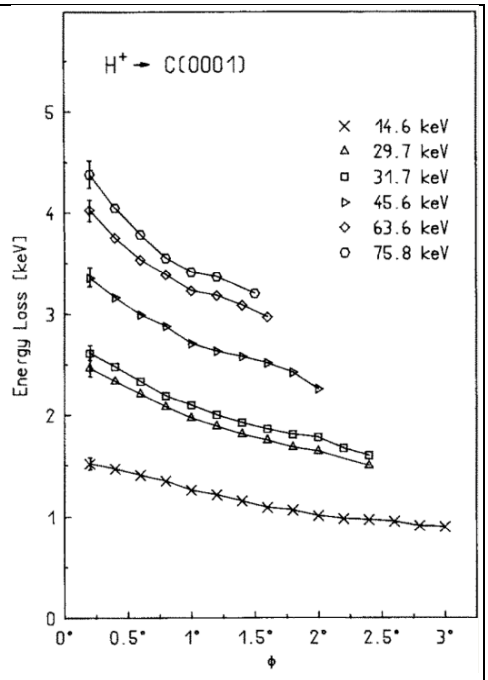

Figure 5.15 Energy loss vs. Incident angle, taken from Ref. [120].

Let us now concentrate in more details on the energy loss spectra. A two-dimensional plot of the scattered H° energy loss vs. exit angle is shown in the upper panel of Figure 5.16, 500 eV incident protons are used. The lower panel shows projections from two different zones **a** and **b** of the 2D plot, the insert shows the detail of the left hand side of zone b. Although relatively weak in terms of relative intensity, we clearly distinguish discrete structures in the left side of energy loss spectrum at small exit angles. These features are observed at various energies and with incident H° as well.

Very surprisingly, these features are very similar to those observed on LiF(001), see Figure 5.12. By decomposing the energy loss structures at lower exit angle, we find that the energy loss can be fitted with equally spaced peaks—characteristic of an isolator [34], with an energy difference of 10.6±0.5eV (Figure 5.16).

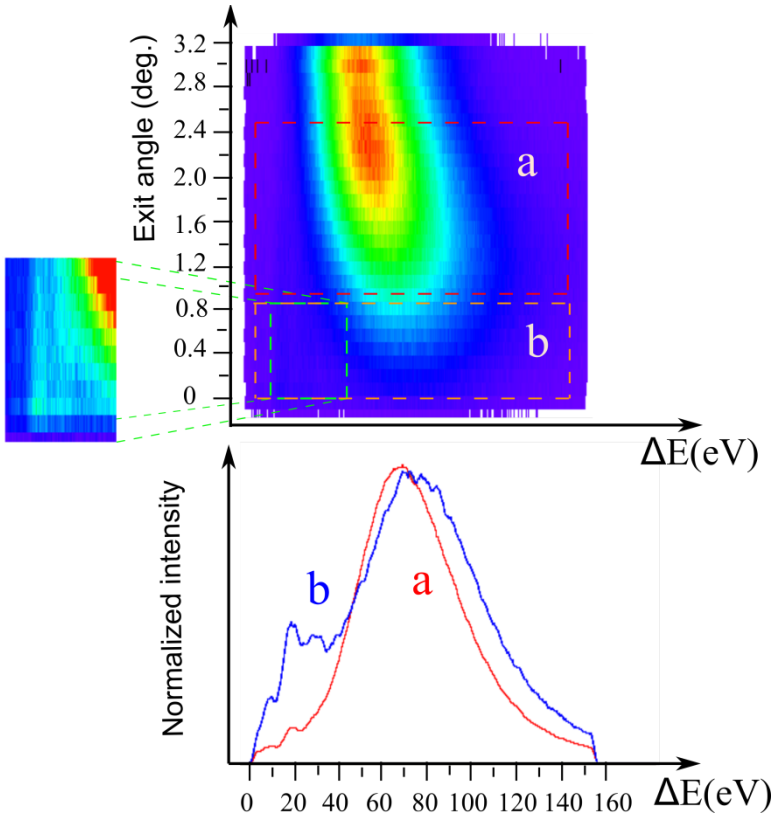

Figure 5.16 Energy loss structures at low exit angles (zone b) and high exit angles (zone a) of H^+ (0.5keV) grazing scattering on HOPG.

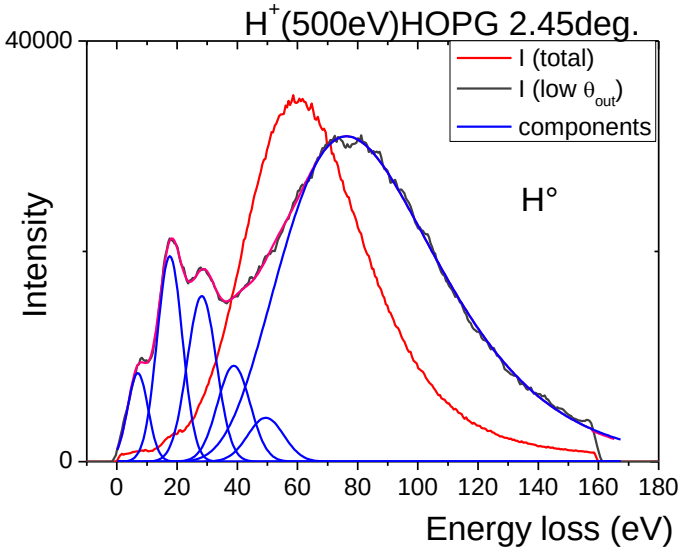

Figure 5.17 Energy loss of 0.5keV proton grazing incidence from HOPG, red line is the total energy loss of scattered H° including all exit angles, black line is from low exit angles only (zone b in Figure 5.16), the red line is a fit using multiple Gaussians and a log-normal [4] (in blue).

In figure 5.16, the energy loss spectrum in fact is composed of two distinct contributions, one with a large mean energy loss comparable to what is observed on metals [17] and another exhibiting discrete structures as observed on ionic insulators, both appear equally characteristic of HOPG.

Taking advantage of the coincidence measurements, we now analyze the time-of-flight (TOF) of the emitted electrons correlated to the energy loss spectrum. The result is shown in Figure 5.18, the left upper panel is the 2-D plot of the electron TOF vs. energy loss of scattered H°. In this spectrum, two separate regions have been identified, marked I and Π. The right panel of Figure 5.18 shows the electron TOF spectra for both zones of the particle energy loss. One clearly sees that the mean energy of electrons correlated to the low energy loss structures (zone I) is substantially lower than for electrons correlated to the metal-like high energy loss component (zone II). Note that the low energy loss structures are also present at larger exit angles, but these are buried in the intense metal-like distribution shifted to lower energy.

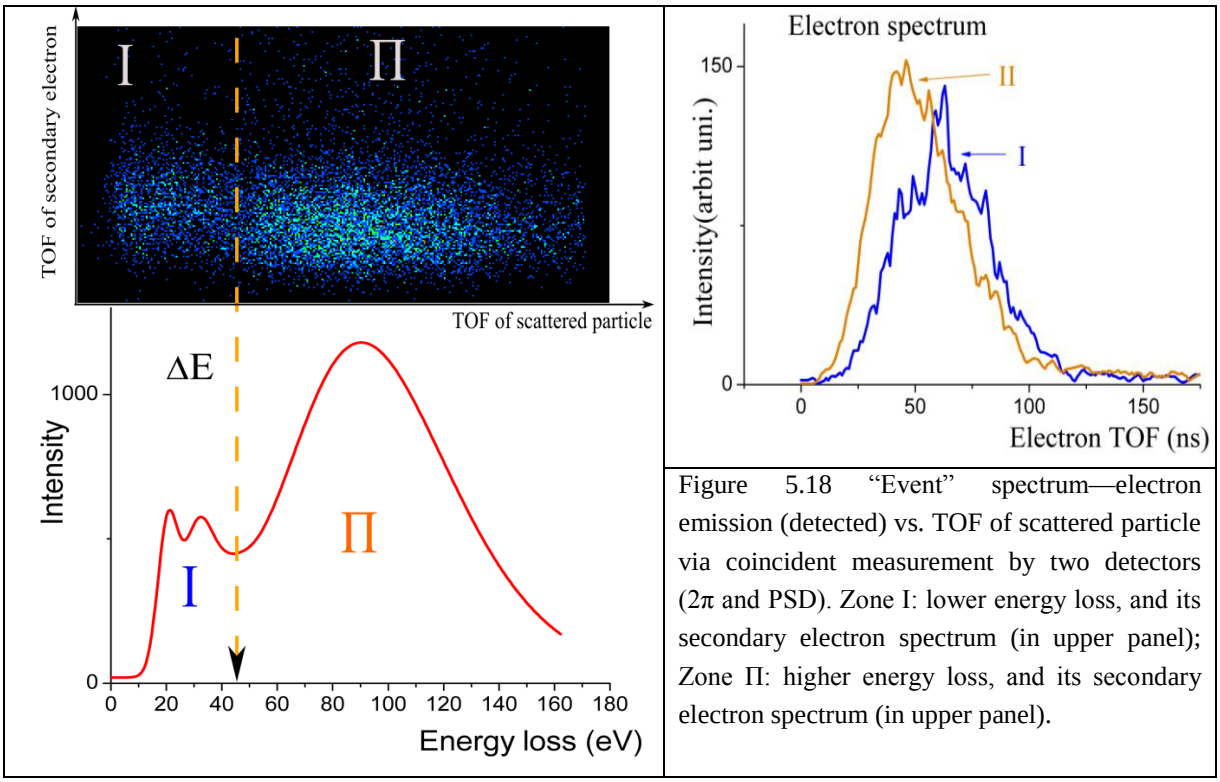

Figure 5.18 "Event" spectrum—electron emission (detected) vs. TOF of scattered particle via coincident measurement by two detectors (2π and PSD). Zone I: lower energy loss, and its secondary electron spectrum (in upper panel); Zone Π: higher energy loss, and its secondary electron spectrum (in upper panel).

For summary, it seems that two different mechanisms, distinguishable in both electron emission and energy loss, contribute to these measured quantities. One produces a metal-like energy loss with electrons emitted with higher energies and the other producing discrete peaks in the energy loss and correlated with electrons emitted with a lower energy.

We now compare the characteristics of these low energy loss structures according the number of emitted electrons. The result is shown in Figure 5.19, the curves are fit as in Figure 5.17 to extract the individual contributions. Both of them exhibit the same behavior, however there is around 2.5 eV energy shift between the two spectra.

From the striking analogy with the spectra typically observed on ionic insulators (figure 5.12), we decide to push this analysis to its logical end. We suppose that these discrete peaks correspond to successive electron captures form the surface to the affinity level of a transient H^-. The energy difference between the peaks is the energy necessary to pick up the electron

from the surface; in LiF(001), it is exactly the formation energy of the surface exciton, the latter being the most probable final state into which the negative ion losses its electron. Then the 2.5 eV energy difference between spectra correlated to 0 and 1 emitted electron is what is required to bring the electron from the exciton to vacuum with some kinetic energy.

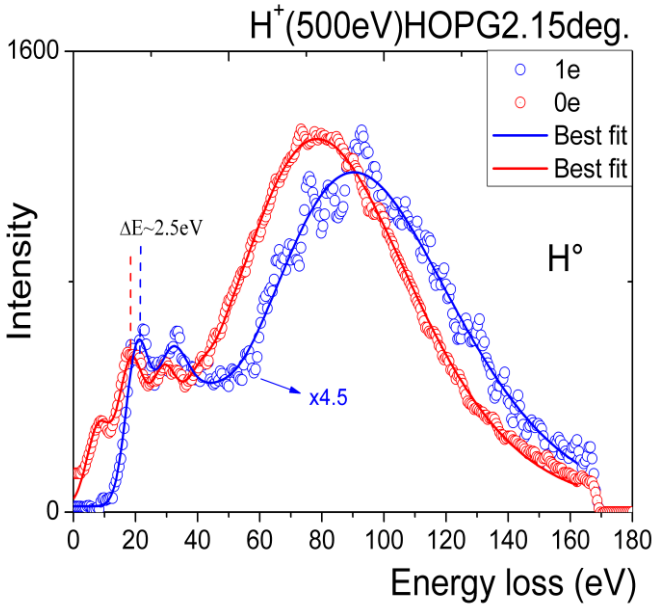

Figure 5.19 Coincidence electron emission measurement of H° diffused with low outgoing angle, 2.5eV difference has been measured between the peaks one electron emitted and no electron emitted.

To proceed further in the analogy with LiF(001), we try to fit the relative intensities of the successive cycles by a binomial distribution. The reason is that on LiF(001), the electrons are localized and can be treated independently; in a grazing scattering geometry, the projectile interacts with n_s successive surface sites and has a binomial probability to pick up n electrons out of the n_s sites. This probability is given by (Table 5.3):

$$\binom{n_s}{n} p^n (1-p)^{n_s-n} \tag{5.1}$$

Where p is the capture probability per site. Unfortunately, n_s and P are not independent, according to our data, they are related by $p=3.5/n_s$.

Table 5.3 intensity of number of electron population distribution

Electron (n)	Intensity(exp)	Intensity(binomial)	Error
0	0.1189	0.1463	23.0%
1	0.3193	0.2871	10.1%
2	0.2883	0.2756	4.4%
3	0.1829	0.1725	5.7%
4	0.0906	0.0792	12.6%

Concerning 3.5 σ electrons extracted and only 0.21 electrons (contribution-I) have been detected, which means that the projectile has lost a large amount of energy without secondary electrons emission. For a given number n electrons extracted, the probability to emit *p* electrons is also well reproduced by binomial law:

$$\binom{n}{p} B^p (1-B)^{n-p} \tag{5.2}$$

where B is the probability or branching ration for this electron to be emitted into vacuum, alternatively the electron could be lost the empty states of the conduction band below the vacuum level; here, the data yield B=0.21, meaning that only 20% of the electrons initially captured form the surface are actually emitted in vacuum.

Till now, many questions have been raised:

- what kind of process is responsible for the energy loss regular cycles ?
- where do the electrons come from since the measured value of 10.5 eV required to pick up an electron is obviously much larger than the graphite work-function ?
- what is the final state of the electrons that are emitted into vacuum?
- What are the two mechanisms contributing to energy loss and electron emission?
- How do we conciliate the apparently opposed features of HOPG?

In order to answer these questions, it's necessary to analyze fine the electronic structure of HOPG.

5.6 Electronic structure of HOPG

Structurally, HOPG is composed by layers of graphene, which is a one-atom-thick planar sheet of sp2-bonded carbon atoms that are arranged in a honeycomb crystal lattice as illustrated in Figure 5.20. Each carbon atom in graphene is bound to its three nearest neighbors by strong planar σ bonds, which involve three of its valence electrons occupying the sp2-hybridized orbitals. In equilibrium the carbon–carbon σ bonds are 2.7a.u. long and are 120◦ apart. These bonds are responsible for the planar structure of graphene and for its mechanical and thermal properties. The fourth valence electron which remains in the half-filled $2p_z$ orbital orthogonal to the adjacent graphene plane forms a weak π bond (6.3a.u. long) by overlapping with other $2p_z$ orbitals. These delocalized π electrons determine the transport properties of HOPG [121].

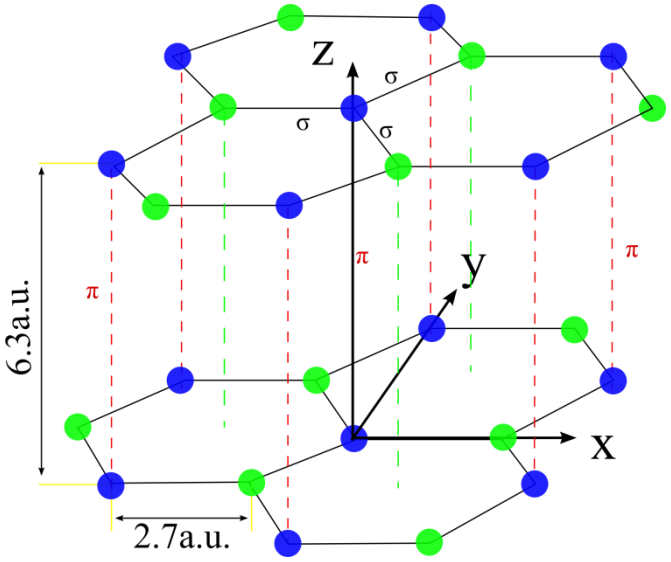

Figure 5.20 Hexagonal lattice of HOPG structure, blue color indicate that there is a weak π bound between the two adjacent layers in the figure, green color means its π bonded layers (not presented here); for the atoms in graphene are connected by σ bond.

According to results of angle resolved photoemission spectra on HOPG [90, 91], there is projected band gap along the Γ direction (Figure 5.21). The other very interesting feature is that in this direction, the least bound electrons come from the localized σ band, at around 5 eV below the Fermi level, while the π band dives 2 eV below [90].

Another important piece of information is that in the interaction between a surface and a projectile, electron transfer is much favored in the direction normal to the surface. This has been shown experimentally and theoretically by comparing Cu(111) and Cu(110) surfaces [122, 123]. Cu(111) exhibits a projected L-gap which increases significantly the formation of negative ions by reducing the probability of electron loss back to the conduction band.

These two pieces of information put together, we understand that negative ion formation on HOPG involves preferentially localized electrons from the σ band, located close to 10 eV

from vacuum, in very good agreement with the measured energy difference in the low energy loss structures.

To complete the photoemission studies, inverse photoemission data (Figure 5.21) show a gap in the Γ direction that extends to close to vacuum level. Because of this positive electron affinity, these levels could well represent the final states in the electron loss by the transient negative ion. From the measured electron TOF, we derive a mean energy that is close to 2 eV for the electrons correlated to the low energy loss structures, meaning the binding energy of those electrons that are not emitted is close to 0.5, i.e. they lie slightly lower than vacuum level.

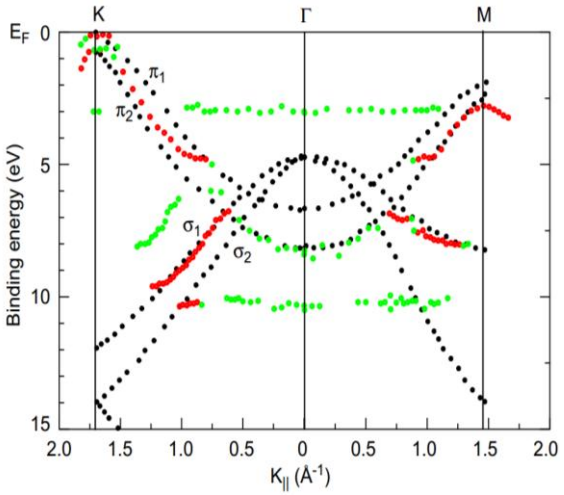

Figure 5.21 Energy versus momentum component parallel to the sample surface (E(k)~$k_{\|}$) for all the strong red circles) and weak (green circles) peaks of the experimental results, black circles represent theoretical band structure of graphite in the Γ*k* and Γ*m* direction of Brillouin zone, cited from Ref. [90].

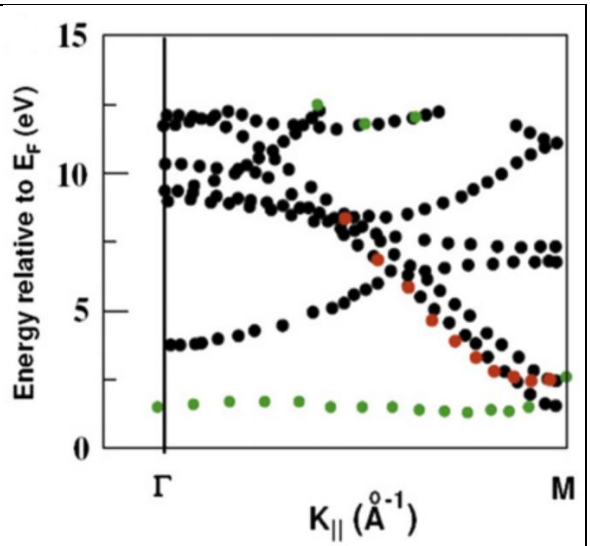

Figure 5.22 Energy relative to E_F from Γ to M direction of Brillouin zone, cited from Ref. [90].

At this point, it is tempting to identify the two distinct mechanisms contributing to both energy loss and electron emission. The metal-like component in the energy loss comes from projectile friction (electronic excitation) through the density of π electrons. These electrons having their momentum preferentially in the surface plane, the energy transfer is favored. A small fraction of the excited π electrons is emitted into vacuum. The discrete structures on the low energy loss side arise from formation of transient negative ions by capture of localized σ electrons at the G point on the Brillouin zone, the detachment of the ions contributes significantly to the electron emission.

Now the idea is that particles having experienced a large energy loss, they also had some probability to go though cycles of negative ion formation and destruction. However the subsequent discrete energy loss features are washed out by the stochastic excitation of the π band electrons. Assuming that the discrete structures in the energy loss spectra only eject σ electrons and that both populations are present in the large metal-like component of the energy loss, we could decompose the electron TOF spectrum to derive these two populations; this is done in figure 5.22. This procedure is then carried on data taken from different exit angles, see Figure 5.23.

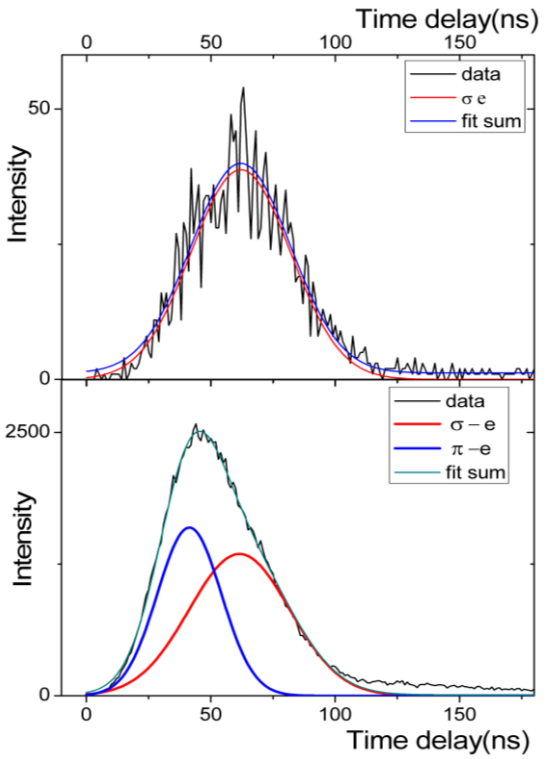

Figure 5.23 electron spectrum decomposition by two components (π and σ-electron) electron emission (left panel←).

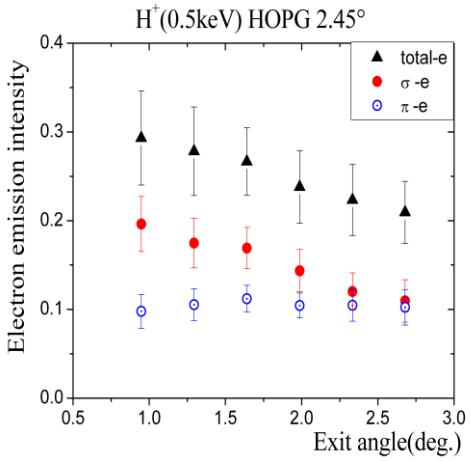

Figure 5.24 Electron emission intensity polar distributions associated to scattered particle and its exit angle, for the σ and π-electron emission are taking from the fits in Figure 5.23.

For π-electron emission, there is no big difference around this scattering angle range; while for σ-electron emission, it decreases fast with increasing exit angle. Generally, larger exit angle, leads to a smaller distance to surface atom at turning point, which makes deep valence band electron easier to excite, this is probably the main reason of H^- ion fraction increasing with incident angle (Figure 5.3). However, the trajectory length is inversely proportional to the incident and exit angle, thus, shorter trajectory length leading smaller number collisional sites, which is mainly the reason for the decreasing σ-electron emission. Since the impacting energy is fixed, the π-electron emission by head-on collision is not affected by the small variation incident angle.

Benefiting from the coincidence measurement, we can quantitatively analyze electron emission and energy loss, see Figure 5.23. Due to the fact that two electronic emission mechanisms are responsible for the observed energy loss (capture of σ electron to the H

affinity level and excitation of π electrons in binary collisions), and which superimpose randomly, making difficult to identify the exact σ and π-electron number that were extracted and excited at larger exit angle and higher energy loss.

In short, among the negative ion H^- fraction on various surfaces [96, 97, 124], the highest negative ion fraction (~10%) till now has been obtained on HOPG surface via hydrogenous particle grazing scattering (Table 5.1). With pure sp2-hybridized electronic structure of HOPG, each atom has 3 σ bonds connected to its adjacent atom in the same graphene layer and one π-bond connected to its adjacent graphene plane, which determine its semi-metal property with typical metal-like work function ~4.6eV. But it also has an insulator-like electronic band gap which extending from below the Fermi level close to about vacuum energy. This band gap acts like L-band gap in front of Cu(111) surface comparing to Cu(110) surface [122, 123], modifies the projectile-surface electron transfer rate, as compared to the free-electron case, by blocking the electron loss from the projectile along the surface normal, which turns out enhanced the negative ion fractions.

Additionally, localized hole on graphite surface after one σ-electron captured onto H^- will suppress electron loss back to surface via resonant ionization. Even though delocalized π-electron distributed all around between two graphenes, electron capturing from σ is prevented losing back to π state from H^- due to Pauli Exclusion Principle. In other words, the probability for an affinity electron loses back to the HOPG surface is strongly reduced because the σ bond is localized. This would result in enhanced negative ion fractions, comparing to a clean metal surface with free-electron for unoccupied conduction band states giving rise to substantial electron loss via resonant ionization (detachment) of negative ions.

5.7 Conclusion

Based on the analysis above, we have quantitatively studied negative ion fraction on HOPG surface via hydrogenous particle with various kinetic energy grazing scattering. According to our measurement, it shows that electron capture kinematic assistant with both parallel (Figure 5.2) and perpendicular (Figure 5.3) velocity. For the parallel velocity effect, ion fraction continues increasing when it reaches to maximum (~9.5%) at 0.35a.u. (Figure 5.5), while at higher velocity (faster than 0.35a.u.) it continues decreasing with increasing velocity. The explanation is, at lower energy, electron capture dominates the negative ion formation, while at higher energy, electron detachment are mainly responsible for the decreasing of the negative ion fraction by electron losing back to surface or emitting to vacuum [82]. However, for the perpendicular velocity assistant effect, negative ion fraction increase linearly with impacting energy normal ($v_{//}$ was fixed) to surface in our energy range (Figure 5.3). While at lower normal energy, negative ion fraction of proton scattering is much higher than that of H° impacting, due to image charge acceleration modifies the trajectory of proton, which increases its normal energy and eventually kinematical assistant increasing the electron capture possibility. Obviously, more data are needed for analyzing the kinematic effect in electron capture and negative ion formation.

Benefit from coincident measurement technique, energy loss and secondary electron emission have also been quantitatively analyzed. At glance view, energy loss on HOPG with both proton and H° increases with its impacting energy. After careful analysis, we found that energy loss decreases with increasing exit angle, which is contrary to the energy loss of proton [118, 119] and He° on LiF(001) surface (our experiment data). Basically, there are two counteracting effects determining the variation of the energy loss with increasing incidence angle: the decreasing interaction length and the increasing electron density of sample. As we already knew that, the trajectory length is inverse proportional with the incident or outgoing angle, furthermore, the energy loss is mainly determined by the interaction length on HOPG sample. Thus, the energy loss will be smaller at larger incident/outgoing angle. Contrarily, our observations are not in this case, but the increasing electron density should take the main responsibility for the energy loss.

Additionally, coincidental electron emission measurement via particle scattering on HOPG with TOF technique, it reveals that electron emission decreases with increasing the exit angle, see Figure 5.24. Combine the electron emission with energy loss vs. exit angle of scattered particle (in Figure 5.13), the larger energy loss, the bigger electron emission, i.e. a large part of energy loss is responsible for electron excitation and further being emitted into vacuum.

Furthermore, the most striking result has been found that, at lower exit angle, two kind of energy loss behavior—cycle-characteristic energy loss and metal-like interaction energy – have been identified (Figure 5.16 and Figure 5.17). A regular 10.6±1.6eV energy difference between two adjacent peaks (see Figure 5.17) reveals that these periodic increments energy

losses due two 1,2,3…electrons excitation from σ state, while for the energy loss of metal-like is responsible for delocalized π-electron head-on collision. The σ and π-electron are deciphered by discrete energy of scattered particle and emitted electron by the coincident event—one electron detected and its associated scattered particle. With quantitative analysis, at each collision sites, where an σ electron has been captured on H^-, a fraction B=21% of the H^- ions successfully escape from the capture site for H^+ (0.5keV) grazing scattering on HOPG surface, whereas 1-B=79% lose their electron to the temporary states. The probability for an H^- ion to detach its electron is very large and on the order of 60%-70% per lattice site.

Obviously, more data are needed for better understanding the mechanism of negative ion formation on HOPG, π and σ-electron emission, and the cycle energy loss, etc.

6. Fast proton diffraction

In this chapter, I will focus on the diffraction of keV ions on LiF(001), which is a link between the electron capture problem described in chapter 4 with the new activity initiated during the thesis of Patrick Rousseau [22] and Pierre Soulisse [39] and which consists of using diffraction of fast atoms to analyze surfaces. The goal was to investigate if diffraction can be used with incident protons. I will show in this chapter that the answer is positive but that we have to consider an inelastic diffraction regime.

After a brief recall on atomic diffraction at thermal energies I detail the specific case of grazing incidence diffraction of fast atoms (GIFAD). Then I will first analyze results with diffraction of neutral atomic hydrogen and then address the entirely new question of diffraction with incident ions.

The observation of diffraction with atoms on surfaces by Esterman and Stern [12] in 1930 is the first demonstration that a complex system (an entire atom made of nucleus and its electrons) can be described by a wave. This demonstrated the De Broglie theory and was a key experiment in the founding of quantum theory. It is only 50 years later, with the advent of supersonic expansions, that helium atomic diffraction (HAS) developed as a surface analysis tool [13]. Extension of this technique to grazing incidence and keV energies have been discovered in 2003 and patented in 2007 [14] in our group at ISMO. Independently, the research group led by Helmut Winter, in Humboldt University of Berlin, has observed this phenomenon in 2006-2007.

Grazing incidence fast atom scattering has been intensively studied because of its potential application for surface analysis. In chapter 4 and 5, we have intensively analyzed the negative ion formation with the same experiment setup. In principle, GIFAD provides detailed information on the shape of the crystal target, more precisely as we will detail further, the shape (profile) of its electronic density at the turning point of the classical trajectory.

So far, no diffraction has been observed for reactive system, like H°_GaAS. As recently shown by Lineman [125], diffraction disappears when inelastic electronic processes are present such as exciton population in collision of H° with LiF surface.

On the other hand, Bundaleski [19] showed that diffraction can be observed on metal surface where the inelastic processes are numerous.

We present here a different class of inelastic process namely the electron capture of H^+ from a LiF(001) surface. On one hand the process can be seen as more violent since one electron has to switch from the valence band to the projectile. On the other hand the process is quasi-elastic since the binding energies are comparable.

6.1 diffraction of matter waves [9](de Broglie)

In quantum mechanics, the concept of matter waves or de Broglie waves reflects the wave–particle duality of matter. In 1905, Albert Einstein postulated that light was emitted and absorbed as localized photons in his paper on the photoelectric effect. These photons would have energy $E = h\nu$, where h is Planck constant, and ν is the frequency of light. Einstein's postulate was confirmed experimentally by Robert Millikan and Arthur Compton over the next two decades. Thus it became apparent that light has both wave-like and particle-like properties. In 1924, Louis de Broglie suggested that all particles have this wave/particle duality. In 1927 at Bell Lab, Davisson-Germer experimentally confirmed the de Broglie hypothesis for electrons by low energy electrons scattering at a crystalline nickel target[10].

The de Broglie relation defines the wavelength λ of a particle with momentum p:

$$\lambda = \frac{h}{p} \tag{6.1}$$

where h is Planck's constant.

Therefore massive particles (relative to electrons) usually have a very small wavelength. However, at low velocity such as that of helium atoms at room temperature used by Estermann and Stern, the de Broglie wavelength is in the nanometers range. Particles with even lower momentum, such as helium atoms at temperatures of only a few nano-Kelvins, might have matter waves with wavelengths as long as a few microns. Under such unusual conditions, the realities of the quantum world are almost brought up into the macro-scale region.

Often, the wavenumber k of the particle can be useful, it is expressed as following:

$$k = \frac{2\pi}{\lambda} = \frac{p}{\hbar} \tag{6.2}$$

where ħ is the Planck constant divide by 2π. For a projectile with mass m_0 and velocity v (non relativistic), the de Broglie wave length and vector is:

[9] http://en.wikipedia.org/wiki/Matter_wave

[10] http://en.wikipedia.org/wiki/Davisson%E2%80%93Germer_experiment

$$k = \frac{m_0 v}{\hbar} = \frac{\sqrt{2m_0 E}}{\hbar} \text{ and } \lambda = \frac{h}{m_0 v} = \frac{2\pi}{k} \tag{6.3}$$

According to the Eq.(6.1), for instance, Helium atom with kinetic energies in the 10-100 meV range, the de Broglie wavelength λ of the incident atoms is close to one Å.

6.2 Experimental conditions

Recently, Grazing Incidence Fast Atom Diffraction on surface has been intensively studied on various samples by our group (Orsay) [4, 14, 17] and the group of H. Winter (Berlin) [15, 125, 126]. The range of energies goes from several hundred eV up to tens of keV for the projectiles used which include He, H atoms and H_2 molecules. The schematic of collision geometry for fast atom diffraction on surface with grazing incident angle has been presented in Figure 6.1.

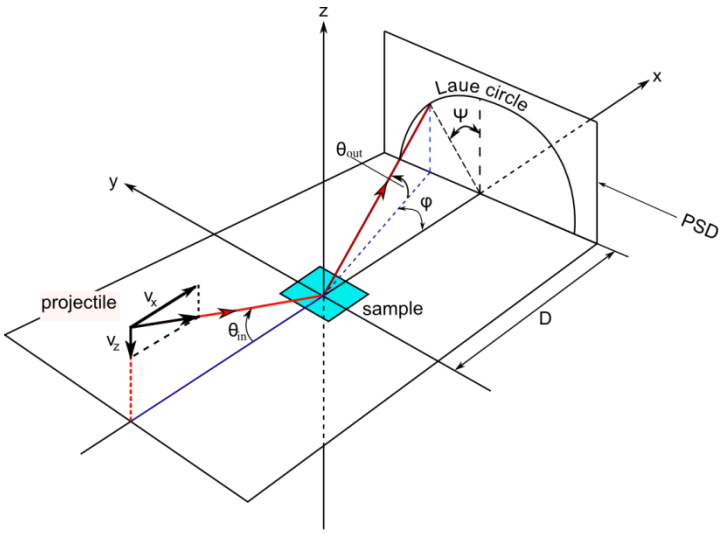

Figure 6.1 Sketch of collision geometry for grazing incidence fast atom diffraction on surface.

With this specific geometry, the incident angle θ_{in} of incoming atomic beam is very small, around 0.5°~2.5° to the target surface so that the momentum component directed towards the surface can be hundred times smaller than the total momentum which make it suitable for diffraction on a crystal lattice. Is this simple approach valid? This will be discussed in section 6.4 but let us recall few basic features of diffraction.

6.2.1 Wavelength of GIFAD

The de Broglie wavelength associated with keV energy is three orders of magnitude smaller than atomic spacing of solid surface. Worse, this wavelength is two orders of magnitude

smaller than the mean thermal atomic displacement in the crystal [14, 127] suggesting that no coherence will remain! Observation shows the contrary!!

The first naïve answer is to say that, in the regime of axial surface channeling, the momentum perpendicular to the surface is decoupled from the fast one parallel to the surface.

$$\lambda_{dB\perp} = \frac{h}{\sin\theta_{in}\sqrt{2m_0E_0}}$$
$$\lambda_{dB//} = \frac{h}{\cos\theta_{in}\sqrt{2m_0E_0}} \qquad (6.4)$$

Where the m_0 is mass of the projectile atoms. Since with grazing incidence condition, θ_{in} is around 1degree, it turns out that the wavelength $\lambda_{dB\perp}$ is comparable to the atomic spacing of solid surface. Thus, the fast atom grazing incidence diffraction can easily be achieved.

6.2.2 Bragg condition[11]

Bragg conditions apply to periodic arrangement of scattering objects, if the incident particle encounters several such objects all scattered amplitudes will interfere. Bragg condition is simply the geometric condition for which these amplitudes will interfere constructively. This condition do no depend on the nature of the scattering object nor do this condition guaranty that scattering will occur. If it occurs scattering can only be observed at positions (angles) compatible with Bragg conditions. Strictly speaking, Bragg condition is defined for an incident plane wave that an infinite number of objects are encountered and the outgoing angles are delta functions infinitely narrow.

For the surface diffraction, at grazing incidence of projectile at certain low index crystal orientation, surface exhibits periodical furrows (Chapter 3), as presented in Figure 6.2. Two beams with identical wavelength and phase approach a crystalline solid and are scattered off from two different rows of surface atoms. The projectiles interactional trajectories with surface atoms are physically the same, but the total travel distances are slightly different, as marked red line (ΔL) in Figure 6.2, where φ is the incident angle of projectile with crystal orientation.

$$\Delta L = a \cdot \sin\varphi$$

As presented in Figure 6.2, projectiles are scattered off after interference with surface atoms, the beams interference is constructive when the phase shift is a multiple of 2π; this condition can be expressed by Bragg's law and are scattered off two different layers. When considering

[11] http://en.wikipedia.org/wiki/Bragg's_law

the two adjacent rows, the second beam traverse an extra length of a*sinθ, the Bragg peaks happen when:

$$a \cdot \sin\varphi = n\lambda \tag{6.5}$$

where n is an integer (0,1,2…), λ is the wavelength of incident wave, d is the spacing between the planes in the atomic lattice. Note that moving particles, including electrons, protons and neutrons, have an associated de Broglie wavelength.

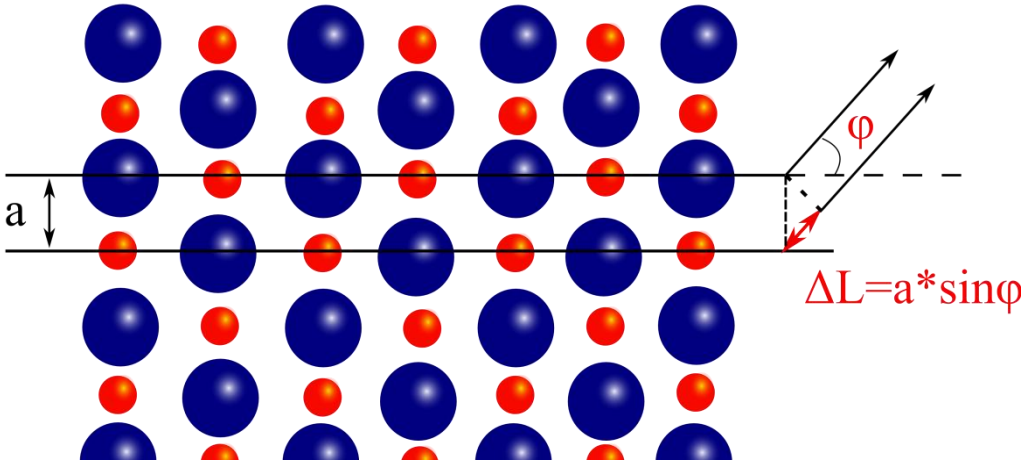

Figure 6.2 Two beams with identical wavelength and phase approach a crystalline solid and are scattered off two different rows of surface atoms.

6.2.3 Reciprocal space

The Bragg law is a consequence of the periodicity of the lattice, but it doesn't refer to the composition of the basis of atoms associated with every lattice point [128]. However, that of the basis component determines the relative intensity of the various orders of diffraction from given set of parallel planes.

For analysis of the periodicity distribution of solid, the most used way is the Fourier analysis. In Fourier transform of the spatial wave function, its lattice dimensions are reciprocal to the original lattice. In this space, the points in the reciprocal space are plotted by the set of vectors (two dimensions in our case):

$$\vec{G} = v_1\vec{b}_1 + v_2\vec{b}_2 \tag{6.6}$$

where v_1, and v_2 are integers, and $\vec{b}_1$ and $\vec{b}_2$ are the axis vectors of the reciprocal lattice. Associate to original lattice, these axis vectors of the reciprocal lattice have:

$$\vec{b}_1 = \frac{2\pi}{\vec{a}_1};\ \text{and}\ \vec{b}_2 = \frac{2\pi}{\vec{a}_2} \tag{6.7}$$

Where a_1, and a_2 are the lattice parameters defined by the three fundamental translation vectors in original lattice. The factors 2π are not used by crystallographers but are convenient in solid state physics [128].

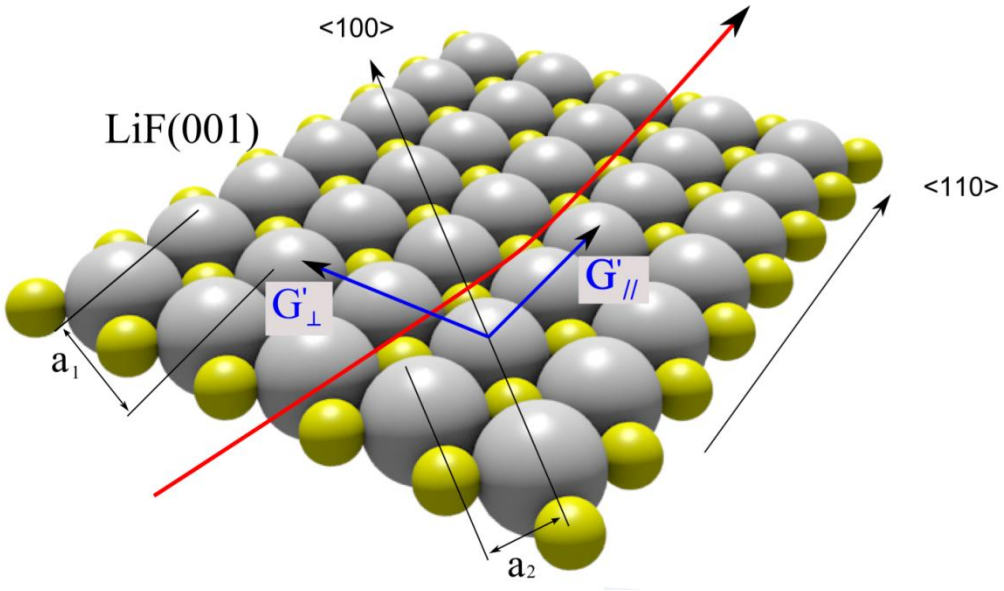

Figure 6.3 Illustration of beam vector exchange when projectile grazing incidence on LiF(001) surface, where G'// and G'$_\perp$ are reciprocal vector ($G_{//}$ and $G_\perp$) associated to real space.

Since $a_1$and a_2 are primitive vectors of the crystal lattice, then $\vec{b}_1$and $\vec{b}_2$ are primitive vectors of the reciprocal lattice. Each vector defined by Eq.(6.7) is orthogonal to two axis vectors of the crystal lattice. Thus $\vec{b}_1$and $\vec{b}_2$ have the property:

$$\vec{b}_i.\vec{a}_j = 2\pi\delta_{ij} \tag{6.8}$$

Where δ_{ij} =1 when i=j, or δ_{ij} =0 if i≠j.

Every crystal structure has two lattices associated with it, the crystal lattice and the reciprocal lattice. A diffraction pattern of a crystal is a map of the reciprocal lattice of the crystal. While a microscope image is a map of the crystal structure in real space. However, if we change the crystal orientation from one to another, the both of the direct lattice and the reciprocal lattice have been changed.

6.2.4 Vector exchange

Generally, when beam with initial wave vector k scattered from surface, the final wave vector turn to k' due momentum transfer with solid atom, where the k+Δk=k', Δk is the change in wave vector. In Fourier transformation of particle scattered from surface, if Δk=G, the scattering intensity will be reinforced, otherwise, it will disappear due to destructive

interference. Due to energy conservation of elastic collision, and Δk=G (Bragg peaks), we have: $(k+G)^2 = k'^2$. So that the diffraction condition is written:

$$2k \cdot G + G^2 = 0 \tag{6.9}$$

This is the central result of the theory elastic scattering of waves in a periodic lattice, G is a reciprocal lattice vector, so is –G, therefore, Eq.(6.9) can be rewritten as:

$$2k \cdot G = G^2 \tag{6.10}$$

This is another statement of the Bragg condition [128].

When the projectile incident direction is very grazing and along a given crystallographic orientation, the surface exhibits periodic furrows consisting of well-aligned atoms, see in Figure 6.4. Set the coordinate of X and Y on the sample surface, where the X-axis is along the beam direction, while Z is normal to the surface. The projectile impinges on the surface in the XZ plane at grazing incidence meaning that its momentum k_z is much smaller that k_x, $\tan(\theta) = k_z/k_x$ and $k_y = 0$. At keV energy range, $|k| \gg |G|$. During the elastic collision process, the momentum G exchanged with the projectile is linear combinations of 2D surface reciprocal lattice vectors $G_{//}$, $G_{\perp}$, i.e.

$$\Delta k = n \cdot G_{//} + m \cdot G_{\perp} \tag{6.11}$$

where m and n are integral with values 0,1,2…

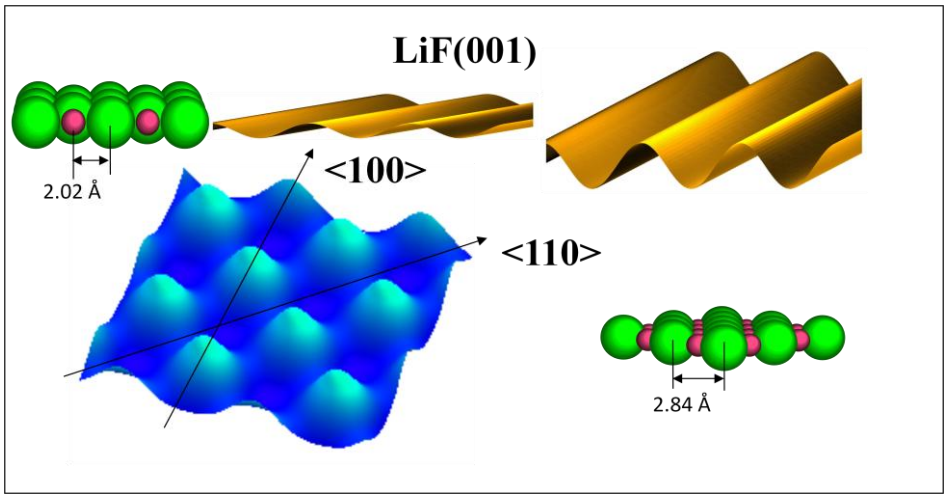

Figure 6.4 Schematic drawing of the averaging effect intrinsic to GIFAD. Along the <100> direction, the maxima and minima of the egg box compensate for each other resulting in a reduced corrugation. Note that the symmetry of the rows (2.02 Å) is not a translation symmetry of the 2D crystal. Along the <110> direction the averaging effect is reduced [129].

Along its trajectory on surface pane XY, momentum exchange of k_x, k_y are associated to G_x, G_y, respectively. Two effects contribute to exclude non zero G_x component when particle

flying above each surface atom—slowing down and reacceleration (Figure 6.5). However, the two components compensate each other and lead to negligible momentum transfer all along the trajectory. But this is not true in the direction normal (G_y) to the beam, because at grazing incidence condition, when the projectile hits an atomic row on the edge, all successive atoms of the row will deflect the projectile in the same direction, i.e. all contributions add up with the same sign (p_{y+} and p_{y-}) allowing significant value of the coupling (Figure 6.5). As a result, the scattered particle appearance on PSD follows the Bragg condition.

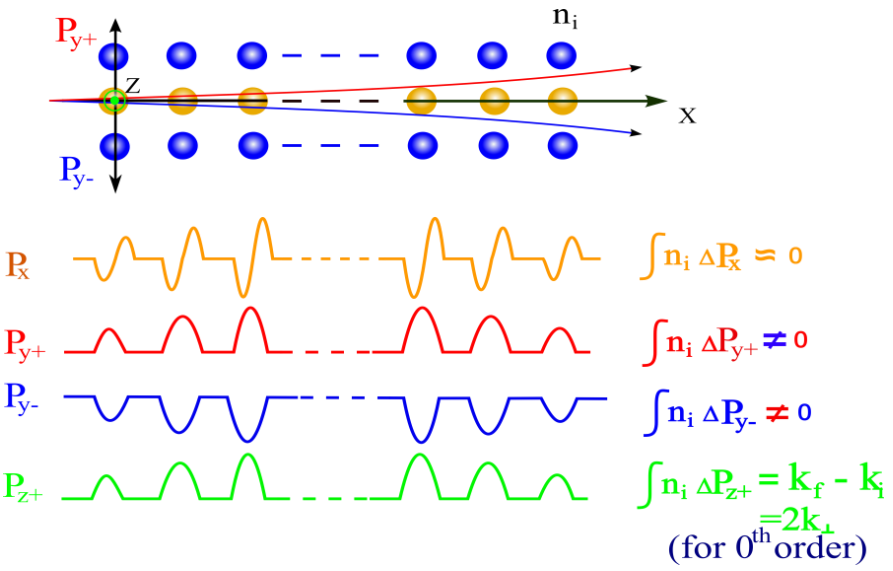

Figure 6.5 Illustration of momentum exchange when particle fly above surface atoms.

In GIFAD the scattering object is a row of atoms, a furrow or atomic string. These are equally spaced by a_y—the periodicity of the washboard, which is given by modulus of the smallest linear combination normal to the beam $G_y=2\pi/a_y$. In this YZ plane, writing the initial and final momentum of the projectile k_i and k_f respectively, the energy conservation give

$$k_{iz}^2 = k_{fz}^2 + k_{fy}^2 \tag{6.12}$$

While Bragg condition is $k_{fy}= m.G_y$. The diffraction pattern is made of spots sitting on a circle of radius k_{iz} and the maximum diffraction order is given by k_{iz}/G_y.[14], and Bragg condition indicates that diffraction will occur only at angle $\varphi=m.G_y/k_\perp$, where $m_{max}=k_{iz}/G_y$.

6.2.5 Beam divergence

Diffraction can only be observed for well-defined conditions. The crystal surface should be clean and flat enough and oriented along a principal (low Miller index[12]) direction etc. But the

[12] http://en.wikipedia.org/wiki/Miller_index

most important one is the beam divergence limitation; considering the Bragg conditions in terms of multiple of an angle δθ, the beam divergence Δθ has to be smaller than δθ. In other words, p_0*Δθ<G or Δθ<G/p_0, which is not easy since, for keV projectile p_0~$p_{//}$ can be quite large. The divergence vector should be smaller than surface reciprocal parameter in y axial [129, 130], i.e.

$$\Delta k_y \le G_y \tag{6.13}$$

where Δk_y is beam vector in y direction, G_y is the surface reciprocal parameter in y coordinate, for the round aperture, we have $\Delta k_y = \Delta k_z$.

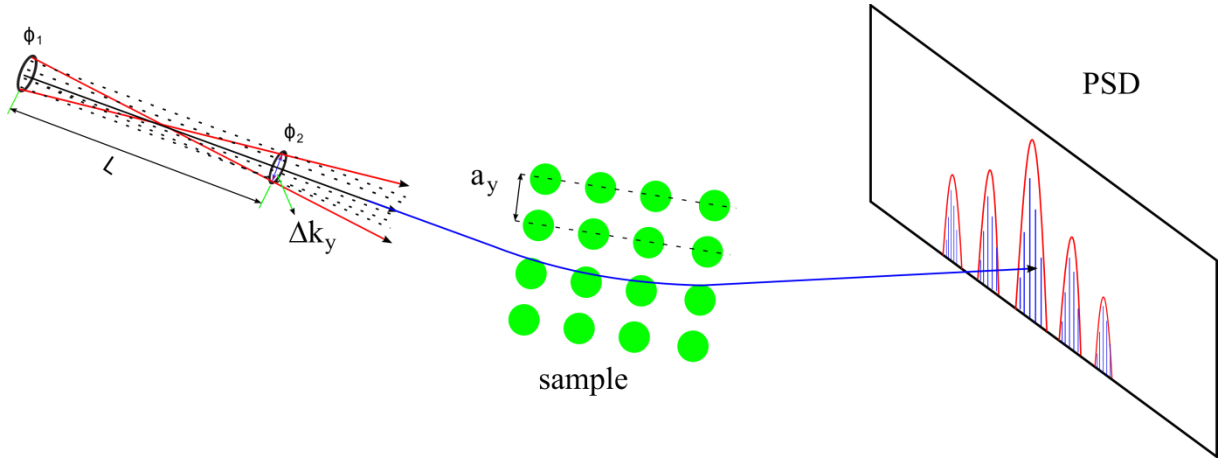

Figure 6.6 Diffraction patterns broadening by the beam divergence, at best the ideal diffraction pattern is convoluted by the beam profile.

The beam divergence is controlled by a set of two diaphragms ϕ_1 and ϕ_2 located L ~700 mm apart. This limits the angular spread Δθ as:

$$\Delta\theta = \frac{\phi_1 + \phi_2}{L} \tag{6.14}$$

Considering particle scattering from LiF(001) incident along the <100> direction. The averaged surface corrugation appears as a one-dimensional periodic washboard with a spacing b/2, where b= 7.616 a.u. is the LiF lattice vector dimension. The effective one-dimensional reciprocal lattice vector is G_y=1.65 (a.u.)$^{-1}$. Thus, in order to observe surface diffraction on LiF(001) along <100> direction, the beam divergent should be smaller than 1.65 (a.u.)$^{-1}$/$p_{//}$.

In our experiment condition, 1mm diameter of first hole of collimator, second slit with 30μm width located 700 mm downstream, which permits that the projectile energy can up to 9.3 keV/a.u., for instance, H° can up to 9.3 keV with experiment condition.

6.3 Empirical analysis model

6.3.1 Corrugation (Hard-Wall model)

Now that the interaction potential is reduced to 2D V(y,z) (after averaging along the x direction) it is relatively easy to display the projectile trajectory in the y,z plane. The situation is therefore very similar to that encountered in thermal helium diffraction where the incidence is quasi normal to the surface. In this field, the Hard Wall model was developed and turned out to be qualitatively correct for limited corrugation. It appears that most of the direction change occurs very close to the equipotential lines. The Hard-Wall model simplifies the problem by considering that the 2D potential can be replaced by a 1D mirror located exactly at the equipotential corresponding to the incident energy. The straight line trajectories simply undergo mirror like (specular) reflection on the curved mirror. The shape of this 1D equipotential line is called the corrugation function $Z_E(y)$ (Figure 6.7).

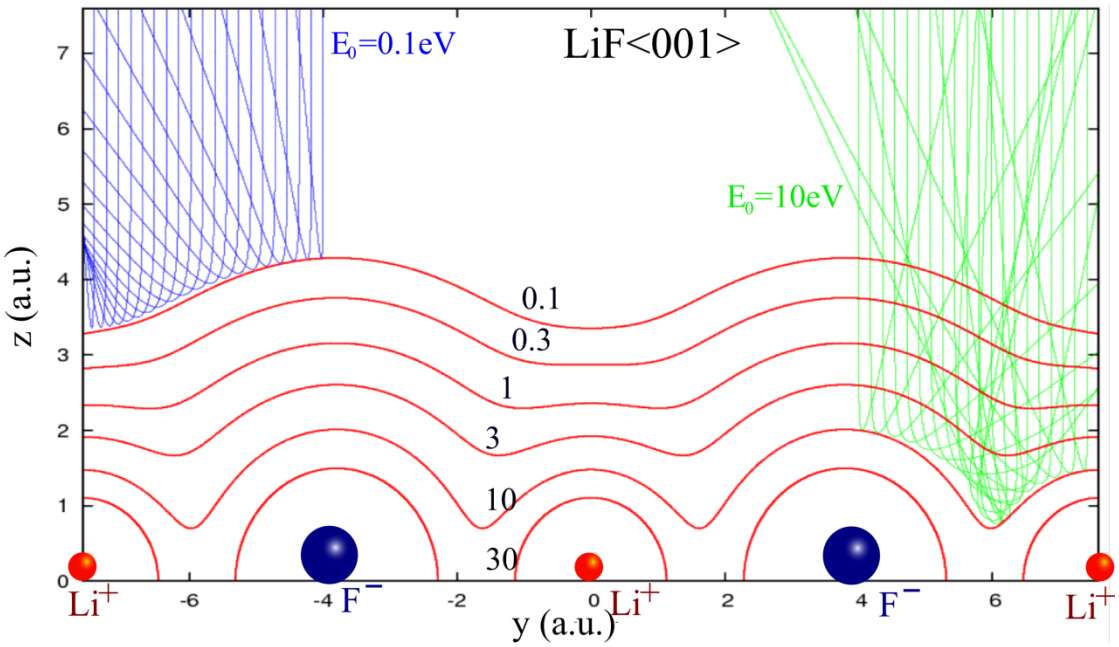

Figure 6.7 Surface potential energy corrugation in a (y,z) plane with He° on LiF(001) surface. The Hard-Wall model, consider mirror like reflexion on the equipotential lines $V(y,z)=E_p$ (potential lines calculated by Maxime DEBIOSAC). For energies Ep lower than one eV the trajectories are turning very close to the equipotential lines supporting the model. This is not the case at E_p=10 eV incident energy (right hand).

The effective wavelength $\lambda_\perp$ that diffracts on this 1D potential corresponds to the normal energy $E_\perp = E_0 \sin^2\theta$ (section 5.2.1), which also decides the turning point. The simplest corrugation function is that with only one Fourier component h_{ztp}

$$Z_t(y) = \frac{1}{2} h_{ztp} \cdot \cos\left(G_y . y\right) \tag{6.15}$$

It allows direct calculation of the intensity I_n of a diffraction order n. I_n is simply given by the square of Bessel function [14, 131]of rank n *i.e.* J_n with a dimensionless argument, $2\pi.h_{ztp}/\lambda_\perp$.

$$I_n(h_{ztp}/\lambda_\perp) = J_n(4\pi.h_{ztp}/\lambda_\perp)^2 \tag{6.16}$$

For specular reflection (zero order), the atoms have no transverse momentum exchanged with the surface. So they either bounced off the top of a row of atoms or in between two rows. If we now consider the matter wave associated with the atom a semi-classical perspective, the probability of observing the incident atom at the 0^{th}order depends on the phase difference between the wave that reflects off the tops and the one that is reflected at the bottom. This phase difference is the path difference divided by $\lambda_\perp/2\pi$ i.e. twice the "corrugation"(way in plus way out) or $4\pi.h_{ztp}/\lambda_\perp$. In practice, the corrugation function is expressed in Fourier component h_i; $Z_t(y)=\Sigma_i h_i/2.\cos(i.G_y.y)$ and the experimental data (all diffraction orders) are fitted with the Hard-Wall prediction. For He° projectile on a LiF(001) surface along both the <100> and <110> direction the fit by a unique cosine function is well adapted and the corrugation function is therefore described by a single parameter (per direction), the corrugation amplitude—h_{ztp}. The corrugation measured by He° projectiles on a LiF(001) surface with a beam aligned along the <100>and <110>direction are presented in Figure 6.8 .

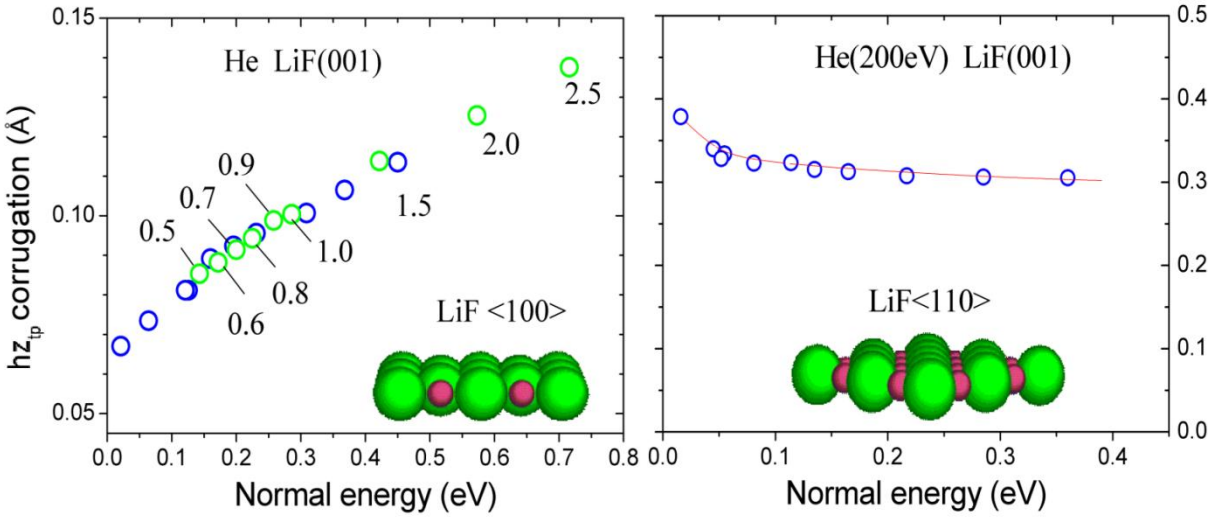

Figure 6.8 Corrugation h_{ztp} from trough to peak as a function of the energy normal to surface along LiF surface <100>and<110>direction, note that the scales are different. The numbers indicated on the figure are for the total projectile energy. All the points nicely follow the same evolution showing the decoupling of parallel and perpendicular motion.

The corrugation is larger along the <110> than along the <100> direction (note the factor ~3 on the scale) but the evolution are opposite, it increases by 0.1 Å along the <100> direction while it decreases by the same amount along the <110> direction as $k_\perp$ increases from 6 to 12$Å^{-1}$. This can be understood qualitatively.

Along the <100>direction, the bottom of the valley corresponds to the "empty space" in between identical rows of alternating Li and F ions. As the projectile normal energy increases, the inter-atomic potential in this empty space progressively reduces until it reaches a threshold value where penetration becomes possible [39, 129], around 15-20 eV in Figure 6.7 above.

At variance, along the <110> direction the bottom of the valley is associated with the rows of Li^+ ions which are supposed to be smaller but also more compact (He-like electronic structure) than the F^- ions forming the top. Thus the top to bottom difference along the <110> direction is decreasing with normal energy.

Note here that, along the <100> direction, the simple 2D cosine Hard-Wall model [4, 132, 133] was predicting a zero mean corrugation. Indeed, in this model and along this direction, the bump (F^- ions) exactly compensate for the dip (Li^+ ions), the observed non zero mean value means that the shape of the "pits" does not exactly compensate that of the "bumps".

6.3.2 The coherence factor

On a perfect surface, each atom gets scattered with a well-defined phase and the periodicity indicates on which direction all cells will interfere constructively. The phase distribution at such Bragg conditions should be a delta function i.e. perfect coherence. Whatever process producing an extra phase will increase the phase distribution at Bragg points. The final coherence is defined as the real part remaining after summation of all amplitudes. If the phase spread is a Gaussian distribution of width σ the coherence is simply $\exp(-1/2\sigma^2)$. The measure of the decoherence is a measure of σ, the width of the phase distribution. When the physical process is known, it provides a unique measurement of this process. This is illustrated with the Debye-Waller treatment of thermal movements.

6.3.2.1 Modified Debye-Waller factor

Elastic scattering intensity is usually reduced by the inelastic processes as the thermal motion of the atoms of the surface atoms. This factor evaluates the decoherence due to thermal vibrations within a harmonic model. In this condition, the coherence factor temperature dependence can be approximated very well by Debye-Waller model for the TEAS or HAS, we have discussed in section 3.3.1. When the surface atom displacement is $\Delta\mathbf{u}$ and the momentum transferred to the surface is $\mathbf{\Delta k}$, the increase path length associated with this displacement give rise to a phase shift (Figure 6.9) given by the product $\mathbf{\Delta k}.\mathbf{u}$ where $\mathbf{\Delta k}=\mathbf{k}_{out}-\mathbf{k}_{in}$ is the wave vector change of direction during the scattering.

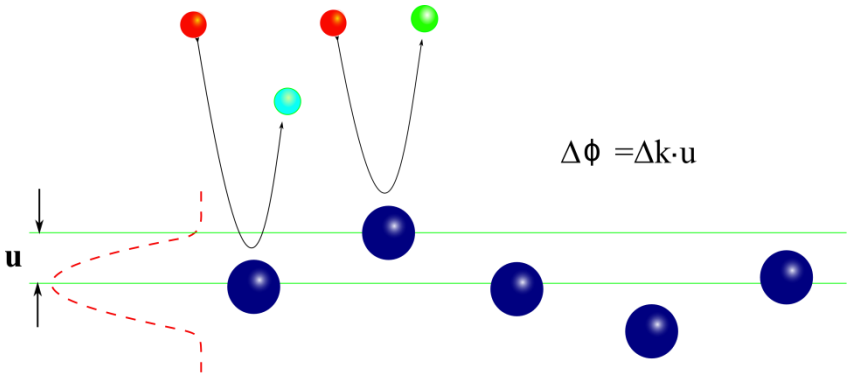

Figure 6.9 Illustration of scattered particle phase shifting due to surface atoms thermal displacement.

Assuming harmonicity of the position **u** (with respect to equilibrium position) of the scattering centers in the material under study, the Boltzmann distribution implies that **u** is normally distributed with zero mean. This Gaussian phase shift therefore translate into a coherence factor also called DWF (Debye-Waller factor) =exp (-<**Δk**.**u**>^{2}**)**. For an isotropic case this scalar product is replaced by $\Delta k^2.\langle \mathbf{u}^2\rangle/3$and one gets a direct relation between u^2 and the coherence of the signal. In a harmonic assumption, the evolution of u with temperature only depends on the curvature ω_D of the harmonic oscillator, a property of the material also called Debye temperature $\theta_D=\hbar\omega_D$. This was established at the beginning of the 20th century for the diffraction of X-rays from bulk materials. For atoms diffracted at the surface, one has to take into account that surface atoms are less restricted in their upward movement and a factor $\sqrt{2}$ is usually introduced. The direct determination of u_z is considered as a major achievement of thermal atom diffraction.

In the case of GIFAD, the projectile has several collision sites with surface atoms before diffusion from the surface, so here we import a variable parameter N_{eff} which is a effective collision or equivalent collision number with surface atoms, defined with FWHM of momentum transfer when projectile collision with the surface atom. We assume that all of these N_{eff} atoms participate the scattering interaction and transfer the same momentum from the projectile, the collision site is a function of incidence angle (N_{eff}~1/ɵ) [20, 129]. According to the Eq.(3.39), the modified Debye-Waller factor can be re-written:

$$I / I_0 = A \cdot \exp(-\frac{4k_\perp^{\ 2}}{N_{eff}(\theta)} \cdot \langle \Delta u^2 \rangle) \tag{6.17}$$

Where *A* is the amplitude of coherence diffraction intensity, and $k_\perp$ is the scattering vector normal to the surface, ɵ is the incident angle.

However, before projectile entre pure potential repulsive region, there is a weak force of attraction between electrically neutral molecules that collide with or pass very close to each other—named van de Waals force. It is caused by the attraction between electron-rich regions of one molecule and electron-poor regions of another (the attraction between the molecules

seen as electric dipoles)[13]. The attraction is much weaker than a chemical bond. Van de Waals forces are the intermolecular forces that cause molecules to cohere in liquid and solid states of matter, and are responsible for surface tension and capillary action.

Thus, Beeby [134] suggested that when calculating Δk one should include the acceleration due to the attractive part of the atom-surface potential. In fact the measurement was so well established that any departure from the standard DWF was interpreted as a measure of the "Beeby" attraction energy. Indeed, it was shown that, in the case of a long range attractive potential well with a depth E_b, the effective normal energy to take into account is $E_\perp+E_b$. This effect was confirmed by special resonances called trapping resonance where the projectile can be trapped for some time inside the attractive well.

6.3.2.2 Experimental determination of Coherence

The theoretical derivation of the coherence factor does not provide any indication concerning where the incoherent intensity may appear! However, it is clear that this incoherent intensity is not subject to particular increase at Bragg position! In other words the incoherent part should be structure-less compared with the Coherent one.

In crystallography, it can be interesting to define the coherence factor as the ratio of diffracted intensity relative to the total scattered intensity. Most often the diffraction peaks are surrounded by non-zero intensity and this intensity can be defined as the background intensity; total intensity = diffracted + background. To do so an easy way is to subtract the diffracted intensity located at the Bragg position.

For simple cases it turned out that the scattered intensity is well fitted by a set of two component line profile; a narrow one ($w_{coh}<G_y$) describing the diffracted intensity and a broad one ($w_{incoh}>G_y$) describing the background. Each peak has only its intensity as a free parameter whereas the w_c, w_i and the ratio between the two component termed a are adjusted for all peaks.

The first narrow width is the coherent part while the second one is classical scattering, and has a larger width than the distance between two diffraction orders (G_y), see Figure 6.10. The total intensity of any diffraction peak n is modeled by the following formulation [39] which describes both the coherent and incoherent components:

$$I_n(x) = A_n \bullet (r.\exp(-\frac{1}{2}(\frac{x-x_n}{w_{coh}})^2) + (1-r) \bullet \exp(-\frac{1}{2}(\frac{x-x_n}{w_{incoh}})^2)) \qquad (6.18)$$

[13] http://en.wikipedia.org/wiki/Van_der_Waals_force

Where x_n is the position of the n^{th} diffraction order i.e. $x_n = x_0+n.G_y$, and x_0 the position of the specular peak.

The first term corresponds to the coherent or "quantum" part represented here by a Gaussian distribution (a Lorentzian would be adequate too), and the second term represent the incoherent or “classical” scattering modeled by a Gaussian distribution, their widths are w_{coh} and w_{incoh}, respectively. The “r” factor is set for all the peaks so that the fraction of the intensity coherent of the sum (the total intensity) corresponds to the definition of the coherence factor such as that Debye-Waller: $r = I_{diff}/I_{tot}$.

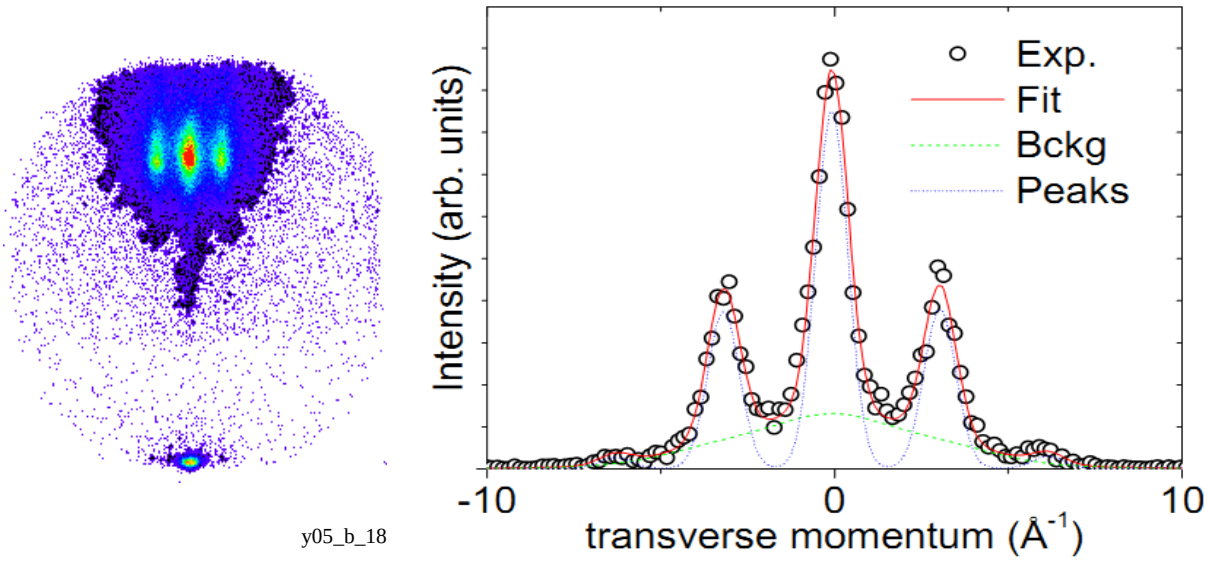

Figure 6.10 For 200 eV Helium atoms scattered on LiF(001) surface along the <100> direction at 1.5 deg. incidence [129], the diffraction image is shown on the left while a horizontal slice is fitted (red curve) with a two components line profile. The sum of all narrow components (blue dotted curve) represents the coherent intensity while the sum of the broad components (green dashed curve) represents the background, the momentum transfer along y-axis is presented in Appendix_D.

We have tried several line profiles for the narrow peak associated with diffraction. Most often both Gaussian and Lorentzian profiles produce an excellent fit. The coherence ratio r is usually larger when estimated by Lorentzian since Lorentzian already produce a natural “leak” in between Bragg peaks. At variance, only a Gaussian profile was able to reproduce the background. This is because the minimum width needed to remove any kind of structure at the Bragg position ($w_{incoh>}\sim G_y$) was already generating a background signal larger than the experimental one. The example presented in Figure 6.10, is taken from Ref. [129]. The ratio r thus determined is the effective Debye-Waller factor, here r =0.65. This is thousand times larger than that measured in TEAS at room temperature! The reason is that, in grazing incidence, the momentum transfer is not achieved in a single collision with a surface atom but spread among a much larger number of collision sites [4, 14, 15]. Assuming an effective number N_{eff} of active site participating equally to the scattering $\theta_{out}-\theta_{in}=2\theta_{in}$, each deflection

at a given lattice site is only $2.\theta_{in}/N_{eff}$ and therefore $\delta k=\Delta k/N_{eff}$. The total dephasing $\Delta\phi_{GIFAD}$ along a complete trajectory is now due to the sum over a large number (N_{eff}) of comparatively weak contributions. What is the net effect?

Assuming uncorrelated thermal movements, the dephasings width add up quadratically:

$$\Delta\phi_{GIFAD}{}^2 = N_{eff}\,\delta\phi^2 \tag{6.19}$$

Where $\delta\phi = \Delta\phi/N_{eff}$ (because $\delta\phi = \delta k.u=\Delta k/N_{eff}$ .u). As a result, the Eq.(6.19) turns to be:

$$\Delta\phi_{GIFAD}{}^2 = N_{eff}\cdot(\Delta\phi / N_{eff})^2 = \Delta\phi^2 / N_{eff} \tag{6.20}$$

From the results fitted by modified Debye-Waller model (Eq.(6.17)) in Figure 6.11, we can see that the model fits very well with the experimental data, but not the standard DWF. Considering the $N_{eff} = 4/\Gamma a\theta$ as derived in chapter 3 and identifying the angle of incidence θ with the ratio $k_\perp/k_{//}$ (small angle approximation). One gets:

$$DWF_{GIFAD} = A\cdot\exp(-\Gamma a\, k_\perp{}^3.u^2 / k_{//}) \tag{6.21}$$

which is useful for angular variation at fixed energy (fixed $k_{//}$), it predicts that the DWF scales as $\exp(-\theta^3)$. The total phase width is much less that it would be in a single collision. The effect can be extremely large as show in the Figure 6.11 where the standard DWF and the above formula are compared with measurements using helium on LiF. This allows GIFAD to probe the surface at larger normal energy and much higher surface temperature than TEAS (where surfaces were usually cooled at liquid nitrogen temperatures).

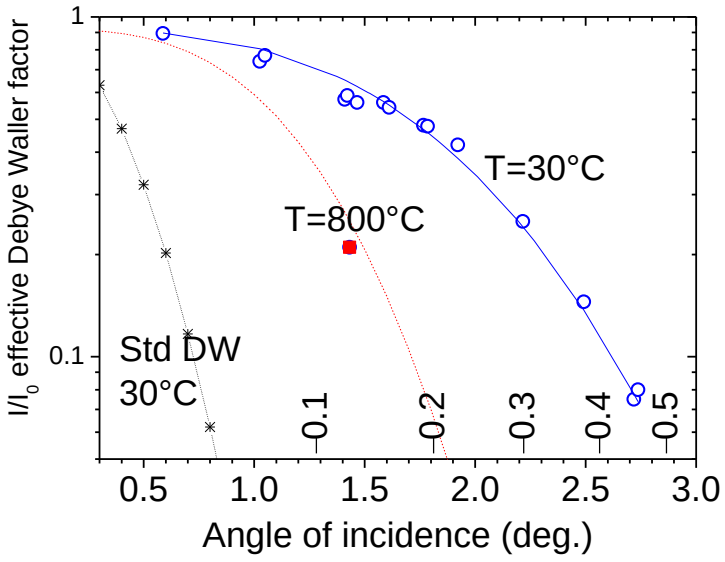

Figure 6.11 The effective Debye-Waller factor as estimated in Figure 6.10 is reported vs. the angle of incidence for 200eV helium atoms and compared with the modified Debye-Waller formula (Figure 6.17). The blue circles

correspond to data taken at room temperature while the red square is for a LiF target heated at 800°C. A surface Debye temperature of 490K was considered. The estimations are multiplied by 0.92 which is taken as the maximum coherence. The line with crosses stands for the unmodified Debye-Waller factor at room temperature [129].

In fact dephasing due to thermal movements can be tuned as low as needed by lowering the angle of incidence θ because, as demonstrated in chapter 3, N_{eff} increases linearly with 1/θ, $N_{eff}=4/\Gamma.\theta.a$, here a is the lattice parameter. This means that whatever the temperature, there should be a threshold angle below which diffraction could be observed. In practice, the minimum angle is limited by the quality of the surface, if the mean terrace length L_t is too small there is almost no chance for the projectile to find a "clean" place of length $L_{eff}=N_{eff}.a$ where diffraction could take place.

From the measured decoherence L_{eff} (and therefore the stiffness Γ) could be deduced. This result is probably correct but remains to be checked in a detailed study.

6.3.2.3 Beeby effect

Another effect can interfere here namely the so called "Beeby effect" [134] quoted above. If the interaction potential between projectile and surface exhibits an attraction well of depth E_b then the effective momentum transfer is not $E_\perp^{1/2}$ but $(E_\perp+E_b)^{1/2}$, see Figure 6.12. Since in the condition of GIFAD, the projectile is attracted by the well of atom surface interaction potential before reaching to the pure repulsive potential region. According to Hard-Wall model (section 6.3.1), projectile will be rebounded back to vacuum once it reach to surface equipotential line where $E_\perp=V(r)$, this is so call turning point of projectile trajectory, see Figure 6.7. The most prominent difference of GIFAD from TEAS is that, there is an N collision sites before being rebounded from surface instead of single for TEAS. Along these N interaction collision sites, the projectile is immerged into pure repulsive potential, since the absolute zero potential line locate z >10 a.u. above surface, and the attractive potential is resident above zero surface equipotential line, see Figure 6.12. As long as the projectile is rebounded from its turning point, it will be scattered into vacuum since attractive potential well (17.8 meV for H° on LiF(001) is not strong enough to retract projectile to surface in the condition of GIFAD. Thus, the projectile has been accelerated twice by the attractive potential at the incoming part and outgoing part all along its trajectory.

To adapt this correction to GIFAD, two modifications are needed that both reduce the coherence. There is more energy (momentum) to share among less sites i.e.

1) One (the same as in TEAS) accounts for the acceleration, the momentum $k_\perp$ is now given by $k_\perp = \sqrt{2m(E_0\theta^2 + E_b)}$.

2) The other one is a reevaluation of N_{eff}, the effective number of scattering because this number also depends on the normal energy $E_\perp$, since $\theta_{in} = \sqrt{\frac{E_\perp}{E_0}}$.

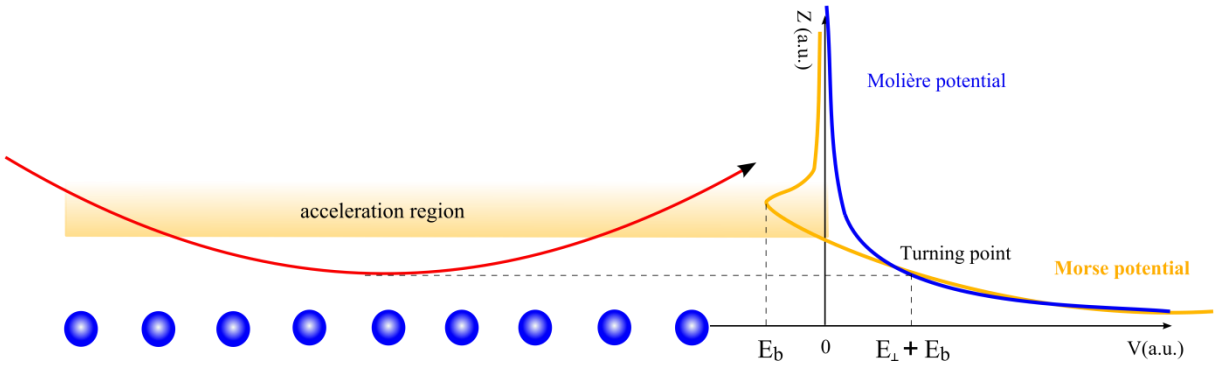

Figure 6.12 Illustration of depth of atom-surface interaction potential.

However, the effective incident angle has been increased when projectile crossing the attractive potential well above the surface, since the normal energy has been increased to ($E_\perp$+E_b). Accordingly, the effective incident angle turns to be:

$$\theta_{eff} = \sqrt{\frac{E_\perp + E_b}{E_{//}}} \tag{6.22}$$

Using the formula derived above, $DWF_{GIFAD} = \exp(-\Gamma a\, k_\perp^3.u^2/k_{//})$ both effects are accounted using the modified normal momentum $k'_\perp=(k_\perp^2+2mE_b/\hbar^2)^{1/2}$.

$$I / I_0 = A \cdot \exp(-8(k_\perp^2 + \frac{2mE_b}{\hbar^2})^{3/2} \cdot \frac{\Gamma \cdot a}{k_{//}} \cdot u^2) \tag{6.23}$$

As can be seen in the above formula, the effect is unimportant as soon as the angle of incidence is such that the normal energy is much larger than the depth of the potential well.

6.4 Diffraction and inelastic processes

6.4.1 Excitation of metal electrons

GIFAD was first demonstrated on the surface of wide band gap insulators [14, 125] where electronic excitations are largely suppressed for small enough projectile normal energies [34, 135]. In 2008, our group demonstrated that diffraction can be observed [19] on a metal surface, the Ag(110) surface. The Figure 6.13 show the diffraction pattern for 500 eV and 1 keV helium atom and an Ag crystal aligned along different directions. The very rapid increase of the energy loss distribution between 1 and 2 keV projectile energy (Figure 6.14) suggests that electron excitation is the dominant source of decoherence in this case.

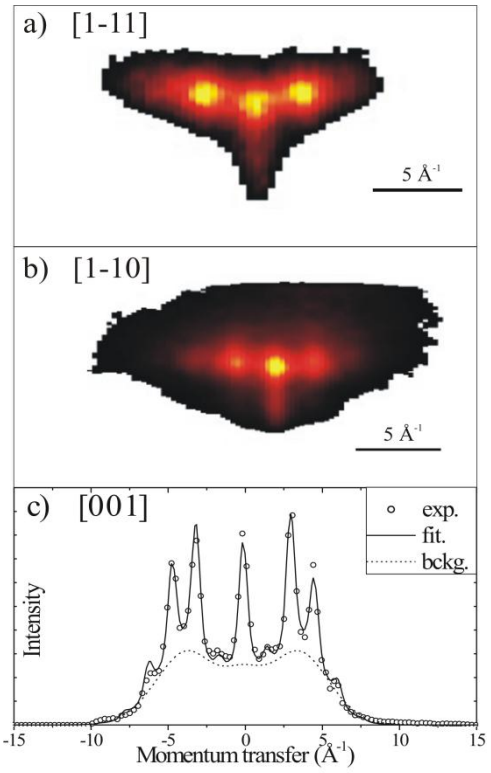

Figure 6.13 Diffraction patterns recorded on Ag (110) surface with He atom. From top to bottom, the total energy is 1000, 500, and 500 eV while the angle of incidence is 1°,1°, and 0.75° so that the normal energy is 360, 180, and 86 meV, respectively. (a) and (b) are 2D raw images, whereas (c) is an intensity plot of a horizontal slice showing the experimental data together with a fit by Gaussians (0.5Å-1 FWHM) [19].

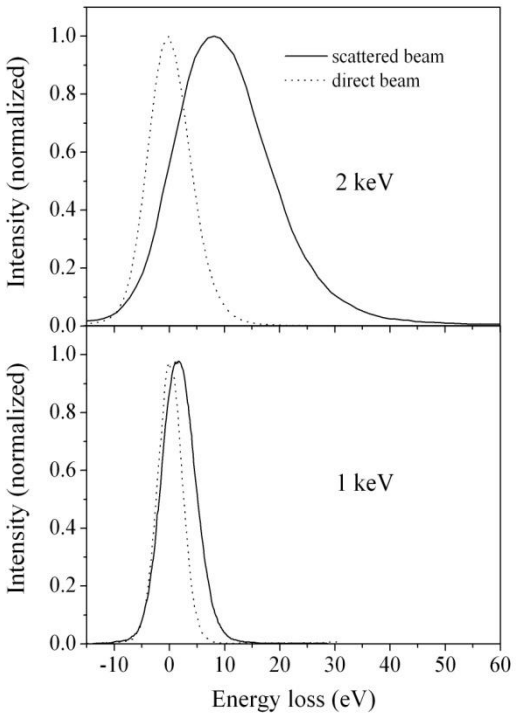

Figure 6.14 Energy loss spectra of 1 and 2 keV He scattered off the Ag(110) surface along the <1$\bar{1}$0> direction [19].

Later on, N. Bundaleski *et al.* proposed a model to describe this decoherence though simple momentum exchange to free electrons close to the Fermi level [136]. In grazing incidence, the energy loss due to elastic electron-atom collision is dominated by head-on collision. When a conduction electron with initial momentum k_i gets close enough to the helium atom, it can be

scattered elastically i.e. at a different direction k_f with $|k_f|=|k_i|$. The elastic cross section can be evaluated from the values measured in the gas phase whereas the metallic origin of the electron can included by forcing k_i to be an occupied level whereas k_f should be an unoccupied level. This is possible only if the helium atom is moving causing the Fermi sphere to be shifted by an amount corresponding to its velocity. As a result some electrons are preferentially pushed in the forward direction generating a net energy loss of the helium atom. These collisions also produce scattering with lateral redirection of the electrons. The scattering is equally likely towards positive or negative values of k_y, it introduces a k_y broadening that could be responsible for the decoherence [136].

From Figure 6.15(b), we can see that the angular straggling increases with energy, even if the momentum spread is independent from the diffraction process, these k_y distributions are interpreted as peak profiles and already give rise to a significant degradation of the diffraction contrast. Since vector difference of the adjacent diffraction patterns is G_y, 500eV would be narrow enough to observe diffraction along any of the directions, while for kinetic energy of 2keV, the coherence scattering would be hardly recognizable, this has also been experimentally proved by our group on Ag surface [19], as presented in Figure 6.13 and Figure 6.14. At higher projectile normal energies, the distance to surface atom at turning point will be shorter so that the electron density will be higher increasing the energy loss. More important, increasing the projectile velocity, increases the shift of the Fermi sphere causing a rapid increase of both the energy loss and decoherence as presented in Figure 6.14.

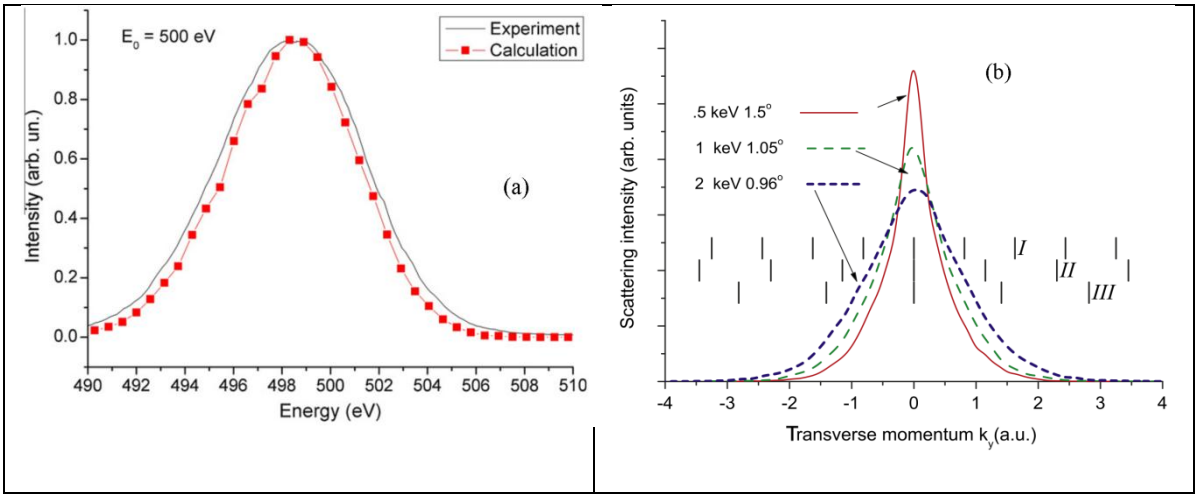

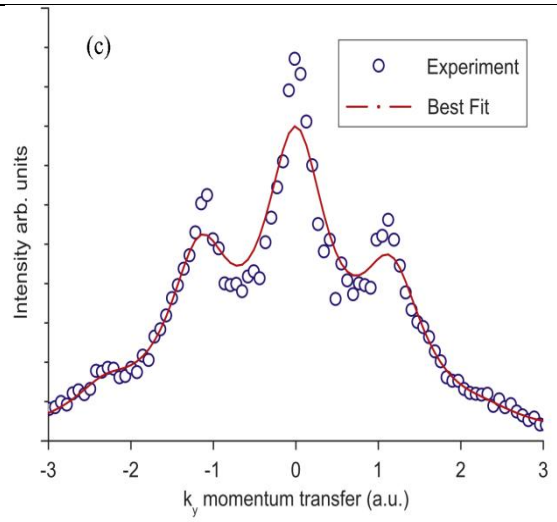

Figure 6.15 comparison between theoretical calculation base on momentum exchange via free electron in Fermi level and experimental data of He atom grazing scattering on Ag(110) surface [136]. (a): theoretical calculation and experimental result of 500 keV He atoms scattered from Ag(110) surface; (b): calculated momentum transverse distribution k_y due to interaction of He projectile with electrons encountered along its classical trajectory close to the surface, the reciprocal lattice vectors corresponding to the tree crystal directions<100>,<11-1> and <110> of Ag(110) are labeled as I, II and III; (c):diffraction pattern observed in blue circle for 500 eV He on Ag(110) surface from [19], and the red line is the best fit using the calculated in (b).

Diffraction on metal surface has also been demonstrated by the Berlin group on Ni(110) Ref. [130]. They also have found that diffraction pattern is increasingly blurred with impacting energy higher than 1.5 keV, and classical scattering dominates in terms of a relatively broad and diffuse angular distribution. The blurring of the diffraction pattern with increasing projectile energy was attributed to the increasing role of decoherence phenomenon for the scattering process due to electronic excitation. Such random collision with conduction electron will have a similar effect on the coherence as the lattice thermal vibration, however, contrast to TEAS, GIFAD has a higher tolerance for the sample temperature, but it's very sensitive to the electronic excitation since it has a long collisional length compare to TEAS.

It was very surprising that there is a little difference between the diffraction patterns scattered by He isotopes [130], see Figure 6.16. since the two He isotopes with same energy and polar incidence angle are scattered from the same potential, in a classical picture, the trajectories are the same. However, in quantum scattering system, the mass difference is associated to the difference of de Broglie wavelenghts $\lambda = \frac{h}{mv}$, which leads to slightly different phases and diffraction patterns for ^{3}He and ^{4}He atoms.

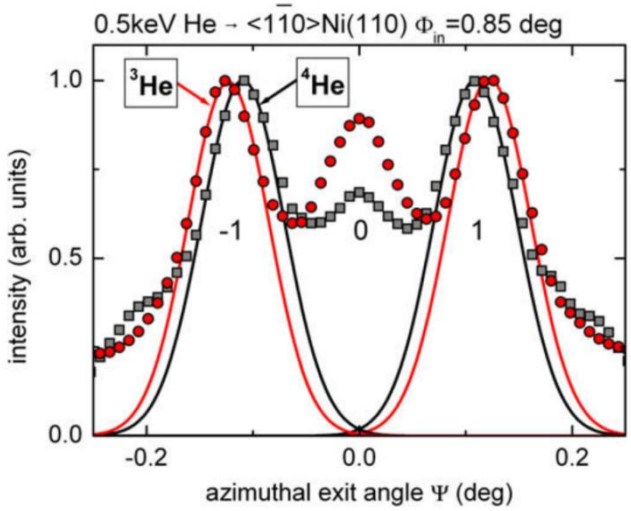

Figure 6.16 Projected intensities as a function of azimuthal exit angleΨ for scattering of 500 eV ^{3}He (circles) and ^{4}He (squares) under θ_{in}=0.85°from Ni(110) along <1$\bar{1}$0>. Solid curves: Gaussian peaks as guides to the eyes and for accentuation of shift of projected intensities of first diffraction order for both He isotopes [130].

6.4.2 Excitation of bound electrons

Recently, inelastic diffraction phenomenon also has been investigated by H. Winter and his coworker [125] when using H° grazing scattering on insulator LiF(001) surface. On this insulator surface, the large value of the electronic band gap (around 13eV for LiF) largely decreases the probability of electron excitation at low energy and low normal energy. However, at large enough incidence angle exciton population becomes likely and has been studied in details. As detailed in section 3.2, this electronic excitation of the surface corresponds to a quasi-Rydberg state localized on the F^- ions. In the gas phase, negative ions do not have excited states but, on an ionic crystal, the coulomb field of the Li^+ ions (six in the bulk and five at the surface) surrounding the F^- ions produce a so called Madelung field which amounts to ~8 eV at the F^- site [20]. In fact the 12eV work-function can be regarded as the Madelung field plus the ~3.5eV electron affinity of F° free atom. The exciton is a bound state in this Madelung potential well. Its value at the surface is below that of the bulk because the electron wave function can expand to the vacuum. The exciton population was demonstrated in our group [34] and its population mechanism was shown to derive from the same mechanism as the one leading to the formation of H^- negative ions by the Berlin group [49]. The details have been discussed in chapter 4.

Using a pulsed H° beam (the primary H^+ beam is pulsed prior to neutralization) Lienemann et al [125] were able to produce scattering profiles associated with elastic scattering (Figure 6.17 d.) and with exciton population (Figure 6.17 c.). The very broad profile clearly demonstrates that the inelastic processes leading to the exciton population completely destroy the diffraction.

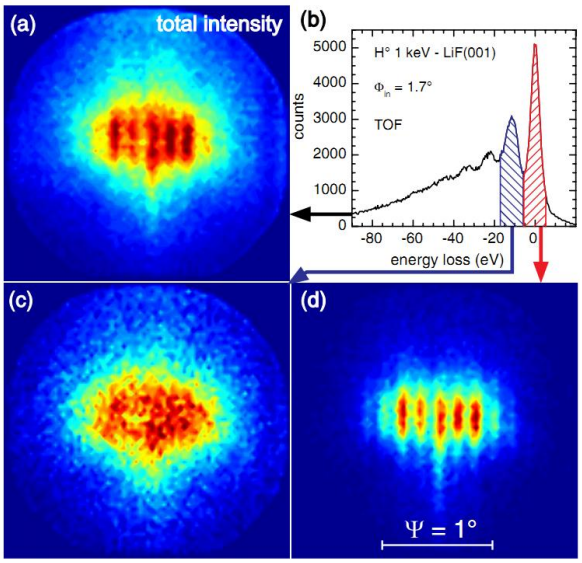

Figure 6.17 For 1 keV H° projectiles at 1.7 deg. incidence on LiF(001) surface [125], the 2D images of scattered H°particle associated to different parts of the energy loss spectrum displayed in (b); a) the entire spectrum, c) the second peaks and d) the first peak i.e. the elastic peak, picture was taken from Ref. [125].

We have confirmed this result at lower energy where the exciton population is less likely but the result is the same; no diffraction can be identified in scattering pattern associated with the inelastic peak (Figure 6.18).

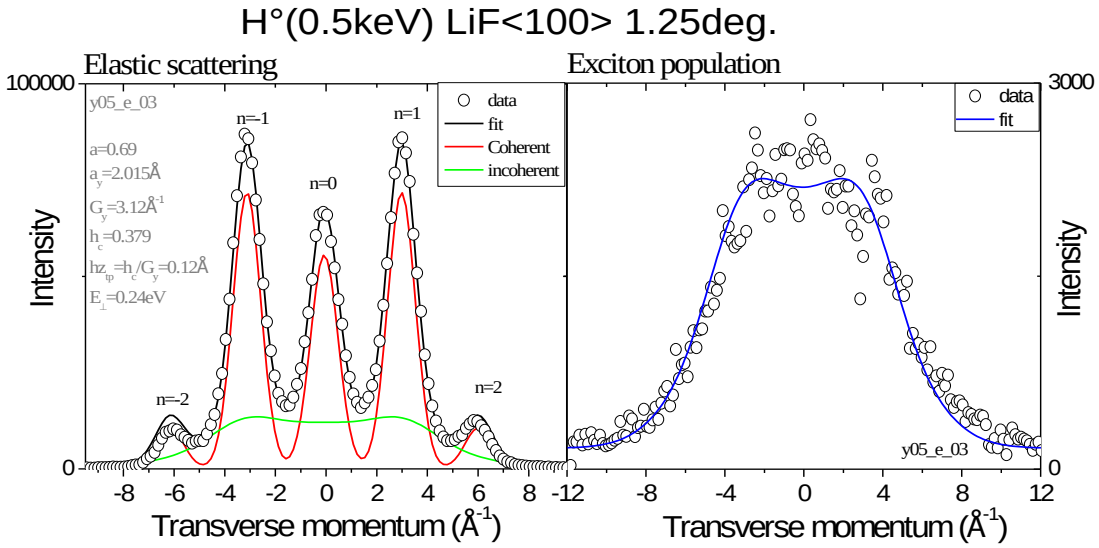

Figure 6.18 Diffraction spectra recorded on a LiF(001) surface aligned along the <100>direction for H° projectile with a normal energy of 240 meV. For the left panel of elastic scattering: the intensity I_n given to each diffraction order is split in two components; a narrow one of intensity I_n.a plus a broad one of intensity (1-a).I_n. The red line is the sum of the narrow peaks and represents the coherent intensity, the green line is the sum of the broad peaks and is an estimate of the background, and the solid dark is total intensity of the fit through the experiment. The ratio "a" thus determined is the effective Debye-Waller factor, here a=0.69. For the right panel: it represents the inelastic scattering intensity; the blue solid line is the fit through data which indicates a zero value (within error bar) for the coherent ratio *a*.

The only point that remains unclear is the role of all the individual processes taking place in the exciton population. The electron attachment (1 in Figure 3.14) and the transfer to the exciton band (2 in Figure 3.14). The electron attachment to the H^- is a well identified Demkov-like electronic transition between individual bound states and could preserve coherence? The second step where the H^- ion loses its electron to the exciton band is not so well defined because the exciton band is rather broad. In other words, the question is still opened as to the detailed contributions leading to decoherence in this inelastic process. In other words, the inelastic process observed here is not as simple as it could so that the question is still opened.

Before analyzing result on inelastic diffraction by H^+ we need to analyze the diffraction results from H°.

To analyze the diffraction intensities, two options are possible. One is independent optimization of the intensity of each peak, providing as many numbers as observed diffraction peaks and then interprets them (or not) separately. Alternately, one can directly adjust the entire spectrum with a model constraining the relative intensities. The second option has the advantage of considerably reducing the number of degrees of freedom but it only makes sense that if the agreement is reasonably good [39]. For the system studied here, H^+ and H° on LiF(001), this latter approach was chosen because a simple cosine potential turned out to be enough to well explain all observed diffraction orders [4, 129, 133]. Along the <100> direction, all the relative intensities of the peaks only depend on one parameter h_{ztp} the trough to peak corrugation amplitudes that describe the shape of the surface "seen" by the particles. The corrugation is rather weak as illustrated by the few diffraction orders observed in spite of a comparatively large normal energy $E_\perp$ (therefore small $\lambda_\perp$).

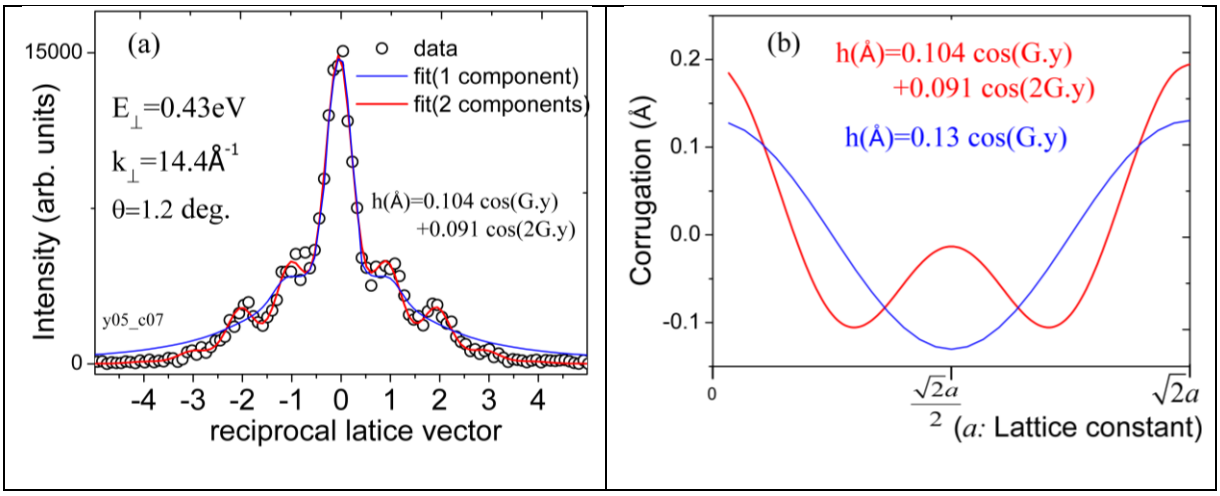

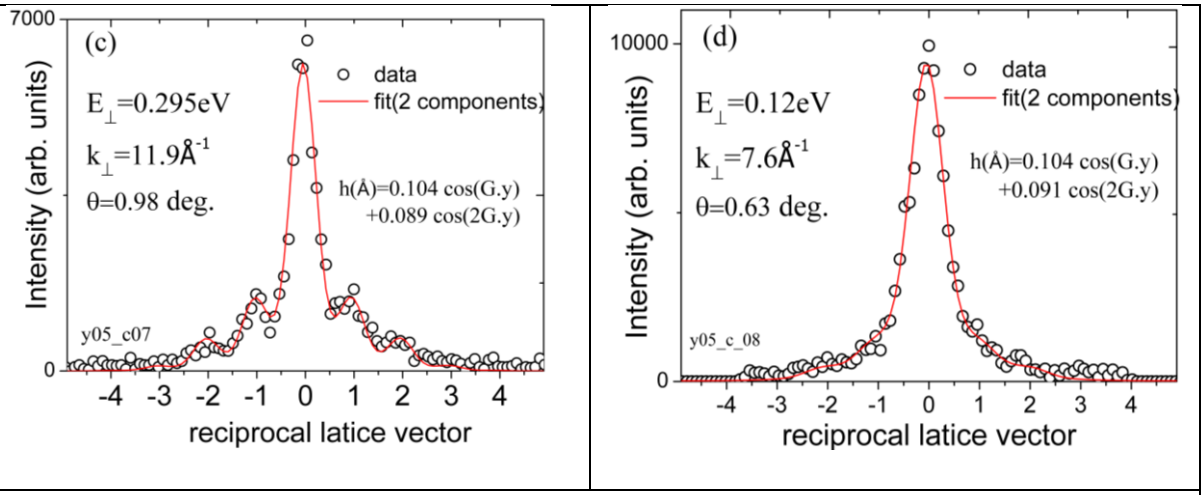

Figure 6.19 Diffraction profiles of 1keV H° along the LiF<110> direction and normal energie of (a) 0.43 eV (c) 0.295 ev and (d) 0.12 eV. The diffraction pattern are compared with two fits using the Hard-Wall model, the blue line is the best fit using a pure cosine function and gives a rather poor agreement whereas the red line describes the surface with an additional harmonic component (two Fourier components). The associated Hard-Wall are depicted in (b) in absolute scale (the distance to the surface is not known.).

Along the <110> direction the fit of the diffraction image by a Hard-wall model including a single cosine function (Eq.(6.15)) is very poor (the blue line in Figure 6.19 (a)). Along this direction, the F and Li atoms form separate rows and a second Fourier component can be introduced to evaluate the Li contribution.

$$Z_t(y) = \frac{1}{2} h_1 \cdot \cos\left(G_{y1}.y_1\right) + \frac{1}{2} h_2 \cdot \cos\left(G_{y2}.y_2\right) \tag{6.24}$$

With this simple modification, the model (red lines in Figure 6.19) fits the experimental results. The Figure 6.19 b displays the shape of the Hard-Wall obtained in the fit and shows a surprisingly large contribution of the second harmonic component. This could be due to a selective attraction of the H° atoms to the Fluorine atoms (ions) or to the polarization by the Li^+ and F^- rows [137].

Interestingly, though the Hard-Wall potential derived has a large corrugation, the importance of high index diffraction orders (large values of m) is very limited as if the two components of the potential cooperate destructively for large m. At 0.12 eV normal energy it seems that only the specular peak is important as if the surface would be a perfect mirror. However, this remains compatible with the same highly corrugated Hard-Wall potential as shown by the red line.

Like He°_LiF(001) system, the corrugation of H° on LiF(001) is larger along the <110> than that of along the <100> direction (note the factor ~1.5 on the scale) but the evolution are opposite, it increases linearly with scattering wave vector normal to surface $k_\perp$ along <100>, but both (h_1, h_2) decrease with increasing vector $k_\perp$ in <110> direction, see Figure 6.20.

The evolution with normal $k_\perp$ brings information on the differential nature of the top and bottom of the valley. If the top of the valley is "harder" than the bottom the corrugation is expected to increase with $k_\perp$. This is the case along the <100> where, as for He projectile, we concluded that inter-row potential is necessarily softer that top of the row potential. In fact the inter-row potential even disappears for normal energies around 10 eV when penetration becomes possible. Along the <110> direction the situation is more difficult to discuss because the shape is now described by two fourrier components which do not show significant evolution within large error bars.

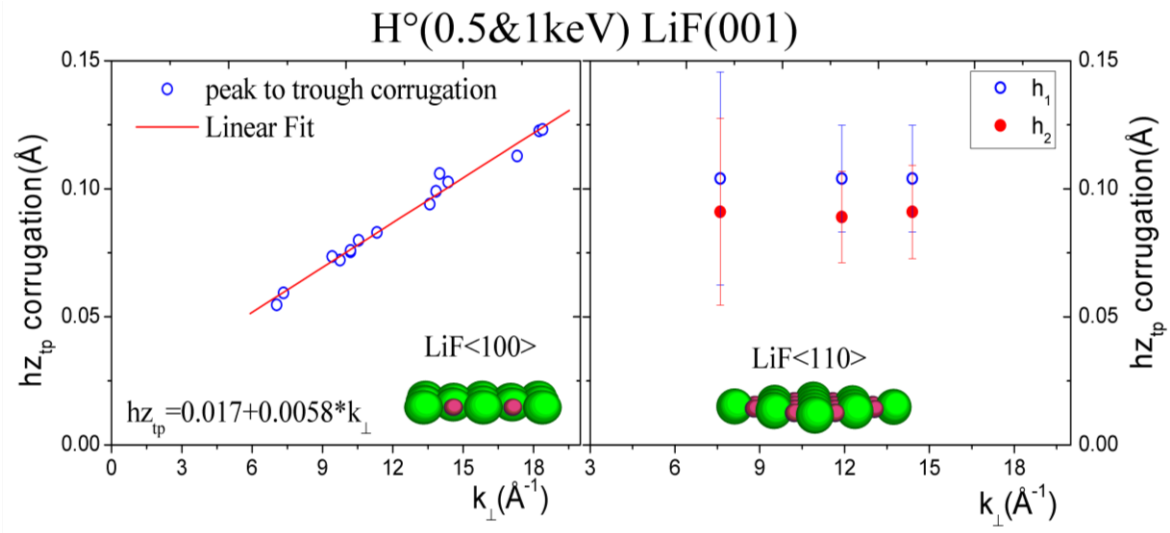

Figure 6.20 Corrugation from trough to peak increases linearly with impact vector normal to surface along LiF surface <100>, but slightly decreases along <110> direction, note that their scales are not the same.

For temperature variation such as the one presented below in Figure 6.21 along the <100> direction, the diffracted intensity is again fitted by a Hard-Wall model but only a=I/I_0 and w_{coh} the width of diffracted peak were left free in analysis of the temperature varitation. In this figure, we see that the coherence factor decreases rapidly with increasing target temperatures. As described in section 6.3, this is understood as due to the increased amplitude of the thermal movement of the surface atoms. In GIFAD, the induced decoherence is drastically reduced due to the fact that the projectile does not scatter on individual atoms but on rows of atoms. These rows of N atoms tend to have an effective amplitude reduced by $N^{1/2}$ as explained in our modified Debye model (Eq.(6.23)). For the experimental results, each point has an effective collision sites corresponding to, a roughly 18 sites has been obtained (blue square in Figure 6.21) by employing modified Debye model. From this model we derive here an effective collisions sites around 16±3 for standard LiF parameter (T_{Debye} = 530K) [4] from the

fit in Figure 6.21. Where, the physical meanings behind of the fitted parameters are explained in Table 6.1.

Table 6.1 Fitted parameters according to Modified Debye model.

In Figure 6.21 : Temperature dependence A_1: coherence scattering amplitude $\alpha = \frac{2k_n^2}{N_{eff}(\theta)} \cdot \frac{3\hbar^2}{M\Theta_D^2 k_B}$	In Figure 6.22 : incident angle dependence A_2: coherence scattering amplitude $\beta = \frac{4mE_0}{N_{eff}(\theta)} \cdot \frac{3\hbar^2 T}{M\Theta_D^2 k_B}$
where: m is the mass of projectile; M is the mass of target; E_0 is the projectile total energy; T is the sample temperature; Θ_D is surface Debye temperature (530K was taken for LiF(001) surface, which is $1/\sqrt{2}$ times the bulk; k_B is Boltzmann constant. For the both collision sites illustrated in the two figures, it has taken into account the Beeby factor.	

Taking into account the Beeby factor or the well depth of the atom-surface interaction potential 17.8 meV for H° on LiF(001) surface [138], the effective number collision sites increase to 18±3, see Figure 6.21.

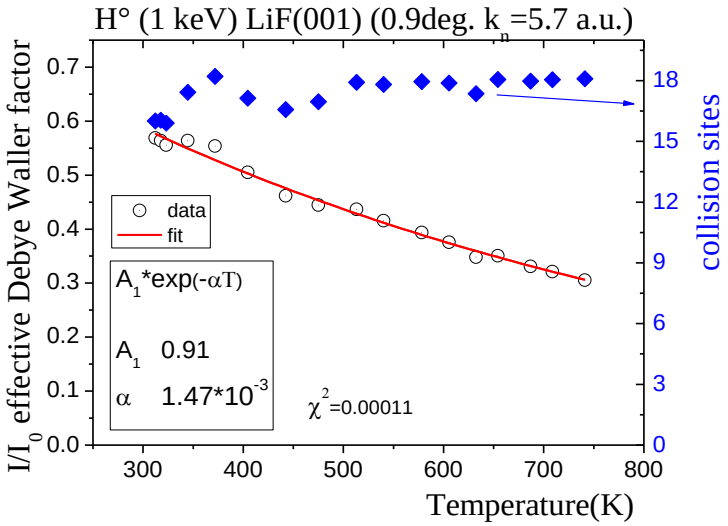

Figure 6.21 Temperature dependence of the coherence factor (empty circle is the experimental data, and red line is the fit by the given formula), and blue square represents number of collision sites estimated from each data point.

Table 6.1 Fitted parameters according to Modified Debye model.

In Figure 6.21 : Temperature dependence A_1: coherence scattering amplitude $\alpha = \frac{2k_n^2}{N_{eff}(\theta)} \cdot \frac{3\hbar^2}{M\Theta_D^2 k_B}$	In Figure 6.22 : incident angle dependence A_2: coherence scattering amplitude $\beta = \frac{4mE_0}{N_{eff}(\theta)} \cdot \frac{3\hbar^2 T}{M\Theta_D^2 k_B}$

where: m is the mass of projectile; M is the mass of target; E_0 is the projectile total energy; T is the sample temperature; Θ_D is surface Debye temperature (530K was taken for LiF(001) surface, which is $1/\sqrt{2}$ times the bulk; k_B is Boltzmann constant. For the both collision sites illustrated in the two figures, it has taken into account the Beeby factor.

The evolution of decoherence with the angle of incidence has also been analyzed for H° atoms on LiF(001) surface aligned along the <100> direction. The evolution 'a'=I/I_0 is displayed in Figure 6.22, as well as fit by the expected $\exp(-\beta\theta^3)$ dependence explained in section 6.3.2. With this model, only N_{eff} is unknown but expected to a scale as $1/\theta$, so taking 1° as a reference for impact of 1keV H° on LiF<100> surface at room temperature we find: $N_{eff}(1°)=20.0\pm2.1$ (see Table 6.1). For comparison with temperature variation detailed in Figure 6.21, we evaluate the value at incident angle 0.9°, which is $N_{eff}(0.9°)=22.3\pm2.1$, and taking into account the Beeby factor, this value increases to 24.5 ± 2.1, we can see that these two values are comparable with the effective collisional sites deduced by diffraction temperature dependence (in Figure 6.21).

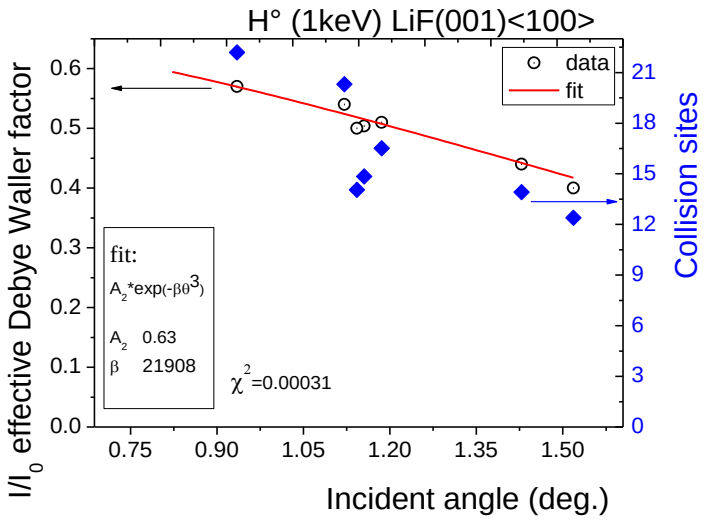

Figure 6.22 Incidence angle dependence of coherence diffraction factor for H° impact on LiF(001) surface at room temperature (300K).

From the result presented in Figure 6.22 diffraction intensity decreases rapidly as the incidence angle increases. The maximum diffracted intensity, it is only around 0.63 (value of prefactor in the fit formula) which much smaller than that of He° scattering on LiF(001) surface 0.9 reported in reference [129, 139]. This is probably due to the contribution of inelastic processes already important at 1 keV for H° whereas these are still limited for helium.

6.5 Diffraction of fast protons

In section 6.3&6.4, we have analyzed the known decoherence sources. On metals, our group have observed clear diffraction signal in spite of evidence that electron excitation is taking place [17] close to the Fermi edge. For He° atoms scattered on Ag diffraction is clearly observe until 1keV energy and become almost impossible to distinguish above this energy (may be for incidence below 0.4°). However, Lienemann *et al* [125] have shown that diffraction is completely lost when a LiF surface exciton is created (Figure 6.17), suggesting that localized electronic transition lead to complete decoherence.

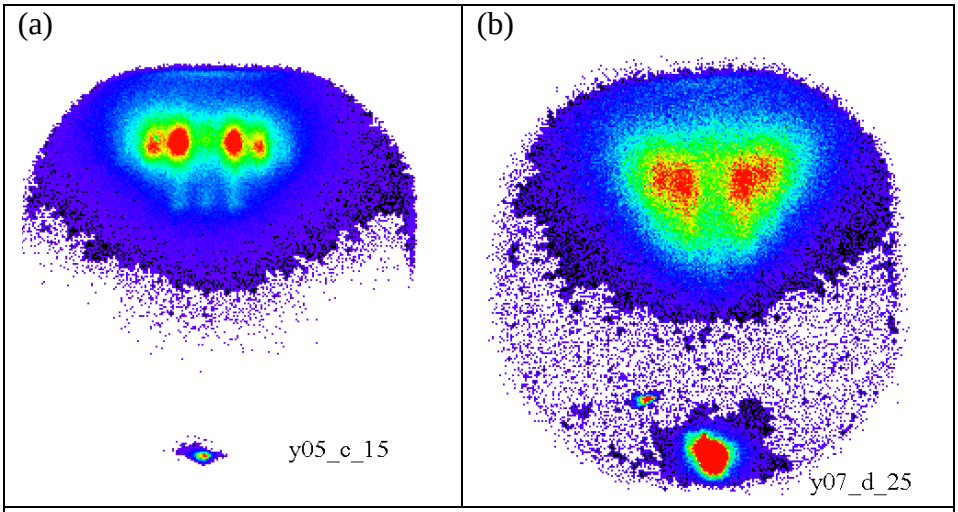

Figure 6.23 Two dimension (total) scatteringbeam profile along <100> orientation of LiF(001) surface. (a) H°(1keV) scattering on LiF(001) surface with 1.5degree incident angle; (b) H^+ (1keV) scattered on LiF(001) surface with 1degree incident angle (total spectrum intensity).

Until now, it seems that inelastic collision process can efficiently suppress surface diffraction. However, surprising results have been observed by proton grazing scattering on LiF(001) surface, see Figure 6.23(b), indicating that, diffraction features still can be observed whereas at least one electron has been extracted from deep valence band via proton neutralization. Note that the apparently much larger beam profile in Figure 6.23(b) is due to saturation of the color scale.

Furthermore, in order to analyze proton diffraction, the scattered 2D beam profile can be split in several components according to the energy loss spectrum which reveals different collision processes, see Figure 6.24. As already observed by several authors [4, 34, 116, 136, 139, 140], the energy loss spectrum shows several peaks very similar to those observed with incident H° particles. The only difference is that all peaks are shifted to higher energy loss. In particular, the first peaks cannot be ascribed to elastic scattering because it correspond to the quasi resonant electron capture by the incident proton. The clear shift of few eV to larger energy loss is interpreted as due to the energy loss by creation of optical phonons (Figure 3.13)

during the way in of the trajectory. Selecting this first peak in the energy loss, the 2D images the scattering profiles below show clear modulation suggesting that diffraction is present (see Figure 6.24 (a) and Figure 6.26 (a)).

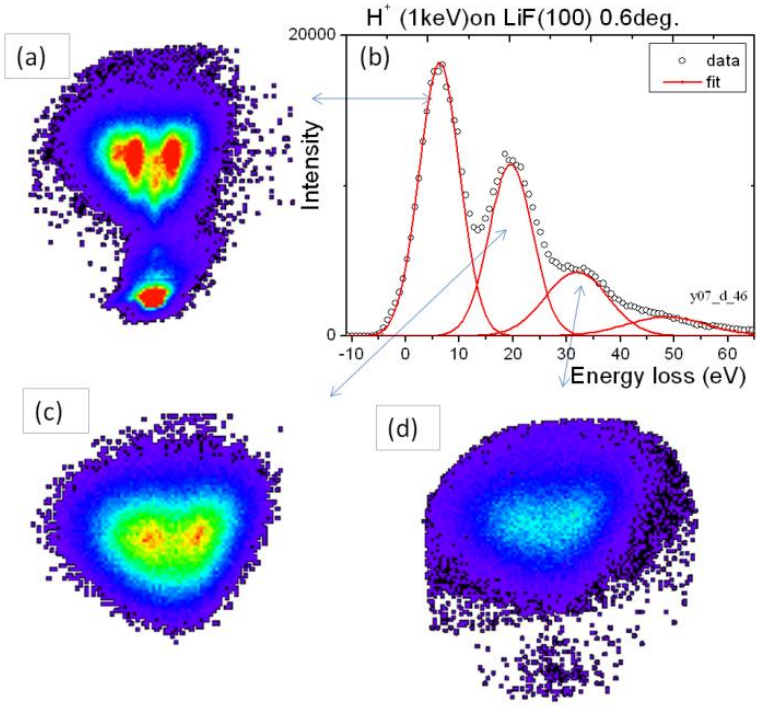

Figure 6.24 Angular distributions recorded with position sensitive detector and energy loss spectrum via TOF for scattering of 1keV H^+ ions from LiF(001) under θ_{in}=0.6deg. along LiF<100>orientation. (a) 2D scattering intensity of outgoing H° associated to only neutralization on LiF surface; (b) energy loss spectrum, (c) intensity coincident with energy loss around 20eV; (d) intensity coincident with energy loss around 35eV. (a=0.13)

As a positive ion flies over an ionic crystal, it attracts the halogen ions and repels the alkali (Figure 3.24 and Figure 6.25) by coulomb potential and creates optical phonon on the LiF surface (as been discussed in section 3.5). This corresponds to the imaginary part of the dielectric constant, whereas the real part corresponds to polarization giving rise to image charge and acceleration of the ion towards the surface. Thus, the trajectory of proton is different than that of H°, it is modified and the equivalent normal energy is increased by this image charge energy gain.

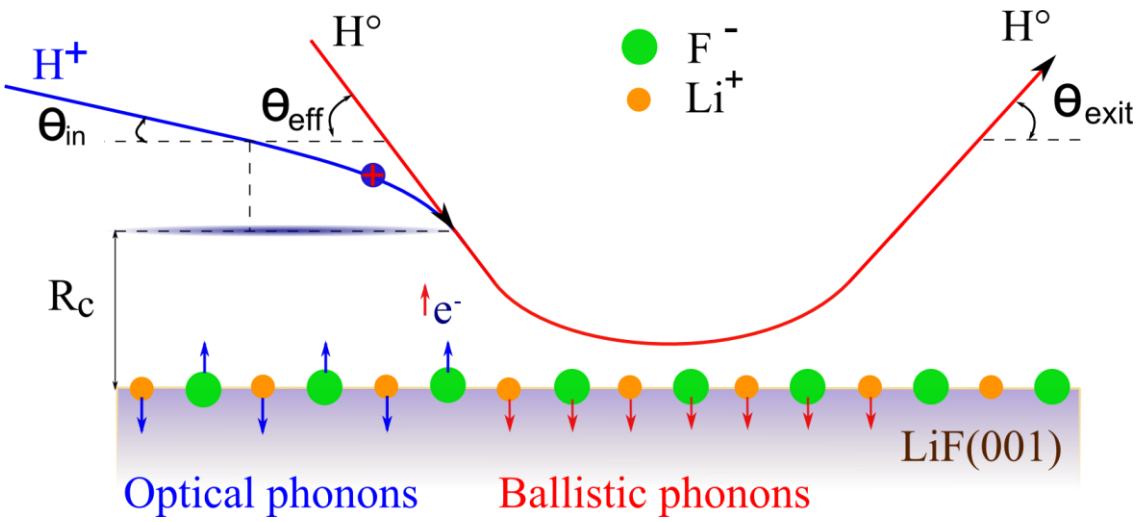

Figure 6.25 Exaggerated schematic of proton and H° grazing scattering trajectory on LiF(001) surface (for the specular reflex, $\theta_{eff}=\theta_{exit}$, R_c represents the distance of first electron capture).

The first electron capture from the F(2p) valence band when proton grazing scattering on LiF(001) surface will take place at rather large distance (R_c~10a.u. see Figure 6.25) [49]. Electronic level of projectile will be shifted in front of surface by its image charge, the detail has been discussed in Chapter 4. The electron reservoir of LiF surface located below its large band gap, 13eV below vacuum level. This value is close to ionization level of H° which is 13.6eV. Thus, the energy defect is rather weak. Thus, proton resonant neutralization probability is very high. As already observed [34, 135] no proton survives the interaction with the surface and mainly atomic hydrogen is detected together with a weak fraction of H^- negative ions [44]. This is comparable to the situation of H° scattering on LiF surface (Chapter 5), no charge state effect has been observed for energy higher than 1keV [44, 141], proton and H° lose it initial charge state "*memory*" during the scattering process, the further collision behavior is that of an incident H°.

Since the incoming protons efficiently captures an electron from the F(2p) valence band before collision with surface atom, the subsequent collision process with surface atom is the same as that of hydrogen neutral (Figure 6.25). Coincident measurement between the secondary electrons and the charge state of the scattered projectiles demonstrates the role of the H^- ions formed on the surface as precursors for electron emission and exciton population [34], and form atomic hydrogen may undergo cycles of electron capture and loss, see Figure 6.26(c) and Figure 6.24(b). The cycles energy loss mechanism on LiF surface has been well analyzed by several authors [34, 125, 142], it shows several peaks separated byΔE~15 eV corresponding to the removal of successive electrons from the valence band. Our attention will only focus on the first peak of the energy loss spectrum and its scattering profile. Since the corresponding protons have only captured one electron and not participated to the population of excitons.

The most interesting aspect is the diffraction itself, because this was not expected in this inelastic context. What can we measure and what can we understand?

The Figure 6.26 displays the intensity plot which demonstrates that the observed structures are located at the Bragg peak positions (the same as that observed for incident H°). We have applied exactly the same fitting procedure to these data in order to evaluate the coherence of the signal by separating a background from diffracted signal.

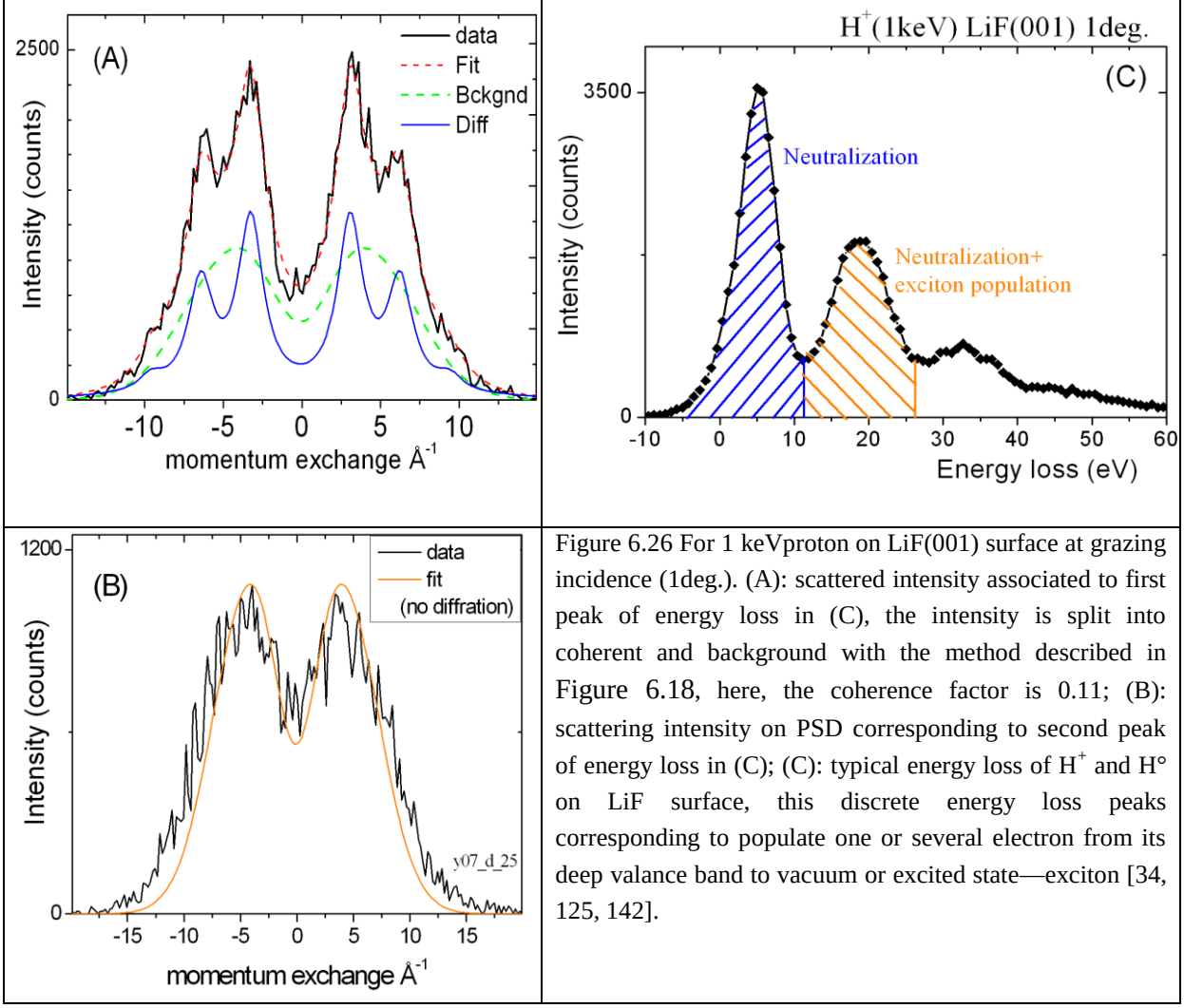

Figure 6.26 For 1 keVproton on LiF(001) surface at grazing incidence (1deg.). (A): scattered intensity associated to first peak of energy loss in (C), the intensity is split into coherent and background with the method described in Figure 6.18, here, the coherence factor is 0.11; (B): scattering intensity on PSD corresponding to second peak of energy loss in (C); (C): typical energy loss of H^+ and H° on LiF surface, this discrete energy loss peaks corresponding to populate one or several electron from its deep valance band to vacuum or excited state—exciton [34, 125, 142].

Only three parameters are left free; the width of the diffraction peaks, the trough to peak corrugation and the ratio a between the diffraction peaks and the background. Since these three parameters obviously act on different aspect of the spectrum, the fitting procedure is very robust. The results indicate a width of the peaks which is larger than that observed with incident H°. The coherence ratio is also comparatively larger and the h_{ztp} is much larger than the one observed for incident H° in the same condition.

As we have demonstrated in section 6.3.3 for H° projectiles, a single parameter is enough to fit the diffraction data by a Hard-Wall based on single harmonic cosine potential. This

parameter h_{ztp}, the trough to peak corrugation amplitude is defined as $Z_t(Y) = \frac{1}{2} h_{ztp} \cdot \cos(G_y \cdot y)$ and allows tracking of small detail evolutions.

The Figure 6.24(a) and Figure 6.26 (a) display the intensity profile along the Laue circle, and the distinct feature at Bragg positions corresponding here to multiple by 3.12Å^{-1} (reciprocal vector G). Such features are lost when the energy loss associated to exciton population or electron emission in the second peak in the energy loss. For each scattered particle with different exit and azimuthal angles, the energy loss spectrum displays well resolved structure already attributed to the excitation of surface excitons (Figure 6.26 (c) and Figure 6.24 (b)). Alternately, diffraction diagram can be selected according to the energy loss in order to separate particles associated or not with exciton population. As already shown by the work of Lienemann [125], the population of one or two excitons produces a broad profile. At variance, the particles associated only with quasi elastic electron capture display structure sitting at Bragg conditions suggesting that diffraction is still present.

We analyze here this simple model where electron capture and diffraction would be completely separated. Before electron capture, the coulomb interaction couples the ionic projectile H^+ with the surface. As detailed in Chapter 3, this interaction has two consequences associated respectively with the real and imaginary part of the LiF dielectric constant ε(ω).

The real part of ε(ω)describes the frequency dependent polarization of LiF and gives rise to the image charge attraction $V_{im} = \frac{1-\varepsilon(0)}{1+\varepsilon(0)} \frac{q^2}{4Z}$. The imaginary part describes the absorption by the media i.e. the energy transfer to the LiF crystal and is dominated here by the coupling to the optical phonons.

Within the present model, we suppose that the image charge energy gain ΔE is acquired before diffraction so that the effective momentum of the H° atom is $k_\perp=(E_0\sin^2(\theta)+E_{im})^{1/2}$. Reversely, the effective momentum of the H° product can be measured from the linear relation (plotted in Figure 6.20 and Figure 6.29) between the observed h_{tp} and k_p: $h_{tp}= 0.017 + 0.0058*k_\perp$(Å^{-1}) or $k_\perp= (h_{tp}-0.017)/0.0058$ (Å^{-1}) . The observed value of h_{tp}=0.1 Å points to a H° momentum of $k_\perp$=15 Å^{-1}. By comparison with the initial momentum $E_0\sin^2(\theta)$ the image charge measured here via the diffraction profile is E_{im}=0.45±0.1eV (plotted in Figure 6.28).

This value is also measured via the scattering profile as detailed in section 3.4 and in Figure 3.23.

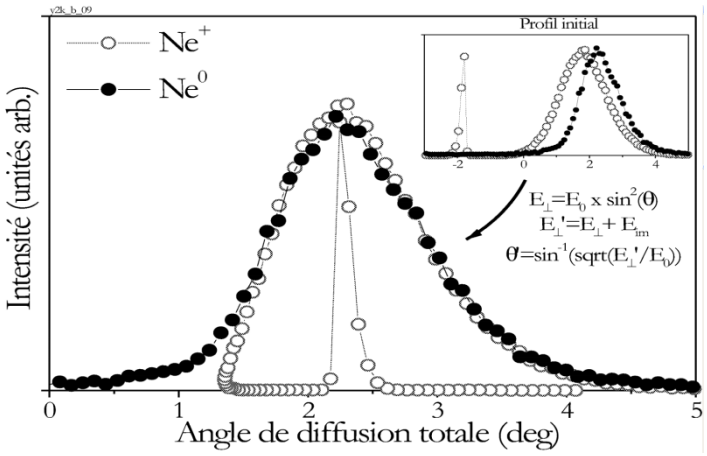

Figure 6.27 For Neon projectile where both Ne° and Ne^+ products are present, the image charge energy can be evaluated accurately by defining an effective angle such that $E'_{\perp}=E_0\sin^2\theta+E_{im}$.

However, the scattering profile is comparatively broad reducing the accuracy of this determination. The evaluation of the image charge energy is shown on Figure 6.28 for different angles of incidence.

In fact, there is another way to measure the image charge acceleration of ion grazing scattering on insulator surface. With the same experiment condition, using neutral beam scattering as a reference, the difference in scattering angle measured with incident charged particle corresponds to the energy gain due to image charge acceleration. This method was successfully applied by the group of H. Winter in 1995 to measuring image charge acceleration of multicharged Xe^{q+} ion in front of LiF(100) surface [49].

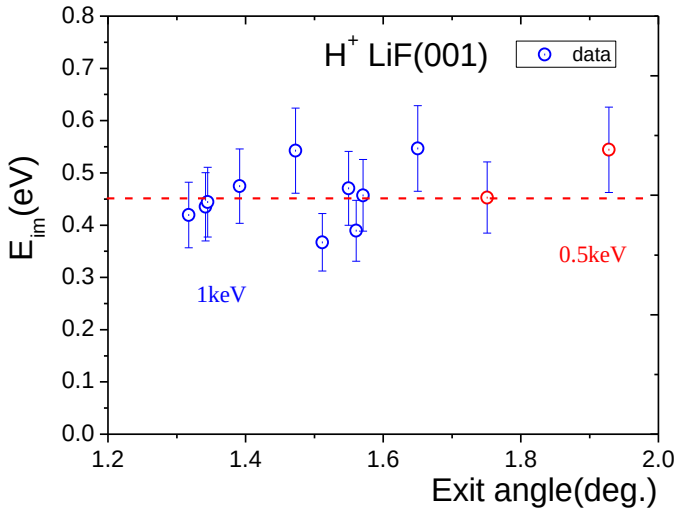

Figure 6.28 Energy gain due to image charge acceleration when proton with 1keV (blue circle) and 0.5keV (red circle) grazing incidence on LiF(001) surface, dash line is guide to eyes only.

This image energy can be converted in a measure of the distance to the surface where electron capture occurs. From this a capture distance of 10 a.u. is deduced. Such a distance is much

larger than the turning point of the trajectory which is close to 3~4a.u. (in the case of He_LiF(001) system). Since the potential is exponential, the momentum transfer to/from the surface at the point of electron capture is around $\exp(-\Gamma.Z_c/Z_t)$ times smaller than the momentum transfer taking place close to the turning point (where Ñ site participate). This is consistent with the initial assumption that the trajectory can be split in two parts.

The energy loss to optical phonons accumulated along this first part of the trajectory can be estimated from [40, 73, 143].

$$S(Z) = \frac{2q^2}{\pi v_{//}^2} \int_0^{\infty} \omega d\omega K_0\left(\frac{2\omega Z}{v_{//}}\right) \mathrm{Im}\left(\frac{1-\varepsilon(\omega)}{1+\varepsilon(\omega)}\right) \tag{6.25}$$

Numerical integration of along the ionic trajectory from –infinite to Z_c=10a.u. at $v_{//}$= 0.1a.u. gives an estimated energy loss to phonons of 7.8eV [49]. This could be compared with the energy loss of 6±2eV (absolute uncertainty) measured by energy loss but it is not yet clear from what part of the valence band (top middle or bottom) are the electrons captured. In addition, the formula Eq.(6.25) has not be fully validated on a quantitative level.

Since proton at grazing incidence on LiF(001) surface is going out as neutral, the subsequent collision process with surface atom is exactly the same as that of neutral hydrogen. Both H° and H^+ see the same corrugation along <100>orientation of LiF(001) surface.

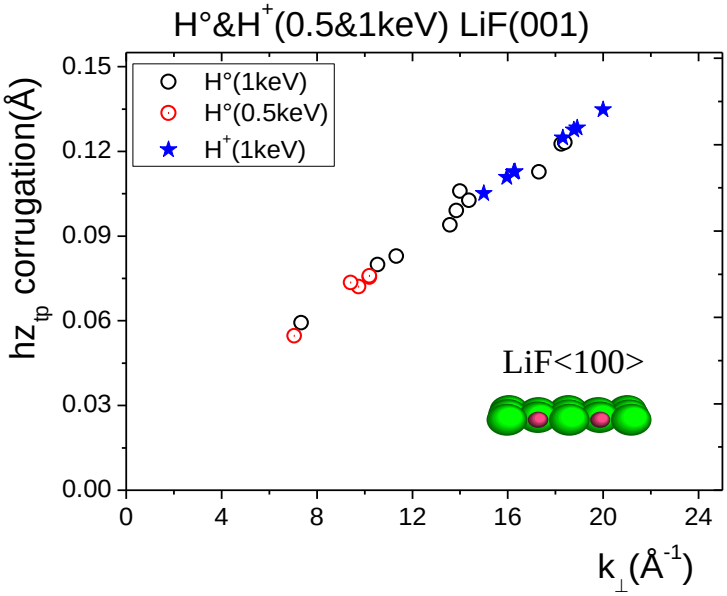

Figure 6.29 Corrugation from trough to peak increases linearly with impact vector of H° and H^+ normal to surface along LiF(001) surface <100>direction, the circle is for H°, but red circle is 500eV, blue star is for 1keV of proton. (note that this figure is the same as Figure 6.20 plotted above for H° scattering)

Assuming that the image energy remains constant at 0.45eV, the effective impact energy on the surface can be recovered as $E_{eff} = E_0.\sin(\theta_{in})^2 + E_{im}$. With this correction, the apparent

corrugation of all the diffraction images corresponding to 500eV and 1keV energies and different angles of incidence nicely align along the data corresponding to incident H°.

Considering the image charge acceleration, the wavenumber of proton normal to the surface has been modified. Thus, according to the statement above—corrugation increasing linearly with scattering vector normal to surface along <100> direction, the subsequent collision process of proton with surface atom is exact the same as that of hydrogen neutral after neutralization, the outgoing of scattering vector can be deciphered (Figure 6.29). Surprisingly, the outgoing wavenumber also has the linear relationship with corrugation along<100> of LiF surface (Figure 6.29), for the calculation detail, please see Appendix-C.

The increased apparent corrugation is then explained as due to the image charge energy gain before diffraction. What about coherence?

The Figure 6.29 below reports the observed coherence for incident H^+ and H° plotted as a function of the apparent $k_\perp$, i.e. taking into account the image charge acceleration. The coherence is clearly reduced by a factor ~2.5.

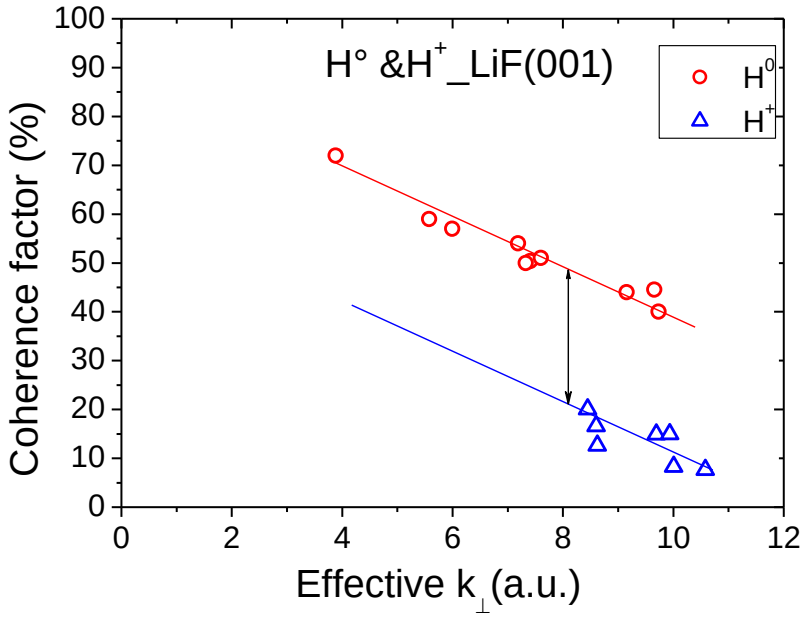

Figure 6.30 Comparison of proton and H° diffraction on LiF(001) surface in grazing incidence.

The advantage of this procedure is that the whole diffraction spectrum can be fitted by one to three parameter (h_{ztp}, a and w_{coh}). This allows a very simple data reduction as depicted in Figure 6.20 above where the through to peak evolution was plotted as a function of H° normal energy. Of course, the Hard-wall model may be quantitatively incorrect but the data reduction certainly remains valid because it is supported by quality of the fit (as shown in Figure 6.26 (a)). In other words, at minimum, the hard-wall model can be used as a convenient way to describe the data even is the actual corrugation, as derived from full quantum approach is

probably different. In his thesis, Schüller [37] suggest a difference on the order of 25% for the corrugation amplitude between a Hard-Wall approach and more complex calculation.

7 Conclusion

In this thesis, we have experimentally analyzed the interaction of hydrogen with energy from several hundred eV to few keV scattering on surfaces under grazing incidence: H^- formation on HOPG from H° and H^+ diffraction on a LiF(001) surface. Both experiments were performed in the same experimental setup (Figure 1.2 and 2.1)—with grazing scattering geometry and a PSD located downstream to record scattered particles. For charge state analysis a set of electrostatic plates is inserted between sample and PSD. During the experiment, coincident measurement technique is used to identify the energy loss associated to 0, 1, 2…electrons emission.

Clear evidence of diffraction with inelastic scattering by proton on LiF(001) has been obtained, which has not been observed before. Indeed, the group of H. Winter [125] reported that no diffraction exists with inelastic scattering of H° on LiF(001). However, according to our result, a coherence scattering factor still exists even though the electron capture by the proton is an inelastic process.

In the case of pure elastic collision region, the trajectory length has been calculated [32] within a classical binary model for the energy/momentum transfer. Atom-surface Molière potential was used to model the projectile surface atoms interaction. A simple formula has been obtained to estimate the number of collision sites $N=6/(\Gamma a \theta)$, where Γ is the stiffness (inverse of the range or characteristic attenuation distance R_o, $\Gamma=1/R_o$) of the potential parameter which depends on collision partners, a is the lattice constant and θ is the incidence angle.

For proton diffraction, image charge acceleration plays a very important role by modifying the normal scattering vector. Since the GIFAD diffraction pattern is very sensitive to the normal scattering vector, this has been used to measure the image charge acceleration for proton scattering on LiF(001): E_{im} = 0.45±0.05eV.

For the shape of surface potential, a single harmonic $Z_t(Y) = \frac{1}{2} h_{ztp} \cdot \cos(G_y \cdot y)$ function is adequate to reproduce the data along the <100> direction parameter within a Hard-Wall model. In other words, the diffracted intensities are well reproduced by Bessel functions. As a result a single parameter, the corrugation amplitude h_{ztp}, expressed in atomic units (a_0) or in angstroms is needed to represent the data and to track the small evolutions. This corrugation amplitude increases with the angle of incidence. This is explained by the fact that there is no

atom sitting in between the rows of alternating F and Li atoms. As the energy increases, the depth of the valley increases faster that the height of the top is diminishing, resulting in an enhanced corrugation. Along the <110> direction the fit of the diffraction images by a Hard-wall model using a single cosine function (Eq.6.15) is very poor and a second harmonic component has been added. The fit reveals a very strong contribution of the Li rows. Indeed, along <110> direction, the potential "seen" by H° has well separated contribution from F and Li atoms independently. It is likely that an attraction to the fluorine rows leads to smaller ionic radius than for helium projectiles where this effect is not observed. For Helium even along the 100 direction, a single cosine is enough to represent the data with Hard-Wall model allowing data reduction to a simple corrugation parameter. Along this direction the corrugation amplitude decreases with the normal energy. In this case, the valley corresponds to row of Li atoms (ions). These Li^+ ions are smaller than F^- but also harder ($1s^2$) than F^- ions. Thus, the top of the valley is "softer" than the bottom and the difference between these values i.e. the corrugation will decrease with $k_\perp$ along the <110>. The fact that diffraction is also observed in the inelastic regime of electron capture is interpreted as a two-step process; first the ion interacts with optical phonons until it reaches ~10 a.u. distance where electron capture takes place. Then the so formed H° atom diffract on the surface. In this respect, all the decoherence processes that have taken place before diffraction are simply interpreted as dispersion of the initial conditions just as beam broadening does.

For negative ion formation from HOPG, we report here the highest fraction of H^- (~10%) measured in grazing scattering experiments on a surface that is covered by alkali atoms; it is larger than those obtained on ionic insulators, the latter being typically 10 times larger than those measured on clean metals [144-148]. These results confirm the high yields of negative hydrogen ions from graphite reported in the literature. The negative ion fraction is affected by both parallel and perpendicular velocities. For the perpendicular velocity effect, negative ion fraction increase linearly with impacting normal energy ($v_{//}$ was fixed) in our energy range (Figure 5.3); in terms of parallel velocity dependence, we observe a maximum negative ion fraction around 0.35 a.u. (3 keV), which compares very well with observations made on LiF(001). The final H^- fraction results from a competition from electron capture to the affinity level and electron loss to the surface empty states or to vacuum. At low impact energy, formation probability increases rapidly above a threshold near 0.1 a.u., while at higher energy survival of the negative ion traveling at large speeds nearly parallel to the surface declines as the collisions become more "violent" [82]. By comparing negative ion fractions measured either with atoms or ion impinging on the HOPG, we conclude that there is a total loss of memory on the initial charge state; the deviation observed at very low normal energies is due to the image charge effect. These independence on the incident charge state leads to the conclusion that simultaneous double electron capture (one-step formation of H^- by H^+ projectiles) if present is a very weak process.

Finally, these general properties (yield, velocity effect) of the negative ion production of HOPG resembles very much those reported on LiF(001); this was surprising in view of the electronic properties of graphite.

A finer analysis of the coincidence data yields subtle information on the capture mechanism:

I. The main feature of the energy loss (H^+ 0.5keV) distribution measured with H^+-HOPG appears similar to that typically observed on metals, namely a skewed gaussian peak located near 60 eV with a straggling of 40 eV. However, weak structures are visible on the low energy loss side of the spectrum. These structures are very similar to those observed on ionic insulators where cycles of capture and loss have been identified.

II. For total electron emission, the measured yield is very comparable to those measured on LiF(001) and therefore much larger than that measured on metals.

III. Correlation between the energy loss of the scattered particle and the energy distribution of the emitted electrons clearly points to two distinct electron emission mechanisms.

Quantitative analysis of the low energy loss structures yields a binding energy around 10.5 eV for the electrons involved in the capture process.

Previous theoretical studies have shown that electron transfer form a surface to levels of an atomic close to the surface takes place predominantly in the direction normal to the surface. For this reason, this process is very sensitive to features in projected band structure. According to photoemission studies of HOPG, the band structure at the Γ point (Brillouin zone) is such that:

- the least bound electrons correspond to the σ band at binding energy close to 5 eV below the Fermi level, i.e. close to 10 eV with respect to vacuum level, the π band lies nearly 2 eV below the σ band

- a band gap of nearly 9 eV is observed

On the basis of all these elements, a scenario can be drawn in which electron transfer to the affinity level, taking place with highest probability along the Γ direction on the Brillouin zone, involve mainly localized σ electrons at 10 eV below vacuum. Following this capture process, subsequent loss (also more favorable along Γ) is suppressed due to the projected band gap. Then this σ band is responsible for negative ion formation and so contributes substantially to electron emission. The metal-like energy loss, due to excitation of electrons close to the Fermi level, rather involves the delocalized π electrons.

To complete this scenario that tends to describe HOPG as insulator from the point of view of negative ion formation, we still need to demonstrate that holes created in the σ band remain

localized during the time of the interaction, as it is for e.g. LiF(001). Such a result can only derive from theoretical calculations.

Obviously, more data are needed for a more complete description of the negative ion formation on HOPG. Based on the data analysis, some prospects are proposed for a future work:

1) Carry a more careful measurement of the total energy dependence of the negative ion fraction, keeping the normal energy constant; this would yield a much better insight into the parallel velocity effect.

2) Coincidence data acquired in the experiment suggested above should also yield valuable information on the Demkov electron transfer probability and therefore may provide additional hints on the projected electronic structure of HOPG.

3) Re-study the negative ion fraction and electron emission with different surface orientation. Since a factor of 2 in the electron yield is observed when comparing the results for differently oriented HOPG surfaces [149], i.e. sample surface parallel or perpendicular to the graphitic planes, what about the negative ion fractions, and the π and σ-electron emission?

And for the proton inelastic diffraction:

4) Try to isolate the contribution of the optical phonons to decoherence by varying the angle of incidence. This would affect the ion trajectory prior to electron capture.

Appendix A: Kinetic energy loss binary collision—small angle approximation

During the atoms/ions grazing incidence scattering on surface, usually, the collision between projectile and surface atoms can be treated as consecutive binary collision. However, the kinetic energy loss of elastic binary collision, it strongly depends on the scattering angle ɵ, the energy loss can be calculated by the formula (3.33).

$$\Delta E = E_2 = E_0[1-\frac{1}{(1+\mu)^2}(\sqrt{1-\mu^2\sin^2\theta}+\mu\cos\theta)^2] \tag{7.1}$$

where μ is the mass ration, the mass of projectile M_1 divided by the mass of surface atoms M_2. According to the geometry of grazing scattering, each scattering angle is θ <<1 deg in our case. so the formula (7.1) in Taylor series:

$$(1+x)^\alpha = \sum_{n=0}^{\infty}\binom{\alpha}{n}x^n = 1+\alpha x+\frac{\alpha(\alpha-1)}{2}x^2+\ldots+\frac{\alpha(\alpha-1)\ldots(\alpha-n+1)}{n!}x^n \tag{7.2}$$

For all |x|<1 and all α.

So for any angle we have $\sin\theta = \theta-\frac{\theta^3}{3!}+\frac{\theta^5}{5!}-\cdots$, and $\cos\theta = 1-\frac{\theta^2}{2!}+\frac{\theta^4}{4!}-\ldots$, when ɵ<<1°, taking the first level Taylor is enough for the approximation. Base on the Taylor series, so the energy loss formula(7.1):

$$\Delta E = E_0[1-\frac{1}{(1+\mu)^2}(\sqrt{1-\mu^2\theta^2}+\mu(1-\frac{\theta^2}{2})]^2 \tag{7.3}$$

Here we just take the second approximation, so we have:

$$\begin{aligned}\Delta E &= E_0[1-\frac{1}{(1+\mu)^2}((1-\frac{1}{2}\mu^2\theta^2)+\mu(1-\frac{\theta^2}{2}))^2] \\ &= E_0[1-\frac{1}{(1+\mu)^2}((1+\mu)-\frac{1}{2}\mu\theta^2(\mu+1))^2] \\ &= E_0[1-\frac{1}{(1+\mu)^2}(1+\mu)^2(1-\frac{1}{2}\mu\theta^2)^2] \\ &= E_0\mu\theta^2\end{aligned}$$

Here we only consider the first and second levels of Taylor approximation, because the third or the fourth are several order of magnitude smaller than the second in case of θ<<1°. Therefore, the kinetic energy loss of binary collision at very small scattering angle can be expressed:

$$\Delta E = E_0\mu\theta^2 \tag{7.4}$$

Appendix B Screening functions of atom-atom potential

The following three pages describe various screening functions which are listed for sake of clarity and historical importance. The most used screening function is based on the Thomas—Fermi (TF) description, which treats all atoms as identical aside from scaling factors [31]. The TF-approximation permits a simple estimation of the charge density of a multi-electron system. In this model, electrons of the atom are treated by Fermi-Dirac statistics. They behave as an ideal gas of particle energy E that fills the potential well around the positively charged core up to the Fermi level. From the charge density at the distance r to the atomic nucleus the potential of a point charge results in the case of r too:

$$V(r) = \frac{-Ze^2}{r} f(\frac{r}{a_{TF}}) \tag{7.5}$$

where a_{TF} is Thomas—Fermi screening length and given by

$$a_{TF} = \frac{1}{2}(\frac{3\pi}{4})^{3/2} \frac{\hbar^2}{m_e e^2 Z^{1/3}} = 0.8853 \frac{a_0}{Z^{1/3}} \tag{7.6}$$

where $a_0 = \hbar^2 / m_e e^2$ is the Bohr radius, and the screening function f (r/a_{TF} = x)'s differential equation is obtained as:

$$f''(x) = f(x)^{3/2} / \sqrt{x} \tag{7.7}$$

The screening function is often approximated by a series of exponentials. The one often used was given by Molière which is in the form of three exponentials:

$$f(x) = 0.35e^{-0.3x} + 0.55e^{-0.2x} + 0.1e^{-6x} \tag{7.8}$$

The Eq. (7.5) and (7.6) were derived by a single atom, thus, the Thomas—Fermi screening length for binary collision should consider the effective charge number. Therefore, the mean value of Z_{eff} is given by $Z_{eff} = (Z_1^{1/2} + Z_2^{1/2})^2$, so the Thomas—Fermi screening length in the form of Firsov lead to:

$$a_F = a_{TF} = \frac{0.8853 a_0}{(\sqrt{Z_1} + \sqrt{Z_2})^{2/3}} \tag{7.9}$$

Lindhard et al [150] also suggest using the atomic TF screening function for the interatomic screening length with form:

$$a_L = \frac{0.8853 a_0}{(Z_1^{2/3} + Z_2^{2/3})^{1/2}} \tag{7.10}$$

However, the screening lengths presented in Eq. (7.9) and (7.10) do not differ significantly from each other. In all cases the screening lengths scale approximately with $Z^{1/3}$ of the colliding atoms. In addition, the potential equation $V(r) = \frac{Z_1 Z_2 e^2}{r} f(r)$ with Firsov's screening Eq.(7.9) and composed of Molière solution (7.7) result shielding Eq. (7.8), called Molière potential. The Molière potential is one of the generalized potentials, i.e. it is an analytic function that depends only on the atomic numbers and for all combinations of valid Z_1 and Z_2.

For the purpose of comparison, we incite several screening function models, these analytical forms are derived by fitting simple mathematical expression (7.7) to the exact solutions obtained by numerical integration [31], and reference therein. The earliest and best-known of these fits is the Sommerfeld asymptotic form:

$$f(x) = \{1 + (\frac{x}{12^{2/3}})^{0.772}\}^{-3.886} \tag{7.11}$$

Later, Lindhard and his co-workers had given an approximate, so-called "standard" Thomas-Fermi screen functions, as:

$$f(x) = 1 - \frac{x}{(3 + x^2)^{1/2}} \tag{7.12}$$

Additional screening functions have also been developed using different classical models of the atom, the simplest screening function is pure exponential according to Bohr:

$$f(x) = e^{-x} \tag{7.13}$$

And the screening function for Lenz-Jensen atom is

$$f_{LJ}(x) = 0.7466 e^{-1.038x} + 0.2433 e^{-0.3876x} + 0.01018 e^{-0.206x} \tag{7.14}$$

Another attempt to find an analytic function which accurately predicts the interatomic potential between atoms, Zeigler, Biersack and Mark Litt (ZBL) [38] calculated the RF potential of 261 randomly selected atom pair combinations. The model based on the hypothesis that each atom is a sphereically symmetric charge distribution. The total coulomb potential energy was taken as:

$$V_c(r) = V_{nm} + V_{en} + V_{ee} \tag{7.15}$$

where V_{nm} is the electron static potential energy between the nuclei, V_{en} is the interaction energy between each nucleus, and V_{ee} is the pure electrostatic interaction energy between the two electron distributions due to the Pauli principle. The calculated total interaction potential was used together with the screening function $V(r) = \frac{Z_1 Z_2 e^2}{r} f(r)$ to produce the "universal" screening function:

$$f_u(x) = 0.1818e^{-3.2x} + 0.5099e^{-0.9423x} + 0.2802e^{-0.4028x} + 0.02817e^{-0.2016x} \tag{7.16}$$

where the reduced distance is given by $x = \frac{r}{a_U}$, but the universal TF screening length is a little different from other models and defined by

$$a_U = \frac{0.8854 a_0}{Z_1^{0.23} + Z_2^{0.23}} \tag{7.17}$$

The Hartree-Fock(HF)[14] atomic model, also called self-consistent field method (SCF) derives the charge distribution outside of nuclei from quantum-mechanical principal but in the independent electron approximation (mean field model). It provides a more realistic model of electron density distributions. It induces changes which depend on the particular shell structure so that a slightly different atomic number can have rather different shields at certain distances.

Comparing the expression of Molière and universal or ZBL potential, both of them have a small form:

$$V(r) = \frac{Z_1 Z_2 e^2}{r} \sum_i a_i e^{-\frac{b_i}{a_F} r} \tag{7.18}$$

where a_i and b_i are the constant parameters indicated in the Eq.(7.8) and (7.16), respectively, a_F is the interatomic screening length, which depends on the parteners species.

O' Connor and Biersack [151] have adjusted this coefficient on a number of experiments to produce semi empirical values well accepted simply because they fit the experiment. They found that a correction factor needed for better agreement between the empirical potentials and the Molière potential, especially for the potential below 10eV, which is:

$$c = 0.0485(\sqrt{Z_1} + \sqrt{Z_2}) + 0.51 \tag{7.19}$$

[14] http://en.wikipedia.org/wiki/Hartree%E2%80%93Fock_method

Appendix C: Corrugation and image energy of proton scattering on LiF(001) surface

Proton at grazing incidence on LiF(001) surface, it will be neutralized once the first electron capture are around ~10a.u. above the surface, so the subsequent collision process with surface atom is exact the same as that of neutral hydrogen. With the experiment result, we measure the distance D (the sum of scattering the angle) between the beam and the scattered particles.

For neutrals, this angle is equal to 2 times the incidence angle (specular reflexion ($D=2*\theta_{in}$.)) and the normal energy is simply $E_{\perp}= E_0\sin^2(\theta_{in})$. But for protons, there is an image charge acceleration E_{im} before the impact so that specular reflexion occurs with an energy $E_{\perp}= E_0\sin^2(\theta) + E_{im}$. Therefore the angle measured is $D=\theta_{in} + \theta_{out}$, where θ_{out} is exit angle.

When the equatorial plane is observed, we know θ_{in} and therefore E_{im}. If diffraction is observed we should have a new measurement of the impact energy on the surface because the impact takes place as a neutral.

1) For hydrogen neutral scattering on LiF(001) along <100> direction, the relationship of amplitude of corrugation (h) and wavenumber (k) normal to the surface, we have:

$$h_0 = 0.017 + 0.0058k_{\perp}^{0}$$

As presented in Figure 6.20.

As we discussed above, proton grazing incidence on LiF(001) surface, proton will be neutralized above LiF surface at several Å, so the collision process is the same as hydrogen, and the relationship of amplitude of corrugation and wavenumber normal to the surface should be the same as with hydrogen neutral, but where the momentum is corrected for the image charge acceleration such as:

$$h_p = 0.017 + 0.0058k_{\perp}^{p}$$

When analyzing diffraction, the quantity measured is a ration h/λ, now the program Lect_mci compensates for the incident wavenumber, so that the user has a chance to work directly with a physical amplitude.

In fact the amplitude $h_{trough\_to\_peak} = h_i/G$ where G is the projected reciprocal lattice vector taken as dX in the program.

So if we measure h_n as if the projectile would be a neutral, the wavenumber considered is D/2, It means that the exact corrugation should be:

$h_p = h_{pn}\ 0.5*(k_{in} + k_{out})/k_{out}$

where h_p is what we want to know (the corrected value). h_{pn} is the value given by the program assuming that projectile is neutral. k_{in} and k_{out} are the wavenumbers such that $D= k_{in} + k_{out}$ and $k_{in}=\sqrt{2mE_0 \sin^2\theta_{in}}/\hbar$, $k_{out}=\sqrt{2m(E_0 \sin^2\theta_{in}+E_{im})}/\hbar$. For these parameters, we know: D, i.e. $k_{in}+k_{out}$; h_{pn} the corrugation produced by Lect_mci assuming a neutral particle;

The relation between k and h at the moment of neutral impact derived from study of H° impact. So we have:

$h_p=0.017+0.0058k_{out}$ (1)

$k_{out}=\sqrt{k_{in}^2+2mE_{im}}$) (2)

$k_{in}+k_{out}=D$ (3)

$h_p=h_{pn}*(k_{in}+k_{out})/(2*k_{out})$ (4)

There are 4 unkown numbers in 4 equations, it's easy to solve the unknown parameters.

Take the equation (1) and (3) into equation (4), we can get k_{out}, because it's a quadratic equations in one unknown of k_{out}, and there are two roots which one is positive and another one is negative, but during experiment, the wavenumber can never be negative value, so we only take the first one, which is:

K_{out}= (-0.1+sqrt(0.1*0.1+4*0.07*D*h_{pn}))/(2*0.0058*2) (5)

And take the result (5) into equation (1) or (4), we can get the real corrugation value.

h_p=0.017+0.058*(-0.1+$\sqrt{0.01+0.28\cdot D\cdot h_{pn}}$)/(2*0.0058*2) (6)

With the equation (2), the image charge effect can be calculated, because k_{in} is known due to the fact that k_{out} and D are known. The vibration of energy gain due to image charge effect also can be solved out, see Figure 6.28**,** and the corrected corrugation from trough to peak vs. vector k_{out} is illustrated in following figure.

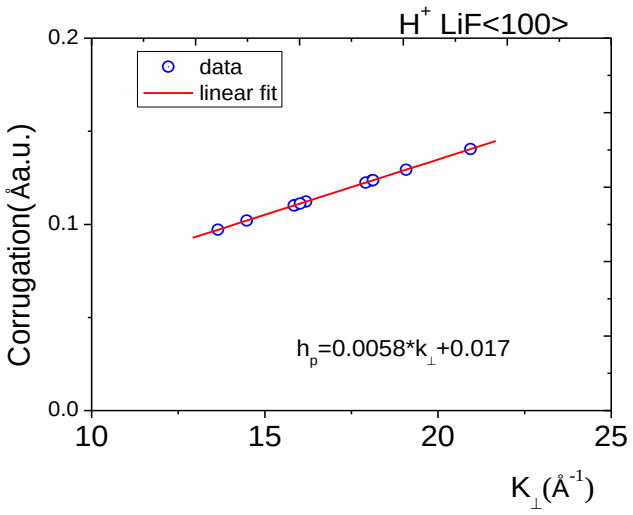

Corrected corrugation from trough to peak vs. outgoing scattering vector normal to the surface.

Appendix D: Momentum transverse along y-axis

In the experiment of GIFAD, the diffraction patterns lay on Laue circle in PSD with a radius equal to the normal energy $E_{\perp}$, as presented in Figure 6.18. Projectile interferes with surface atoms and then being scattered into detector, constructive or destructive interference on PSD depends on its phase shifts during the collision process.

In elastic collision process, outgoing angle has the same value of incidence, thus, the momentum normal for the 0^{th} diffraction pattern has the same absolute value but in opposite sign. However, for the ±1, ±2…diffraction patterns, have momentum transfer along y-axis with surface atoms:

$$k_f = k_i + n \cdot G_y \tag{7.20}$$

Where n is integral with value 0, ±1, ±2…, and G_y is the surface reciprocal parameter ($2\pi/a_y$). For the momentum transverse between adjacent patterns in Y-axis Δk, we have:

$$\Delta k = \frac{\sqrt{2mE_0}}{\hbar}\Delta\varphi \tag{7.21}$$

In the condition of maximum diffraction patterns, Δφ equal incident angle and then $\Delta k = k_{\perp}$.

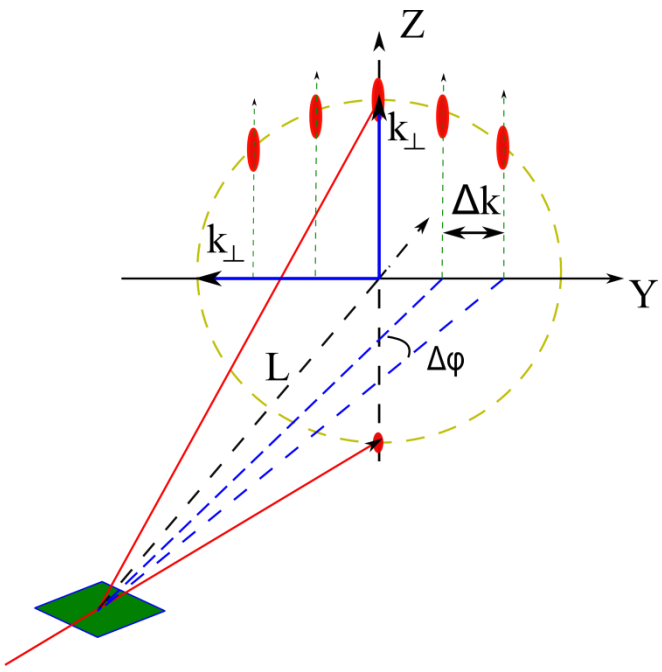

Illustration of diffraction geometry and momentum transfer.

In the experiment condition, Δφ can be easily deciphered since the distance from sample to PSD (L) and the diameter of detector is measurable, thus,

$$\Delta k = \frac{\sqrt{2mE_0}}{\hbar} \cdot \frac{\Delta y}{L} = \frac{\sqrt{2mE_0}}{\hbar} \cdot \frac{(y - y_0) \cdot \rho}{L} \tag{7.22}$$

where ρ is distance per pixel according to Y-axis, in our case, each pixel is 0.186mm/pixel (256*256), and the distance from sample to PSD L is 615mm. In the case of 0.5keV H° grazing scattering on LiF(001) surface along <100>, $\Delta k = 3.11 Å^{-1}$, see Figure 6.18. Along this crystal orientation, $G_y = 2\pi/a_y = 3.095 Å^{-1}$, where a_y is half of lattice parameter of LiF crystal (2.03Å).

Comparing experimental result and theoretic calculation, the results fit very well with each other. This technique also affords a method to detect the surface lattice parameter once we get the diffraction pattern.

Reference

1. Rabalais, J.W., *Principles and applications of ion scattering spectrometry*. surface chemical and structural analysis. 2003: Wiley-interscience. 13.
2. Gutser, R., D. Wuenderlich, and U. Fantz, *Negative hydrogen ion transport in RF-driven ion sources for ITER NBI.* Plasma Physics and Controlled Fusion, 2009. **51**(4).
3. Fubiani, G., et al., *Modeling of secondary emission processes in the negative ion based electrostatic accelerator of the International Thermonuclear Experimental Reactor.* Physical Review Special Topics-Accelerators and Beams, 2008. **11**(1).
4. Manson, J.R., H. Khemliche, and P. Roncin, *Theory of grazing incidence diffraction of fast atoms and molecules from surfaces.* Physical Review B, 2008. **78**(15): p. 155408.
5. Rabalais, J.W., *Principles and Applications of Ion Scattering Spectrometry.* WILEY-INTERSCIENCE, 2003.
6. Amersfoort, P.W.V., *Formation of negative ions on a metal surface*, in *Physics*. 1987, FOM Institute AMOLF: FOM-Institute, Amsterdam, the Netherlands.
7. Gruebler, W. and P.A. Schmelzbach, *Production of Intense Beams of Polarized Negative Hydrogen-Ions by Double Charge-Exchange in Alkali Vapor.* Nuclear Instruments & Methods in Physics Research, 1983. **212**(1-3): p. 1-4.
8. Wurz, P., R. Schletti, and M.R. Aellig, *Hydrogen and oxygen negative ion production by surface ionization using diamond surfaces.* Surface Science, 1997. **373**(1): p. 56-66.
9. Lederer, S., et al., *Electronic excitations during grazing scattering of hydrogen atoms on KI(001) and LiF(001) surfaces.* European Physical Journal D, 2007. **41**(3): p. 505-511.
10. Seely, D.G., et al., *Production of Long-Lived H(2)(-), HD(-), and D(2)(-) during Grazing Scattering Collisions of H(2)(+), H(3)(+), D(2)(+), D(3)(+) and D(2)H(+) Ions with KBr, KCl, and LiF Surfaces*, in *Application of Accelerators in Research and Industry*. 2009, Amer Inst Physics: Melville. p. 159-163.
11. Roncin, P., et al., *Energy loss of low energy protons on LiF(100): Surface excitation and H- mediated electron emission.* Physical Review Letters, 1999. **83**(4): p. 864-867.
12. I.Estermann and A. Stern, Z.Phys., 1930. **61**(95).
13. Desjonqueres, M.-C., Spanjaard, D., *Concepts in Surface Physics*. 2nd ed. Book. 1996, Gif sur yvette: springer.
14. Rousseau, P., et al., *Quantum scattering of fast atoms and molecules on surfaces.* Physical Review Letters, 2007. **98**(1): p. 4.
15. Schueller, A., S. Wethekam, and H. Winter, *Diffraction of fast atomic projectiles during grazing scattering from a LiF(001) surface.* Physical Review Letters, 2007. **98**(1).

16. Khemliche, H., et al., *Grazing incidence fast atom diffraction: An innovative approach to surface structure analysis.* Applied Physics Letters, 2009. **95**(15).

17. Bundaleski, N., et al., *Grazing Incidence Diffraction of keV Helium Atoms on a Ag(110) Surface.* Physical Review Letters, 2008. **101**(17): p. 4.

18. Schueller, A., et al., *Fast Atom Diffraction from Superstructures on a Fe(110) Surface.* Physical Review Letters, 2009. **102**(1).

19. Bundaleski, N., et al., *Grazing Incidence Diffraction of keV Helium Atoms on a Ag Surface.* Physical Review Letters, 2008. **101**(17).

20. Villette, J., *Étude Expérimentale de l'Interaction Rasante d'Atomes et d'Ions sur les Surfaces Isolantes*, in *Physics*. 2000, University Paris Sud 11: Paris.

21. Momeni, A., *Etude expérimentale des processus multi-électroniques lors de collisions d'ions en incidence rasante sur une surface de LiF(001)* in *Physics*. 2003, University Paris sud: Paris.

22. Rousseau, P., *Collisions rasantes d'ions ou d'atomes sur les surfaces: de l'échange de charge à la diffraction atomique*, in *Physics*. 2007, University Paris Sud 11: Paris.

23. Roncin, P., et al., *Energy loss and secondary electron measurements in collisions at grazing angle of 10 keV Oq+ ions on LiF surface.* Physica Scripta, 1999. **T80B**: p. 231-233.

24. Schenkel, T., et al., *Interaction of slow, very highly charged ions with surfaces.* Progress in Surface Science, 1999. **61**(2-4): p. 23-84.

25. Kohrbruck, R., et al., *Electron-Emission Following the Interaction of Highly-Charged Ions with a Pt(110) Target.* Physical Review A, 1993. **48**(5): p. 3731-3740.

26. Motohashi, K., M. Flores, and Y. Kanai, *Secondary-ion emission from GaN(0001) and dodecanethiol/Au(111) surfaces irradiated with Ar(q+) (q=4-8)*, in *14th International Conference on the Physics of Highly Charged Ions*. 2009.

27. Motohashi, K., *Fragmentation and desorption in low-energy highly charged ion collisions with molecules and surfaces*, in *14th International Conference on the Physics of Highly Charged Ions*. 2009.

28. Aumayr, F., A.S. El-Said, and W. Meissl, *Nano-sized surface modifications induced by the impact of slow highly charged ions - A first review.* Nuclear Instruments & Methods in Physics Research Section B-Beam Interactions with Materials and Atoms, 2008. **266**(12-13): p. 2729-2735.

29. Shimizu, S., et al., *Ion beam deceleration characteristics of a high-current, mass-separated, low-energy ion beam deposition system.* Review of Scientific Instruments, 1996. **67**(10): p. 3664-3671.

30. Morosov, V.A., et al., *2 pi spectrometer: A new apparatus for the investigation of ion surface interaction.* Review of Scientific Instruments, 1996. **67**(6): p. 2163-2170.

31. Nastasi, M.M., J. W. ; Hirvonen, J. K., *Ion-Solid Interactions: Fundamentals and Applications* ed. Cambridge University Press (March 29. 1996.

32. Cordier, K., *Diffusion rasante d'un atome par une surface isolante*. 2000: Paris.

33. Turkenburg, D.J.B.a.W.C., *Inelastic Energy-Loss Structure in Nonviolent Heavy-Atom Collisions.* Phys. Rev. Lett. , 1970. **25**(633).

34. Roncin, P., et al., *Energy loss of low energy protons on LiF Surface excitation and H-mediated electron emission.* Physical Review Letters, 1999. **83**(4): p. 864-867.

35. Kido, Y., S. Semba, and Y. Hoshino, *Inelastic energy loss and spectrum shape for medium energy He ions undergoing a large-angle single collision with Si(111)-root 3 x root 3-Sb.* Nuclear Instruments & Methods in Physics Research Section B-Beam Interactions with Materials and Atoms, 2004. **219**: p. 599-603.

36. Mertens, A., et al., *Excitation vs electron emission near the kinetic thresholds for grazing impact of hydrogen atoms on LiF(001).* Physical Review B, 2002. **65**(13).

37. Schüller, A., *Quantum rainbow scattering under axial surface lattice guidance of faster atoms- Fast Atom Diffraction*, in *Physics*. 2010, Humboldt University: Berlin.

38. J.F. Ziegler, J.P.B., U. Littmark., *The stopping and range of ions in solids*. The Stopping and ranges of ions of matter ; v. 1. 1985, New York: Pergamon.

39. Soullisse, P., *Développment d'un dispositif expérimental pour la diffraction d'atomes rapides et étude surface d'isolants ioniques*, in *Physics*. 2011, University paris sud 11: Paris.

40. Borisov, A.G., et al., *Evidence for the stopping of slow ions by elicitations of optical phonons in insulators.* Physical Review Letters, 1999. **83**(25): p. 5378-5381.

41. Villette, J., *Etude expérimentale de l'interaction rasante d'atomes et d'ions sur des surfaces isolantes*, in *Laboratoire des collisions atomiques et moléculaires*. 2000, University Paris sud 11. p. 154.

42. Siketic, Z., et al., *Time of flight elastic recoil detection analysis with a position sensitive detector.* Review of Scientific Instruments. **81**(3).

43. Dezelah, C.L.I.V., et al., *A pyrazolate-based metalorganic tantalum precursor that exhibits high thermal stability and its use in the atomic layer deposition of Ta2O5.* Journal of the American Chemical Society, 2007. **129**(41): p. 12370-+.

44. Winter, H., *Collisions of atoms and ions with surfaces under grazing incidence.* Physics Reports-Review Section of Physics Letters, 2002. **367**(5): p. 387-582.

45. Winter, H., et al., *Electronic processes during impact of fast hydrogen atoms on a LiF surface.* Nuclear Instruments & Methods in Physics Research Section B-Beam Interactions with Materials and Atoms, 2003. **212**: p. 45-50.

46. Roncin, P., et al., *Evidence for F- formation by simultaneous double-electron capture during scattering of F+ from a LiF surface.* Physical Review Letters, 2002. **89**(4).

47. Kaviany, M., *Principles of heat transfer*, ed. Wiley-IEEE. 2002.

48. William H. Press, S.A.T., William T. Vetterling, Brian P. Flannery, *Numerical Recipes in C: The Art of Scientific Computing*, ed. Cambridge University Press (March 29. 1992.

49. Auth, C., et al., *Image Charge Acceleration of Multicharged Ions in Front of the Surface of an Insulator.* Physical Review Letters, 1995. **74**(26): p. 5244-5247.

50. Zemih, R., et al., *Image potential effect on the specular reflection coefficient of alkali ions scattered from a nickel surface at low energy.* Nuclear Instruments & Methods in Physics Research Section B-Beam Interactions with Materials and Atoms, 2002. **193**: p. 396-402.

51. Robin, A., et al., *Highly charged ions impinging on a stepped metal surface under grazing incidence.* Physical Review A, 2003. **67**(5).

52. Hidouche, A., et al., *Specular reflection model study of the image effect in He+/a : Si scattering at low energy.* Nuclear Instruments & Methods in Physics Research Section B-Beam Interactions with Materials and Atoms, 2005. **230**: p. 178-184.

53. Wethekam, S., et al., *Neutralization of charged fullerenes during grazing scattering from a metal surface.* Physical Review Letters, 2007. **99**(3).

54. Yamazaki, Y., *Production of hollow atoms (ions) in HCl-surface collision.* Physica Scripta, 1997. **T73**: p. 293-297.

55. Lemell, C., et al., *Image acceleration of highly charged ions by metal surfaces.* Physical Review A, 1996. **53**(2): p. 880-885.

56. Limburg, H., *Hollow-Atom Probing of Surfaces*, in *Physics*. 1996.

57. Villette, J., et al., *Subsurface-channeling-like energy loss structure of the skipping motion on an ionic crystal.* Physical Review Letters, 2000. **85**(15): p. 3137-3140.

58. Echenique, P.M. and A. Howie, *Image Force Effects in Electron-Microscopy.* Ultramicroscopy, 1985. **16**(2): p. 269-272.

59. Brusdeylins, G., et al., *Observation of Surface Optical Phonons in Naf(001) by Inelastic He-Atom Scattering.* Physical Review Letters, 1985. **54**(5): p. 466-469.

60. Bracco, G., et al., *Surface Optical Phonons in Lif(001) Observed by Inelastic Helium Scattering.* Physical Review B, 1986. **34**(12): p. 9045-9046.

61. Scheer, J.A., et al., *High negative ion yield from light molecule scattering.* Nuclear Instruments & Methods in Physics Research Section B-Beam Interactions with Materials and Atoms, 2005. **230**: p. 330-339.

62. Peko, B.L. and T.M. Stephen, *Absolute detection efficiencies of low energy H, H-, H+, H-2(+) and H-3(+) incident on a multichannel plate detector.* Nuclear Instruments & Methods in Physics Research Section B-Beam Interactions with Materials and Atoms, 2000. **171**(4): p. 597-604.

63. Ishikawa, J., et al., *Negative-Ion Implantation Technique.* Nuclear Instruments & Methods in Physics Research Section B-Beam Interactions with Materials and Atoms, 1995. **96**(1-2): p. 7-12.

64. Souda, R., et al., *Capture and loss of valence electrons during low energy H+ and H- scattering from LaB6(100), Cs/Si(100), graphite and LiCl.* Surface Science, 1999. **421**(1-2): p. 89-99.

65. Merino, J., et al., *Charge transfer of slow H atoms interacting with Al: Dynamical charge evolution.* Physical Review B, 1998. **57**(3): p. 1947-1956.

66. Maazouz, M., et al., *Effect of metal band characteristics on resonant electron capture: H- formation in the scattering of hydrogen ions on Mg, Al, and Ag surfaces.* Physical Review B, 1997. **55**(20): p. 13869-13877.

67. Tarvainen, O., *The effects of cesium equilibrium on H(-) ion beam production with LANSCE surface converter ion source.* Nuclear Instruments & Methods in Physics Research Section a-Accelerators Spectrometers Detectors and Associated Equipment, 2009. **601**(3): p. 270-275.

68. Groß, A., *Theoretical Surface Science: A Microscopic Perspective*. 2009: Springer.

69. Limburg, H., et al., *Negative ion formation in collisions slow C, O and E ions with Al surface.* Izvestiya Akademii Nauk Seriya Fizicheskaya, 1998. **62**(4): p. 797-800.

70. Folkerts, L., et al., *Time Scales for Charge Equilibration of O-Q+ (3-Less-Than-or-Equal-to-Q-Less-Than-or-Equal-to-8) Ions During Surface-Channeling Interactions with Au(110).* Physical Review Letters, 1995. **74**(12): p. 2204-2207.

71. Bahrim, B., B. Makarenko, and J.W. Rabalais, *Mechanism of negative ion formation in low velocity collisions at surfaces.* Surface Science, 2003. **542**(3): p. 161-166.

72. Borisov, A.G. and V. Sidis, *Theory of negative-ion conversion of neutral atoms in grazing scattering from alkali halide surfaces.* Physical Review B, 1997. **56**(16): p. 10628-10643.

73. Borisov, A.G., et al., *Formation of negative halogen ions in grazing scattering from an Al(111) surface: Multielectron effects.* Physical Review B, 1999. **59**(12): p. 8218-8231.

74. Maazouz, M., et al., *Electron capture and loss in the scattering of fluorine and chlorine atoms and ions on metal surfaces.* Surface Science, 1998. **409**(2): p. 189-198.

75. Bauschlicher, C.W., et al., *On the Electron-Affinity of the Oxygen Atom.* Journal of Chemical Physics, 1986. **85**(6): p. 3407-3410.

76. Winters, H.F. and D. Haarer, *Influence of Doping on the Etching of Si(111).* Physical Review B, 1987. **36**(12): p. 6613-6623.

77. Jacquot, C., et al., *Negative ion production in large volume source with small deposition of cesium.* Review of Scientific Instruments, 1996. **67**(3): p. 1036-1038.

78. Philipp, P., et al., *Neutral cesium deposition prior to SIMS analysis of inorganic and organic samples.* Surface and Interface Analysis. **42**(9): p. 1499-1506.

79. Garcia, E.A., et al., *Hydrogen scattering from a LiF ionic surface: Madelung potential and local environment effects.* Physical Review B, 1999. **59**(20): p. 13370-13378.

80. Auth, C., et al., *Formation of negative ions in grazing scattering from insulator surfaces.* Physical Review A, 1998. **57**(1): p. 351-361.

81. Winter, H., *Scattering of atoms and ions from insulator surfaces.* Progress in Surface Science, 2000. **63**(7-8): p. 177-247.

82. Zhou, H., et al., *Energy loss of keV fluorine ions scattered off a missing-row reconstructed Au(110) surface under grazing incidence* Physical Review A, 2012. **85**(1).

83. Ustaze, S., et al., *Electron capture and loss processes in the interaction of hydrogen, oxygen, and fluorine atoms and negative ions with a MgO surface.* Physical Review Letters, 1997. **79**(18): p. 3526-3529.

84. Schulz, G.J., *Resonances in Electron Impact on Atoms.* Reviews of Modern Physics, 1973. **45**(3): p. 378-422.

85. Kurahashi, M. and Y. Yamauchi, *Metastable helium atom stimulated desorption of H+ ion.* Physical Review Letters, 2000. **84**(20): p. 4725-4728.

86. Schiesko, L., et al., *A comparative study of H(-) and D(-) production on graphite surfaces in H(2) and D(2) plasmas.* Plasma Sources Science & Technology. **19**(4).

87. Schiesko, L., et al., *Negative ion surface production through sputtering in hydrogen plasma.* Applied Physics Letters, 2009. **95**(19).

88. Tsumori, K., et al., *Large ion yields in hydrogen scattering from a graphite surface.* Journal of Applied Physics, 1997. **81**(9): p. 6390-6396.

89. Vidal, R.A., et al., *Electron capture and loss in the scattering of H+ from HOPG graphite.* Surface Science, 2011. **605**(1-2): p. 18-23.

90. Kundu, R., et al., *Electronic structure of single crystal and highly oriented pyrolytic graphite from ARPES and KRIPES.* Physica B-Condensed Matter, 2012. **407**(5): p. 827-832.

91. Negishi, H., et al., *Electronic structures of HOPG and stage-2 IBr-GIC studied by angle resolved photoemission.* Journal of Physics and Chemistry of Solids, 2006. **67**(5-6): p. 1145-1148.

92. Hecht, T., et al., *Role of the 2D surface state continuum and projected band gap in charge transfer in front of a Cu111 surface.* Physical Review Letters, 2000. **84**(11): p. 2517-2520.

93. Isakhanov, Z.A., et al., *Optimum ion implantation and annealing conditions for stimulating secondary negative ion emission.* Technical Physics. **56**(4): p. 546-549.

94. Bonetto, F., et al., *Experimental and theoretical study of charge transfer in hydrogen ion scattering from a graphite surface.* Applied Surface Science, 2007. **254**(1): p. 62-64.

95. Winter, H., C. Auth, and A.G. Borisov, *Formation of negative ions in grazing scattering from a LiF(100) surface.* Nuclear Instruments & Methods in Physics Research Section B-Beam Interactions with Materials and Atoms, 1996. **115**(1-4): p. 133-136.

96. Lienemann, J., et al., *Negative ion formation during scattering of fast ions from diamond-like carbon surfaces.* Nuclear Instruments & Methods in Physics Research Section B-Beam Interactions with Materials and Atoms, 2011. **269**(9): p. 915-918.

97. Von Gemmingen, U. and R. Sizmann, *Charge states of slow hydrogen ions reflected at single crystal surfaces.* Surface Science, 1982. **114**(2-3): p. 445-458.

98. Kovach, G., et al., *Thin film carbon layers with continously changing bonding properties*, in *Materials Science, Testing and Informatics III*. 2007, Trans Tech Publications Ltd: Stafa-Zurich. p. 207-214.

99. Roentdek GmbH, K., Ruppertshain, *DLD40, Germany.* from the reference of J.Lienemann's reference. **2011**(http://dx.doi.org/10.1016/j.nimb.2010.11.054).

100. Vanwunnik, J.N.M., J.J.C. Geerlings, and J. Los, *The Velocity Dependence of the Negatively Charged Fraction of Hydrogen Scattered from Cesiated Tungsten Surfaces.* Surface Science, 1983. **131**(1): p. 1-16.

101. Gleeson, M.A. and A.W. Kleyn, *Effects of Cs-adsorption on the scattering of low energy hydrogen ions from HOPG.* Nuclear Instruments & Methods in Physics Research Section B-Beam Interactions with Materials and Atoms, 1999. **157**(1-4): p. 48-54.

102. R M Eastment, C.H.B.M., *Work function measurements on (100), (110) and (111) surfaces of aluminium.* J. Phys. F: Met. Phys. , 1973. **3**(9): p. 1738.

103. Wyputta, F., R. Zimny, and H. Winter, *H- Formation in Grazing Collisions of Fast Protons with an Al(111) Surface.* Nuclear Instruments & Methods in Physics Research Section B-Beam Interactions with Materials and Atoms, 1991. **58**(3-4): p. 379-383.

104. Lienemann, J., et al., *Negative ion formation during scattering of fast ions from diamond-like carbon surfaces.* Nuclear Instruments & Methods in Physics Research Section B-Beam Interactions with Materials and Atoms. **269**(9): p. 915-918.

105. Takahashi, T., H. Tokailin, and T. Sagawa, *Angle-resolved ultraviolet photoelectron spectroscopy of the unoccupied band structure of graphite.* Physical Review B, 1985. **32**(12): p. 8317-8324.

106. Shirley, D.A., *High-Resolution X-Ray Photoemission Spectrum of the Valence Bands of Gold.* Physical Review B, 1972. **5**(12): p. 4709-4714.

107. Echenique, P.M., et al., *Nonlinear stopping power of an electron gas for slow ions.* Physical Review A, 1986. **33**(2): p. 897-904.

108. Robertson, J., *Electronic structure of diamond-like carbon.* Diamond and Related Materials, 1997. **6**(2-4): p. 212-218.

109. Ryu, S., et al., *Raman Spectroscopy of Lithographically Patterned Graphene Nanoribbons.* Acs Nano, 2011. **5**(5): p. 4123-4130.

110. Sueyoshi, T., et al., *Low-density band-gap states in pentacene thin films probed with ultrahigh-sensitivity ultraviolet photoelectron spectroscopy.* Applied Physics Letters, 2009. **95**(18).

111. Vitali, L., et al., *Phonon and plasmon excitation in inelastic electron tunneling spectroscopy of graphite.* Physical Review B, 2004. **69**(12).

112. Lederer, S., et al., *Kinetic electron emission from the selvage of a free-electron-gas metal.* Physical Review B, 2003. **67**(12).

113. Aono, M. and R. Souda, *Inelastic Processes in Ion-Scattering Spectroscopy of Solid-Surfaces.* Nuclear Instruments & Methods in Physics Research Section B-Beam Interactions with Materials and Atoms, 1987. **27**(1): p. 55-64.

114. *An electron spectroscopic investigation of the interaction of methanol with polycrystalline aluminum*. 1980. p. 388.

115. Winter, H.P., et al., *Electron emission for grazing slow atom and ion impact on monocrystalline metal and insulator surfaces.* Physica Scripta, 2005. **72**(1): p. C12-C21.

116. Lederer, S., et al., *Electronic excitations during grazing scattering of hydrogen atoms on KI and LiF surface.* European Physical Journal D, 2007. **41**(3): p. 505-511.

117. Winter, H., et al., *Statistics of electron and exciton production for grazing impact of keV hydrogen atoms on LiF surface.* Journal of Physics B-Atomic Molecular and Optical Physics, 2002. **35**(15): p. 3315-3325.

118. Winter, H., C. Auth, and A. Mertens, *Stopping of low energy protons during grazing scattering from a LiF(001) surface.* Nuclear Instruments and Methods in Physics Research Section B: Beam Interactions with Materials and Atoms, 2000. **164-165**(0): p. 559-565.

119. Kimura, K., G. Andou, and K. Nakajima, *Surface-plasmon-assisted secondary-electron emission from an atomically flat LiF(001) surface.* Nuclear Instruments and

Methods in Physics Research Section B: Beam Interactions with Materials and Atoms, 2000. **164-165**(0): p. 933-937.

120. Stolzle, F. and R. Pfandzelter, *Observation of Discrete Energy-Loss Peaks in Grazing-Angle Scattering of Protons from a Graphite Surface.* Surface Science, 1991. **251**: p. 383-386.

121. Andrei, E.Y., G. Li, and X. Du, *Electronic properties of graphene: a perspective from scanning tunneling microscopy and magnetotransport.* Reports on Progress in Physics, 2012. **75**(5).

122. Hecht, T., et al., *Effect of the projected band gap on the formation of negative ions in grazing collisions from Cu surfaces.* Faraday Discussions, 2000. **117**: p. 27-40.

123. Hecht, T., et al., *Role of the 2D surface state continuum and projected band gap in charge transfer in front of a Cu(111) surface.* Physical Review Letters, 2000. **84**(11): p. 2517-2520.

124. Gleeson, M.A. and A.W. Kleyn, *Effects of Cs-adsorption on the scattering of low energy hydrogen ions from HOPG.* Nuclear Instruments and Methods in Physics Research Section B: Beam Interactions with Materials and Atoms, 1999. **157**(1â€“4): p. 48-54.

125. Lienemann, J., et al., *Coherence during Scattering of Fast H Atoms a LiF surface.* Physical Review Letters, 2011. **106**(6): p. 067602.

126. Schueller, A., et al., *Fast atom diffraction during grazing scattering from a MgO surface.* Surface Science, 2012. **606**(3-4): p. 161-173.

127. Schueller, A. and H. Winter, *Diffraction of fast atoms under axial surface channeling conditions.* Nuclear Instruments & Methods in Physics Research Section B-Beam Interactions with Materials and Atoms, 2009. **267**(4): p. 628-633.

128. KITTEL, C., *Introduction to Solid State Physics*, ed. I. John Wiley & Sons. 1995.

129. Rousseau, P., et al., *Surface analysis with grazing incidence fast atom diffraction-GIFAD*, in *24th Summer School and International Symposium on the Physics of Ionized Gases*. 2008.

130. Busch, M., et al., *Fast atom diffraction at metal surface.* Surface Science, 2009. **603**(3): p. L23-L26.

131. Masel, R.I., R.P. Merrill, and W.H. Miller, *Quantum scattering from a sinusoidal hard wall: Atomic diffraction from solid surfaces.* Physical Review B, 1975. **12**(12): p. 5545-5551.

132. Lapujoulade, J., *An Effective Hard-Wall Model for the Calculation of the Debye-Waller Factor in Atom Surface Diffraction.* Surface Science, 1983. **134**(2): p. L529-L536.

133. Armand, G. and J.R. Manson, *Scattering of Neutral Atoms by an Exponential Corrugated Potential.* Physical Review Letters, 1979. **43**(24): p. 1839-1842.

134. Beeby, J.L., *The scattering of helium atoms from surfaces.* J. Phys. C: Solid State Phys., 1971. **C4**(L359).

135. Auth, C., et al., *Threshold in the stopping of slow protons scattered from the surface of a wide-band-gap insulator.* Physical Review Letters, 1998. **81**(22): p. 4831-4834.

136. Bundaleski, N., et al., *Decoherence in fast atom diffraction from surfaces.* Nuclear Instruments & Methods in Physics Research Section B-Beam Interactions with Materials and Atoms, 2011. **269**(11): p. 1216-1220.

137. Miraglia, J.E. and M.S. Gravielle, *Production of excitons in grazing collisions of protons with LiF surfaces: An onion model.* Physical Review A. **84**(6).

138. Finzel, H.U., et al., *Atom-surface scattering with velocity-selected H and D atomic beams from LiF and NaF.* Surface Science, 1975. **49**(2): p. 577-605.

139. Winter, H. and A. Schueller, *Fast atom diffraction during grazing scattering from surfaces.* Progress in Surface Science, 2011. **86**(9-10): p. 169-221.

140. Aigner, F., et al., *Fast-Atom Diffraction at Surfaces*, in *Xxvi International Conference on Photonic, Electronic and Atomic Collisions*. 2009.

141. Winter, H., C. Auth, and A.G. Borisov, *Formation of negative ions in grazing scattering from a LiF surface.* Nuclear Instruments & Methods in Physics Research Section B-Beam Interactions with Materials and Atoms, 1996. **115**(1-4): p. 133-136.

142. Winter, H., et al., *Statistics of electron and exciton production for grazing impact of keV hydrogen atoms on a LiFsurface.* Journal of Physics B-Atomic Molecular and Optical Physics, 2002. **35**(15): p. 3315-3325.

143. PerezPerez, F.J., et al., *Collective effects in the energy loss of large hydrogen clusters.* Physical Review A, 1996. **54**(5): p. 4145-4152.

144. Lienemann, J., et al., *Negative ion formation during scattering of fast ions from diamond-like carbon surfaces.* Nuclear Instruments and Methods in Physics Research Section B: Beam Interactions with Materials and Atoms, 2011. **269**(9): p. 915-918.

145. Maazouz, M., et al., *Electron capture and loss in the scattering of hydrogen and oxygen ions on a Si surface.* Surface Science, 1998. **398**(1â€“2): p. 49-59.

146. Amanbaev, E.R., D.K. Shestakov, and I.K. Gainullin, *Features of electron exchange under grazing scattering of negative hydrogen ions by a spherical cluster of aluminum atoms.* Journal of Surface Investigation-X-Ray Synchrotron and Neutron Techniques, 2009. **3**(6): p. 865-868.

147. GarcÃ-a, E.A., et al., *Ion fractions in the scattering of hydrogen on different reconstructed silicon surfaces.* Surface Science, 2006. **600**(10): p. 2195-2206.

148. García, E.A.P., C. González; Bolcatto, P. G.; Passeggi, M. C. G.; Goldberg, E. C., *Ion fractions in the scattering of hydrogen on different reconstructed silicon surfaces.* Surface Science, 2006. **600**(10): p. 2195-2206.

149. Cernusca, S., et al., *Ion-induced kinetic electron emission from HOPG with different surface orientation.* Europhysics Letters, 2005. **70**(6): p. 768-774.

150. Lindhard, J., *Citation Classic - Range Concepts and Heavy-Ion Ranges - Notes on Atomic-Collisions .2.* Current Contents/Physical Chemical & Earth Sciences, 1983(25): p. 20-20.

151. Oconnor, D.J. and J.P. Biersack, *Comparison of Theoretical and Empirical Interatomic Potentials.* Nuclear Instruments & Methods in Physics Research Section B-Beam Interactions with Materials and Atoms, 1986. **15**(1-6): p. 14-19.